Propulsion Characteristics and Visual Servo Control of Scaled-up Helical Microswimmers

Tiantian Xu

UPMC
SORBONNE UNIVERSITÉS

UNIVERSITÉ DE PIERRE ET MARIE CURIE

ECOLE DOCTORALE

SCIENCES MÉCANIQUES, ACOUSTIQUE, ÉLECTRONIQUE ET ROBOTIQUE

T H È S E

pour obtenir le titre de

Docteur

de l'Université de Pierre et Marie Curie

Mention : Robotique

Présentée par

Tiantian Xu

Propulsion Characteristics and Visual Servo Control of Scaled-up Helical Microswimmers

Thèse dirigée par Stéphane Régnier

soutenue le 13/03/2014

Jury :

Rapporteurs :	Pr. Christine Prelle	-	Université de Technologie de Compiègne
	Pr. Pierre Renaud	-	INSA Strasbourg
Directeur :	Pr. Stéphane Régnier	-	Université de Pierre et Marie Curie
Co-directeurs :	Pr. Nicolas Andreff	-	Université de Franche-Comté
	Dr. Gilgueng Hwang	-	Laboratoire de Photonique et de Nanostructures
Examinateurs :	Dr. Riccardo Scorretti	-	Université Lyon 1
	Pr. Jérôme Szewczyk	-	Université de Pierre et Marie Curie
Invité :	Dr. Li Zhang	-	Chinese University of Hong Kong

Acknowledgements

The research described in this thesis was carried out from October 2010 to February 2014 at the Institut des système intelligent et de Robotique (ISIR) in the University Pierre and Marie Curie in Paris (UPMC). This thesis is undertaken in the Micro-nano robotique group (MICROB) directed by Prof. Stéphane Régnier. My thesis work is financially supported by the Franche-Comté Region and the Centre National de la Recherche Scientifique (CNRS).

First of all, I would like to thank my supervisors Stéphane Régnier, Nicolas Andreff, and Gilgueng Hwang for their encouragement, helpful guidance, great care, valuable advices, and continuous and indispensable assistance. Stéphane Régnier, professor at UPMC, guided me through all the years in the good direction of my research. It is really my pride to perform my Ph.D. research under his supervision and it is a fact that this thesis would not have been possible unless his supervision. Gilgueng Hwang, researcher in Laboratoire de Photonique et de Nanostructures (LPN), worked on the helical microswimming before. He helped me a lot at the beginning of my thesis to be be familiar with the subject. Nicolas Andreff, professor at Femto-ST in Besançon, helped me a lot in the visual servoing control part. His help is very important for me to finish my thesis. I would like to thank all of them for their availability for numerous discussions and their motivating investments in the research through my thesis.

I would also like to thank Sinan Haliyo, assistant professor in our team, for his great support on configuration of the system in Linux; Sylvain Pledel, the mechanical engineer, for the mechanical parts that he made for me; Christophe Grand for the rapid prototyping parts; Thomas Seon, researcher in fluid mechanics, for the valuable discussion about viscous liquids and his help of the measurement of the viscosity of the liquids.

I would also like to thank all the current and former members of ISIR, specially the members of our team MICROB, for their friendship and support. They have made the entire graduate experience educational, entertaining, and enjoyable. We had a lot of interesting discussions. I'm happy to list their names here: Jean Ochin Abrahamians, Soukeyna Bouchebout, Aude Bolopion, Mokrane Boudaoud, Laura Cohen, Allister Fourtet, Tianming Lu, Abdenbi Mohand Ousaid, Gillaume Millet, Zhenjiang Ni, Cécile Pacoret, Antoine Weill-Duflos.

At last, I want to give all my loving thanks to my parents. They have lost a lot time to have me around due to my research abroad. Without their encouragement and understanding it would have been impossible for me to finish this work. I would also like to thank the family Best, who is my host family when I arrived in France at Lille. The whole family is very kind and adorable. I'm very close to the family during my eight years in France. They helped and supported my a lot. I would also like to thank my dear boyfriend for sharing the pleasing and difficult moments during all my graduate years. His encouragement and supports helps me a lot to finish my thesis.

30/01/2014
in Paris

Abstract: Helical microswimmers capable of propulsion at low Reynolds numbers have been proposed for numerous applications, ranging from in vitro tasks on lab-on-a-chip (e.g. transporting and sorting micro objects; mechanical components micro assembly...) to in vivo applications for minimally invasive medicine (e.g. targeted drug delivery; brachytherapy; hyperthermia...), due to their micro sizes and accessibility to tiny and clustered environments.

Several kinds of magnetically actuated helical swimmers with different geometry parameters, head shapes, and magnetic positioning have been proposed in prior works. However, the influence of the geometry parameters, the head shape and the magnetic positioning (head, coated tail...) has not been clearly studied. As far as we know, the existing helical microswimmers are primarily open-loop controlled, due to the complexity of the control of the magnetic field actuating the helical propulsion, and the limited number of feedback options processing the required precision. This thesis aims to:

- compare the swimming performances of helical swimmers with different designs to further improve their design and to characterize their swimming properties.
- realize a visual servo control of helical swimmers.

Scaled-up helical microswimmers at the millimeter scale are designed and swim at low Reynolds numbers. The design of these scaled-up helical microswimmers can be a guideline for the micro-fabrication of helical microswimmers. A visual servo control of the scaled-up helical microswimmer orientation in the 3D space, and a path following on the horizontal plane have been realized. The control method will be applied on helical microswimmers in future works.

Keywords: Microswimmer, low Reynolds number, helical propulsion, visual servoing, path following

Résumé : L'utilisation de micronageurs hélicoidaux capables de se mouvoir dans des liquides à faible nombre de Reynolds trouve son intérêt dans beaucoup d'applications: de tâches in-vitro dans des laboratoires sur puce (transport et tri de micro-objets; assemblage de micro-composants...), à des applications in-vivo en médecine mini-invasive (livraison interne et ciblée de médicaments, curiethérapie, thermothérapie...); grace à leur dimensions microscopiques et agilité permettant l'accès à des endroits normalement très restreints.

Plusieurs types de nageurs hélicoidaux actionnés magnétiquement possédant divers paramètres géométriques, formes de tête et positions de la partie magnétique ont été proposés dans de précédents travaux. Cependant, l'influence de tous ces paramètres n'a pas clairement été étudiée. À notre connaissance, les micronageurs hélicoidaux dans l'état de l'art sont principalement contrôlés en boucle ouverte, en raison de la complexité de la commande du champ magnétique actionnant la propulsion, et du nombre limité de retours ayant des critères satisfaisants. Cette thèse vise à:

- comparer les performances de déplacement de nageurs hélicoidaux avec des conceptions différentes afin d'améliorer leur design et de les caractériser.
- réaliser un asservissement visual de nageur hélicoidal.

Pour se faire, des nageurs hélicoidaux de tailles millimétriques ont été conçus et sont mis en conditions à faible nombre de Reynolds. La conception de ces "millinageurs" servira de base à la conception de micronageurs. Une commande boucle fermée par retour visuel de l'orientation d'un micronageur hélicoidal dans un espace 3D, et un suivi de trajectoires sur plan horizontal ont été effectués. Cette méthode de commande sera par la suite appliquée à des micronageurs hélicoidaux.

Mots clés : Micronageur, faible nombre de Reynolds, propulsion hélicoidale, asservissement visuel, suivie du chemin

Contents

List of abbreviations

ABF Artificial Bacterial Flagella.

ABS Acrylonitrile Butadiene Styrene.

CT Computed Tomography.

DLT Direct Linear Transformation.

DoE Design of Experiments.

DoF Degrees of Freedom.

FDM Fused Deposition Modeling.

GLAD GLancing Angle deposition.

HNB Helical NanoBelt.

IBVS Image-Based Visual servoing.

MBE Molecular Beam Epitaxy.

MEMS Micro Electronic Mechanical System.

MRI Magnetic Resonance Imaging.

MTB Magnetotactic bacteria.

PBVS Pose-Based Visual servoing.

PDMS Polydimethylsiloxane.

PID Proportional-Integral-Derivative.

RFT Resistive Force Theory.

RPM Rotating Permanent Magnet.

SEM Scanning Electron Microscope.

SHM Scaled-up Helical Microswimmer.

SVD Singular Value Decomposition.

ViSP Visual Servoing Platform.

List of symbols

λ_U Control parameter for magnetic field control

$\mathcal{R}_c = (C, x_c, y_c, z_c)$ Camera coordinate system

$\mathcal{R}_{cs} = (C_s, x_{cs}, y_{cs}, z_{cs})$ Coordinate system of the side camera

$\mathcal{R}_{ct} = (C_t, x_{ct}, y_{ct}, z_{ct})$ Coordinate system of the top camera

$\mathcal{R}_{ims} = (O_{ims}, x_{ims}, y_{ims})$ 2D metric image coordinate system of the side camera

$\mathcal{R}_{imt} = (O_{imt}, x_{imt}, y_{imt})$ 2D metric image coordinate system of the top camera

$\mathcal{R}_{im} = (o_{im}, x, y)$ 2D image metric coordinate system

$\mathcal{R}_{ips} = (O_{ips}, u_{ips}, v_{ips})$ 2D pixel image coordinate system of the side camera

$\mathcal{R}_{ipt} = (O_{ipt}, u_{ipt}, v_{ipt})$ 2D pixel image coordinate system of the top camera

$\mathcal{R}_{ip} = (o_{ip}, u, v)$ 2D image pixel coordinate system

$\mathcal{R}_w(O, x, y, z)$ World coordinate system

μ_0 Permeability constant

ω Angular velocity of the self-rotation of the SHM

Ω_x Angular velocity of the steering of the SHM on the horizontal plane

$\overrightarrow{\tau}$ Applied magnetic torque

$\overrightarrow{f_a}$ Applied nonfluidic force

$\overrightarrow{f_{app}}$ Apparent weight

$\overrightarrow{M}$ Dipole moment

$\overrightarrow{n}$ Normal vector of the axis of the SHM

ρ Density of the liquid

$\mathbf{B}$ The magnetic field generated by the 3D Helmholtz coil pairs

$\mathbf{B}_{\parallel \mathbf{n}}$ Magnetic field parallel to the axis $\mathbf{n}$

$\mathbf{B}_{\perp \mathbf{n}}$ Magnetic field perpendicular to the axis $\mathbf{n}$

$\mathbf{h}_s$ Normal vector of the plane defined by the center of the side camera and the axis of the SHM in the world coordinate system

$\mathbf{h}_t$ Normal vector of the plane defined by the center of the top camera and the axis of the SHM in the world coordinate system

$\mathbf{K}$ Camera calibration matrix

$\mathbf{K}_s$ Calibration matrix of the side camera

$\mathbf{K}_t$ Calibration matrix of the top camera

$\mathbf{n} = (n_x, n_y, n_z)^T$ Axis of the SHM in the world coordinate system

$\mathbf{n}^*$ Target orientation of the SHM

$\mathbf{s}$ Current values of the features

$\mathbf{s}^*$ Desired values of the features

$\mathrm{d}_{\mathrm{phase}}$ Phase different of the currents

θ_d Direction angle of the SHM

θ_d^* Angle between the current tangent of the reference path and the z axis

θ_d^* Target direction angle of the SHM

θ_e Direction angle error between the SHM and the reference path

θ_i Inclination angle of the SHM

${}^{cs}\mathbf{M}_{tp}$ Transformation matrix from the test pattern to the side camera coordinate system

${}^{cs}\mathbf{R}_{tp}$ Rotation matrix from the test pattern to the side camera coordinate system

${}^{cs}\mathbf{t}_{tp}$ Translation matrix from the test pattern to the side camera coordinate system

${}^{ct}\mathbf{M}_{cs}$ Transformation matrix from the top camera to the side camera coordinate system

${}^{ct}\mathbf{M}_{tp}$ Transformation matrix from the test pattern to the top camera coordinate system

${}^{ct}\mathbf{R}_{cs}$ Rotation matrix from the top camera to the side camera coordinate system

${}^{ct}\mathbf{R}_{tp}$ Rotation matrix from the test pattern to the top camera coordinate system

${}^{ct}\mathbf{t}_{cs}$ Translation matrix from the top camera to the side camera coordinate system

${}^{ct}\mathbf{t}_{tp}$ Translation matrix from the test pattern to the top camera coordinate system

${}^{ims}\mathbf{g}$ Barycenter of the SHM on the side camera image plane

${}^{imt}\mathbf{g}$ Barycenter of the SHM on the top camera image plane

${}^{w}\mathbf{M}_{cs}$ Transformation matrix from the side camera to the world coordinate system

${}^{w}\mathbf{M}_{ct}$ Transformation matrix from the top camera to the world coordinate system

${}^{w}\mathbf{Q} = ({}^{w}X, {}^{w}Y, {}^{w}Z)^T$ Coordinates of a point Q in the world system

$^{w}\mathbf{R}_{cs}$ Rotation matrix from the side camera to the world coordinate system

$^{w}\mathbf{R}_{ct}$ Rotation matrix from the top camera to the world coordinate system

$^{w}\mathbf{t}_{cs}$ Translation matrix from the side camera to the world coordinate system

$^{w}\mathbf{t}_{ct}$ Translation matrix from the top camera to the world coordinate system

$^{w}\tilde{\mathbf{Q}} = (^{w}X, ^{w}Y, ^{w}Z, 1)^{T}$ Homogeneous coordinates of a point Q in the world system

a Propulsion parameter

b Propulsion parameter

B_0 Magnetic flux density generated at the center of the coil pairs

B_x Magnetic field generated by small Helmholtz coil pairs

B_y Magnetic field generated by Medium Helmholtz coil pairs

B_z Magnetic field generated by big Helmholtz coil pairs

c Propulsion parameter

$c(s)$ Curvature of the reference path

d Distance between the SHM and the reference path

f Rotation frequency

G 3D position of the barycenter of the SHM

g Barycenter of of an object in the image

k_d Control parameter for 2D path following task

k_t Control parameter for 2D path following task

m_{pq} 2D $(p+q)^{th}$ order moments of a grey-level image

n Number of turns

R Radius of curvature of the reference path

Re Reynolds number

s Curvilinear coordinate of the reference path

U_b Output voltage of big Helmholtz coil pairs

U_m Output voltage of medium Helmholtz coil pairs

U_s Output voltage of small Helmholtz coil pairs

U_x Maximum output voltage of small Helmholtz coil pairs for B_0

U_y Maximum output voltage of medium Helmholtz coil pairs for B_0

U_z	Maximum output voltage of big Helmholtz coil pairs for B_0
v	Linear propulsion velocity of the SHM
v_h	Linear advance velocity of the SHM on the horizontal plane

General introduction

Microrobots have the potential for numerous applications ranging from in vitro tasks on lab-on-a-chip (e.g. transporting and sorting micro objects; micro-assembly of mechanical components...) to in vivo applications for minimally invasive medicine (e.g. targeted drug delivery; brachytherapy; hyperthermia...), due to their micro sizes and accessibility to tiny and clustered environments. Some contexts, such as microfluidic channels for in vitro tasks and blood vessels or urinary system, often imply that the microrobots have to swim in fluid. However, at the microscale, the fluid becomes extremely viscous and the Reynolds number of the microswimmers dramatically lowers. The corkscrew type rotating propulsion proposed by Purcell is one of the swimming technique suitable for swimming at low Reynolds numbers. Magnetic Helical microswimmers, inspired by E. coli bacteria, are driven by a rotating magnetic field, and convert the rotary motion to a linear motion at low Reynolds numbers.

For more than ten years, researchers have developed several kinds of magnetically actuated helical swimmers with different geometry parameters, head shapes, and magnetic positioning. However, the influence of the geometry parameters, the head shapes and the magnetic positioning has not been clearly demonstrated. Therefore, the design of the helical swimmers is still not fixed. As far as we know, the existing helical swimmers are primarily open-loop controlled, due to the complexity of the control of the magnetic field actuating the helical propulsion, and the limited number of feedback options with the required precision. Therefore, the two major objectives of this thesis are:

- to compare the swimming performances of helical swimmers with different designs to further improve their design and to characterize their swimming properties.
- to realize a visual servo control of helical swimmers.

In order to achieve the objectives, scaled-up helical microswimmers, which are defined as the helical swimmers with overall lengths higher than 1 mm, but still swim at the low Reynolds numbers, are proposed in this thesis. The fluid motion around the helical swimmer is only characterized by the Reynolds number. Therefore, the swimming properties of helical swimmers should be the same if they swim at the same Reynolds numbers, which make a dimensionless study possible. The scaled-up helical microswimmers facilitate the fabrication with different designs and the observation by vision.

The scaled-up helical microswimmers used in the experiments are presented in Chapter 2. The experimental setup, including a magnetic actuation system and a vision system are also presented. The magnetic actuation system is composed of three orthogonally arranged Helmholtz coil pairs. The generated rotating magnetic field is controlled by the supplied currents. The Helmholtz coil pairs are difficult to be scaled up. Therefore, a rotating permanent magnet manipulator is built for the bigger version of the scaled-up helical microswimmers. The vision system is composed of a camera with an optical lens and a camera with an endoscope connected by a coupler lens in order to solve the line of sight problem. The barycenter and the orientation of helical

swimmers are real-time tracked. Some methods of the estimation of the swimming characteristics, such as rotation frequency, translation velocity, and the propulsion matrix of the helical swimmers are also introduced in this chapter.

The influence of geometry parameters of the helical swimmers on their swimming performances are studied in Chapter 3. The design of the geometry parameters of the helical swimmers is fixed after the swimming performances comparison. Then, the rotational propulsion characteristics of the helical swimmers with different head shapes and magnetic positioning are studied. The influence factor on the rotational propulsion characteristics is discussed. The design of the head shape and the magnetic positioning are then determined. The design of the scaled-up helical microswimmers can be a guideline for the fabrication of helical microswimmers. The propulsion matrix of the helical swimmer is identified. The propulsion linear velocity is predicted using the estimated propulsion matrix. At last in this chapter, an open-loop steering of the helical swimmer is presented. Based on the steering characterization of the helical swimmers, a 3D steering strategy is proposed to improve the efficiency.

The visual servo control of the scaled-up helical microswimmers is discussed in Chapter 4. The vision system with two cameras is firstly calibrated. A 3D pose estimation, including the orientation and the position of the helical swimmers in the 3D space is then established. A control law is designed for the magnetic field. The visual servo control for the orientation of the helical swimmers is realized in the 3D space. As helical swimmers are nonholonomic systems, a path following task is planned. The 2D path following task on the horizontal plane is proposed based on the established state model of the helical swimmers and the control law of the magnetic field. The visual servo control of the 2D path following is validated by following a straight line with the initial position both on and off that line. 3D path following task in the space is as well discussed for the perspectives. More complicated paths should be tested in future works. Once validated by the scaled-up helical microswimmers, the visual servo control can be applied to helical microswimmers by using the optical lenses suitable to the resolution. Some perspectives for future works is as well discussed at last.

Chapter 1

Introduction

Contents

Helical microswimmers capable of propulsion at low Reynolds number have the potential to apply on microfluid, lab-on-a-chip, and minimally invasive medicine. Due to the scaling of physical effects, locomotion of microswimmers is different from that of the classical swimmers. Traditional fabrication and power-supply methods become unfeasible at microscales. In this chapter, a state of the art about the helical microswimmers is introduced, including the state of the art of their locomotion, fabrication, actuation, localization and visual servo control.

1.1 Motivations

Microrobots include the robots from 1 micrometer to 1 millimeter [Chaillet 2013]. Microrobots are shown on a scale bar, with some intuitive small objects, such as an E. coli bacteria, a red blood cell, and an ant in Figure 1.1. Untethered, controllable, mobile microrobots have been proposed for numerous applications ranging from in vitro tasks on lab-on-a-chip to in vivo applications for minimally invasive medicine [Abbott 2007]. Although the specific applications of microrobots are still in an early concept stage, the direction in which the field is heading is rapidly solidifying.

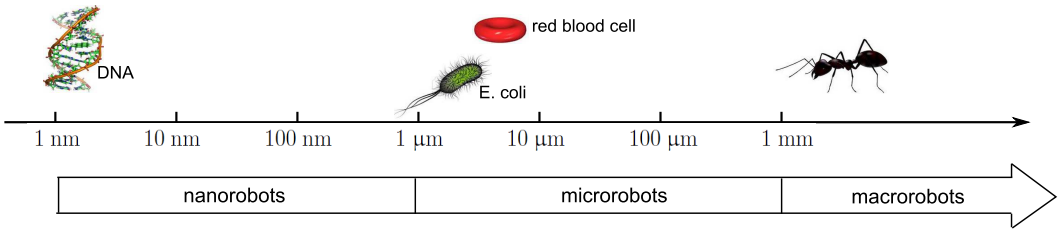

Figure 1.1: The micro and nano scale.

Let us summarize the application of microrobots from in vitro to in vivo applications.

1.1.1 In vitro applications

Due to their micro sizes and accessibility to tiny and clustered environments, microrobots can be used for various in vitro tasks, such as manipulation of micro-objects. A helical microswimmer of 38 µm in length capable of pushing and rotating a microsphere of 6 µm in diameter in fluid is demonstrated in [Zhang 2009a]. The manipulation of micro-objects enables micro-assembly [Bolopion 2009, Gauthier 2010, Xie 2012, Bolopion 2012]. As for potential applications, advanced manufacturing relies on the micro-assembly of small mechanical components, using micro-agents manipulating micro-objects in order to build assembled systems. For example, Micro-Opto-Electro-Mechanical Systems (MOEMS) sense or manipulate optical signals on a very small scale using integrated mechanical, optical, and electrical systems, therefore their fabrication requires a precise micro-assembly system. Another example is the fabrication, packaging and interconnection of different micro-components in the Micro Electronic Mechanical System (MEMS) where micro-assembly is vital.

Microrobots are also suitable fields for industrial biotechnology and medicine use. They are promising tools for the treatment of biological cells because of their high throughput and high repeatability. Indeed, microrobots operate at the same scale as organic cells, allowing efficient in vitro interactions in order to move and sort cells. Integration of a microfluidic chip and robotics based on micro-electromechanical systems technology is an innovation for biomedicine. Accurate motion control, high propulsion power, and the pumping mechanism of motion permit the microrobot to load multiple objects and transport them to desired locations in the microfluidic chip [Sanchez 2011, Hwang 2013]. They perform adaptable tasks on corpuscles such as blood cells sized from $6-10$ µm. A system consists several microrobots is developed in [Truper 2004], that can automatically sort different cells by transporting them to different repositories. High-speed microrobotic actuation driven by permanent magnets in a microfluidic chip can output a force of the order of millinewtons [Hagiwara 2012, Hagiwara 2013]. These magnetically actuated microrobots are capable of delivering microbeads in microchannels [Feng 2011].

1.1.2 In vivo applications

In vivo applications of microrobots is especially applied in minimally invasive surgery. Minimally invasive procedures are linked with a variety of patient-oriented benefits ranging from reduction of recovery time, medical complication, infection risks, and postoperative pain to increase quality of care, including preventative care. At the small scales world, microrobots have the potential to perform tasks that are currently difficult or impossible [Tendick 1998, Mack 2001, Carrozza 2003]. Some locations in the human body would become available for wireless intervention, including the circulatory system, the urinary system, and the central nervous system, if we were able to create microrobots with a maximum dimension of only a few millimetres or less. Microrobots will undoubtedly lead to the development of therapies.

Nelson classified the medical microrobot tasks in [Nelson 2010]. Microrobots can be used for targeted therapy including targeted drug delivery, brachytherapy, and hyperthermia. Targeted drug delivery can increase simultaneously the drug concentration in a region of interest and reduce the risk of side effect in the rest of the body. Brachytherapy is the placement of a radioactive source near unwanted cells such as tumor. The unwanted cells close to the radioactive source can be killed by the radiated energy. Hyperthermia refer to the local delivery of heat energy to destroy unwanted cells. Microrobots can also be used to remove material by mechanical means. Microrobots use rotary motion to perform ablation task, for example, in the removal of fatty deposits from the internal walls of blood vessels. Microrobots can act as simple static structures whose positions are controllable, such as stents to keep vascular passageways open, occlusions to clog a blood vessel that nourishes a tumor, and implants like electrodes for brain stimulation. Microrobots can also be used to transmit informations that would otherwise be difficult or impossible to obtain. At the same time, their positions can be used to localize the unknown internal phenomena such as internal hemorrhage. Some tasks require very simple structures, making them feasible near-term goals. Figure 1.2 summarizes the above medical tasks.

In lots of contexts, such as in microfluid channels for in vitro tasks and in the blood

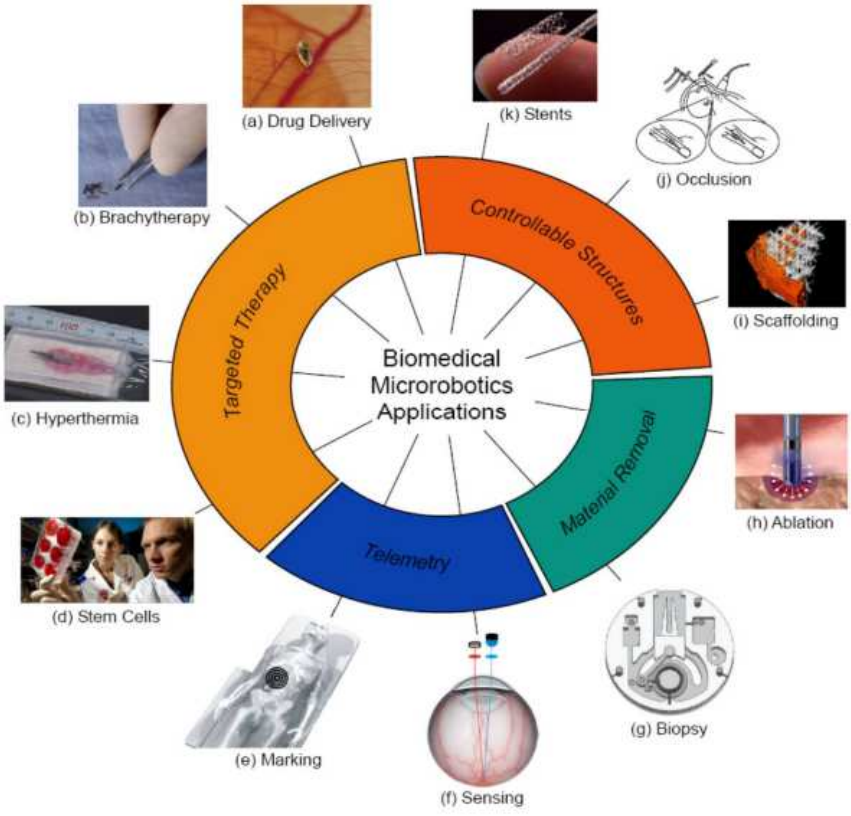

Figure 1.2: Numerous in vivo medical applications of microrobots [Nelson 2010].

vessels or urinary system for medical applications, the microrobots have to swim in fluid. The microrobots working in fluid-filled lumens, tubes, and cavities are called microswimmers. In this thesis, the research is focused on the microswimmers.

1.2 Swimming at low Reynolds numbers

As the swimmers are scaled down to the microscale, the fundamental physics governing the devices remain the same, but the relative importance of physical effects changes [Purcell 1977]. In this section, the physics of the swimmers at the microscale are introduced. Then, the locomotion suitable for swimming at the microscale, inspired by the micro-organisms is presented.

1.2.1 Reynolds number

The Reynolds number is a dimensionless quantity. Osborne Reynolds defined the Reynolds number as the ratio of the inertial forces to the viscous forces a hundred years ago. A typical inertial stress is given by a Bernoulli-like dynamic pressure, which can be expressed as $\sigma_{inertial} \sim \rho v^2$, and leading to an inertial force $f_{inertial} \sim \rho v^2$, where v is the velocity, ρ is the density of the fluid. A typical viscous stress on a rigid body is given by $\sigma_{viscous} \sim \eta v/L$, leading to a typical viscous force on the body of the form $f_{viscous} \sim \eta v/L$, where L is a characteristic linear dimension, η is the dynamic

viscosity of the fluid [Lauga 2009]. Thus the Reynolds numbers can be expressed as follows:

$$Re = \frac{\text{inertial forces}}{\text{viscous forces}} = \frac{\rho v L}{\eta} = \frac{vL}{\nu} \tag{1.1}$$

where ν is defined as the kinematic viscosity of the fluid.

Since the characteristic linear dimension is small, swimming in microscales is defined as swimming at low Reynolds number. The Reynolds numbers for some swimming microorganisms are listed in Table 1.1. In water ($\rho \approx 10^3$ kg/m^3, $\eta \approx 10^{-3}$ Pa$\cdot$s), a swimming bacterium, such as E. coli, moves with Reynolds number of $10^{-5} - 10^{-4}$. A human spermatozoon travelling around 200 µm/s moves with Reynolds number of 10^{-2}. Larger ciliates such as Paramecium with a length of 100 µm travelling at about 1 mm/s has a Reynolds number of 0.1.

Table 1.1: Summary of swimming velocities, characteristic lengths, and Reynolds numbers of some swimming microorganisms [Lauga 2009].

	Velocity	**Characteristic length**	**Reynold number**
E. coli	10 µm/s	$1 - 10$ µm	$10^{-5} - 10^{-4}$
Spermatozoon	200 µm/s	50 µm	10^{-2}
Paramecium	1 mm/s	100 µm	0.1

1.2.2 Navier-Stokes equations

The general properties of flow at low Reynolds numbers have been investigated in [Purcell 1977, Sleigh 1988, Kim 1991, Lauga 2009]. To solve the force distribution on an organism, the flow field v and pressure p in the surrounding fluid need to be found. The Navier-Stokes equations describe the motion of Newtonian fluid substances. These equations arise from applying Newton's second law: conservation of momentum, to fluid motion, with the assumption that the fluid stress is the sum of a diffusing viscous term and a pressure term. The general form of the Navier-Stokes equations of fluid motion is:

$$-\nabla p + \nabla \cdot \vec{T} = \rho \frac{\partial \vec{v}}{\partial t} + \rho(\vec{v} \cdot \nabla)\vec{v} \tag{1.2}$$

where $\vec{T}$ is the stress tensor and ρ is the fluid density. The conservation of mass can be expressed as:

$$\frac{\partial \rho}{\partial t} + \nabla \cdot (\rho v) = 0 \tag{1.3}$$

In the case of the incompressible flow of Newtonian fluids, the incompressible flow assumes constant viscosity and density. A simplification of the Navier-Stokes equations is obtained below:

$$\begin{cases} -\nabla p + \eta \nabla^2 \vec{v} = \rho \dfrac{\partial \vec{v}}{\partial t} + \rho(\vec{v} \cdot \nabla)\vec{v} \\ \nabla \cdot v = 0 \end{cases} \tag{1.4}$$

where η is the constant dynamic viscosity.

At low Reynolds number regimes, the viscous forces dominate before the inertia forces. The inertia terms of the Navier-Stokes equations are thus negligible. The Navier-Stokes equation can be simplified as follows:

$$\begin{cases} \eta \nabla^2 \vec{v} = \nabla p \\ \nabla \cdot v = 0 \end{cases} \tag{1.5}$$

This equation is only exact for $Re = 0$, but it is considered as a valid approximation for $Re \ll 1$. This equation is linear and independent of time. These properties lead to some important consequences for locomotion, as we discuss below.

1.2.3 Reciprocal motion and non-reciprocal motion

As pointed out above, the linearity and time-independence of Navier-Stokes Equation (1.5) leads to a rate-independence property. If a body undergoes surface deformation, the distance travelled by the swimmer between two configurations does not depend on the rate at which the surface deformation occurs, but only on its geometry, which means the sequence of shapes the swimmer passes through between these two configurations.

An important consequence of rate-independent swimming at low Reynolds numbers is the so-called "scallop theorem": if the sequence of shapes displayed by a swimmer deforming in a time-periodic fashion is identical when viewed after a time-reversal transformation, then the swimmer cannot move on average. Note that the condition is not that the motion be strictly time-reversal invariant, with the same forward and backwards rate, but only that the sequence of shapes is the same when viewed forward or backward in time. This kind of motion is termed as reciprocal motion. Reciprocal motion cannot be used for locomotion at low Reynolds numbers. Purcell illustrated the futility of reciprocal motion with the example of a scallop. A scallop opens its shell slowly and closes it fast, squirting out water, to move ahead. At low Reynolds numbers, the scallop moves ahead by closing its shell, but it's back to where it started by opening its shell. No net displacement can be created. Therefore, non-reciprocal motions are required for a net displacement at low Reynolds numbers.

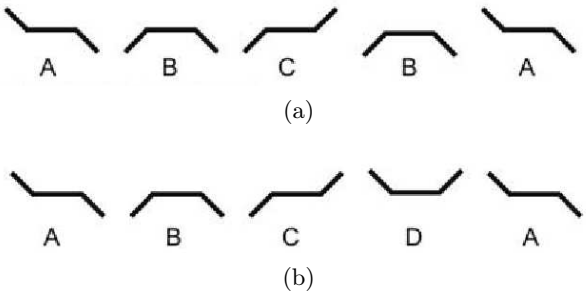

Figure 1.3: The 2-hinged theoretical swimmer proposed by Purcell [Purcell 1977]: (a) The reciprocal series of configurations ABCBA leads to a back and forth motion only, known as the "scallop theorem". (b) The non-reciprocal series of angle configurations ABCDA creates a net displacement after a whole cycle.

In his papers, Purcell proposed a simple example of non-reciprocal motion by a theoretical two-hinged swimmer composed of three rigid links rotating out of phase with

each other, which is depicted in Figure 1.3. The two hinges offer two Degrees of Freedom (DoF) and the swimmer can go through a series of angle configurations. A reciprocal motion is illustrated by Figure 1.3a, which is a series of configurations ABCBA. If this sequence is reserved in time, the new sequence is ABCBA, which is identical with the origin sequence. The non-reciprocal series of configurations ABCDA, as shown in Figure 1.3b, which can be reversed in time into the series of configuration ADCBA, results in a net displacement after one cycle. However, this is only a hypothetical non-reciprocal motion. It has not been yet figured out whether it exists in the nature. In micro-animal kingdom, there are at least two other solutions to the problem of swimming at low Reynolds numbers, which is introduced in the next section.

1.2.4 Locomotion of micro-organisms

Nature has a great deal to teach us about microswimmer design. Micro-organisms are able to swim at low Reynolds number by generating non-reciprocal motions. Purcell described two techniques that microorganisms adopt to generate non-reciprocal motion in his highly cited paper "Life at Low Reynolds Numbers" [Purcell 1977]: a flexible oar oscillation (Figure 1.4a) and a corkscrew-type rotating propulsion (Figure 1.4b).

(a) (b)

Figure 1.4: Two techniques to generate non-reciprocal motion: (a) The flexible oar oscillation: flagella create patterns such as traveling waves. (b) The corkscrew-type rotating propulsion: a molecular motor spins passive bacterial flagella [Abbott 2009].

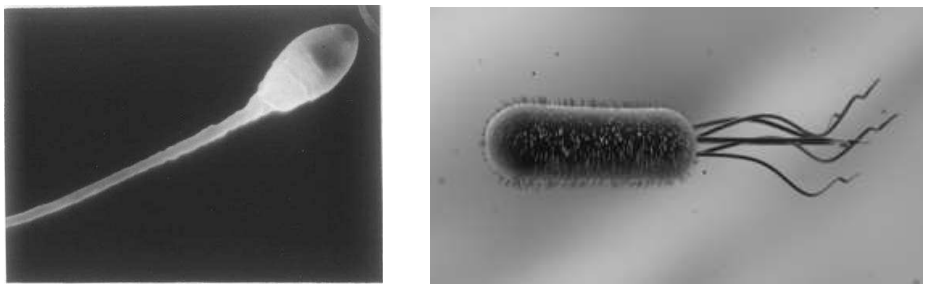

(a) (b)

Figure 1.5: (a) A spermatozoa has a flexible tail. It stocks its tail to generate a flexible oar oscillation to advance. (b) An image of an E. coli O157:H7 bacterium with a bundle of flagella. The bundle of flagella is driven into a helical shape to generate a corkscrew-like propulsion.

The flexible oar oscillation is used by some eukaryotes such as spermatozoa (see Figure 1.5a) to propel themselves. Eukaryotic flagella are active organelles that deform

to create paddling motion, such as traveling waves or circular translating movements. The corkscrew-type rotating propulsion is used by some prokaryotes such as E. coli bacteria (see Figure 1.5b) [Berg 1973, Berg 2004]. E.coli cells consist of a rod-shaped body and a bundle of passive flagella. The bundle of flagella is driven by a molecular rotary motor into a helical shape to generate a corkscrew-like motion.

1.2.5 Bio-inspired microswimmers

A number of robotic swimming methods have been shown to work at relatively small scales, but will have reduced effectiveness as size decreases to the microscale because they make use of reciprocal motion [Abbott 2009]. Various microswimmers designs, as shown in Figure 1.6, inspired by the nature micro-organisms, use non-reciprocal motions can be adapted to make effective motions at low Reynolds numbers.

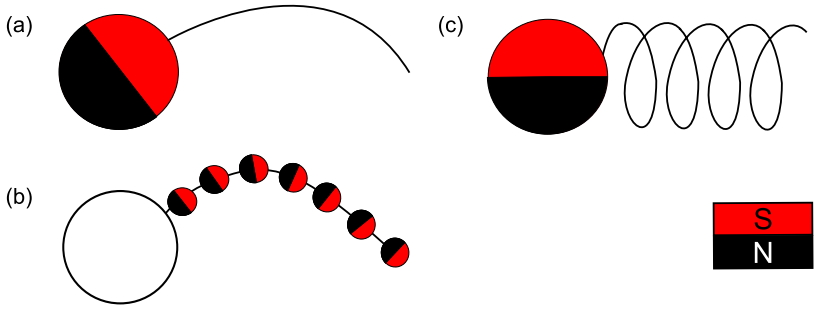

Figure 1.6: (a) Flexible beam attached to a magnetic head. (b) Flexible magnetic micro-bead tail. (c) Rigid helical tail fixed to a magnetic head.

A flexible flagellum is the easiest mechanism inspired from the micro-creature. It is a one dimensional structure. The challenge is to fabricate a simultaneously flexible and stable structure at microscale. A flexible beam can be actuated by a uniform oscillating magnetic field while attached to a magnetic head [Guo 2008]. Another approach to form a flexible flagellum is to use self-assembled magnetic beads. The magnetic force between magnetic beads is limited and fast rotation of these bead chains can lead to disassembly due to the fluidic drag forces [Melle 2003]. Hence, Dreyfus connected the magnetic particles with DNA strands [Dreyfus 2005]. The overall length of is approximately 24 µm. In fact, a chain of beads actuated with an oscillating field does not result in a non-reciprocal motion. However, attaching a payload to one end of the chain breaks the motion symmetry of the travelling wave along the bead chain. The transport of a single red blood cell is demonstrated. A kink in the chain also breaks the symmetry and allows propulsion at microscale [Roper 2006]. More recently, a flexible flagellum with cultured contractile cardiomyocytes in presented in [Williams 2014], which is capable of self-propulsion without external magnetic field. The main challenge of the flexible flagella is the motion control with precision.

Rotating rigid helical flagella which convert the rotary motion to a linear motion, is another approach of propulsion at low Reynolds numbers inspired by bacterial propulsion. A centimeter scaled helical tail attached to a rotary motor is tested in the viscous liquid to simulate the propulsion at low Reynolds numbers [Behkam 2005, Behkam 2006]. However, the motor is difficult to be scaled down to

micrometer. Therefore, researchers use magnetically actuated helical swimmers. Artificial rigid helical flagella attached to magnetic heads with several tens of micrometer are presented in [Bell 2006, Zhang 2009b, Hwang 2010, Mahoney 2011], a rigid helical tail with magnetic coating is presented in [Ghosh 2009]. More details of these helical microswimmers are presented in Section 1.3.2. The structure of rigid helical microswimmers are more solid than self-assembled flexible flagella. The motion control of the magnetic helical swimmers can be realized by the control of the rotating magnetic field. A helical swimmer can be propelled forwards or backwards simply by reversing the direction of rotation. Therefore, the helical flagella actuated by a rotating field are more suitable for control and future applications in microscales. One of the main challenges for helical microswimmers is the fabrication of the 3D complex structures at the microscale, which is introduced as follows.

1.3 Helical microswimmers

In recent years, helical microswimmers have become a growing area of interest for microrobot researchers. In this section, the state of the art of the micro-fabrication process of the helical microswimmers is introduced at first. Then, the state of the art of the helical microswimmers is presented. At last, the helical propulsion model is presented.

1.3.1 Helical microswimmer fabrication process

In recent years, thanks to the development of micro-fabrication, a number of fabrication methods have been found that are capable of small-scale helix fabrication. The main challenge for fabricating microrobots are the repeatability of the process, and the control over design parameters. Three micro-fabrication methods of helical microswimmers is presented.

1.3.1.1 Self-scrolling method

The first functional helical microswimmers was fabricated in 2006, using the self-scrolling technique of InGaAs/GaAs bilayer [Bell 2006]. Lots of helical microswimmers are fabricated based on this self-scrolling method [Hwang 2009, Zhang 2009b, Zhang 2010a, Hwang 2010, Hwang 2011]. The fabrication process is illustrated schematically in Figure 1.7.

The initial layers are grown on semi-insulating Gallium Arsenide (GaAs) using a Molecular Beam Epitaxy (MBE) system equipped with a valved cracker for As and solid sources for Ga and In (Figure 1.7a). After a thin GaAs buffer layer, a 500 nm thick sacrificial AlGaAs layer is deposited. A 15.6 nm thick layer consisting of $In_{15}Ga_{85}As$ is deposited on the top of the sacrificial layer. $In_{15}Ga_{85}As$ is GaAs with 15% of Ga atoms replaced by In atoms. A 15.6 nm thick layer of GaAs is deposited on the top of the InGaAs layer. InGaAs has the same structure as GaAs, but its crystal mesh size is slightly superior than that of GaAs, because In atomic ray is superior to that of Ga. At the intersection of the bilayer, adaptation of each mesh over the other generates a internal strain.

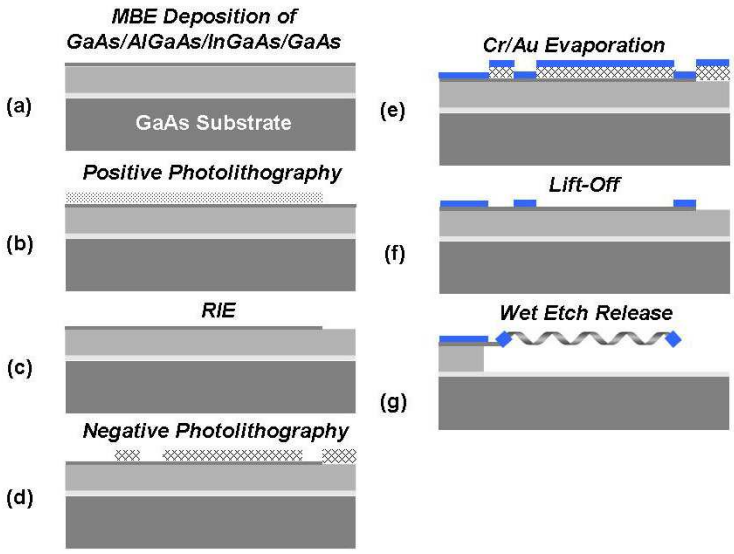

Figure 1.7: Basic fabrication process sequence (a-g): initial planar bilayer patterned through conventional microfabrication techniques, assembles itself into 3-D structures during wet etch release because of the internal strain. Metal pads and support bars are created through negative photolithography and lift-off [Hwang 2009].

The initial pattern can be created through photolithography (Figure 1.7b). After the development of photoresist, Reactive Ion Etching (RIE) is used to transfer the pattern to ribbon (Figure 1.7c). The bars to which the structure fixed at the end are created through a lift-off process with negative photoresist (Figure 1.7d, e, f). The 10 nm thick Cr layer serves as an adhesive layer. The 100 nm thick Au layer is used for electrical contacts.

Finally, a 2% hydrofluoric acid (HF) aqueous solution is used to selectively etch the AlGaAs sacrificial layer under the InGaAs/GaAs bilayer (Figure 1.7g). During this wet etching, the patterned bilayer curled up releases the internal strain and forms 3-D structures. After the wet etch release, the chips are rinsed in deionized water and subsequently in isopropyl alcohol. They are dried with a supercritical CO_2 dryer so that the structures would not be damaged from surface tension.

The direction of the scrolling is determined by the anisotropy in stiffness of the InGaAs/GaAs bilayer. Figure 1.8 illustrates that the scrolling direction of the ribbon is <100> on a (001) GaAs wafer. The radius of the helix is adjusted by tuning the thickness of the ribbon. A square plate nickel head is mounted on the helical filament for magnetic actuation. The square width and thickness of the nickel head can be adjusted with the lithography step and metal deposition step, respectively.

1.3.1.2 GLancing Angle deposition (GLAD) method

In 2009, even smaller helical microswimmers are fabricated by GLAD method, which is presented in [Ghosh 2009]. This method uses spherical seeds on which helical pillars are grown through the rotation of a tilted stage during evaporation. The process is shown in Figure 1.9a.

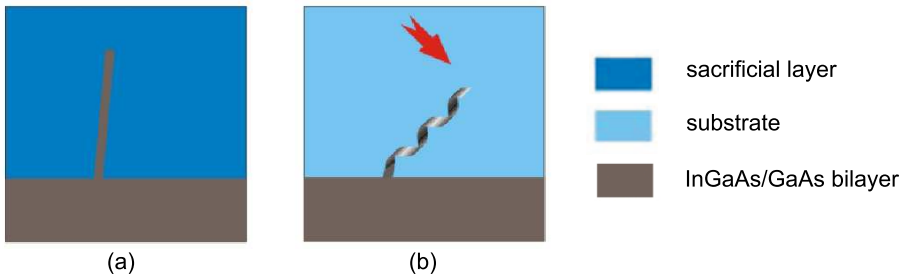

Figure 1.8: (a) InGaAs/GaAs bilayer is patterned by photolithography in a ribbon-like shape for the helical tail. (b) The ribbon-like structure self-forms a helix tethered at one end by releasing the internal stress after wet etching of the sacrificial layer. The red arrow indicates the scrolling direction of the ribbon, i.e., <100> on a (001) GaAs wafer [Zhang 2010a].

The helical structures are freed from the wafer by sonication. They are magnetized by depositing a cobalt layer along one half of the helix and permanently magnetizing them perpendicular to their helical axes in a subsequent step.

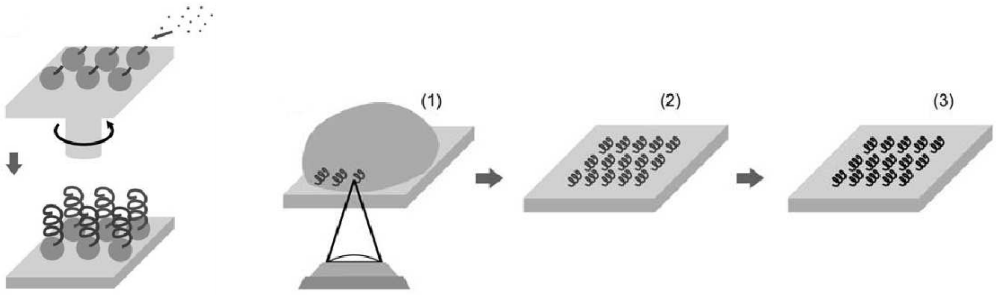

Figure 1.9: (a) GLAD fabricated helical swimmers. Pillars are deposited at an angle and under constant rotation of the stage, resulting in helices on the spherical seeds. (b) 3D lithography with a direct laser writing tool. (1) Polymerization of the photoresist at the focal point of the laser. (2) development and subsequent rinsing and (3) magnetic metal coating. [Peyer 2013].

1.3.1.3 Microscale rapid prototyping method

Another approach to controlled fabrication of micro helical swimmers is "microscale rapid prototyping" method, which is based on 3D lithography. A laser beam is focused into the photoresist and a two-photon polymerization (TPP) occurs at the focal point of the laser. A piezoeletric stage moves the glass substrate with the photoresist in 3D following a pre-programmed trajectory. In this manner, polymer structures of arbitrary shapes can be written. With this method, various design features can be added to the helical based shape, such as, for example a claw for micro-object transport [Tottori 2012]. Arrays of thousands of micro-structures can be fabricated within a few hours. They can be detached manually or by sonication to create suspensions

of microrobots. The magnetic material can either be deposited in a subsequent step by evaporation or micro particles can be incorporated in the polymer before the laser writing step.

1.3.2 State of art helical microswimmers

Here, the state of the art of the artificial helical microswimmers is presented. Although some of them are in the millimeter scale and are not strictly said "microswimmers", they swim in viscous liquids. Therefore, they can be classified as scaled-up helical microswimmers. All of the presented helical swimmers swim at low Reynolds numbers.

1.3.2.1 The first spiral-type swimming mechanisms

The first spiral-type swimming mechanism is introduced in 1996 by a Japanese group of Tohoku University [Honda 1996]. The swimmer composes of a small cubic $SmCo_5$ magnet, which is a strong permanent magnet made of an alloy of samarium and cobalt with each side of 1 mm, attached to a spiral wire, as shown in Figure 1.10. The diameter of the helix is 1 mm and the length is 21.7 mm.

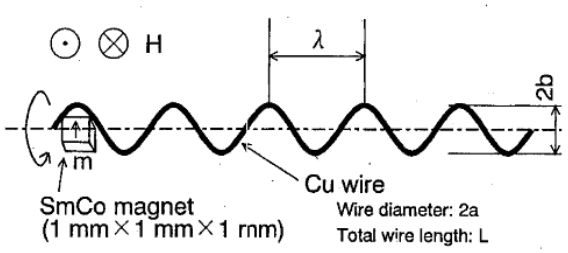

Figure 1.10: First spiral-type swimming machine designed by Tohoku University in 1996.

An external rotating magnetic field actuates the magnet to rotate. The strength of the applied magnetic field varies from 50 mT to 70 mT. The mechanism propelled by waves travelling along the spiral. The swimming velocity increased linearly with the excitation frequency and depended on the shape of spiral.

According to the swimming performances tested at low Reynolds number ($Re < 1$), researchers predicted that the spiral-type mechanism is suitable for swimming in the microworld.

1.3.2.2 A magnetic screw capable of travelling through meat

Some years later, the same group developed a magnetic screw capable of swimming through gel and organismal organ [Ishiyama 2000, Ishiyama 2001a, Ishiyama 2001b]. This mechanism consists of a NdFeB magnet (2 mm in diameter and 7.5 mm in length) and a brass tip with a spiral shape (4 mm in length), as shown in Figure 1.11a.

The intensity of the applied field varies from 4 mT to 10 mT. The magnetic screw rotates synchronously with the external rotating field until a certain frequency called "step-out frequency". At this frequency, the swimming velocity shows maximum. In

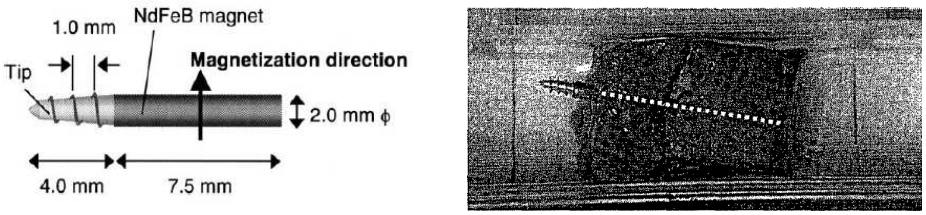

(a) (b)

Figure 1.11: (a) A magnetic screw swimming machine designed by Ishiyama in 2000. (b) The magnetic screw is capable of travelling through the bovine meat.

higher frequency than step-out frequency, the rotation of the mechanism can not synchronize to the external frequency, the swimming velocity decreases. Swimming performances are tested in a wide range of Reynolds numbers from 6×10^{-7} to 430. The velocity of the mechanism depends on the environmental media. The mechanism can swim at a maximum velocity of 0.022 mm/s at $Re = 6 \times 10^{-7}$. They predict that this magnetic screw can still be scaled down to micrometer-sized machine.

The mechanism is also examined in the bovine meat (see Figure 1.11b). The strength of the applied magnetic field is 15 mT, and the frequency is 10 Hz. Though the action is not very smooth, the mechanism runs through the meat at about 1 mm/s. The result suggests that the helical magnetic mechanism has a great potential to run in the human organs.

1.3.2.3 Artificial bacterial flagella of a size comparable to E. coli

In 2007, the first helical swimmers of a size comparable to E. coli, which are capable of swimming in both water and paraffin oil, called "Artificial Bacterial Flagella (ABF)" are made by a group at ETH Zurich [Bell 2007]. They demonstrate some characteristics of the ABF later [Zhang 2009b, Zhang 2009a, Zhang 2010b, Zhang 2010a].

ABF consists of a helical tail made by self-scrolled GaAs/InGaAs bilayer and a thin-square-plate soft-magnetic made by Cr/Ni/Au trilayer head on one end, as shown in Figure 1.12. The length of ABF is approximately 38 µm, the diameter and the thickness of helical tail is approximately 2.8 µm and 30 nm. The dimension of the square-plate is 4.5 µm × 4.5 µm × 200 nm. The thickness of Ni layer is 180 nm. The Reynolds number of ABF is in the range of 10^{-4}.

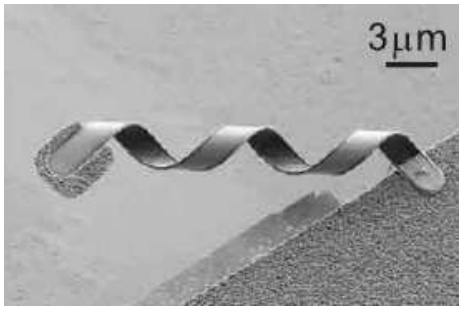

Figure 1.12: Artificial bacterial flagella made by ETH Zurich [Zhang 2009b].

The swimming locomotion of ABF is provided by low strength magnetic field generated by three orthogonal electromagnetic coil pairs. The flux density of the applied field in the experiment varies from 1 mT to 2 mT. ABF velocity increases linearly regarding the frequency until reaching a maximum value and then the velocity reduces and becomes less deterministic with the increasing field frequency. This phenomena is consistent with the previous low-Reynolds-number experiments of the helical swimmers at the millimeter scale [Ishiyama 2000]. The maximum velocity is 18 µm/s with a 2 mT field, which is equivalent to 0.5 body-length per second. This maximum relative velocity of ABF is not yet as high as E. coli, which can swim 10 body-length per second. ABF can as well be steered in water by applied magnetic torque. ABF can achieve some simple tasks, such as translation and rotation of microspheres with 6 µm of diameter.

1.3.2.4 Helical NanoBelt actuated by an electro-osmotic force

A group at ISIR and LPN demonstrated that electro-osmotic propulsion of Helical NanoBelt (HNB) shows much higher swimming performances in terms of swimming velocity and manipulation force [Hwang 2010, Hwang 2011]. Electro-osmosis propulsion is presented in detail in Section 1.4.1.

HNB has a similar geometry as ABF, a helical tail attached to a head in tube form, as shown in Figure 1.13. The diameters of the tube head and the tail are 2.1 µm. The length of the head is 12 µm and the total length of HNB is 74 µm. Moreover, a 10 nm thick ferromagnetic metal layer is added to the surface of helical tail. Their entire surface becomes functional to propulsion in comparison to the ABF's soft magnetic head as the only functional part and the tail as a passive part.

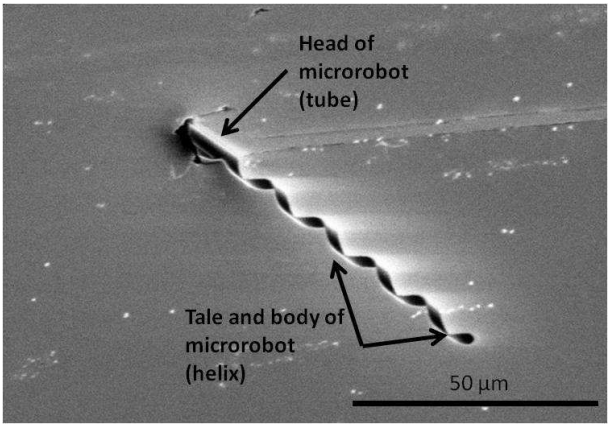

Figure 1.13: Helical nanobelt (HNB) made by ISIR in 2010 [Hwang 2010].

These electro-osmotic propelled HNB swimmers achieves speeds of 24 body lengths per second under an external electric field of 239 V/mm. E. coli bacteria moves at approximately 10 body lengths per second [Berg 2004]. The cheetah, as the fastest land animal, has a speed of 110 km/h, approximately 25 body lengths per second by comparison [Hildebrand 1959]. HNBs' swimming directions can be easily controlled by differentiating the field gradient.

Unusual and discontinuous pumping propulsion is observed from high-speed camera analyses. The swimming performance appears to depend highly on the surface conditions.

1.3.2.5 Artificial magnetic glass nano-structured propellers

In 2009, a group at Harvard University presented even smaller helical swimmers with a diameter of 200 nm and a length of 2 µm using GLAD method [Ghosh 2009]. The helical microswimmer is shown in Figure 1.14. A permanent magnetic film with a thickness of 30 nm is evaporated onto one side of the swimmer. They demonstrate that the magnetic material is not always restricted to the head, but may be directly applied to the surface of the helical tail as well.

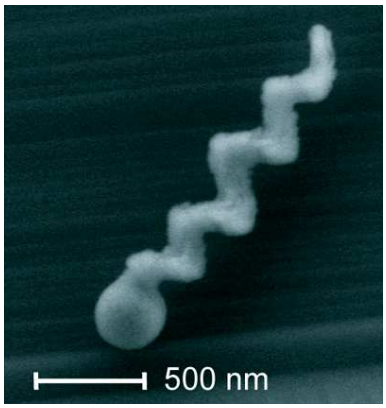

Figure 1.14: Scanning Electron Microscope (SEM) image of an individual glass screw with nano-structured helicity [Ghosh 2009].

The helical microswimmers can be propelled at speeds of about 40 µm $\perp$ s, which is equivalent to 20 body lengths per second, with a rotating magnetic field of 6 mT at about 150 Hz. These artificial swimmers are not only similar in size to a bacterial cell, but they also moves at the similar speed. The helical microswimmers can draw a curved line with a preprogrammed magnetic field. They are also able to push microbeads with a diameter of 5 µm.

1.3.2.6 Millimeter-scaled helical swimmers at the low Reynolds number

A millimeter-scaled helical microswimmer using micro wire electrical discharge machining is fabricated in [Mahoney 2011], as shown in Figure 1.15a. The helical swimmer is made from Nitinol, with a cylindrical magnetic head. The magnetic head is permanent magnet (nickel-plated NdFeB). The 5 mm long helix has 3.5 turns. The outer diameter is 1 mm, the pitch is 1 mm, the helix ribbon width is 0.2 mm.

The helical swimmer is actuated by three orthogonally arranged Helmholtz coil pairs. The helical swimmer swim in viscous liquids to simulate the low Reynold number regime. It rotates at 2.23 Hz to balance its own weight of 8.9 mg. The author shows a open-loop controlled swimming of the helical swimmer, which enables a "U-turn" trajectory. An image sequence of the swimming is shown in Figure 1.15b. The

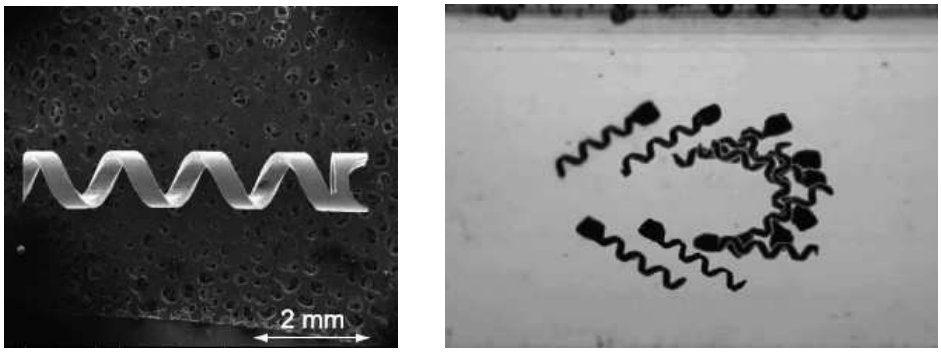

(a) (b)

Figure 1.15: (a) Scanning electron micrograph of the fabricated helix. (b) Image sequence of a "U-turn" trajectory [Mahoney 2011].

swimming velocity in the experiment is up to 0.35 mm/s, which is equivalent to 0.07 body length per second.

1.3.2.7 Helical microswimmers with object holder

More recently, Tottori presents claw shaped headed helical microswimmers to transport objects in [Tottori 2012]. The helical microswimmers are made of polymer, and fabricated by 3D direct laser writing rapid prototyping method presented in Section 1.3.1. The helical microswimmers with object holder is shown in Figure 1.16a.

The diameters of the helical microswimmers vary from 1 μm to 8 μm. The lengths vary from 4 μm to 64.5 μm. The Ni/Ti thin bilayers are deposited on the surface of the polymer helical microswimmers by electron beam evaporation for magnetic actuation and improvement of surface biocompatibility. The nickel layer is ferromagnetic, which contributes to the propulsion.

Transportation of 6 μm-diameter polystyrene particles in purified water is demonstrated using individual helical microswimmers with a micro-holder fabricated conjointly with the helical body. The procedure of object transport can be separated into four stages: approaching, loading, transporting in 2D and 3D, releasing, as shown in Figure 1.16b. The micro particle can be transported over one surface and steered to another lower surface. Then, it can be transported back to the initial higher surface.

1.3.2.8 Summary

The specifications of the helical swimmers presented above are summarized in Table 1.2. They are also shown on a scale bar with the E. coli bacteria in Figure 1.17. The helical swimmers with an overall length beyond 1 mm are defined as scaled-up microswimmers, because they are still in the low Reynolds number regime. They have different geometry parameters, head shapes, and magnetic positioning. Their swimming performances are different as well. However, no one has demonstrated the influence of the geometry parameters, head shapes, and magnetic positioning on the swimming performance.

From here, one of the main objectives of this thesis is to compare the swimming performance of the helical swimmers with different geometry parameters, head shapes,

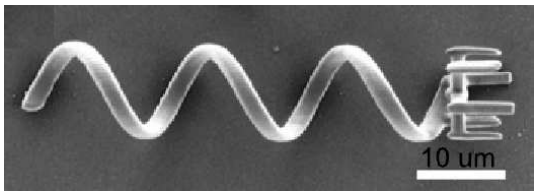

(a)

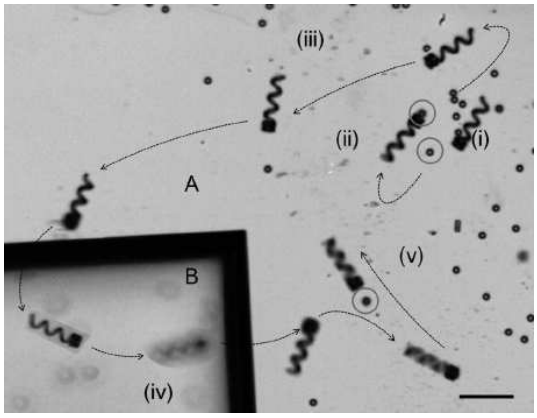

(b)

Figure 1.16: (a) Polymer helical swimmer with a claw shaped holder head. (b) Transport procedure: (i) approaching, (ii) loading, (iii)-(iv) transporting 2D and 3D, and (v) releasing [Tottori 2012].

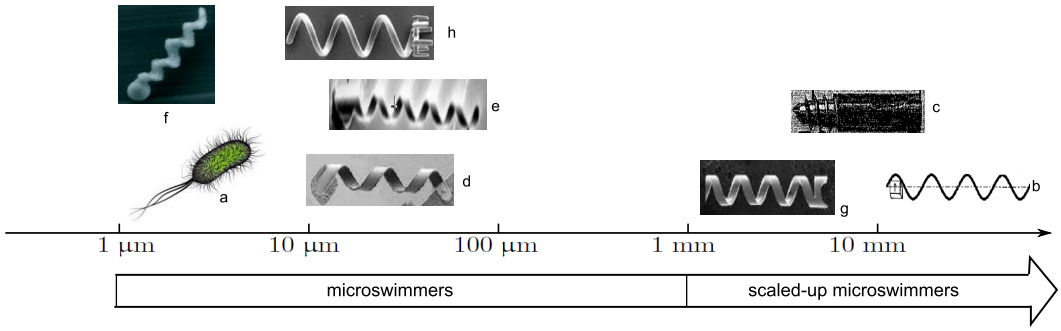

Figure 1.17: The helical swimmers in the literature shown on a scale bar.

and magnetic positioning, to find the influence factors on the swimming performance, in order to further optimize the design of the helical microswimmers. However, making different geometry parameters and head shapes requires several weeks of works and high cost. In this thesis, scaled-up helical microswimmers at the millimeter scale are used in viscous liquids, in order to facilitate the fabrication and observation. The reason and the feasibility of the scaled-up helical microswimmers be discussed in detail in Section 2.1.1. As the micro-fabrication process of the helical microswimmers is mastered, the helical swimmers at the millimeter scale will be easily scaled down in future works.

Table 1.2: Summary of the helical swimmers in the literature.

	a	b	c	d	e	f	g	h
Author	(E.coli)	Honda	Ishiyama	Zhang	Hwang	Ghosh	Mahoney	Tottori
Year	–	1996	2000	2007	2009	2009	2011	2012
Head shape	rod	cube	cylinder	square-plate	cylindrical tube	sphere	cylindrical	claw
Magnetic material	–	SmCo5	NdFeB	Ni	Ni	NdFeB	NdFeB	Ni
Length	$1-10$ μm	21.7 mm	4 mm	38 μm	62 μm	2 μm	5 mm	$4-64.5$ μm
Diameter	$0.5-0.7$ μm	1 mm	2 mm	2.8 μm	2.1 μm	0.2 μm	1 mm	$1-8$ μm
Thickness	20 nm	–	–	27 nm	27 nm	2 nm	0.16 mm	290 nm
Functional part	bioenergy	magnetic head	magnetic head	magnetic head	electro-osmosis	magnetic coating	magnetic head	magnetic coating
Power strength	–	$50-70$ mT	$4-15$ mT	$1-2$ mT	239 V/mm	6 mT	–	$1-4$ mT

1.3.3 Helical propulsion model

Gray and Hancock [Gray 1955] developed in 1955 a simplified Resistive Force Theory (RFT) to derive an expression for the propulsive velocity of sea-urchin spermatozoa. RFT is a very intuitive approach for modelling slender body dynamics at low Reynolds numbers. The underlying assumption of RFT is that the hydrodynamic forces are proportional to the local body velocity, with the constant proportionality being defined as the coefficient of resistance. RFT is used to determine the forces caused by velocity on an infinitesimally small length of helix by Lighthill in [Lighthill 1976]. RFT takes the velocity v of one of these small segments of the helix, decomposes the velocity into components parallel and perpendicular to the segment, and relates them to parallel and perpendicular drag forces acting on the segment with the differential forces:

$$\mathrm{d}f_{\perp} = \varepsilon_{\perp} v_{\perp} \mathrm{d}s \tag{1.6}$$

$$\mathrm{d}f_{\parallel} = \varepsilon_{\parallel} v_{\perp} \mathrm{d}s \tag{1.7}$$

where $\varepsilon_{\perp}$ and $\varepsilon_{\parallel}$ are the viscous drag coefficients, which have a number of empirical approximations. To get the total drag forces on the helical swimmer, the local filament forces $\mathrm{d}f_{\perp}$ and $\mathrm{d}f_{\parallel}$ can be transformed into the body coordinate system and integrated along the whole length of the helix. For steady-state motion, the external applied forces and torques on the helical swimmer have to balance the propulsive force and torque created by its rotation. Therefore, the relationship between the external applied forces and torque with the linear velocity and rotation speed are established. According to the integration along one direction or three directions, two different propulsion models are obtained and introduced in the following sections.

1.3.3.1 1D helical propulsion model

The 1D helical propulsion model is proposed by Purcell in [Purcell 1977]. Only two degrees of freedom are considered: rotation at angular speed ω around its axis and translation at velocity v along that axis (see Figure 1.18). By integrating the RFT along only one direction of the helical axis, the result is a 2×2 propulsion matrix relating the velocity and rotation speed to the external force and torque.

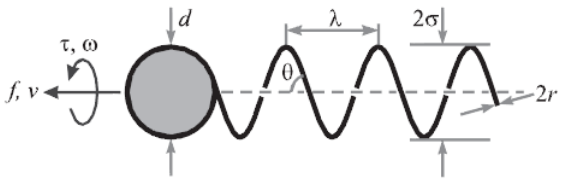

Figure 1.18: 2-DoF propulsion of a helical swimmer: rotation around its axis and translation along that axis [Abbott 2009].

$$\begin{bmatrix} f \\ \tau \end{bmatrix} = \begin{bmatrix} a & b \\ c & d \end{bmatrix} \begin{bmatrix} v \\ \omega \end{bmatrix} \tag{1.8}$$

The 2×2 matrix is called the propulsion matrix P of the helical propeller. The hydrodynamicists call this matrix the resistance matrix. The constants a, b, c and d

are proportional to the fluid viscosity η and depend otherwise only on the shape and the size of the helical propeller. If every dimension of the propeller is increased by the factor k, the new propulsion matrix P' has elements $a' = ka$, $b' = k^2 b$, $c' = k^2 c$ and $d' = k^3 d$.

Purcell proved in his paper [Purcell 1997] that the propulsion matrix must be symmetrical. The motion is actually described by only three constants:

$$\begin{bmatrix} f \\ \tau \end{bmatrix} = \begin{bmatrix} a & b \\ b & c \end{bmatrix} \begin{bmatrix} v \\ \omega \end{bmatrix} \tag{1.9}$$

The rotary and translational motion are coupled by the off-diagonal parameter b. Hence, an external applied force can induce a rotary motion, and vice versa, a torque can induce a translational motion. Purcell pointed out that the propulsive efficiency is more or less proportional to the square of the off-diagonal element of the matrix. These propulsion parameters are computed as [Abbott 2009]:

$$a = 2\pi n\sigma \left(\frac{\varepsilon_{\parallel} \cos^2\theta + \varepsilon_{\perp} \sin^2\theta}{\sin\theta} \right) \tag{1.10}$$

$$b = 2\pi n\sigma^2 (\varepsilon_{\parallel} - \varepsilon_{\perp}) \cos\theta \tag{1.11}$$

$$c = 2\pi n\sigma^3 \left(\frac{\varepsilon_{\perp} \cos^2\theta + \varepsilon_{\parallel} \sin^2\theta}{\sin\theta} \right) \tag{1.12}$$

where n is the number of the turns of the helix, θ is the angle between the axis of the helix and the direction of scrolling, σ is the rayon of the helix, and the constant $\varepsilon_{\parallel}$ and $\varepsilon_{\perp}$ are the viscous drag coefficients.

In case of a magnetic field actuated helical swimmer, the fundamental control input is the rotation frequency of the magnetic field, the nonfluidic applied force can be considered as the second input. The helical swimmer rotates in sync with the applied field, nearly instantaneously raching an equilibrium phase shift such that the magnetic torque counterbalances the fluidic drag torque. It is more instructive in this case to rearrange the linear equations with the nonfluidic applied force f and the rotation velocity ω of the helical swimmer as the input variables. Figure 1.19 shows the behavior observed with this type of swimming.

This 2-DoF axial model has been used with success to study the feasibility of helical swimming [Abbott 2009] and to characterize basic swimming properties [Zhang 2009b, Xu 2012].

1.3.3.2 3D helical propulsion model

Magnetic actuated helical microrobot are based on the assumption that the microswimmers behave similarly to bacteria, which are approximately neutrally buoyant. Therefore, the researchers pointed the helical swimmer in direction of desired velocity [Honda 1996, Ishiyama 2000]. However, man-made helical swimmers are typically heavier than their fluid medium. They sink down during the horizontal propulsion due to their own weight, resulting in a velocity that is not aligned with the thrust direction. Therefore, researchers pointed the helical swimmers in the direction having an angle with the horizontal plane to overcome its gravity [Zhang 2009a]. Mahoney proved in

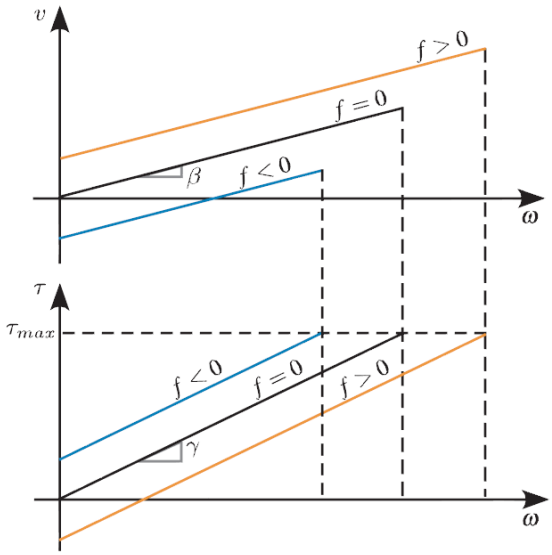

Figure 1.19: Qualitative behavior of helical-propeller swimming, with rotation frequency as the control variable [Abbott 2009].

his paper [Mahoney 2011] that there is a unique combination of angle and rotation speed to achieve the desired velocity. In order to find this combination of angle and rotation speed, Mahoney etablished a 6-DoF helical propulsion model.

Let the helix coordinate frame lie with the $\mathbf{x}_h$ axis parallel to the central axis of the helix, and the $\mathbf{y}_h$ and $\mathbf{z}_h$ axis be arranged as in Figure 1.20. The origin of this coordinate system is located at the center of the helix, denoted by O_h.

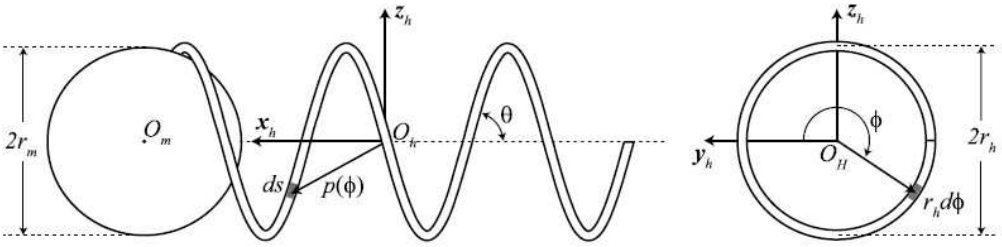

Figure 1.20: Helix coordinate frame.

By integrating the RFT along the three directions, the relationship between the force $\mathbf{f}_h$ and torque $\boldsymbol{\tau}_h$ to translational velocity $\mathbf{v}$ and angular velocity $\boldsymbol{\omega}$ around O_h is obtained as follows:

$$\begin{bmatrix} \mathbf{f}_h \\ \boldsymbol{\tau}_h \end{bmatrix} = \begin{bmatrix} \mathbf{A}_h & \mathbf{B}_h \\ \mathbf{B}_h^T & \mathbf{C}_h \end{bmatrix} \begin{bmatrix} \mathbf{v} \\ \boldsymbol{\omega} \end{bmatrix} \tag{1.13}$$

where:

$$\mathbf{A}_h = \begin{bmatrix} a_{h11} & 0 & 0 \\ 0 & a_{h22} & 0 \\ 0 & 0 & a_{h33} \end{bmatrix}, \quad \mathbf{B}_h = \begin{bmatrix} b_{h11} & 0 & b_{h13} \\ 0 & b_{h22} & 0 \\ 0 & 0 & b_{h33} \end{bmatrix},$$
$$\mathbf{C}_h = \begin{bmatrix} c_{h11} & 0 & c_{h13} \\ 0 & c_{h22} & 0 \\ c_{h13} & 0 & c_{h33} \end{bmatrix} \tag{1.14}$$

$\mathbf{A}_h$, $\mathbf{B}_h$, and $\mathbf{C}_h$ constitute the propulsion matrix. The parameters of the propulsion matrix depend on the shape and the size of the helical propeller and the viscosity of the fluid, which is computed in [Mahoney 2011].

In this thesis, only the 1D helical propulsion model is used, because the 1D model is sufficient to describe the relationship between the advance velocity of a helical swimmer and its self-rotation speed. The parameters of the 1D propulsion matrices of the helical swimmers used in the experiments are identified in Chapter 3.

1.4 Microrobots actuation

In this section, the actuation of the microswimmers is discussed, specially the magnetic actuation method. Then, a state of the art of the magnetic actuation systems is presented.

1.4.1 Actuation method of microrobots

The storage, harvest and transmission of power is a crucial point in wireless microrobot actuation. Without addressing power from the beginning, it is difficult to transform from prototypes to fully miniaturized wireless devices. There are two main actuation method to the microswimmers: the onboard power and the transmitted power.

1.4.1.1 Onboard power

Batteries can offer inexpensive power source, but the total deliverable energy scales down with volume. Therefore, they are not promising for microrobots.

MEMS-based power generators provide higher energy densities than traditional generators and batteries. Several researchers convert various types of energy into electrical energy [Jacobson 2003]. Some use onboard chemical fuels as well as glucose fuel, and others harvest mechanical energy from the environment in the form of vibrations. The operating environment, such as temperature and pH is constrained. A temperature gradient creates a voltage differential, which makes the use of thermal energy another potential option [DiSalvo 1999].

Instead of generating the locomotion for microrobot, Martel uses directly microorganisms that are able to swim, such as a swarm of Magnetotactic bacteria (MTB) [Martel 2009]. They can be localized and controlled by a Magnetic Resonance Imaging (MRI) system. Various strategies are proposed to functionalize the MTB, including attacking nanoparticles to the MTB, pushing or pulling an attached micro-object with one or more MTB, or using a swarm of MTB to move an unattached object. Challenging

issues such as control of the orientation and generation of sufficient forces must still be addressed.

1.4.1.2 Transmitted power

An alternative approach is to design a no power storage or generation system, but a wireless power transmission system to actuate the micro device. Two solutions are introduced below: the electro-osmotic force and the magnetic force.

Electro-osmotic force: Hwang used electro-osmosis force to move the helical swimmers [Hwang 2011]. Electro-osmosis relies on the principle that, on the surface of any body plunged in a liquid, local chemical reactions happen between solid and liquid. They drive to a displacement of electric charges, which results in opposed charges appearing on each side of the thin-layer surface of the solid. An electric potential is created owing to the presence of this thin interfacial layer named Stern layer, known as the zeta potential ζ. As soon as the potential established, applying an electric DC field triggers a relative motion of opposed electric charges. The result is a fluid movement (pump effect) if the solid walls are attached. Otherwise, movement of small objects while floating over the liquid is observed. Figure 1.21 presents the electro-osmosis propulsion principle. The electro-osmotic propulsion is very efficient [Hwang 2011]. However, the use of electro-osmosis force is limited. It can only be applied for moving micro-size objects.

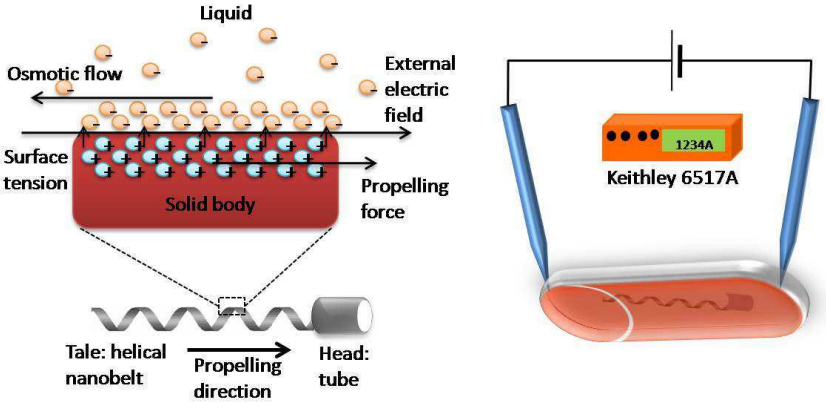

Figure 1.21: Electro-osmosis propulsion for a helical swimmer [Hwang 2011].

Magnetic force and torque: Quasi-static and low-frequency magnetic field is another approach to apply forces and torques directly to magnetic materials at a distance without the need of any tethers, or direct contact. Moreover, the human body is transparent to magnetic field, which means the magnetic permeability of the human body is approximately the same as that of an air vacuum. There are no significant interaction of tissue with low-frequency magnetic fields.

All magnetized objects are exerted both force and torque within an externally imposed magnetic field. The magnetic force and torque developed on a magnetized object are expressed as follows [Jiles 1998]:

$$\overrightarrow{f_m} = \int_{V_m} (\overrightarrow{m} \cdot \bigtriangledown) \overrightarrow{B} \, \mathrm{d}V_m \tag{1.15}$$

$$\overrightarrow{\tau_m} = \int_{V_m} \overrightarrow{m} \times \overrightarrow{B} \, \mathrm{d}V_m \tag{1.16}$$

where V_m is volume of the magnetized object, $\overrightarrow{B}$ is the flux density of the applied field (T), $\overrightarrow{m}$ is the magnetization of the object (A/m). It is also possible to describe the applied magnetic field by the magnetic field intensity $\overrightarrow{H}$ (A/m), where $\overrightarrow{B} = \mu_0 \overrightarrow{H}$ and $\mu_0 = 4\pi \times 10^{-7}$ T $\cdot$ m/A is the permeability of the free space.

The magnetization of the object, which generally varies across the body, can be modelled as constant throughout the body with a value equal to the average magnetization. We often consider the total dipole moment $\overrightarrow{M}$ of a magnetic body, which is the product of the magnetic body volume and the average magnetization. The magnetic force and torque as a function of the dipole moment can be expressed as:

$$\overrightarrow{f_m} = (\overrightarrow{M} \cdot \bigtriangledown) \overrightarrow{B} \tag{1.17}$$

$$\overrightarrow{\tau_m} = \overrightarrow{M} \times \overrightarrow{B} \tag{1.18}$$

From the relationship, we get that the magnetic force is proportional to the gradient of the magnetic field, which is used to move the object in the field to local maximum, and the magnetic torque is proportional to the magnetic field, which act to align the magnetization of an object with the field.

The actuation methods for microswimmers are summarized in Table 1.3 with their advantages and disadvantages. In this thesis, we need an actuation method applicable for swimmers at the millimeter scale, which is able to be scaled down to the microscale. The actuation of the swimmers should be easily controlled. Therefore, the magnetic actuation method is chosen as the actuation method for the helical swimmers by many researchers [Zhang 2009a, Bouchebout 2012, Ivan 2013, Hwang 2014], as well as in this thesis. Next, the magnetic actuation systems are presented.

1.4.2 State of the art of magnetic actuation systems

Controlled magnetic fields can be generated in a variety of ways. The simplest method is the use of electromagnets. McNeil designed a magnetic stereotaxis system, which consisted of three orthogonal pairs of coils in "helmet" configuration, to control magnetic fields throughout a human head [McNeil 1995]. However this design allowed only partial control because full torque and force control is not possible owing to the singularities in the workspace.

Yesin used a combination of uniform magnetic field generated by a Helmholtz coil pair and magnetic gradient generated by a Maxwell coil pair to control a microrobot with elliptical shape [Yesin 2006]. The coil pairs are rigidly connected, and can rotate around the workspace to control the orientation and direction of the magnetic microrobot. The system allows 2 DoF, one in translation and one in rotation.

Kummer of ETH group designed a electromagnetic system named OctoMag, which contains eight electromagnets (see Figure 1.22). OctoMag system enables 5-DoF (3-DoF position and 2-DoF pointing orientation) wireless magnetic control of a fully untethered microrobot [Kummer 2010].

Table 1.3: Summary of the actuation methods for the microswimmers.

Actuation method		Advantage	Disadvantage
Onboard	battery	low-cost, portable	deliverable energy scales down with volume
	chemical/glucose fuel	use the energy directly from the environment	constrained operating environment
	micro-organism (MTB)	applicable to the same size of the micro-organism	control of orientation and sufficient force generation still challenging
Transmitted	electro-osmosis	high efficiency	applicable only for the microscale
	magnetic	applicable for all the scales & controllable	only for magnetic objects

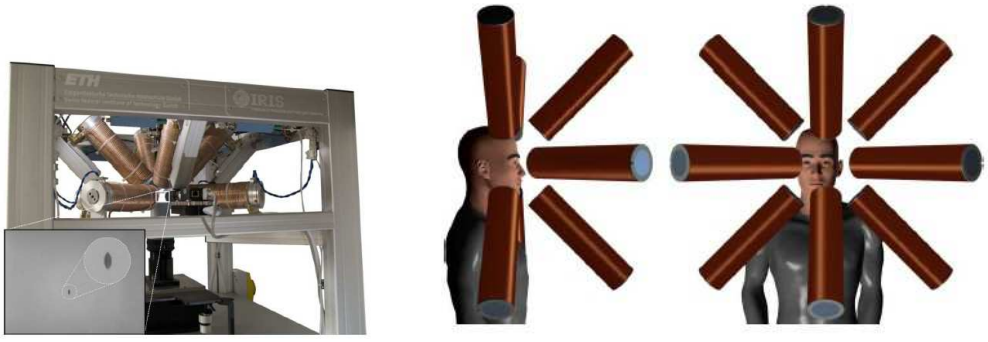

(a) (b)

Figure 1.22: (a) real image, and (b) concept image of OctoMag electromagnetic system for the control of intraocular microrobots [Kummer 2010].

Many researchers use a three-pair-Helmholtz coils orthogonally arranged (see Figure 1.23a) to generate uniform rotating magnetic field at the workspace [Zhang 2010a, Mahoney 2011, Miller 2012]. Three orthogonal Helmholtz coil pairs allows 3-DoF control in rotation. Another device that many researchers use is position controlled rotating permanent magnet (see Figure 1.23b) [Fountain 2010, Mahoney 2011, Xu 2012]. The Rotating permanent magnet can be mounted on a 6-DoF robotic manipulator or a simple translator. Three orthogonal Helmholtz coil pairs and rotating permanent magnet are discussed in detail in Chapter 2.

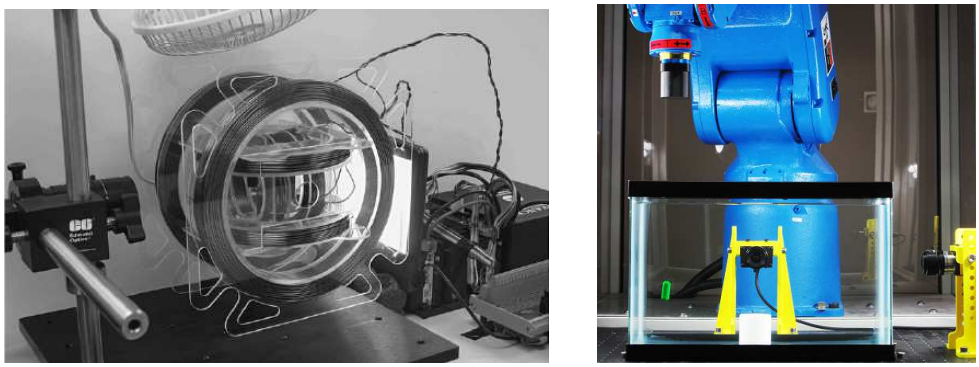

(a) (b)

Figure 1.23: (a) Three Helmholtz coil pairs orthogonal arranged [Mahoney 2011]. (b) A rotating permanent magnet mounted on a Yaskawa Motoman MH5 6-DOF robotic manipulator [Mahoney 2012b].

1.5 Microrobots localization

For the closed-loop motion control of helical microswimmers, the main challenge is to localize and track the helical swimmers position. Various methods have been proposed to localize and track a microrobot. Spatial resolution is an important factor in the determination of microrobots positions. The maximum rate at which the position estimation can be updated is also an important factor for real-time control. Energy effectiveness should be as well considered.

1.5.1 Electromagnetic and magnetic tracking

The principle in electromagnetic tracking is the use of a pair of devices: one acts as a field generator, the other acts as a sensor. The generator emits a low-frequency electromagnetic field that induces a voltage, which is as a function of distance and orientation, on the pick-up coils of the sensor. The accuracy of these systems depends on the presence of other magnetic objects in the environment. Many factors need to be considered, such as material properties, shape, size and position these objects relative to the field generator or sensor, as well as the frequency used for localization.

Magnetic tracking is an alternative methodology for wireless medical microrobots. A magnet is encapsulated in the device to be tracked, and an array of external mag-

netoresistive sensors are used to measure the magnet's field [Hu 2006]. An assumption is that the magnet behaves as a magnetic point dipole, whose field in the 3D space is discussed in Section 2.3.1. The assumption is valid when the measurement is performed at a large distance compared with the body length of the magnet. Magnetic tracking is promising when there are line-of-sight problems, because human body is transparent to static and low-frequency magnetic field. Calibration is usually required before the actual implementation of the tracking algorithm to minimize the effect of background noise.

1.5.2 Magnetic Resonance Imaging (MRI)

A clinical Magnetic Resonance Imaging (MRI) system is a powerful non invasive imaging technique the has played and will play an important role in the medical community. A clinical MRI has the ability to generate large magnetic fields. Ferromagnetic objects, or magnetotactic bacteria are tracked and navigated under real-time MRI. The typical field strength is 1.5 T or stronger [Nelson 2010]. The MRI systems can also be used to provide microrobots locomotion capabilities.

Kalambur presents in his paper [Kalambur 2005] the localization of groups of nanoparticules in an MRI system. Swarms of magnetotactic bacteria are localized as single objects in [Martel 2009]. The spatial resolution of the MRI system is similar to that of the early multislice Computed Tomography (CT) system [Rankin 2005], reaching 0.25 mm $\times$ 0.25 mm $\times$ 1.5 mm in a 3.0 T MRI machine [Schick 2005]. In the same work, an isotropic resolution of 0.57 mm is achieved, but the scan time is 25 s, which is too long for microrobotic applications. The mean error of a 3.0 T MRI machine is less than 1.0 mm [Azmi 2003]. Besides the limitation of the resolution of MRI machine, another drawback of MRI localization is the limited choice of material for fabrication of microrobots [Chinzei 1999]. Ferromagnetic objects cause image artifacts that are sometimes larger than the object to be localized [Felfoul 2004].

In the case of magnetically actuated microrobots, an additional magnetic field gradient for propulsion or a rotation-dedicated rotating magnetic field would be required. However, magnetic field gradient-based propulsion or rotation due to rotating magnetic field would be largely limited when a MRI has to be used with an observation device, because of the conflict between the imaging and propelling magnetic field [Hwang 2010]. This problem can be avoided by using non-magnetic observation device.

1.5.3 Computed Tomography (CT) and fluoroscopy

Computed tomography is a medical imaging procedure that uses computer-processed X-rays to produce tomographic images or 'slices' of specific areas of the body. The patient is placed between an X-ray source and a detector array. A set of projected X-ray images gathered from various view points is used to reconstruct the interior of the final image in 3D. Pixel resolution can reach 0.8 mm for a 512×512 pixel matrix [Fitton 2007], and an isotropic pixel size of 0.195 mm is achieved recently [Duryea 2008]. CT scans are not well suited for imaging regions of soft tissue surrounded by large volumes of high-density material such as bone, because of the underlying process of image reconstruction based on radiation attenuation.

Fluoroscopy also uses an X-ray source and a fluorescent receiver. High-resolution 2D radiographic images can reach about 100 µm pixel resolution [Antonuk 2000].

Both CT and fluoroscopy are suitable for in vivo applications, nevertheless the radiation dosage that a potential patient receives should be taken into consideration. Even more crucial is the dosage received by the medical staff, which can be reduced (but not cancelled) thanks to tele-manipulation techniques.

1.5.4 Ultrasound

For localization in soft tissue, only ultrasound combines good resolution, minimal adverse health effects, high speed, safety, adequate frame rates (up to 100 frames per second) [Xu 2005], and low cost [Vilkomerson 1997]. The major drawbacks of ultrasound are related to low signal-to-noise ratio and the presence of strong wave reflectors such as bones and air pockets. These may produce artifacts in ultrasound images or shield an ultrasound signal. The disadvantage of ultrasonic imaging may be partially overcome through passive localization techniques, based on ultrasound transmission. In applications of the localization, frequencies up to 3 MHz are reasonable, resulting in a resolution of about 500 µm and a penetration depth of $15 - 20$ cm [Vilkomerson 1997].

The localization of a wireless medical microrobot can be accomplished with a microrobot that acts as an emitter by carrying an ultrasound transducer onboard. A cantilever or any other mechanical structure can act as such, vibrating at its resonant frequency. The emitted signal is measured by a set of receivers placed on the surface of the patient's body. Through the use of MRI data gathered offline, localization accuracy can be greatly improved [Fluckiger 2007].

1.5.5 Vision

Vision is a useful robotic sensor since it mimics the human sense of vision and allows for noncontact measurement of the environment. The images are transmitted optically by cameras in combination with optical lenses. Obviously, vision can not be used for tracking microrobots in patient's body because of line-of-sight problems. The illuminating conditions have to be considered as well.

However, vision has several advantages compared with other imaging method. Firstly, high spatial resolution can be achieved by microscopic lenses. The resolution is limited by the light diffraction. Therefore, a resolution of 200 nm can be reached. The limitation can be overcome by using a camera in combination with a SEM, as shown in [Sievers 2005]. Some microrobots are actuated by magnetic field. Another advantage of vision is to avoid the conflict between the imaging and the actuating magnetic field. Thirdly, great energies are required to generate a magnetic field or to emit radiation for MRI, CT and ultrasound. It is not the case for vision, which is a energy-saving method.

1.5.6 Summary

The localization methods of the microrobots are summarized in Table 1.4 with their advantages and disadvantages. In this thesis, the experiments are all in vitro experiments. The non invasive imaging techniques or mini invasive imaging techniques are

not necessary to be taken into consideration. The main criteria are the simplicity of use and the resolution of the system. As a result, vision is a good candidate for the localization of the helical swimmers, due to the good resolution of the vision system with suitable optical lenses, and the ease of use. The vision system can be implanted by a camera connected to a computer with a suitable optical lens. Notice that the vision method is not promising for in vivo application, which requires non invasive imaging techniques.

The closed-loop motion control of the microrobots with vision feedback refers to a visual servo control, which is also called visual servoing. The state of the art of visual servoing is introduced in the next section.

Table 1.4: Summary of the localization methods for the microrobots.

Localization method	**Advantage**	**Disadvantage**
Electromagnetic	low-cost device & promising for line-of-sight problem	only for magnetic objects
MRI	non invasive imaging technique, promising for line-of-sight problem & provide locomotion	low resolution & conflict with actuation system & no portable & cost lots of energy
CT & fluoroscopy	non invasive imaging technique & high resolution	not promising for soft tissue surrounded by large volumes of high-density materials & radiation dosage
Ultrasound	localization in soft tissue & good resolution	low signal-to-noise ratio
Vision	high resolution with sophisticated optical devices & energy saving & no conflict with actuation magnetic field & ease to use & applicable for all objects	line-of-sight problem & lighting problem

1.6 Visual servoing for microrobots

In this section, a short history and two basic methods of visual servoing are introduced. Then, the state of the art of visual servoing for microrobots is presented.

1.6.1 Introduction of visual servoing

Visual servoing, also called visual servo control, is the fusion of results of many elemental areas including high-speed image processing, computer vision and control theory. At the early stage, typically visual sensing and manipulation are combined in an open-loop

system, "looking" then "moving". The accuracy of the resulting operation depends directly on the accuracy of the visual sensor and the robot end-effector [Hutchinson 1996]. An alternative to increasing the accuracy of these subsystems is to use a visual-feedback control loop. A closed-loop position control for a robot end-effector by a machine vision referred to as visual servoing. The term "visual servoing" appears to have been first introduced by Hill and Park [Hill 1979] in 1979 to distinguish their approach from earlier experiments where the system alternated between picture taking and moving. In 1980, Sanderson and Weiss [Sanderson 1980] introduced a taxonomy of visual servo system:

- Dynamic look-and-move systems: The vision system provides input to robot controller that then uses joint feedback to internally stabilize the robot.
- Direct visual servo systems: The visual controller directly computes the input to the robot joints and robot controller is eliminated.

As pointed out by Hutchinson [Hutchinson 1996], nearly all of the reported systems used the first approach, dynamic look-and-move system.

There are two camera-robot configurations for visual servoing: eye-in-hand configuration and eye-to-hand configuration. The eye-in-hand configuration consists in camera mounted on the end effector of the robot, as shown in Figure 1.24a. In the eye-to-hand configuration, the camera is fixed in the workspace, as shown in Figure 1.24b. As regards as the application for microrobots, it is impossible to mount a visual sensor on a microrobot considering the size. Only the eye-to-hand configuration is considered for microrobots.

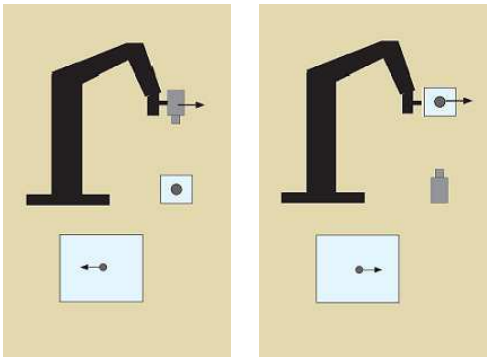

(a) (b)

Figure 1.24: Top: (a) Eye-in-hand configuration. (b) Eye-to-hand configuration. Bottom: Opposite image motion produced by the same robot motion. [Chaumette 2007]

1.6.2 Basic components of visual servoing

The aim of vision-based control schemes is to minimize an error $\mathbf{e}(t)$, which is typically defined by [Chaumette 2006]:

$$\mathbf{e}(t) = \mathbf{s}({}^{c}\mathbf{p}(t)) - \mathbf{s}^{*} \tag{1.19}$$

where $\mathbf{s}^*$ is the desired values of the features, $\mathbf{s}$ is the current values of the features, and ${}^c\mathbf{p}(t)$ is the relative pose between the camera and the object at instance t.

When the control variables are defined in the camera frame, the variation of the visual feature $\mathbf{s}$ related to the relative movements between the camera and the scene is given by:

$$\dot{\mathbf{s}} = \frac{\partial \mathbf{s}}{\partial {}^c\mathbf{p}} \frac{\partial {}^c\mathbf{p}}{\partial t} + \frac{\partial \mathbf{s}}{\partial t} = \mathbf{L_s} \cdot {}^c\mathbf{v}_o + \frac{\partial \mathbf{s}}{\partial t} \tag{1.20}$$

where $\mathbf{L_s} \in \mathbb{R}^{k\times 6}$ is the visual features interaction matrix that represents the differential relationship between the features s and the camera frame [Hutchinson 1996]. ${}^c\mathbf{v}_o = \mathbf{v}_c - \mathbf{v}_o$ presents the relative instantaneous velocity between the camera frame and the object frame expressed in the camera frame. v_c is the instantaneous camera velocity and $\mathbf{v}_o$ is the instantaneous object velocity. $\dfrac{\partial \mathbf{s}}{\partial t}$ presents the variation of $\mathbf{s}$ due to the object own motion. In the case that the object is rigid (no deformations), $\dfrac{\partial \mathbf{s}}{\partial t}$ disappears, then:

$$\dot{\mathbf{s}} = \mathbf{L_s}\mathbf{v}_c \tag{1.21}$$

Using (1.19) and (1.21), we obtain the relationship between camera velocity and the time variation of the error:

$$\dot{\mathbf{e}} = \mathbf{L_e}\mathbf{v}_c \tag{1.22}$$

where $\mathbf{L_e} = \mathbf{L_s}$. Using a classical control law such that the visual error $\mathbf{e}$ is expected to converge to zero exponentially ($\dot{\mathbf{e}} = -\lambda\mathbf{e}$), the relationship becomes as follow:

$$\mathbf{v}_c = -\lambda {\mathbf{L_e}}^{+}\mathbf{e} \tag{1.23}$$

where ${\mathbf{L_e}}^{+} \in \mathbb{R}^{6\times k}$ is chosen as the Moore-Penrose pseudo-inverse of $\mathbf{L_e}$, that is

$${\mathbf{L_e}}^{+} = ({\mathbf{L_e}}^T\mathbf{L_e})^{-1}{\mathbf{L_e}}^T \tag{1.24}$$

when $\mathbf{L_e}$ is of full rank 6. This choice allow $\| \dot{\mathbf{e}} = -\lambda\mathbf{L_e}\mathbf{L_e^+}\mathbf{e} \|$ and $\| \mathbf{v}_c \|$ to be minimal. When $k = 6$, if $\det \mathbf{L_e} \neq 0$ it is possible to invert $\mathbf{L_e}$, giving the control:

$$\mathbf{v}_c = -\lambda\mathbf{L_e}^{-1}\mathbf{e} \tag{1.25}$$

In real visual servo system, it is impossible to know perfectly in practice either $\mathbf{L_e}$ or $\mathbf{L_e^+}$. Therefore, an approximation or an estimation of one of those two matrices must be realized. Both the pseudoinverse of the approximation of the interaction matrix and the approximation of the pseudoinverse of the interaction matrix are noted as $\widehat{\mathbf{L_e^+}}$. The control law can be expressed as follows:

$$\mathbf{v}_c = -\lambda\widehat{\mathbf{L_e^+}}\mathbf{e} \tag{1.26}$$

This is the basic design implemented by most visual servo controllers.

Visual servoing schemes mainly differ in the way that $\mathbf{s}$ is designed. In the following sections, we introduce two different approaches: (1) an Image-Based Visual servoing (IBVS) in which $\mathbf{s}$ consists of a set of features that are immediately available in the image data; (2) a Pose-Based Visual servoing (PBVS) in which $\mathbf{s}$ consists of a set of 3D parameters, which must be estimated from image measurements.

1.6.3 Image-Based Visual Servoing (IBVS)

In IBVS, the error is defined directly in terms of 2D image feature parameters. Visual features can be selected in 2D image space as point coordinates, parameters representing straight lines or ellipses, region of interest, contours. In all cases, the parameters defining the internal camera calibration are required.

First advantage of IBVS is that the positioning accuracy is robust to errors in camera calibrations and image noise, since the features are directly expressed in the image space [Hutchinson 1996, Chaumette 2006]. Another advantage of IBVS is that the target can be constained to remain visible during the execution of a task if both the initial and desired image feature locations are within the camera field of view [Chaumette 1998].

However, IBVS is not without its shortcomings. Firstly, it is hard to predict the trajectory of the end effector and robot may reach its joint limits [Marey 2010]. Furthermore, the trajectories of the end effector are often suboptimal [Chaumette 2006]. Finally, usual IBVS is only local asymptotically stable and may fail in the presence of large displacement to realize [Chaumette 1998, Cervera 1999], in which case the camera may cross a singularity of the interaction matrix [Chaumette 2006].

1.6.4 Position-Based Visual Servoing (PBVS)

In PBVS, features are extracted from the image and used to compute or estimate the relative pose between the object and the camera frames in Cartesian space or to reconstruct the 3D coordinates. Computing that pose from a set of measurements in one image requires the cameras intrinsic parameters and the 3D model of the object observed.

Compare to IBVS, PBVS has a global asymptotic stability of a controller to stabilize the pose of the camera from any initial condition if 3D estimation is perfect. PBVS allows the camera to follow theoretically an optimal trajectory in the Cartesian space, but generally not in the image space.

Errors in calibration and image measurement propagate errors in the 3D world. Even a small error in the image measurements can lead to errors in the pose that can impact significantly the accuracy of the system [Chaumette 2006]. Furthermore, there is no control in the image which implies that the target object may leave the camera field of view [Malis 1999].

1.6.5 Visual servoing for microrobots

Microrobots are increasingly called upon to perform more manipulation tasks. However, these operations are primarily open-loop, due to the limited number of feedback options with the required precision [Kratochvil 2009]. Manipulations are often performed in conjunction with devices such as optical microscopes, or SEM, which all provide sensory feedback in the form of a monocular image. One major challenge of performing visual servoing tasks for microrobots is the image quality. Real-time visual feedback from microscopes is typically noisy and blurred when observing microrobots in high-speed motion, as shown in Figure 1.25. It creates significant challenges for an image processing system. The major challenge of performing visual servoing tasks inside a SEM is

balancing the needs of image quality with real-time imaging. The sequential scanning used to create a SEM image necessitates lower framerates than those available with optical cameras.

Figure 1.25: Image sequence of a helical microswimmer in motion [Zhang 2009a].

Some visual servoing tasks for microbots with simple geometries have been realised. For example, Mikawa described an observation system for monitoring a micro mass axis alignment system with each arm having a diameter of several micrometers, and a controller based on the visual servoing method for controlling a micro machine [Mikawa 1996]. The system can be controlled based on visual information on image planes rather than in 3D space. The misalignment error of optical fibres are decreased due to the visual servo controller.

CAD model based methods have been applied to help more precise motion feedback for microrobots with more complicated geometries. Kratochvil used to track a micro-gripper, which is shown in Figure 1.26a, in real-time inside a SEM [Kratochvil 2009]. Tamadazte proposed a automated microassembly system using 3D pose-base visual servo control, supplied by a CAD model-based tracking algorithm [Tamadazte 2009]. The objects for assembly are shown in Figure 1.26b.

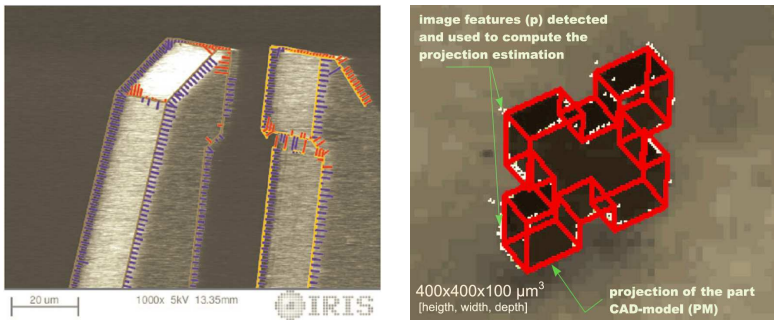

(a) (b)

Figure 1.26: (a) Microgripper tracked inside a SEM [Kratochvil 2009]. (b) Micro-objet for assembly [Tamadazte 2009].

However, as far as we know, the real-time visual servoing tasks has not been applied for helical microswimmers, due to complexity of the control of the magnetic field actuating the helical propulsion, and the low image quality created by the complexity of the geometry and the high speed rotation (see Figure 1.25). Therefore, the other main objective of this thesis is to realize a visual servo control of the helical swimmers.

1.7 Overview of thesis

As presented in the chapter, helical microswimmers capable of helical propulsion inspired by E.coli bacterial swimming behaviors are promising for swimming at low Reynolds numbers, because the helical propulsion is a non-reciprocal motion. The helical microswimmers have a great potential for numerous applications ranging from in vitro tasks, such as micro-manipulation and micro-assembly, to in vivo tasks, such as targeted drug delivery, if the motion of the helical microswimmers is controllable. The major challenge is to realize a closed-loop motion control of the helical microswimmers. In order to realize the control, the characterization of the swimming properties is crucial.

Several magnetically actuated artificial helical swimmers have been proposed and presented in this chapter. They have different geometry parameters, head shapes, and magnetic positioning. And as far as we know, none of the proposed helical swimmers has been controlled by a closed-loop controller. Therefore, the two major objectives of this thesis are:

- to compare the swimming performances of helical swimmers with different designs to further improve their design and to characterize their swimming properties.
- to realize a visual servo control of helical swimmers.

Scaled-up helical microswimmers, which are defined as the helical swimmers with overall lengths higher than 1 mm, but still swim at the low Reynolds numbers, are proposed in this thesis. The scaled-up helical microswimmers facilitate the fabrication and localization by vision. The investigation of the swimming properties of the different helical swimmers are presented in Chapter 3. The realization of a visual servo control of the helical swimmers is demonstrated in Chapter 4. The detailed plan of this thesis is described as follows:

Chapter 2 is an overview of the system, including the helical swimmers, the experiment setup, and some methods of the swimming characteristics estimation. The specifications and the fabrication of all scaled-up helical microswimmers used in this thesis are presented. The experimental setup includes a magnetic actuation system and a vision system. The magnetic actuation system is described from the design to the generation of the controlled magnetic field. A real-time tracking method with the barycenter and the orientation is presented as well. The methods of the estimation of the swimming characteristics, such as rotation frequency, translation velocity, and the propulsion matrix of the helical swimmer is introduced at last.

In Chapter 3, the influence of the geometry parameters of the helical swimmers on their swimming performances is studied, in order to further improve the design of the helical swimmers. Then, the rotational propulsion characteristics of the helical swimmers with different head shapes and magnetic positionings are investigated. The design of the helical swimmers is discussed both at the microscale and the millimeter scale. The propulsion matrices of the helical swimmer in different viscous liquids are identified. The linear propulsion velocity is simulated based on the estimated propulsion matrix. At last, an open-loop steering control of the helical swimmers is presented. The steering of the helical swimmers have not been extensively studied in the literature.

However, the steering is very important to realize a 3D motion of the helical swimmers. A strategy of steering is proposed to improve the steering efficiency.

In Chapter 4, the calibration of the camera systems is at first presented. Then, a pose estimation, including the orientation and the position of the helical swimmers in the 3D space is presented. The control law of the actuating magetic field is established. The visual servo control for the orientation of the helical swimmers is realized in the 3D space. Path following tasks are planned for helical swimmers. The 2D path following task on the horizontal plane is realized by following a straight line with the initial position both on and off that line. 3D path following task in the space is as well discussed for future applications. Some perspectives are discussed at last.

Chapter 2

Overview of the system

Contents

In this chapter, the helical swimmers used in the experiments is presented, as well as the viscous liquids. The magnetic actuation systems used are the three orthogonally arranged Helmholtz coil pairs and a rotating permanent magnet manipulator. The control of the strength and the rotation frequency of the rotation magnetic field generated by the magnetic actuation systems are presented respectively. The visual tracking of the helical swimmers with its barycenter and axis on the 2D image is then introduced. At last, the methods to analyse the rotation frequency and the swimming velocity of the helical swimmers is presented in detail, which is useful to the characterization of the swimming property of the helical swimmers.

2.1 Scaled-up Helical Microswimmers (SHMs)

As presented before, in this thesis, the helical swimmers used in the experiments are the scaled-up helical microswimmers at the millimeter scale. In this section, the reason and the feasibility of using the SHMs is presented in detail. The design and fabrication of the different SHMs is also described.

2.1.1 Why the scaled-up helical microswimmers?

The control of helical microswimmers has not been clearly realized mainly due to the limited observation tools to characterize the swimming characteristics and to identify the propulsion matrices at the microscale. Up to now, different helical microswimmers have been proposed as introduced in Section 1.3.2. These helical microswimmers have different geometry parameters (diameter, pitch, width, number of turns), different head shapes including square-plate, cylinder and sphere, and magnetic positioning.

Understanding how these geometry parameters, head shapes and magnetic positioning influence the swimming performance allows improvements in helical microswimmers design. Making different geometry parameters and head shapes requires several weeks of work and high cost. It is then not suitable to modify the geometry parameters. We then have the idea to scale the helical microswimmers up to the millimeter scale. The SHMs are feasible, because the fluid motion around the helical swimmer is only characterized by a dimensionless parameter: the Reynolds number (see Section 1.2.1). Therefore, the propulsion behaviors of helical swimmers should be the same if they swim at the same Reynolds numbers, which make a dimensionless study possible. To emulate at an upper-scale the environment of microscale swimmers swimming at low Reynolds numbers, one can use more viscous liquid, such as glycerol. Once the optimal design for the helical swimmers at the millimeter scale is determined, it can be applied as a guideline to the fabrication of the helical swimmers at the microscale. The helical swimmers can be scaled down to the microscale without difficulties, because the micro-fabrication process of helical microswimmers is mastered as presented in Section 1.3.1.

In addition, the SHMs can be easily viewed with regular optical devices. The quality of images should be good enough for tracking. Therefore, they are also good candidate to test the visual servo control at the first step. Once the visual servo control is validated on the SHMs, it can be applied to helical microswimmers by using suitable optical devices with a high resolution in future works. The designs of the SHMs with different geometry parameters, head shapes, and magnetic positioning are presented as follows.

2.1.2 Design and fabrication of scaled-up helical microswimmers

The SHMs are classified and named by their inner diameters. Two categories of SHMs are made: SHM1s are those with inner diameters of 1 mm; and SHM5s are the SHMs with inner diameters of 5 mm.

2.1.2.1 SHM1s

Two categories of SHM1s are fabricated. SHM1s in the first category are made of titanium, with magnetic layers coated on the surface of helical tails. SHM1s in the second category are made of resine, having non magnetic tails and magnetic heads. They are all named SHM1-mhX (mh means magnetic head, and X is the number).

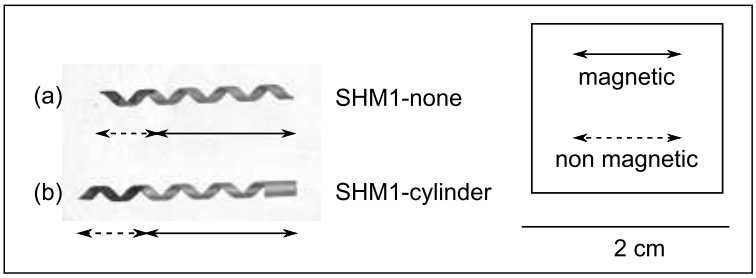

Figure 2.1: SHM1s with inner diameters of 1 mm, are made of titanium. They are coated by ferromagnetic layers (nickel).

SHM1s with magnetic tails: The titanium SHM1s are made by *i.materialise* (*http://i.materialise.com/*). They are presented in Figure 2.1. Their geometry parameters are scaled from HNB as well, which are presented in Table 2.1. According to their head shapes, the SHM1 without a head is named SHM1-none, and the SHM with a cylindrical head is named SHM1-cylinder.

They are coated by ferromagnetic material: nickel. For the thick layer coating, electroplating is used. Titanium oxides very easily. The titanium is thus deoxidized by hydrochloric acid right before the electroplating. The titanium models are placed onto the negative electrodes and the positive electrode is placed near the models. These are immersed in a nickel bath with the application of electric potential between the two electrodes. The deposition rate is calibrated onto the dummy silicon surface coated with a titanium layer. The end of the helical tail is used to make an electric contact during the electrolytic deposition process, thus the last pitch is not coated. The thickness of nickel layers are estimated as $20 - 50$ μm.

SHM1s with magnetic heads: The resine SHM1-mhXs are made by *3d prod* (*http://www.3dprod.com/*). They are presented in Figure 2.2. The advantage of the resine SHM1-mhXs is the low cost and the quick fabrication, which allows fabrication of large numbers of SHM1-mhXs with different geometry parameters (pitch, width, numbers of turns). The different geometry parameters are defined by a 2^3 factorial design, which are depicted in Table 2.2, using design of experiments method. The design of experiments is presented in more detail in Section 3.1. The minimal thickness imposed by *3d prod* is 0.3 mm. Each SHM1-mhX has a cylindrical tube head, with a 0.5 mm thick slit at the middle. A circle-plate permanent magnet (Supermagnete S-1.5-0.5-N) magnetized in the diameter with 1.5 mm of diameter and 0.5 mm of thickness is seated in the slit. Note that SHM1-mh8 is the scaled-up model of HNB.

Table 2.1: Specifications of the HNB and the SHMs [Hwang 2010, Xu 2012].

Parameters	**HNB**	**SHM5**	**SHM1-none/-cylinder**
Inner diameter	2.1 µm	5 mm	1 mm
Thickness	27.2 nm	1 mm	0.3 mm
Pitch	14 µm	20 mm	4 mm
Width	2.5 µm	7.2 mm	1.44 mm
Length	62 µm	90 mm	18 mm
Nb of turns	4.5	4.5	4.5
Weight	–	(a) 1.75 g	(a) 0.04 g
		(b) 2.08 g	(b) 0.05 g
		(c) 2.63 g	
		(d) 1.85 g	
		(e) 4.98 g	
Magnetic material	Nickel	NdFeB	Nickel
Magnetic layer	30 nm	1 mm	$20 - 50$ µm

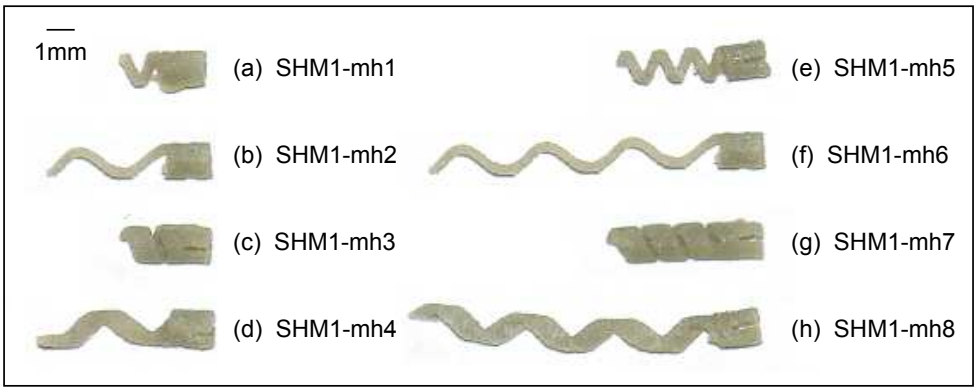

Figure 2.2: SHM1s with inner diameters of 1 mm, made of resine. Their geometry parameters are defined by a 2^3 factorial design. Magnetic heads are seated in the slits of the heads.

Table 2.2: Geometry parameters specifications of resine SHM1-mhXs.

SHM1-mhX	diameter (mm)	pitch (mm)	width (mm)	nb of pitch	length (mm)
1	1	1.5	0.5	1.5	2.25
2	1	4	0.5	1.5	6
3	1	1.5	1.2	1.5	2.25
4	1	4	1.2	1.5	6
5	1	1.5	0.5	3.5	5.25
6	1	4	0.5	3.5	14
7	1	1.5	1.2	3.5	5.25
8	1	4	1.2	3.5	14

2.1.2.2 SHM5s

The family of SHM5s with their names are depicted in Figure 2.3. All SHM5s geometry parameters are scaled from HNB, which appeared in [Hwang 2010], except for the thickness. It means that they are also scaled-up from SHM1-mh8. The geometry parameters specifications of HNB and SHM5s are described in Table 2.1. The basic structures of SHM5 are made of Acrylonitrile Butadiene Styrene (ABS) (ABSPlus P400) by a rapid prototyping machine (Stratasys Dimension SST 768) using Fused Deposition Modeling (FDM) method. The thermoplastics are liquefied and deposited by an extrusion head, which follows a tool-path defined by a STL file. The materials are deposited in layers as fine as 0.25 mm. Therefore, the thickness of SHM5s is designed as 1 mm thick for having enough layers to enforce the structure.

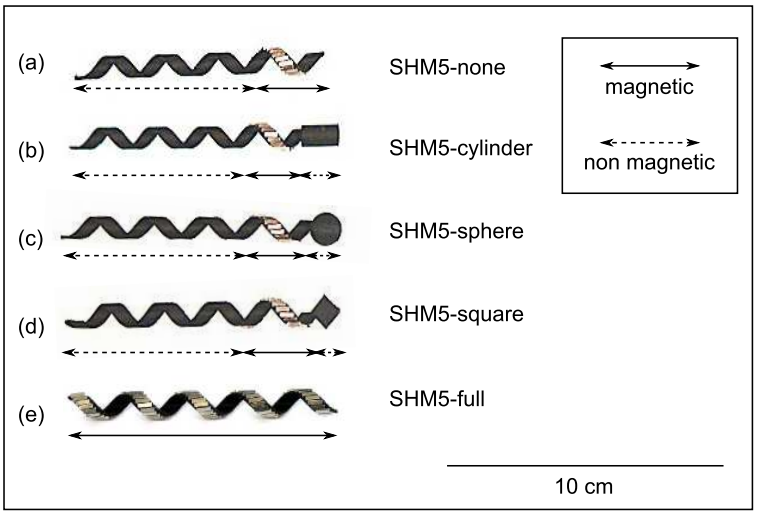

Figure 2.3: SHM5s with inner diameters of 5 mm. (a)-(d) The first turn of helical tail is cover by magnets. (e) The whole helical tail is covered by magnets.

The SHM5s have magnetic helical tails and non-magnetic heads. Their first pitches (see Figure 2.3 (a)-(d)) or entire surface (see Figure 2.3 (e)) of their helical tails are covered with several NdFeB permanent magnets from Supermagnete (5 mm $\times$ 1.5 mm $\times$ 1 mm). The magnetic layer coated on the surface of the helical tails are not uniform. The heads of the SHM5s are in different shapes: without a head (Figure 2.3 (a)), with a cylindrical head (Figure 2.3 (b)), spherical head (Figure 2.3 (c)) and square head (Figure 2.3 (d)). Those heads are not magnetic.

2.1.3 Swimming at low Reynolds numbers

As explained in Section 2.1.1, to simulate the low Reynolds number environments, viscous liquids must be used. Glycerol solutions are good candidates, because glycerol is a water-soluble, colorless, odourless, viscous liquid. Glycerol solutions with different concentrations show different viscosities. The concentrations of the glycerol solutions used in the experiments are 30%, 50%, 60%, 70%, 75%, 80%, 85%, 90%, 95%, and 100%.

The Reynolds number can be calculated as in equation (1.1), using the characteristic linear dimension and the velocity of the SHM, the density and viscosity of the liquid. The viscosity of the liquid is measured by a falling ball viscometer (Brookfield KF10). The viscosity of glycerol solutions is sensitive to the environmental temperature. The measured experimental temperature is about 23 °C. The density of the liquid is measured by a portable density meter (DMA 35). For the rotational propulsion characteristics studies, the translational velocities are considered as zero. In order to calculate the Reynolds numbers for rotational propulsion characteristics, we assume that the linear velocities are 1 pitch per second. The characteristic linear dimensions are taken as the hydraulic diameters of the SHMs. The hydraulic diameter of a tube is defined as the difference between its outer diameter and inner diameter, which is its thickness. Table 2.3 summarizes the measured viscosities of glycerol solutions used and the calculated Reynolds numbers at which the two sizes of SHMs swim in the rotational propulsion experiments.

Table 2.3: Measured viscosity of different glycerol solution and calculated Reynolds numbers at which SHM5s and SHM1s swim in the rotational propulsion experiments.

% of Glycerol	**viscosity** (mPa · s)	**density** (g/m^3)	**Re(SHM5)**	**Re(SHM1)**
30%	3.2	1.09	–	0.54
50%	8.5	1.14	2.68	–
60%	16.1	1.17	1.45	0.11
70%	32.4	1.19	0.73	0.06
75%	43.7	1.20	0.54	–
80%	66.5	1.21	0.36	0.03
85%	124.6	1.22	0.20	–
90%	260.0	1.23	0.09	0.008
95%	552.0	1.24	–	0.004
100%	1524.0	1.26	–	0.001

In water, a swimming bacterium such as E.coli has a $Re \approx 10^{-5} - 10^{-4}$. A human spermatozoon moves with $Re \approx 0.01$. The larger ciliates such as paramecium swims with $Re \approx 0.1$ [Lauga 2009]. The HNBs swim with $Re \approx 3.4 \times 10^{-4} - 3.6 \times 10^{-2}$ [Hwang 2011]. In the experiments for characterization of rotational propulsion properties, the Reynolds numbers at which the SHMs swim are $Re \approx 0.001 - 3$. It is technically difficult to further decrease the Reynolds numbers at which the SHMs swim. Nevertheless, with these experimental conditions, the rotational propulsion behaviors of the SHMs are studied at low Reynolds numbers.

The SHMs are actuated by a rotating magnetic field. In the following two sections, two magnetic actuation systems used in the experiments are presented: a 3D Helmholtz coil pairs system and a Rotating Permanent Magnet Manipulator (RPMM).

2.2 3D Helmholtz coil pairs system

A 3D Helmholtz coil pairs system consists of three orthogonally arranged Helmholtz coil pairs capable of generating rotating magnetic field around any axis in the 3D space is used in the experiments to actuate the helical swimmers. In this section, the principle of the Helmholtz coil pair is at first introduced. The design and the fabrication of the 3D Helmholtz coil pairs system are then described. Then, the vision system is presented afterwards. The control of the rotation magnetic field generation both in the 2D and 3D space is presented at last.

2.2.1 Helmholtz coils principle

A Helmholtz coil pair is made up of two, identical, circular coils aligned on the same axis and separated by a distance h equal to the radius R of the coil. Each coil carries an equal electrical current flowing in the same direction. This arrangement of coils is invented by a German physicist, Hermann von Helmholtz, over a century ago. Helmholtz coils have been used in applications in which highly uniform magnetic fields are required. The magnetic field produced by Helmholtz coils is homogeneous at the center of the coils. The magnetic flux density norm B at the center of the coils is described by:

$$B = \left(\frac{4}{5}\right)^{3/2} \frac{\mu_0 n I}{R} \tag{2.1}$$

where n is the number of turns per coil, I is the current flux density running through the coils, R is the radius of a coil, and $\mu_0 = 4\pi \times 10^{-7}\ \mathrm{T \cdot m/A} = 1.26 \times 10^{-6}\ \mathrm{T \cdot m/A}$ is the permeability constant.

The simulation of the magnetic field generated by a Helmholtz coil pair by Comsol is depicted by Figure 2.4a. The magnetic flux density norm along the axis direction of the coil pair and along the direction perpendicular to the axis and at the middle of the two coils is shown in Figure 2.4b. The magnetic flux density norm along these two direction shows the homogeneity of the field at the center of the coil pair.

One Helmholtz coil pair can generate a uniform magnetic field at the region of interest in one direction. Therefore, three orthogonal arranged Helmholtz coil pairs can generate a uniform magnetic field at the region of interest in any direction in the space. Furthermore, it can generate a rotating uniform magnetic field around any axis in the space.

2.2.2 3D Helmholtz coil pairs system design and realisation

It is decided that the small coils have an inner open space larger than 8 cm for the ease of use. This would allow enough room for samples access. The Helmholtz coils pairs are designed for a maximum 15 mT at the center of the coils space. The maximal current in one coil is designed at about 3 A due to the the heating problem of the resistances. The diameter of the small coils is decided to be 50 mm. With the diameter of the coil and the current, the number of turns is estimated as 500. The diameter of the copper wire is chosen as 0.8 mm. This diameter of the copper wire is relatively high in order to avoid overheating of the wire. The width of the coils is designed to have a good compromise between the width and the thickness of the coils. In the

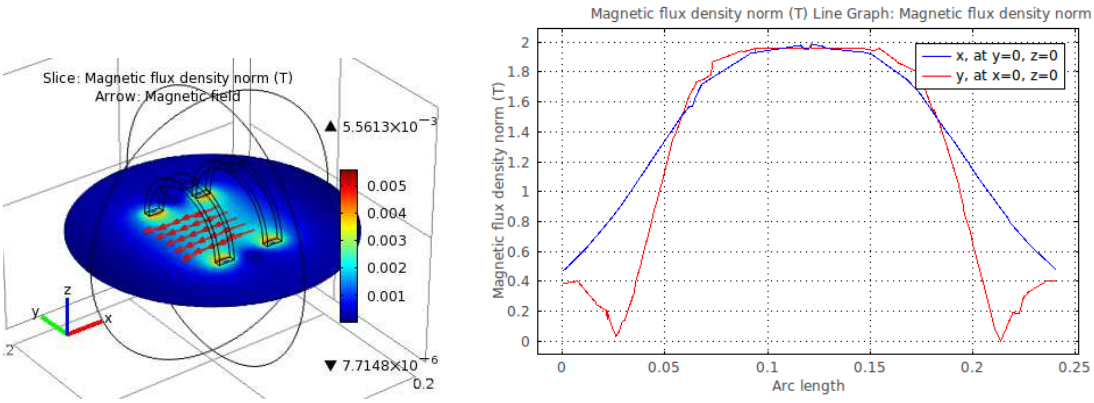

(a) (b)

Figure 2.4: (a) The simulation of the Magnetic field generated by a Helmholtz coil pair by Comsol. (b) Magnetic flux density along the axes of the two coils, which is homogeneous at the center of the two coils.

best rolling conditions, the thickness of the 500 turns copper wire of 0.8 mm diameter is estimated as 13.3 mm with a width of 24 mm. After the estimation of the space that 500 turns of copper wire would take, the diameters of the medium and the big coils can be determined. Finally, the parameters of the three Helmholtz coil pairs are summarized in Table 2.4.

Table 2.4: Specifications of three-pair-Helmholtz coils design for B=15 mT.

	Radius (mm)	Nb of turns	Current (A)	Witch (mm)	Thickness (mm)
Small	50	500	1.67	24	13.3
Medium	80	600	2.22	24	16
big	110	600	3.06	24	16

The CAD design of the three Helmholtz coil pairs with a mechanical support for the coils (blue part) is depicted by Figure 2.5a. A plateform is designed at the center of the Helmholtz coils to hold the container with the SHM in the liquid. The plateform should be semi-transparent and be able to disperse the light, so that a LED can be placed at the bottom of the support to backlight the SHM at the workspace of the Helmholtz coils through the plateform.

The mechanical support for the coils and the supports of the small and medium coils are made of ABS by rapid prototype machine (Dimension 768 Series). The supports of the big coils is made of aluminium for two reasons: firstly, the dimension surpasses the prototype machine capacity (203 mm × 203 mm × 305 mm); secondly, aluminium is good conductor of heat. The resistances of the big coils are greater, so the big coils create more heat. The supports made of aluminium are good heat radiators. The copper wires are mounted manually. The measured resistances of each coils are

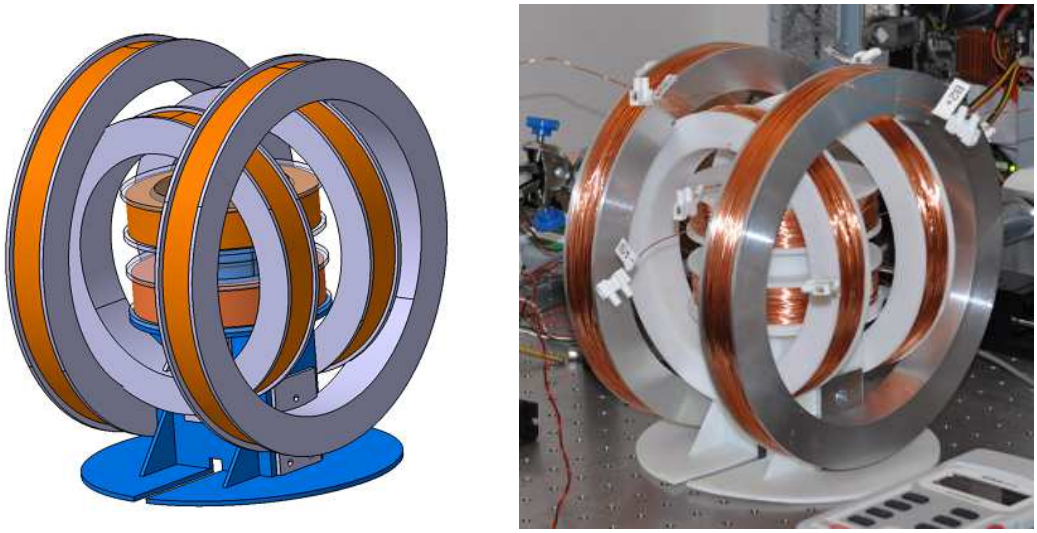

(a) (b)

Figure 2.5: (a) Three orthogonal arranged Helmholtz coil pairs CAD design. (b) Three orthogonal arranged Helmholtz coil pairs experimental setup.

shown in Table 2.5. The resistances of two coils in the same pair are nearly identical, which ensure the currents passing through the two coils in the same coil pair are nearly identical. That influences the homogeneity of the magnetic field generated by the coil pair. Unexpected magnetic gradient will be created, if the currents are not identical.

Table 2.5: Measured resistances (Ω) of each coils to validate that the two coils of each pair are identical.

Small		Medium		Big	
R1	R2	R1	R2	R1	R2
7.2	7.2	10.1	10.2	15.3	15.2

Each set of Helmholtz coils is driven by an ADS 50/5 4-Q-DC servoamplifier of Maxon motor control amplifier, capable of 5 A continuous current and 10 A peak current. The amplifiers are alimented by a TDK-Lambda SWS300-48 DC power supply, capable of 6.7 A current and 48 V voltage. The amplifiers are used on current control mode, the output current are thus constant for a fixed input voltage. Analog communication between the PC and the amplifiers is accomplished with a Sensoray 626 Analog and Digital I/O card (S626).

2.2.3 Vision system implementation

A stereo vision system with two cameras, the top camera and the side camera, are integrated in the system. As shown in Figure 2.6, the top camera is on the top, and the side camera is beside the Helmholtz coils. The two cameras are both firewire

cameras. The top camera is a Pike F032B. The maximal frame rate is 208 fps at full resolution (640×480). A lens with 25 mm of focal length is mounted on the top camera. The side camera is a Guppy Pro F032. The maximal frame rate is 82 fps at full resolution (656×492). Due to the limited side opening, an endoscope (Bipol) with a diameter of 2.7 mm is connected on the side camera by a coupler lens. The focal length of the coupler lens is 30 mm.

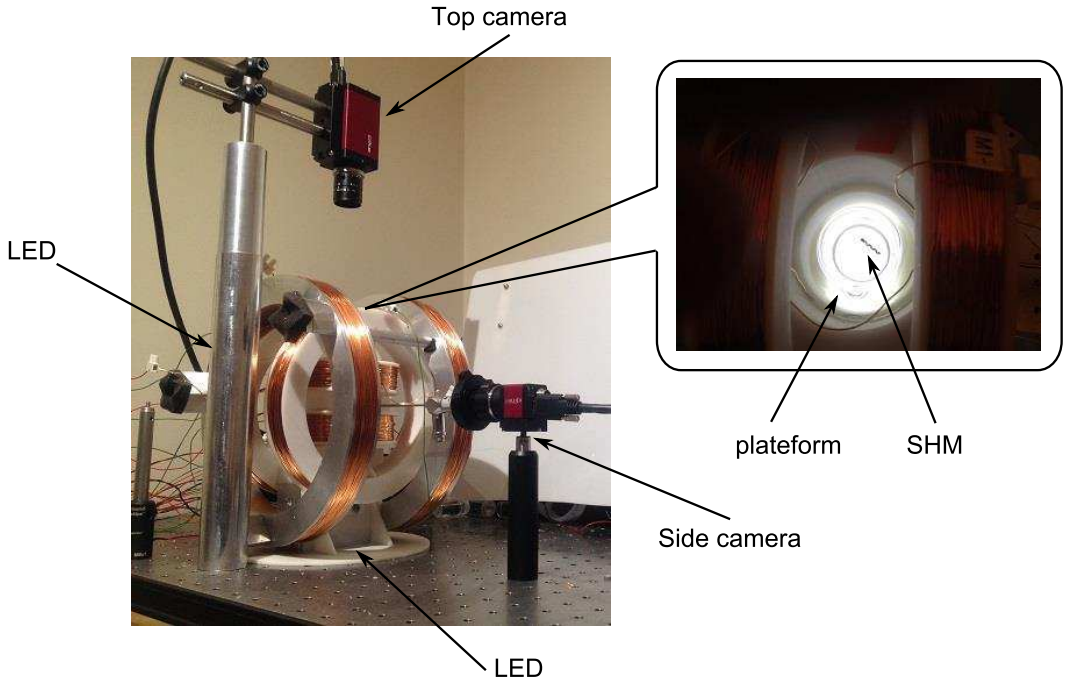

Figure 2.6: 3D Helmholtz coil pairs experiment setup with two cameras.

2.2.4 Magnetic field calibration and generation

For the actuation of the magnetic SHMs with a 3D Helmholtz coil pairs setup, the rotating magnetic field should be generated with a desired magnetic field strength and rotation frequency. Two methods to generate rotating magnetic field with Helmholtz coil pairs are introduced below. The first method is the generation of a rotating magnetic field around an axis x, y, or z. As the magnetic field is in the planes yOz, xOz, or xOy anytime, it can be defined as the 2D rotating magnetic field. The second method is the generation of a rotating magnetic field around any axis in the space. Therefore it can be defined as the 3D rotating magnetic field. In order to generate the rotating magnetic field with a desired magnetic field strength, the Helmholtz coil pairs should be calibrated.

2.2.4.1 Magnetic field calibration

To calibrate the Helmholtz coil pairs means to find the relationship between the strength of the magnetic field generated at the center of the coil pairs and the currents passing through the coils. From equation (2.1), as the number of turn (n) and the resistance

for one coil pair (R) are fixed, the generated magnetic field flux density (B_0) depends only on the current (I) through the coils. The currents pass through a coil pair are constant for a fixed output voltage of the PCI card. Thus the generated magnetic field depends only on the output voltage of the PCI card.

The relationship between the generated magnetic field and the commanded output voltage of the PCI card is calibrated in the center of the workspace using a Hirst GM08 gaussmeter. Figure 2.7 depicts the measured magnetic flux density at the center of the Helmholtz coil pairs generated individually by the three Helmholtz coil pairs. The capacity of this Helmholtz coil pairs is limited by the output power of the power supply applied to the big coils. The practical maximal magnetic field that the 3D Helmholtz coil pairs can generate is about 12 mT for the big coils.

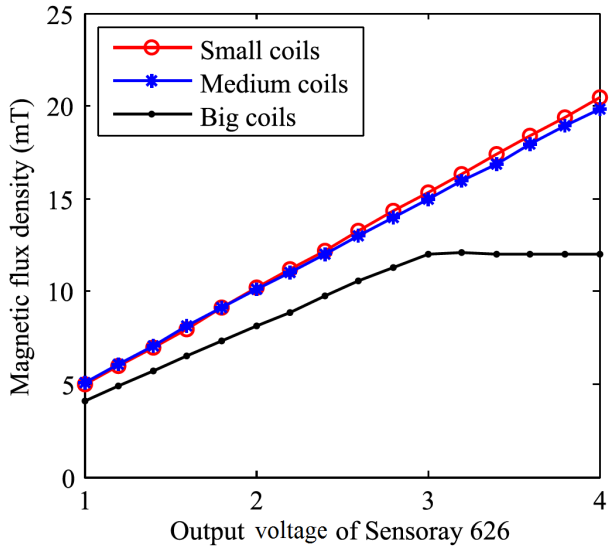

Figure 2.7: Magnetic flux density of the magnetic field generated individually by the three Helmholtz coil pairs in function of the output voltage of the PCI card.

In the following experiments, rotating magnetic fields with the magnetic flux density of $B_0 = 5$ mT and $B_0 = 10$ mT at the center of the workspace are used. Table 2.6 describes the output voltage of the PCI card corresponding to each coils to generate 5 mT or 10 mT magnetic field.

Table 2.6: Specifications of the PCI card output voltages to generate a magnetic field with magnetic flux densities of $B_0 = 5$ mT and $B_0 = 10$ mT.

Magnetic flux density (B_0)	U_x (V)	U_y (V)	U_z (V)
5 mT	1	1	1.2
10 mT	2	2	2.4

2.2.4.2 World coordinate system

Here, the world coordinate system $\mathcal{R}_w = (O, x, y, z)$ is defined by the directions of the magnetic field generated by the three Helmholtz coil pairs. The center O is defined by the center of the three coil pairs. The x axis is defined as the magnetic field direction when we apply a current to the small coil pair. Thus, the x axis is in the direction of the axis of the small coil pair, which can be shown in Figure 2.8. Similarly, the y axis is defined as the magnetic field direction when we apply a current to the medium coil pair, and the z axis is defined as the magnetic field direction when we apply a current to the big coil pair. Make sure that the orientation of the vector space (x, y, z) is right-handed, or the current through the big coil pair should be changed.

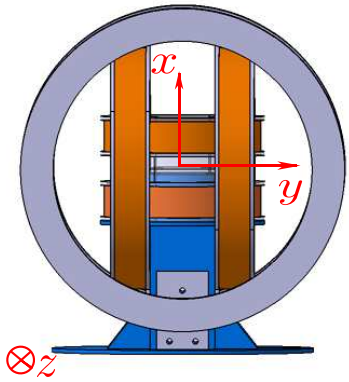

Figure 2.8: World coordinate system $\mathcal{R}_w = (O, x, y, z)$ is defined by the directions of the magnetic field generated by the three Helmholtz coil pairs.

2.2.4.3 2D rotating magnetic field control

In the following part, we take the example of the generation of a rotating magnetic field around the axis x. The rotating magnetic field around the axis x at an instant t is noted as $\mathbf{B}_{\perp\mathbf{x}}$. As the magnetic field is always perpendicular to the axis x, the magnetic field along the axis x is zero. Then, the equation of the rotating magnetic field $\mathbf{B}_{\perp\mathbf{x}}$ at the instant t can be expressed as:

$$\mathbf{B}_{\perp\mathbf{x}} = \begin{bmatrix} B_x \\ B_y \\ B_z \end{bmatrix} = \begin{bmatrix} 0 \\ B_0 \cdot \cos(2\pi f t) \\ B_0 \cdot \cos(2\pi f t + \mathrm{d}_{\mathrm{phase}}) \end{bmatrix} \tag{2.2}$$

where $\mathrm{d}_{\mathrm{phase}} = -\frac{\pi}{2}$ presents the phase difference, note that $\mathrm{d}_{\mathrm{phase}} = \frac{\pi}{2}$ if the magnetic field rotates around $-x$, f is the rotation frequency, and B_0 is the magnetic flux density generated at the center of the workspace.

A simulation of Equation (2.2) with Comsol multiphysics of the generation of a rotating magnetic field around the axis x with the Helmholtz coil pairs is illustrated in Figure 2.9. The frequency of the rotating field is 1 Hz. The red arrows show the direction of the magnetic field at the instant t. This demonstrates the rotation of the magnetic field.

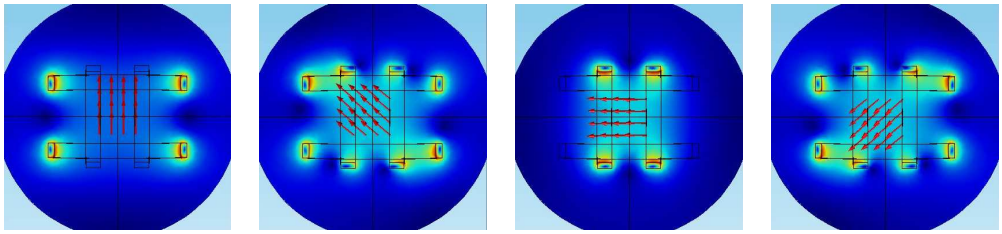

(a) t=0 s (b) t=0.125 s (c) t=0.25 s (d) t=0.375 s

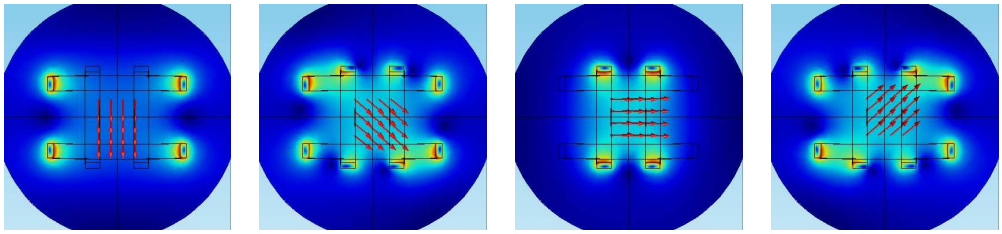

(e) t=0.5 s (f) t=0.625 s (g) t=0.75 s (h) t=0.875 s

Figure 2.9: Simulation of 2D rotating magnetic field with a frequency of 1 Hz.

Table 2.7 summarizes the PCI card output voltages and the phase difference to generate a rotating magnetic field with a magnetic flux density of $B_0 = 10$ mT at the center and around the axes x, y, or z.

Table 2.7: Specifications of the PCI card output voltages and the phase difference to generate a rotating magnetic field with a magnetic flux density of $B_0 = 10$ mT around the axes x, y, or z.

Axis of rotation	U_x (V)	U_y (V)	U_z (V)	d_{phase} $(+/-\frac{\pi}{2})$
x	0	2	2.4	$B_z : -$
$-x$	0	2	2.4	$B_z : +$
y	2	0	2.4	$B_x : -$
$-y$	2	0	2.4	$B_x : +$
z	2	2	0	$B_y : -$
$-z$	2	2	0	$B_y : +$

A graphic user interface of the generation of the rotating magnetic field is illustrated in Figure 2.10. The output voltages of the PCI card and the phase difference should be referred to Table 2.7. In the program, the sample time is 40 ms. The generation of the rotating magnetic field is validated by the movement of a magnetic pole in the generated field. This program of the generation of the 2D rotating magnetic field is very useful for the SHM's swimming characterisation experiments.

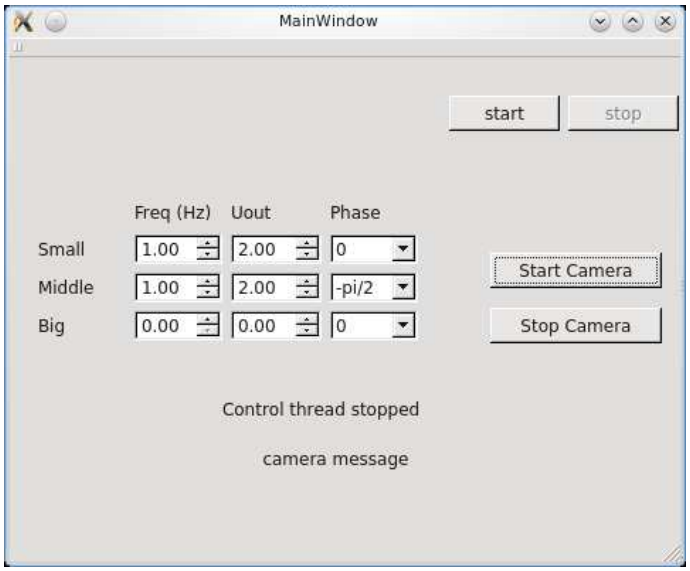

Figure 2.10: Graphic user interface using Qt Designer to generate a 2D rotating magnetic field.

2.2.4.4 3D rotating magnetic field control

The generation of a rotating magnetic field around an axis in 3D space is more complicated. A method to generate a rotating magnetic field around an axis $\overrightarrow{n}$, expressed in the world coordinate system with $\mathbf{n} = (n_x, n_y, n_z)^T$, is introduced as follows.

Giving a rotating magnetic field around the vector $\mathbf{n}$ is equivalent to write the parametric equation of a vectorial circle with the normal vector $\mathbf{n}$ and with the radius physically presenting the magnetic field strength.

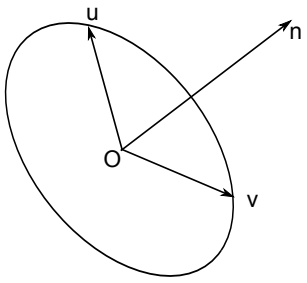

Figure 2.11: Rotating magnetic field around the axis $\mathbf{n}$. Note that $\mathbf{u}$ and $\mathbf{v}$ are the base vectors in the plane orthogonal to $\mathbf{n}$.

Consider $\mathbf{u}$ a vector in the plane which is perpendicular with $\mathbf{n}$, therefore $\mathbf{u}$ and $\mathbf{n}$ are orthogonal. We can let $\mathbf{u}$ be

$$\mathbf{u} = \begin{bmatrix} u_x \\ u_y \\ u_z \end{bmatrix} = \begin{bmatrix} n_y \\ -n_x \\ 0 \end{bmatrix} \tag{2.3}$$

with $n_x \neq 0$ or $n_y \neq 0$. Note that $\mathbf{v}$ is a vector orthogonal both to $\mathbf{u}$ and $\mathbf{n}$. Let $\mathbf{v}$ be

$\mathbf{v} = \mathbf{n} \times \mathbf{u}$.

$$\mathbf{v} = \begin{bmatrix} v_x \\ v_y \\ v_z \end{bmatrix} = \begin{bmatrix} n_x n_z \\ n_y n_z \\ -n_x^2 - n_y^2 \end{bmatrix} \tag{2.4}$$

Note that $\tilde{\mathbf{u}}$ and $\tilde{\mathbf{v}}$ are the unit vectors of $\mathbf{u}$ and $\mathbf{v}$, so that $\tilde{\mathbf{u}}$ and $\tilde{\mathbf{v}}$ are the basis vectors of the plane orthogonal to the axis $\mathbf{n}$. Thus,

$$\tilde{\mathbf{u}} = \begin{bmatrix} \tilde{u_x} \\ \tilde{u_y} \\ \tilde{u_z} \end{bmatrix} = \frac{1}{\|\mathbf{u}\|} \begin{bmatrix} u_x \\ u_y \\ u_z \end{bmatrix} = \frac{1}{\sqrt{u_x^2 + u_y^2 + u_z^2}} \begin{bmatrix} n_y \\ -n_x \\ 0 \end{bmatrix} \tag{2.5}$$

and

$$\tilde{\mathbf{v}} = \begin{bmatrix} \tilde{v_x} \\ \tilde{v_y} \\ \tilde{v_z} \end{bmatrix} = \frac{1}{\|\mathbf{v}\|} \begin{bmatrix} v_x \\ v_y \\ v_z \end{bmatrix} = \frac{1}{\sqrt{v_x^2 + v_y^2 + v_z^2}} \begin{bmatrix} n_x n_z \\ n_y n_z \\ -n_x^2 - n_y^2 \end{bmatrix} \tag{2.6}$$

Remark that if $n_x = 0$ and $n_y = 0$, we can chose $\tilde{\mathbf{u}} = (1, 0, 0)^T$ and $\tilde{\mathbf{v}} = (0, 1, 0)^T$.

Then, the parametric equation of the vectorial circle with the radius r and normal vector $\mathbf{n}$ can be written as:

$$\begin{cases} x = r \cdot (\tilde{u_x} \cos(2\pi f t) + \tilde{v_x} \sin(2\pi f t)) \\ y = r \cdot (\tilde{u_y} \cos(2\pi f t) + \tilde{v_y} \sin(2\pi f t)) \\ z = r \cdot (\tilde{u_z} \cos(2\pi f t) + \tilde{v_z} \sin(2\pi f t)) \end{cases} \tag{2.7}$$

This parametric equation can be written in matrix form by developing $\tilde{\mathbf{u}}$ and $\tilde{\mathbf{v}}$:

$$\begin{bmatrix} x \\ y \\ z \end{bmatrix} = \frac{r \cos(2\pi f t)}{\|\mathbf{u}\|} \begin{bmatrix} n_y \\ -n_x \\ 0 \end{bmatrix} + \frac{r \sin(2\pi f t)}{\|\mathbf{v}\|} \begin{bmatrix} n_x n_z \\ n_y n_z \\ -n_x^2 - n_y^2 \end{bmatrix} \tag{2.8}$$

Thus, the rotating magnetic field $\mathbf{B}_{\perp \mathbf{n}} = (B_x, B_y, B_z)^T$ around the vector $\mathbf{n}$ can be expressed as:

$$\mathbf{B}_{\perp \mathbf{n}} = \begin{bmatrix} B_x \\ B_y \\ B_z \end{bmatrix} = \frac{B_0 \cos(2\pi f t)}{\|\mathbf{u}\|} \begin{bmatrix} n_y \\ -n_x \\ 0 \end{bmatrix} + \frac{B_0 \sin(2\pi f t)}{\|\mathbf{v}\|} \begin{bmatrix} n_x n_z \\ n_y n_z \\ -n_x^2 - n_y^2 \end{bmatrix} \tag{2.9}$$

with $\|\mathbf{u}\| = \sqrt{n_y^2 + n_x^2}$ and $\|\mathbf{v}\| = \sqrt{(n_x n_z)^2 + (n_y n_z)^2 + (-n_x^2 - n_y^2)^2}$, and where f is the rotation frequency, t is the time, B_0 is the magnetic flux density at the center of the workspace. The magnetic flux density B_0 depends only on the output voltage of the PCI card. Then, the control variables of the system, which are the output voltages for the three coils (U_s, U_m, U_b), can be expressed as:

$$\begin{bmatrix} U_s \\ U_m \\ U_b \end{bmatrix} = \frac{\cos(2\pi f t)}{\|\mathbf{u}\|} \begin{bmatrix} U_x n_y \\ -U_y n_x \\ 0 \end{bmatrix} + \frac{\sin(2\pi f t)}{\|\mathbf{v}\|} \begin{bmatrix} U_x n_x n_z \\ U_y n_y n_z \\ -U_z (n_x^2 + n_y^2) \end{bmatrix} \tag{2.10}$$

where U_x, U_y, and U_z are respectively the output voltage from the PCI card to the small, medium, and big coils to generate a magnetic field of B_0. The values can be referred to Table 2.6.

This generation method of the 3D rotating magnetic field around the axis **n** is validated by the coincidence of the axis **n** of the rotating field and the axis of the SHM1-mh8 which is rotating around its own axis in the rotating field, because its magnetization is perpendicular to its axis. The calculation of the normal vector of the axis of a SHM by vision is introduced in Section 4.2.1.

2.2.5 Summary

The composition, control variables, and the output of the 3D Helmholtz coil pairs system integrated with a vision system is summarized in Table 2.8. Figure 2.12 describes a block-diagram of the 3D Helmholtz coils system. The currents passing through the Helmholtz coils are controlled by the PC through a PCI card and three amplifiers. The amplifiers are alimented by a power supply. The 3D Helmholtz coil pairs system is designed for the visual servo control of the SHM. The SHM is controlled by the magnetic field generated by the 3D Helmholtz coils. The position (g) and orientation (θ) of the SHM in the image can be communicated with the PC through a vision-based tracking algorithm. The tracking and the estimation methods are introduced later in Section 2.4.

Table 2.8: Summary of the 3D Helmholtz coil pairs system with a vision system.

Item	**Description**
Application	rotating magnetic field generation
Composition	3 Helmholtz coil pairs & 2 cameras & 2 LEDs & PCI card & 3 amplifiers & power supply
Control variables	U_s, U_m, and U_b
System output	$\mathbf{B}(\mathbf{n}, f)$

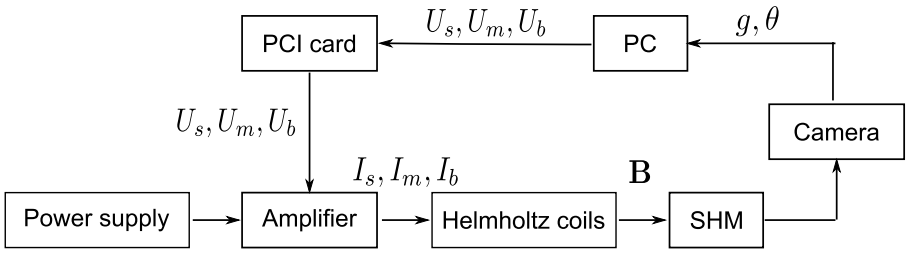

Figure 2.12: Block-diagram of the Helmholtz coils system. The control variables of the system are the output voltages of the PCI card U_s, U_m, and U_b. The frequency and the axis of the rotating magnetic field are controlled. The vision system returns the position (g) and orientation (θ) of the SHM.

2.3 Rotating Permanent Magnet Manipulator (RPMM)

As the Helmholtz coils systems are difficult to scale up to the size required for medical use, because of the energy efficiency and cost, actuating the magnetic robots with a RPMM is considered. In this section, the design of the fabrication of a RPMM system is introduced. The frequency of the magnetic rotation is controlled by a PID controller, which is presented afterwards.

2.3.1 RPMM principle

Lots of researchers actuate the magnetic robots with a RPMM [Lee 2009, Fountain 2010, Mahoney 2012b, Mahoney 2012a]. The dipole moment of the magnet is noted as $\mathbf{M}$, which is always perpendicular to its rotation axis $\boldsymbol{\Omega}$. The magnetic field generated by a RPMM can be accurately modelled with the point-dipole model [Furlani 2001]. The magnetic field $\mathbf{H}$ at a position $\mathbf{p}$ relative to the center of the RPMM can be expressed as follows:

$$\mathbf{H} = \frac{1}{4\pi|\mathbf{p}|^3}\left(\frac{3\mathbf{p}\mathbf{p}^T}{|\mathbf{p}|^2} - \mathbb{I}\right)\mathbf{M} \tag{2.11}$$

where $\mathbb{I}$ is the identity matrix. Note that $\mathbb{H} = \frac{3\mathbf{p}\mathbf{p}^T}{|\mathbf{p}|^2} - \mathbb{I}$, then the magnetic field $\mathbf{H}$ is expressed as:

$$\mathbf{H} = \frac{1}{4\pi|\mathbf{p}|^3}\mathbb{H}\mathbf{M} \tag{2.12}$$

Mahoney proved in his paper [Mahoney 2012b] that the magnetic field vector at every point in space, generated by a rotating magnetic dipole such as a permanent magnet, rotates around a fixed axis $\boldsymbol{\omega}$. This desired rotation axis of the local magnetic field at the position $\mathbf{p}$ is normal to the plane containing $\mathbf{H}$, such that $\mathbf{H}^T\boldsymbol{\omega} = 0$. The local field rotation axis $\boldsymbol{\omega}$ at the position $\mathbf{p}$ is given as follows:

$$\boldsymbol{\omega} = \frac{\mathbb{H}^{-1}\boldsymbol{\Omega}}{|\mathbb{H}^{-1}\boldsymbol{\Omega}|} \tag{2.13}$$

with $\mathbb{H}^{-1} = \frac{1}{2}(\mathbb{H} - \mathbb{I})$. Since $\mathbb{H}$ is constructed using the unit vector of $\mathbf{p}$, $\mathbb{H}$ changes only with the direction of $\mathbf{p}$. Therefore, the local field rotation axes are invariant to the distance in the same direction.

The axial and radial positions, which are defined respectively as the positions on the axis $\boldsymbol{\omega}$ and the positions spanned by the rotating $\mathbf{M}$, have been used in prior works for actuation due to their simplicity. The local field rotation axes for those positions are parallel to the RPMM rotation axis, as shown in Figure 2.13. The magnetic swimmers are exclusively operated in axial and radial positions of a RPMM, the applied field rotates around an axis parallel to the rotation axis $\boldsymbol{\Omega}$ of the RPMM [Mahoney 2012b].

2.3.2 RPMM design and realisation

The permanent magnet used is a set of ten permanent magnet rings from *supermagnete*. The inner and outer diameter of these rings are respectively 6 mm and 15 mm. The

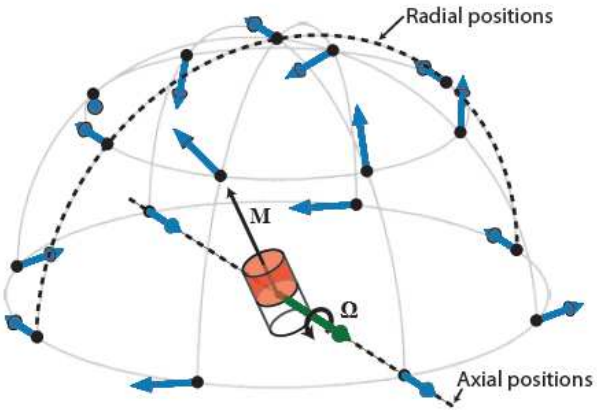

Figure 2.13: When a dipole magnet with moment **M** rotates around an axis $\boldsymbol{\Omega}$ with **M** perpendicular to $\boldsymbol{\Omega}$, the field vector at any given postion rotates around, and is perpendicular to, a constant axis. The axis at various positions are illustrated with large blue arrows [Mahoney 2012b].

total length of the magnet is 60 mm. The magnetic field magnitudes around the magnet are measured using a Hirst GM08 gaussmeter. The magnetic field strength at the operation position, which is defined as 2 cm from the center of the RPMM, is about 30 mT. The hole of the magnet is used to fix itself with a housing. The 3D design of the housing is shown in Figure 2.14a. The housing is made of ABS and realized by a rapid prototyping method. The housing is fixed on the axis of a motor. The permanent magnet is driven by the motor with the connection of the housing.

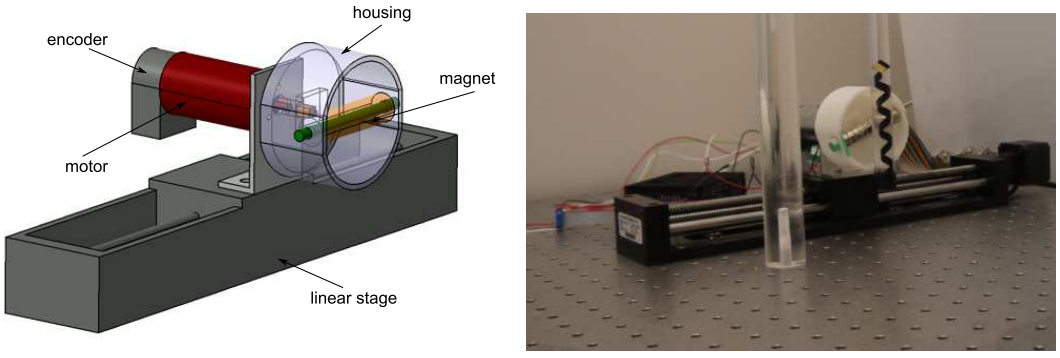

(a) (b)

Figure 2.14: (a) The 3D Catia model of the RPMM system, and (b) the RPMM system used in the experiments : A permanent magnet is rigidly connected with a motor, which is mounted on a linear stage.

An electric DC motor, Maxon motor (12 V, 15 W), is used in the following experiments to rotate the permanent magnet. The maximal speed of the motor is 2860 turns/min (47 Hz). The motor is driven by a 4-Q-DC servoamplifier of Maxon motor control amplifier, capable of 2 A continuous current. Analog communication between the PC and the amplifiers is accomplished with a Sensoray 626 Analog and Digital

I/O PCI card (S626). A Maxon incremental encoder (3 channels, 500 counts per turn) is used to comunicate the angular position of the motor to the PCI card, in order to realize a frequency control.

The motor is fixed on a linear stage, in order to combine the rotation with a translation. The linear stage used in the following experiments is a Newmark ETL-250 linear motion stage with a travel range of 250 mm and a maximal speed of 220 mm/s. Figure 2.14 presents respectively a 3D catia model of the RPMM system, and the RPMM system used in the experiments.

2.3.3 Rotation frequency control

The rotation frequency of the rotating magnetic field of the RPMM is controlled by the rotation frequency of the motor, on which the magnet is mounted. In this section, the rotation frequency control of the motor by a Proportional-Integral-Derivative (PID) controller is introduced.

2.3.3.1 The principle of PID controller

A PID controller calculates an error value, which is defined as the difference between a measured variable and a desired setpoint. The controller attempts to minimize the error by adjusting the process control inputs. The PID controller calculation involves three separate constant parameters: the proportional, the integral and derivative values, denoted P, I, and D. Heuristically, these values can be interpreted in terms of time: P depends on the present error, I on the accumulation of past errors, and D is a prediction of future errors, based on current rate of change [Araki 1992]. The output of the PID controller, $u(t)$, can be expressed in function of the error $e(t)$ as follows:

$$u(t) = K_p e(t) + K_i \int_0^t e(t)\,\mathrm{d}t + K_d \frac{\mathrm{d}}{\mathrm{d}t} e(t) \tag{2.14}$$

where K_p is proportional gain, K_i is integral gain, and K_d is derivative gain. The three gains are tuning parameters.

2.3.3.2 PID controller algorithm

The input parameter of our system is the voltage sent to the amplifier from the PCI card. The amplifier is on current mode, which means that the output current of amplifier is fixed for a fixed input voltage. The output of the system to be controlled is the rotation speed of the motor. The incremental encoder returns the angular position Φ of the motor at an instant t. The current rotation speed can be calculated as $\mathrm{d}\Phi/\mathrm{d}t$. The error should be the difference between the measured rotation speed and the desired rotation speed.

Algorithm 1 is implemented in the program to calculate the output voltage of the PCI card in function of the rotation speed error. The variables of the algorithm are the desired rotation speed (setSpeed), the measured rotation speed (measureSpeed), and the sample time ($\mathrm{d}t$). The sample time is the time of every calculation of voltage output. The output voltage of the PCI card is calculated every 50 ms. Since the sample time is very short, the integral and derivative of the error can be expressed as error$\times \mathrm{d}t$

and (error − previous error)/dt. The P, I, D gains K_p, K_i, and K_d determination is presented as follows.

Algorithme 1 PID controller algorithm

Result: Calculate the output voltage Uout communicated to the motor
Input: setSpeed, measureSpeed, dt
Initialization
previousError ← 0
integral ← 0
Start
e ← setSpeed - measureSpeed
integral ← integral + error×dt
derivative ← (error - previousError)/dt
Uout ← K_p× error+ K_i× integral +K_d× derivative
previousError ←error
wait(dt)
goto **start**

2.3.3.3 P, I, D gains determination

Ziegler-Nichols tuning method is used to determine the P, I, D gains K_p, K_i, and K_d. This method is developed by Ziegler and Nichols [Ziegler 1942]. It begins with setting the integral gain K_i and the derivative gain K_d to zero. The proportional gain K_p is then increased from zero until it reaches the ultimate gain K_u, at which the output of the control loop oscillates with a constant amplitude. The oscillation period is noted as P_u. The ultimate gain K_u and oscillation period P_u are used to set the P, I, D gains.

Table 2.9: P, I, D gains determination by Ziegier-Nichols method.

Control type	K_p	K_i	K_d
P	$0.5K_u$		
PI	$0.45K_u$	$1.2K_p/P_u$	
PID	$0.6K_u$	$2K_p/P_u$	$K_pP_u/8$

From some experiments, the ultimate gain of the system is obtained as $K_u = 0.5$. The oscillation period is $P_u = 0.6$ s. Thus, the P, I, D gains of the system are calculated as $K_p = 0.3$, $K_i = 1$, $K_d = 0.02$. A test for a desired rotation frequency at 5 Hz is realised to validate the P, I, D gains. Figure 2.15 illustrates the rotation frequency of motor revolution in function of time with the P, I, D gains determined before. The time of stationary regime establishment is less than 1 s. The inaccuracy of the stationary regime is less then 4%. The P, I, D gains are acceptable. The frequency of the rotating magnetic field is then controlled.

2.3.4 Summary

The composition, control variables, and the output of the integrated RPMM system is summarized in Table 2.8. A permanent magnet is mounted on a motor. Figure

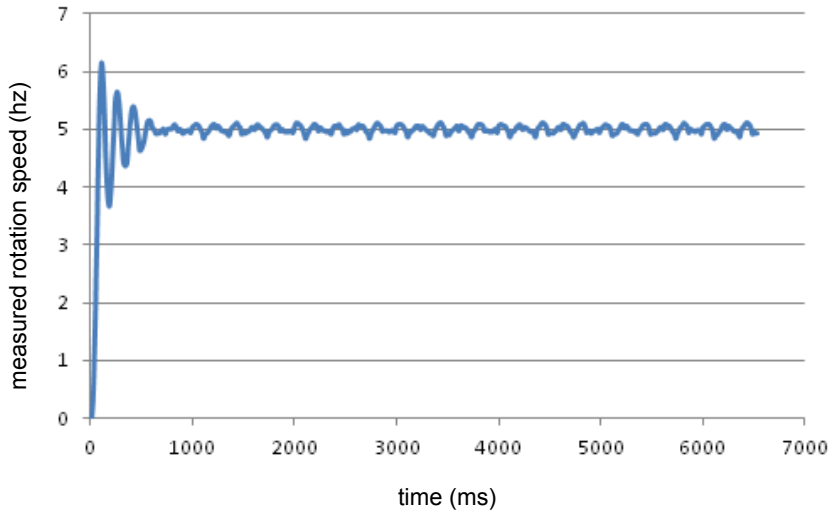

Figure 2.15: Rotation frequency revolution for a desired rotation frequency at 5 Hz with the P, I, D gains $K_p = 0.3$, $K_i = 1$, $K_d = 0.01$.

2.12 describes a block-diagram of the RPMM system. The current passing through the motor is controlled by the PC through a PCI card and an amplifier. The amplifier is alimented by a power supply. The RPMM system is designed only for the swimming properties characterization of the SHMs. No visual feedback is returned to the PC.

Table 2.10: Summary of rotating permanent magnet manipulator system.

Item	**Description**
Application	rotating magnetic field generation
Composition	permanent magnet & motor & encoder & linear stage & amplifier & PCI card
Control variables	U_{out}
System output	$\mathbf{B}(f)$

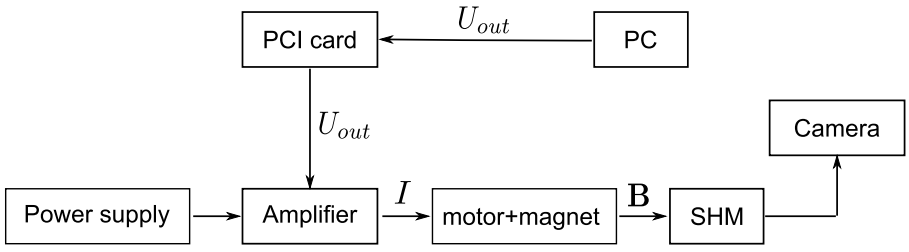

Figure 2.16: Schema of the RPMM system. The control variables of the system are the output voltages of the PCI card U_{out}. The frequency of the rotating magnetic field generated by the system is controlled.

2.4 Vision-based tracking

To quantify the displacement and the orientation of the SHM, no solution other than visual tracking is in the meantime robust, accurate and at real-time. A robust and real-time visual tracking is one of the keys to a successful visual servoing task. In this section, a real-time tracking method of ViSP and a method based on the image moments for the estimation of the barycenter and the axis of the tracked object are introduced.

2.4.1 Tracking of a SHM

The tracking of a SHM in the experiments is realised by Visual Servoing Platform (ViSP) [Marchand 2005]. ViSP is a complete cross-platform library developed and maintained by the INRIA Lagadic team, that allows prototyping and developing applications in visual tracking and visual servoing.

Backlight system is used in the experiments. By using backlight, the image of a SHM is a set of connected pixels with the same gray level. Figure 2.17a shows an image of SHM1-mh8 in the liquid with a backlight. In order to have better contrast with a backlight, the SHMs are painted into black color. Therefore, a SHM is considered as a blob (vpDot class in ViSP) in images, defined by the set of connected pixels with the same gray level.

The initial dot of the SHM is defined by the function *dot.initTracking*, which allows to define the dot by the pixels connected with the initial pixel with the gray level. The initial pixel is defined by a click on one pixel in the image of the SHM. The tracking function *dot.Track* allows to track the dot with the same grey level of the initial dot. An example of the tracked dot of SHM1-mh8 is shown in Figure 2.17b with green pixels.

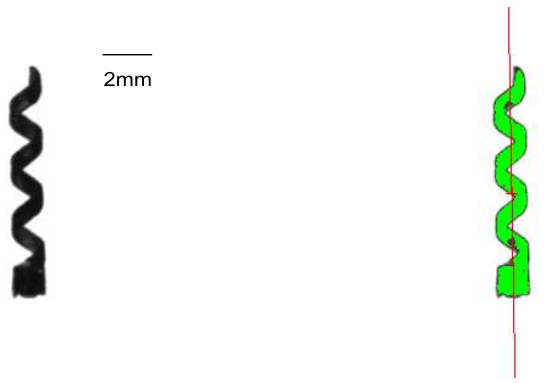

(a) (b)

Figure 2.17: (a) An image of SHM1-mh8. (b) After image processing with ViSP, SHM1-mh8 is tracked (green pixels).

2.4.2 Barycentre of the helical swimmer

The barycentre of a SHM is calculated by ViSP using image moments. The general 2D $(p+q)^{th}$ order moments of a grey-level image $f(x,y)$ are defined as [Horn 1986]:

$$m_{pq} = \iint_I x^p y^q f(x,y)\,\mathrm{d}x\mathrm{d}y \tag{2.15}$$

with $p, q = 0, 1, 2...$

The integration is over the whole image I. Similarly, one can compute the moments of a region in the image, of an object by integrating only over the region R. The zeroth, first and second image moments can be obtained from ViSP. The area of the object can be found when $p = q = 0$ ($A = m_{00}$).

The centroid of the object is defined as the center of mass of a figure of the same shape with the constant mass per unit area. The center of the mass, in turn, is the point where all the mass of the object could be concentrated without changing the first moment of the object about any axis. In 2D case, the first moment about the x-axis is

$$\overline{x} \iint_R f(x,y)\,\mathrm{d}x\mathrm{d}y = \iint_R x f(x,y)\,\mathrm{d}x\mathrm{d}y \tag{2.16}$$

and the moment about the y-axis is

$$\overline{y} \iint_R f(x,y)\,\mathrm{d}x\mathrm{d}y = \iint_R y f(x,y)\,\mathrm{d}x\mathrm{d}y \tag{2.17}$$

where $g = (\overline{x}, \overline{y})$ is the position of the object in the image. Therefore, the position of the object can be calculated by $g = (\overline{x}, \overline{y}) = \left(\frac{m_{10}}{m_{00}}, \frac{m_{01}}{m_{00}}\right)$.

For example, the barycentre of SHM1-mh8 is calculated and marked with a red cross using ViSP, as shown in Figure 2.17b.

2.4.3 Orientation of the helical swimmer

The orientation of an object in the image can be defined by the direction of its axis of least inertia. To do so, we find the line for which the integral of the square of the distance to points in the object is a minimum. That integral is:

$$E = \iint_R r^2 f(x,y)\,\mathrm{d}x\mathrm{d}y \tag{2.18}$$

where r is the perpendicular distance from the point (x, y) to the line. Given a point (x, y) on the object, suppose that the point (x_0, y_0) is the closest point on the line. The distance r between the point and the axis is written by:

$$r^2 = (x - x_0)^2 + (y - y_0)^2 \tag{2.19}$$

As the point (x_0, y_0) is on the axis, x_0 and y_0 can be written by parametric equations with the parameter s as follows:

$$x_0 = -\rho \sin\theta + s\cos\theta \tag{2.20}$$

$$y_0 = \rho \cos\theta + s\sin\theta \tag{2.21}$$

where ρ is the distance from the origin to the closest point on the axis, and θ is the angle between the x axis and the axis of the object, with $\theta \in \left[-\frac{\pi}{2}, \frac{\pi}{2}\right]$. Substituting the parametric equations for x_0 and y_0 into the expression of r, we obtain:

$$r^2 = (x^2 + y^2) + \rho^2 + 2\rho(x\sin\theta - y\cos\theta) - 2s(x\cos\theta + y\sin\theta) + s^2 \tag{2.22}$$

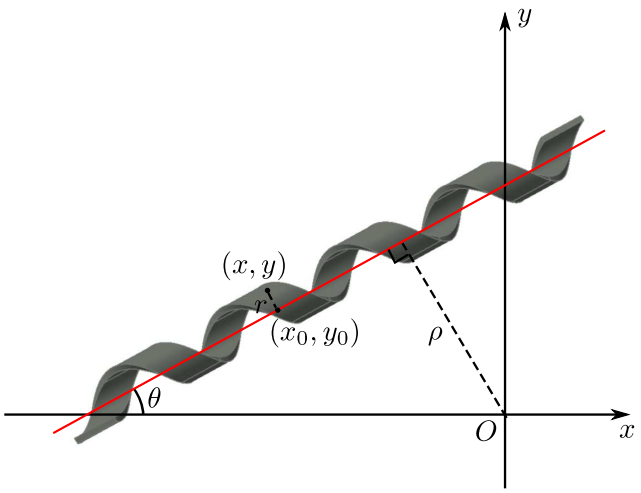

Figure 2.18: Orientation of the SHM in image.

In order to find the closest point (x_0, y_0), (2.22) should be differentiated with respect to s and set to zero, which leads to:

$$s = x\cos\theta + y\sin\theta \tag{2.23}$$

This result can now be substituted back into the parametric equations for x_0 and y_0. From where, the distance r can be thus written as follows:

$$r^2 = (x\sin\theta - y\cos\theta + \rho)^2 \tag{2.24}$$

We now address the minimization of

$$E = \iint_R (x\sin\theta - y\cos\theta + \rho)^2 f(x,y)\,\mathrm{d}x\mathrm{d}y \tag{2.25}$$

by differentiating with respect to ρ and setting the result to zero, which leads to:

$$\overline{x}\sin\theta - \overline{y}\cos\theta + \rho = 0 \tag{2.26}$$

with $(\overline{x}, \overline{y})$ the center of the object area. As the axis of least second moment passes through the center of area, the coordinates are changed to $x' = x - \overline{x}$ and $y' = y - \overline{y}$. We have:

$$x\sin\theta - y\cos\theta + \rho = x'\sin\theta - y'\cos\theta \tag{2.27}$$

Thus

$$E = a_0\sin^2\theta - b_0\sin\theta\cos\theta + c_0\cos^2\theta \tag{2.28}$$

where a, b and c are the second moments given by:

$$a_0 = \iint_{R'} (x')^2 f(x,y)\,\mathrm{d}x'\mathrm{d}y' \tag{2.29}$$

$$b_0 = 2\iint_{R'} (x'y') f(x,y)\,\mathrm{d}x'\mathrm{d}y' \tag{2.30}$$

$$c_0 = \iint_{R'} (y')^2 f(x,y)\,\mathrm{d}x'\mathrm{d}y' \tag{2.31}$$

and a, b, c can be computed by:

$$a_0 = \frac{m_{21}}{m_{00}} - \overline{x}^2 \tag{2.32}$$

$$b_0 = 2\left(\frac{m_{11}}{m_{00}} - \overline{xy}\right) \tag{2.33}$$

$$c_0 = \frac{m_{02}}{m_{00}} - \overline{y}^2 \tag{2.34}$$

Then, E can be expressed in the form as follows:

$$E = \frac{1}{2}(a_0 + c_0) - \frac{1}{2}(a_0 - c_0)\cos 2\theta - \frac{1}{2}b_0 \sin 2\theta \tag{2.35}$$

In order to minimize E, E should be differentiated with respect to θ and set the result to zero. We get:

$$\tan 2\theta = \frac{b_0}{(a_0 - c_0)} \tag{2.36}$$

unless $b_0 = 0$ and $a_0 = c_0$. If $b_0 = 0$ and $a_0 = c_0$, the object is too symmetric to allow us to find an axis in this way, a sphere for example. E is independent of θ. However, the value of θ can be obtained with only the value of $\tan 2\theta$, because there are three possibilities: $\theta = \arctan(\tan 2\theta)$, $\theta = \arctan(\tan 2\theta) + \frac{\pi}{2}$ or $\theta = \arctan(\tan 2\theta) - \frac{\pi}{2}$, with $\theta \in \left[-\frac{\pi}{2}, \frac{\pi}{2}\right]$. In order to define the θ, the width and the height of the tracked dot should be compared. Four cases should be distinguished:

1. if width $>$ height, and $\tan 2\theta > 0$, then $\theta = \arctan(\tan 2\theta) - \frac{\pi}{2}$
2. if width $<$ height, and $\tan 2\theta < 0$, then $\theta = \arctan(\tan 2\theta)$
3. if width $<$ height, and $\tan 2\theta > 0$, then $\theta = \arctan(\tan 2\theta)$
4. if width $>$ height, and $\tan 2\theta < 0$, then $\theta = \arctan(\tan 2\theta) + \frac{\pi}{2}$

This orientation calculation method is at first verified off-line by four pictures of SHM with different orientations corresponding to the four different cases (see Figure 2.19). The SHM is well tracked with the presentation of its barycenter and orientation. In chapter 4, a real time visual tracking of the SHM using this detection of its barycenter and orientation is presented.

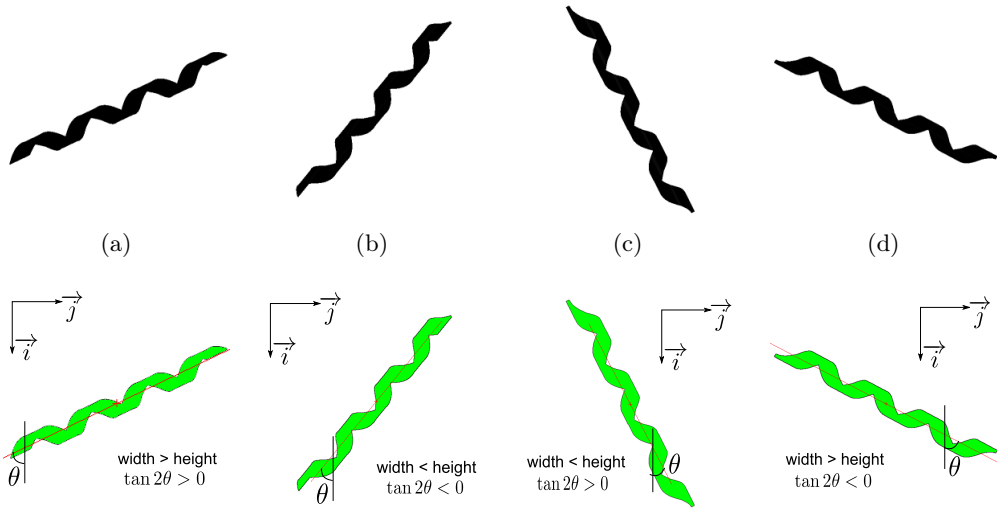

(e) $\theta = -64.5°$ (f) $\theta = -39.4°$ (g) $\theta = 27.5°$ (h) $\theta = 62.6°$

Figure 2.19: (a)-(d) The SHMs with different orientations corresponding to the four different cases. (e)-(h) The tracked SHMs with their barycenters (red crosses), their orientations (red lines), and the calculated θ with respect to the local axis i.

2.5 Swimming characteristics analysis

The swimming characteristics of a helical swimmer can be described by the rotation frequency, the translation velocity, and its propulsion matrix. In this section, the methods to estimate the rotation frequency and translation velocity of the SHM are introduced. A method to identify the propulsion matrix of the SHM is presented as well.

2.5.1 Rotation frequency analysis

The rotation frequency of a SHM is calculated off-line by an image sequence recorded during the experiment. The number of turns is counted between two image frames. The time can be calculated by the frame numbers and the frame rate.

The method is detailed by an example of SHM1-mh8 actuated by a 10 mT rotating magnetic field at 12 Hz in 90% glycerol solution. An image sequence is recorded at 60 Hz frame rate (during one second, 60 images are taken). A random frame is taken as the initial position, for example the 12th frame as shown in Figure 2.20a. One turn is counted when the end of the tail repasses its initial position. At 17th frame in the example, as shown in Figure 2.20f, the SHM1-mh8 rotated one turn from 12th frame. We count the number of turn during at least one second (60 frames). SHM1-mh8 finished its 12th turn at the end of one second (the 72nd frame). That means that SHM1-mh8 rotated 12 turns in 1 second. Therefore, the angular speed of SHM1-mh8 rotated in 90% glycerol solution with a 10 mT rotating magnetic field at 12 Hz is 12 Hz.

Another example is SHM1-mh8 actuated by a 5 mT rotating magnetic field at 12 Hz in 90% glycerol solution. From the 12th frame, SHM1-mh8 finished its 6th turn at 77th frame. 65 frames took 1.083 s. Therefore, SHM1-mh8 used 1.083 s to rotate 6 turns.

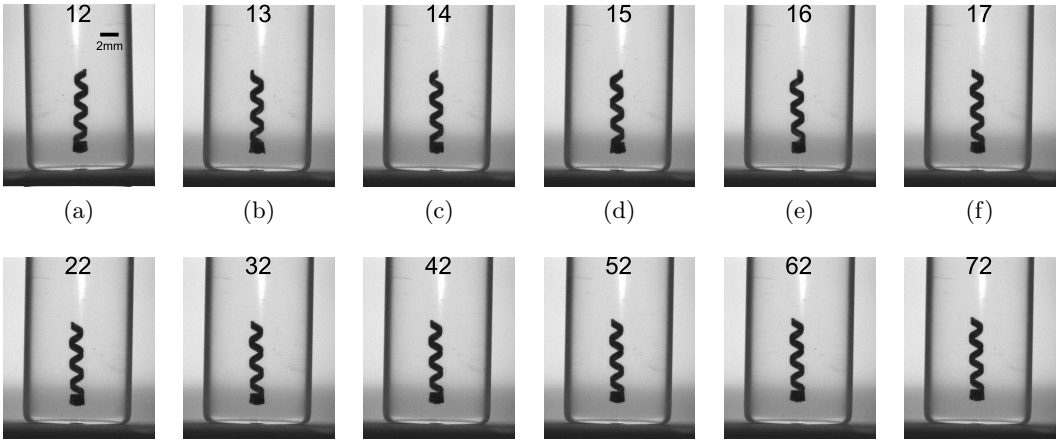

Figure 2.20: An image sequence of SHM1-mh8 actuated by a 10 mT rotating magnetic field at 12 Hz in 90% glycerol solution. The frame rate of the image sequence is 60 Hz. The number on the image describes the number of the frame. From 12 s to 17 s, the SHM rotates one turn; from 12 s to 72 s, the SHM rotates 12 turns. The rotation frequency of the SHM is calculated as 12 Hz.

The angular speed of SHM1-mh8 actuated by a 5 mT rotating magnetic field at 12 Hz in 90% glycerol solution is thus $6 \div 1.083 = 5.54$ Hz.

2.5.2 Translation velocity analysis

The translation velocity of a SHM is calculated by the pixels it travelled per second, and then converted to millimetres per second. The method is detailed with the example of SHM1-mh5 travelled in pure glycerol solution with a 10 mT rotating magnetic field at 3 Hz. The axis of the rotating field is in the horizontal plane. Actuated by the rotating magnetic field, SHM1-mh5 propelled forward, and at the same time it sank down because of its own gravity. Only the advance velocity is calculated in order to compare the swimming performance. Figure 2.21 depicts the position of SHM1-mh5 respectively at 2 s, 4 s, 6 s, 8 s. Thanks to a pixel ruler, the horizontal displacement is 10 pixels between 2 s and 4 s, 9 pixels 4 s and 6 s, and 9 pixels 6 s and 8 s. The advance velocity of SHM1-mh5 can be considered as constant, because the horizontal displacement is uniform. Between 2 s and 8 s, the advance velocity of SHM1-mh5 is calculated as 4.83 pixels per second. The circle magnetic head of 1.5 mm diameter took 26 pixels in the image. Whereafter, the advance velocity is converted to $4.83 \div 26 \times 1.5 = 0.28$ mm/s.

The velocity of a SHM can be calculated in realtime as well. The position of a SHM can be defined by the tracked barycenter. The velocity of the SHM can be then determined by its moved barycenter.

2.5.3 Propulsion matrix identification

In Section 1.3.3, the relationship between the force and torque exerted on a helical swimmer and its translation velocity and angular speed is given in (1.9). Here, a

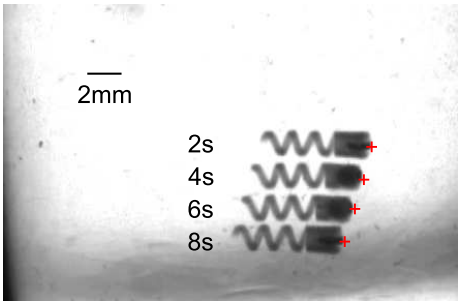

Figure 2.21: Offline translation velocity measure: a fusion image of SHM1-mh5 actuated by a 10 mT rotating magnetic field at 3 Hz in 100% glycerol solution at 2 s, 4 s, 6 s, 8 s.

method to estimate the propulsion parameters through two experiments is introduced.

The SHM is placed vertically in the liquid. We define the inverse direction of the gravity force as the positive direction for translation. The positive direction of rotation is defined by the right hand rule, as shown in Figure 2.22. The fabricated SHMs respect the right-handed chirality. It means that a positive applied torque can generate a positive propulsive velocity. By adjusting the rotation frequency of the magnetic field, a SHM can swim upward and downward, depending on the balance between propulsion, gravity and buoyancy forces acting on the SHM.

Figure 2.22: Upward direction is defined as the positive direction for f and v, the rotation direction in which SHM1-mh8 rotates to generate a positive force is defined as the positive direction for τ and ω.

The first experiment is that find the rotation frequency ω_1 with that rotation frequency the altitude of a SHM is motionless. It means that the translation velocity of the SHM v_1 is zero. From (1.9), since the translation velocity is null, the applied force f_{app} can be expressed as follows:

$$f_{app} = av_1 + b\omega_1 = b\omega_1 \tag{2.37}$$

where the applied force f_{app} is the apparent weight (the resultant of the gravity and buoyancy forces) of the SHM. Then, the parameter b can be calculated as:

$$b = \frac{f_{app}}{\omega_1} \tag{2.38}$$

The second experiment is dropping the SHM in vertical direction in the liquid without any external magnetic force and torque. The dropping velocity is measured as v_2 and angular speed is measured as ω_2. The applied force and torque can be written as:

$$f_{app} = av_2 + b\omega_2 \tag{2.39}$$

$$\tau_{app} = bv_2 + c\omega_2 \tag{2.40}$$

with the applied torque being zero. We can get:

$$a = \frac{f_{app} - b\omega_2}{v_2} \tag{2.41}$$

$$c = \frac{-bv_2}{\omega_2} \tag{2.42}$$

The propulsion parameters a, b, and c are then identified.

The presented estimation methods of the rotation frequency, the translation velocity, and the propulsion matrix of the helical swimmers in this section are used to analyse the swimming properties of the helical swimmers in the next chapter.

2.6 Summary

In this chapter, all of the types of the Scaled-up Helical Microswimmers (SHMs) used in the experiments are presented. The SHMs are designed with different geometry parameters, magnetic positioning, and head shapes. The SHMs swim in viscous liquids to simulate the low Reynolds number regime. Two magnetic actuation systems, a 3D orthogonally arranged Helmholtz coil pairs system and a rotating permanent magnet manipulator, for the generation of the rotating magnetic field are fabricated. The control of the strength and the rotation frequency of the rotation magnetic field generated by the magnetic actuation systems is presented. A real-time tracking method of the SHM with the estimation of its barycenter and axis in the 2D image is as well introduced in this chapter. The method of the estimation of the rotation frequency, the translation velocity, and propulsion matrix of the SHM, which describes the swimming characteristics of the SHM, is presented in this chapter. In the next chapter, the swimming characteristics of the presented SHMs is studied and compared.

Chapter 3

Swimming characteristics of helical swimmers

Contents

In this chapter, the swimming performance of the SHMs with different geometry parameters is compared. The rotational propulsion characteristics of helical swimmers with different magnetic positionings and head shapes are investigated. The design of the magnetic positionings of helical swimmers is discussed both at the microscale and at the millimeter scale. The linear velocity generated by the propulsion is studied based on the estimated propulsion matrices, as well as the required magnetic torque. An open-loop 3D steering of helical swimmers is also studied. A 3D steering strategy is proposed to improve the steering efficiency.

3.1 Geometry parameters of helical tails

In this section, the geometry parameters influence on the swimming performance is studied. A Design of Experiments (DoE) is used to realize the geometry parameters design and to determine the impacts of the geometry parameters.

3.1.1 A brief introduction to the design of experiments

A design of experiments is a series of test runs in which purposeful changes are made to the input variables of a system of process and the effects on the response variables are measured. Factorial design is invented by Ronald Fisher in the 1920s and 1930s for an agricultural research [Fisher 1935]. In factorial designs, multiple factors are investigated simultaneously during the test. Since the 1940s, this method has been successfully applied in the military and in the industry. DoE allows to reduce the overall number of experiments, as well as to explore the interactions between factors [Goupy 2006].

Some terms are commonly used in a design of experiments [Mason 2003]. A "factor" is defined as a controllable experimental variable, which influences the response variable. The "response" is the outcome of an experiment. Each factor must assume some values, defined as levels. The changes that occur on the mean of the values of the response variable correspond to the "effects". Besides the effects caused by the factors, the effects created by the interaction of the factors can be determined. These interactions correspond to combined effects, where the effect of each factor depends on the levels of the other factors.

3.1.2 Choice of the parameters

In our case, the objective of the experiment is to identify the geometry parameters of a helical swimmer that have significant effects on its swimming performance. This leads to an improvement of the geometry design.

Firstly, a quantity value which describes the swimming performance of a helical swimmer should be chosen as the response of the system. This response is the linear advance velocity of the helical swimmer swimming in a 3 Hz rotating magnetic field with a magnetic flux density of 10 mT at the center.

Secondly, the factors should be determined. As the study is dimensionless, what we are interested in is only the shape of the SHMs, not the size. Therefore, the inner diameters of the SHMs are fixed at 1 mm. Other geometry parameters are changed. Three input factors are thus identified: the pitch, the width, and the number of turns, denoted by A, B and C. A simple 2-level full factorial design is chosen according to the objective of the experiment, which requires $2^3 = 8$ different parameters design configurations.

Then, the high level (+) and the low level (−) should be defined for each factor: the pitch is compared between 1.5 mm and 4 mm; the width is compared between 0.5 mm and 1.2 mm; and the number of turns is compared between 1.5 turns and 3.5 turns. These extremities of the geometry parameters are chosen by the parameters of the existing helical swimmers. Table 3.1 depicts the test matrix. This table of test matrix will guide us in designing the geometry parameters of the SHMs. The designed

eight SHMs with different geometry parameters are described in Table 3.2. They are presented in Figure 2.2, and named from SHM1-mh1 to SHM1-mh8. The fabrication of the eight SHM1-mhXs is presented in Section 2.1.2.1.

Table 3.1: Test matrix of the full factorial design for 3 factors and 2 levels [Fisher 1935].

Design	pitch (A)	width (B)	nb of turns (C)	$A \times B$	$B \times C$	$A \times C$
1	−	−	−	+	+	+
2	+	−	−	−	+	−
3	−	+	−	−	−	+
4	+	+	−	+	−	−
5	−	−	+	+	−	−
6	+	−	+	−	−	+
7	−	+	+	−	+	−
8	+	+	+	+	+	+
Level −	1.5 mm	0.5 mm	1.5			
Level +	4 mm	1.2 mm	3.5			

Table 3.2: Specifications of the eight SHMs for geometry parameters study.

	diameter (mm)	pitch (mm)	width (mm)	nb of pitch	length (mm)
SHM1-mh1	1.5	1.5	0.5	1.5	2.25
SHM1-mh2	1.5	4	0.5	1.5	6
SHM1-mh3	1.5	1.5	1.2	1.5	2.25
SHM1-mh4	1.5	4	1.2	1.5	6
SHM1-mh5	1.5	1.5	0.5	3.5	5.25
SHM1-mh6	1.5	4	0.5	3.5	14
SHM1-mh7	1.5	1.5	1.2	3.5	5.25
SHM1-mh8	1.5	4	1.2	3.5	14

3.1.3 Swimming performance of the SHMs with different geometry parameters

The SHM1-mhXs are actuated by a rotating magnetic field generated by the 3D Helmholtz coil pairs, which is presented in Section 2.2. The magnetic flux density at the center is 10 mT, and the frequency of the rotating field is 3 Hz. The axis of the rotating field is in the horizontal plane. When actuated by the rotating magnetic field, the SHMs propelled forward in 100% glycerol in sync with the external field, and at the same time they sank down because of their own gravity. Only the advance velocity is useful to compare the swimming performance.

The swimming velocity is calculated offline from the recorded videos. The method of the calculation is presented in Section 2.5.2. For each SHM, five tests are realized.

The average velocity of the 5 tests is used for the effect estimations. SHM1-mh6s are very fragile, and broke after three tests. Thus, only three tests are used for the velocity estimation of SHM1-mh6. Table 3.3 shows the swimming velocities for each test and the average velocities of the SHM1-mhXs with different geometries. Their incertitudes are expressed in Figure 3.1.

Table 3.3: Swimming velocities of different SHM1-mhXs in 100% glycerol with a 10 mT magnetic field, expressed in mm/s.

Swimming velocity	Run1	Run2	Run3	Run4	Run5	**Average velocity**
SHM1-mh1	0.24	0.34	0.46	0.38	0.34	**0.35**
SHM1-mh2	0.84	0.85	0.86	0.74	1.02	**0.86**
SHM1-mh3	0.25	0.09	0.12	0.13	0.14	**0.15**
SHM1-mh4	0.87	0.77	0.87	0.86	0.86	**0.85**
SHM1-mh5	0.49	0.34	0.41	0.28	0.36	**0.37**
SHM1-mh6	1.42	1.62	1.27	NA	NA	**1.44**
SHM1-mh7	0.23	0.20	0.08	0.15	0.14	**0.16**
SHM1-mh8	1.07	1.24	0.95	0.99	1.23	**1.09**

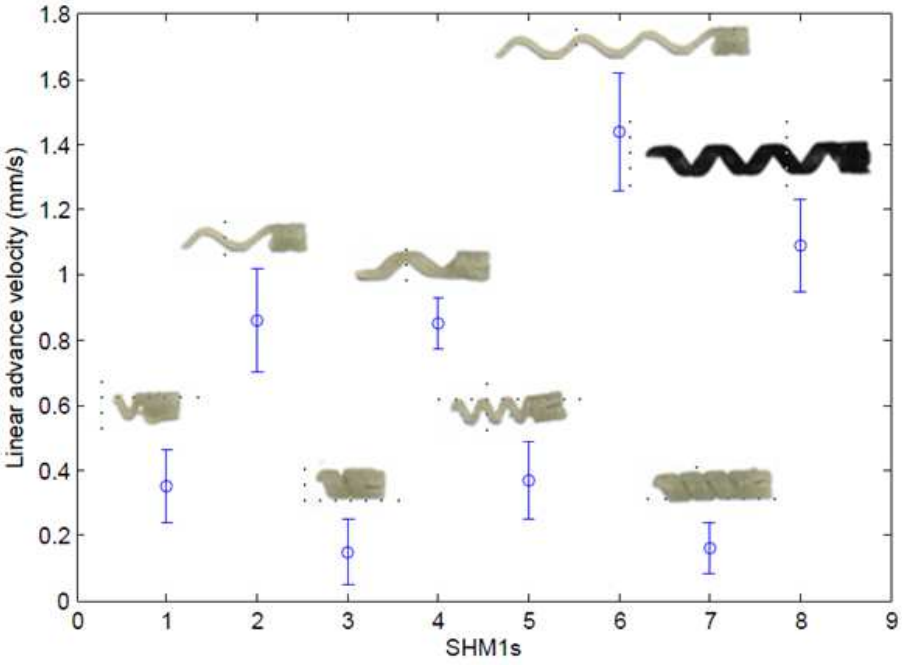

Figure 3.1: Swimming velocities of different SHM1-mhXs in 100% glycerol with a 10 mT magnetic field.

3.1.4 Impacts of the geometry parameters

The effect Y of the factors and the possible interactions are evaluated by the difference between the average response values for each factor or interaction at its highest level (+), and that at its lowest level (-), which can be expressed as:

$$Y_A = \frac{0.86+0.85+1.44+1.09}{4} - \frac{0.35+0.15+0.37+0.16}{4} = 0.80 \quad (3.1)$$

$$Y_B = \frac{0.15+0.85+0.16+1.09}{4} - \frac{0.35+0.86+0.37+1.44}{4} = -0.19 \quad (3.2)$$

$$Y_C = \frac{0.37+1.44+0.16+1.09}{4} - \frac{0.35+0.86+0.15+0.37}{4} = 0.21 \quad (3.3)$$

$$Y_{A\times B} = \frac{0.35+0.85+0.37+1.09}{4} - \frac{0.86+0.15+1.44+0.16}{4} = -0.04 \quad (3.4)$$

$$Y_{B\times C} = \frac{0.35+0.86+0.16+1.09}{4} - \frac{0.15+0.85+0.37+1.44}{4} = 0.07 \quad (3.5)$$

$$Y_{A\times C} = \frac{0.35+0.15+1.44+1.09}{4} - \frac{0.86+0.85+0.37+0.16}{4} = -0.22 \quad (3.6)$$

These effects of the factors and their interactions are depicted in Figure 3.2. The main factor which influences a helical swimmer's performance the most is the pitch, because the effect of the pitch Y_A is the highest. The SHMs with 4 mm of pitch swim faster than those with 1.5 mm of pitch with the same rotating magnetic field. Besides, the number of the pitch has a non ignorable influence. Since the effect of the number of the pitch Y_C is positive, the SHMs with 3.5 turns show better swimming performance than those with 1.5 turns. The width of the helical tail shows a negative effect on the swimming performance, because Y_B is negative. The SHMs with smaller widths of the helical tail show better swimming performance. None of the interaction between the factors show a significant effect.

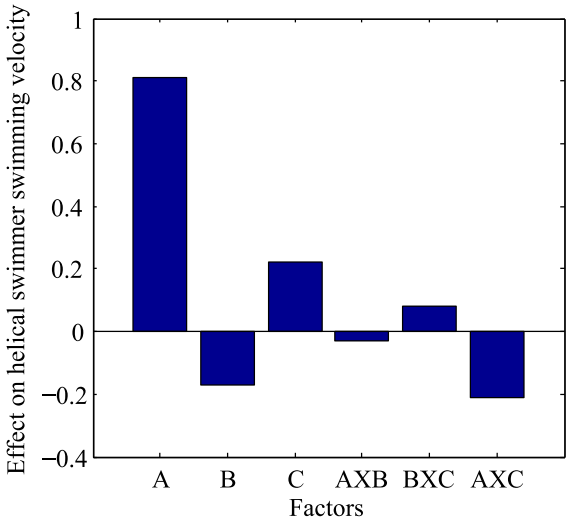

Figure 3.2: Effect of factors and the interactions on swimming velocity.

Although SHM1-mh6 shows the best swimming performance, its structure is too fragile to be used due to the width of the helical tail. Therefore, the best geometry

parameters design of the SHMs is SHM1-mh8. Note that the geometry parameters of SHM1-mh8 are scaled up from HNB [Hwang 2011]. In the following experiments, only SHM1-mh8 and the SHMs with the same shape of SHM1-mh8 (the geometry parameters are also scaled up from HNB, such as SHM5s) is used.

3.2 Rotational propulsion characteristics

The rotational propulsion characteristic of a SHM is defined as the curve of the response rotation frequency of the SHM as a function of the frequency of the external rotation magnetic field. In this section, the rotational propulsion characteristics of the SHMs with different magnetic positionings and head shapes are studied and compared. Afterwards, the head shape and magnetic positioning design of the helical swimmer is discussed both at the millimeter scale and at the microscale.

3.2.1 Rotational propulsion of SHMs with different magnetic positionings

In the first place, the rotational propulsion characteristics of SHMs with different magnetic positionings are studied. The presented artificial helical swimmers have different magnetic positionings: with a magnetic head or with a coated magnetic tail. However, the influence of magnetic positioning on propulsion characteristics has not been shown yet. Here, the rotational propulsion characteristics of the SHMs with the same geometry parameters and head shape, but with different magnetic positionings, are investigated and compared.

3.2.1.1 SHM1-mh8 with a magnetic head

The rotational propulsion characteristic of SHM1-mh8 is investigated in different viscous liquids that ensure the low Reynolds number conditions, with rotating magnetic fields of different strengths. Note that SHM1-mh8 is a SHM with a magnetic head, as shown in Figure 2.2. The viscous liquids are 90% and 95% glycerol solutions, as well as pure glycerol. The corresponding Reynolds numbers are 0.008, 0.004, and 0.001 which can be found in Table 2.3. The rotating magnetic field is generated by a 3D Helmholtz coil pairs setup. The magnetic flux density at the center of the workspace is 5 mT or 10 mT.

Figure 3.3 depicts the rotational propulsion characteristic of SHM1-mh8 in different viscous liquids respectively with 5 mT and 10 mT rotating magnetic fields. The method of rotation frequency estimation of the SHM is presented in Section 2.5.1. SHM1-mh8 rotates at the beginning in sync with the rotating magnetic field until it reaches a maximal rotation frequency. Beyond this maximal rotation frequency, the rotation frequency of SHM1-mh8 decreases gently with the external rotation frequency of the magnetic field.

The maximal rotation frequency is defined as the cut-off frequency. The value of the cut-off frequency strongly depends on the viscosity of the liquid, because a SHM has to overcome the rotational fluidic drag torque which depends on the viscosity of the liquid. The fluidic drag torque increases with the viscosity of the liquid. Thus, the

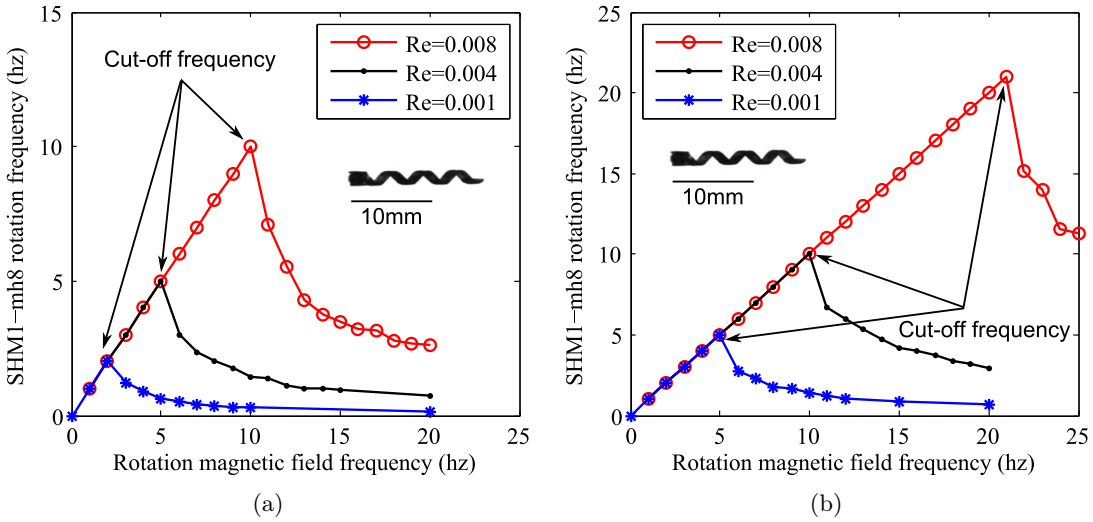

Figure 3.3: Rotation frequency of SHM1-mh8 in a rotating magnetic field generated by a 3D Helmholtz coil pairs with magnetic fields of (a) 5 mT and (b) 10 mT. SHM1-mh8 shows a cut-off frequency with a gentle decline.

value of the cut-off frequency decreases with the viscosity of the liquid. The value of the cut-off frequency also depends on the strength of the magnetic field. The magnetic field applies a magnetic torque on the SHM which overcomes the fluidic drag torque. Therefore, the value of the cut-off frequency increases with the strength of the rotating magnetic field. Beyond the cut-off frequency, the available magnetic torque is not sufficient to keep the SHM rotating synchronously with the applied rotating magnetic field. Within a 10 mT rotating magnetic field of 40 Hz, the rotation frequency of the SHM1-mh8 is 0 Hz in three different glycerol liquids.

Discussion

The cut-off frequency can explain the presence of a maximal translation speed of the helical microswimmers with a magnetic head in prior works [Ishiyama 2001a, Zhang 2009b]. The cut-off frequency is due to the limit of the energy provided by the actuation system. The cut-off frequency should be taken in consideration for future applications, because the swimming performance of a helical microswimmer can be strongly limited due to the high rotation frequency of the applied magnetic field.

3.2.1.2 SHM1-cylinder with an uniformly coated magnetic tail

The rotational propulsion characteristic of SHMs with an uniformly coated magnetic tails is investigated. The SHM used in the following experiments is SHM1-cylinder with a $20-50$ µm thick coated magnetic layer presented in Section 2.1.2.1, which has the same geometry parameters as SHM1-mh8. SHM1-cylinder is uniformly coated with a $20-50$ µm thick ferromagnetic layer.

The response rotation frequency of SHM1-cylinder in pure glycerol liquid with a 10 mT rotating magnetic field can not increase with the frequency of the rotating

magnetic field higher than 1 Hz. The frequency of the SHM1-cylinder in pure glycerol is always 0.08 Hz. We suppose that the rotation frequency of SHM1-cylinder is in saturation. Whereas the total dipole moment of SHM1-cylinder is much lower than that of SHM1-mh8, because the ferromagnetic coating layer is thin, so that the magnetic torque exerted on the SHM is very weak. This saturation is achieved at a frequency lower than 1 Hz. In order to validate our assumption, stronger magnetic fields and less viscous liquids are used.

In the following experiments, the RPMM, which is introduced in Section 2.3, is used. The magnetic flux density at the zone of interest is about 30 mT. The viscous liquids used are 30%, 60%, 80%, and 90% glycerol solutions. The corresponding Reynolds numbers are respectively 0.54, 0.11, 0.03 and 0.008, which can be found in Table 2.3.

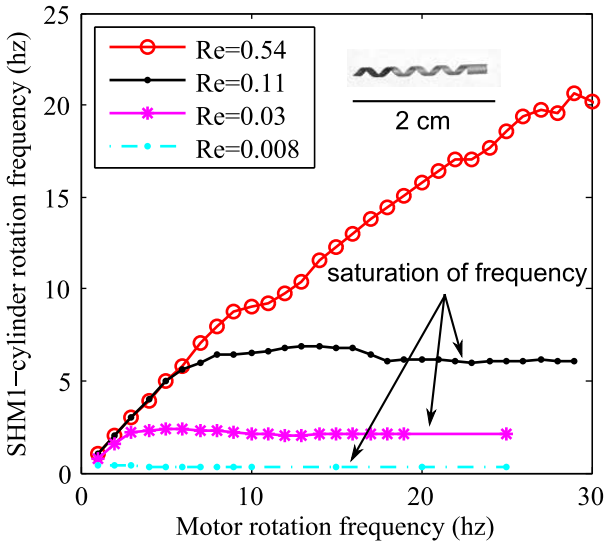

Figure 3.4: SHM1-cylinder with a $20-50$ μm thick coated magnetic layer shows a saturation of frequency with a magnetic field of about 30 mT generated by a RPMM.

The rotational propulsion characteristic of SHM1-cylinder in different viscous liquids is shown in Figure 3.4, which is different from that of the SHM1-mh8 with a magnetic head. At the first step, the rotation frequency of SHM1-cylinder synchronizes with the rotating magnetic field. Then, the rotation frequency of SHM1-cylinder loses the synchronization with the external rotating field, but it keeps increasing. Finally, the rotation frequency stabilizes at a fixed value, which is slightly smaller than its maximum. This value is called the saturation frequency of SHM1-cylinder.

The saturation frequency of SHM1-cylinder depends strongly on the Reynolds number. At a relatively high Reynolds number ($Re = 0.54$), the saturation frequency is not reached before 25 Hz. At a relatively low Reynolds number ($Re = 0.008$), the saturation frequency is reached before 1 Hz. The saturation frequency is 0.4 Hz. The SHM1-cylinder rotates at the saturation frequency in high-frequency rotating magnetic fields, such as 80 Hz.

Discussion

In the case of millimeter-scaled helical swimmers, the SHM with an uniformly coated

magnetic tail is not interesting: because its total dipole moment is not strong enough, due to the layer thickness limited by the coating process, compared to the magnetic heads which are made of permanent magnets. Therefore, the saturation frequency of the SHM with a coated magnetic tail is low compared to the cut-off frequency of the SHM with a magnetic head. However, the helical swimmer with an uniformly coated magnetic tail will be very interesting at the microscale. At the microscale, the total dipole moment of the magnetic head and the coated magnetic tail have the same order of magnitude. As a result, the cut-off frequency of a helical microswimmer with a magnetic head and the saturation of a helical microswimmer with a magnetic coated tail should be similar in the same environments. The difference is that beyond the cut-off frequency, the swimming performance of a helical microswimmer with a magnetic head will strongly decrease, while the performance of a helical microswimmer with a coated magnetic tail will not. Moreover, in a high-frequency rotating magnetic field, the helical microswimmer with a magnetic head will stop rotating, and the helical microswimmer with a coated magnetic tail will rotate at the saturation frequency. We predict that the performance of the helical microswimmer with a coated magnetic tail is more outstanding than that of the helical microswimmer with a magnetic head, which should be verified in future works.

3.2.1.3 SHM5-cylinder with a non-uniformly coated magnetic tail

Sometimes, the magnetic coating is not perfectly uniform due to the process of the micro-fabrications. The influence of the non-uniformity of the magnetic coating layer on the rotational propulsion characteristic of a SHM is studied as follows.

The SHM5-cylinder with a non-uniformly coated magnetic layer, which is introduced in Section 2.1.2.2, is used in the experiment. As the SHM5-cylinder is too long to be placed in the workspace of the 3D Helmholtz coil pairs, the RPMM is used to generate a rotating magnetic field. Recall that the magnetic flux density at the zone of interest is about 30 mT.

Figure 3.5a depicts the rotational propulsion characteristic of SHM5-cylinder. SHM5-cylinder rotates at first synchronously with the applied rotating field until a maximal rotation frequency, which is the same as in the two previous cases. The difference is that, beyond this maximal rotation frequency, SHM5-cylinder suddenly stops rotating. Some oscillations of SHM5-cylinder are observed. This maximal rotation frequency is defined as a cut-off frequency. Beyond this cut-off frequency, the available magnetic torque is no longer sufficient to keep the helical swimmers rotating. The value of the cut-off frequency depends on the Reynolds number as well, which decreases with the Reynolds number.

Discussion

However, the rotation performance of the SHM with a non-uniformly coated magnetic field decreases brutally beyond the cut-off frequency, which is different from the SHM with a magnetic head. It means that the non-uniformly coated magnetic layer of the helical swimmer could strongly limit its swimming performance. If the helical microswimmers are designed with a coated magnetic tails, the coating process should be treated carefully to ensure the uniformity of the magnetic layers, to keep their

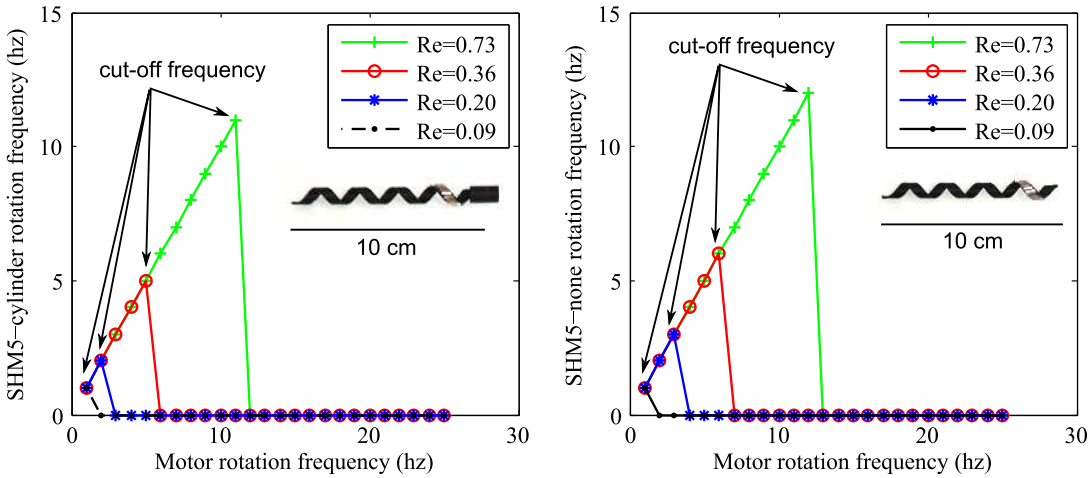

Figure 3.5: Both (a) SHM5-cylinder and (b) SHM5-none with a non-uniformly coated magnetic layer exhibit a cut-off frequency with a brutal stop with a magnetic field about 30 mT generated by a RPMM.

swimming performance.

3.2.2 Rotational propulsion of SHMs with different head shapes

In the state of the art of artificial helical swimmers, several different head shapes for helical swimmers have appeared. However, the influence of head shape on rotational propulsion has not been demonstrated yet. The rotational propulsion characteristics of the SHMs with the same geometry parameters and the same magnetic positioning, but with different head shapes are investigated and compared.

SHM5s are used in the following experiments. All the SHM5s have the same geometry parameters and magnetic positioning, as shown in Figure 2.3. The only difference of the SHM5s is the head shape. Let us start with SHM5-none, the SHM without a head. The rotational propulsion characteristic of SHM5-none in different viscous liquids is shown in Figure 3.5b. SHM5-none shows a cut-off frequency with a brutal stop. The rotational propulsion characteristic of SHM5-none is similar to that of SHM5-cylinder shown in Figure 3.5a.

Then, the rotational propulsion characteristic of SHM5-square and SHM5-sphere, SHMs with square and sphere heads, are studied. They all exhibit a cut-off frequency with a brutal stop. Before the cut-off frequency, they all rotate synchronously with the external rotating field. Figure 3.6 summarizes the values of the cut-off frequency of the SHM5s with magnetic tails and different heads as a function of the Reynolds numbers. SHM5-none has the highest values of the cut-off frequency, because it does not have a head to create additional fluidic drag torque. The square head creates more drag torque than the spherical and cylindrical heads, therefore SHM5-square has the lowest values of the cut-off frequency.

Discussion

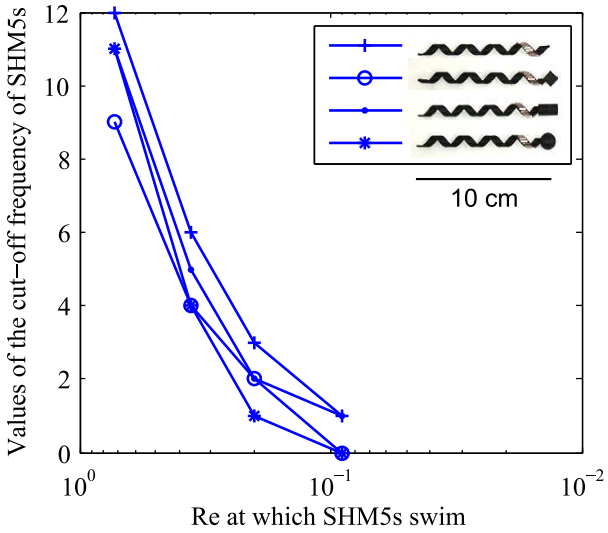

Figure 3.6: Values of the cut-off frequency of SHM5s with the same geometry parameters and magnetic positioning, but with different head shapes.

The head shape of a helical swimmer does not influence the rotational propulsion characteristic. The helical swimmers with the same geometry parameters and magnetic positioning, but with different head shapes exhibit the same rotational propulsion characteristic: the presence of the cut-off frequency. Although the head shape does influence the values of the cut-off frequency, this influence is not significant.

3.2.3 Factors influencing rotational propulsion

The SHMs with different magnetic positionings: magnetic heads, uniformly or non-uniformly coated magnetic tails, exhibit different rotational propulsion characteristics. Here, the factor influencing rotational propulsion characteristic is discussed. Each possible magnetization direction of the SHM which contributes to propulsion is defined as a magnetization phase. We find that the rotational propulsion characteristic depends on the magnetization phase of the helical swimmers:

- SHM1-mh8 with a magnetic head only has one magnetization phase, which is in the plane of the magnetic plate. It rotates synchronously with the external rotating magnetic field until a cut-off frequency. Beyond this cut-off frequency, the rotation frequency of SHM1-mh8 exhibits a gentle decline towards zero.

- SHM5s with a non-uniformly coated magnetic helical tails have several magnetization phases, which depend on the number of the small magnets covered on the helical tails. They rotate in sync with the external rotating field until a cut-off frequency. After they lose the synchronization with the external rotating field, the rotation frequency exhibits a brutal stop to zero.

- SHM1-cylinder with an uniformly coated magnetic helical tail has much more magnetization phases. If the coated magnetic layer of SHM1-cylinder is perfectly uniform, the number of magnetization phases of SHM1-cylinder is infinity. It exhibits a saturation of frequency. The rotation frequency increases synchronously

with the external rotating field, then the increase rate decreases and the rotation frequency saturates at a value slightly smaller than its maximal rotation frequency.

The rotational propulsion characteristics of the SHMs with different numbers of magnetization phases in the experiments are summarized in Table 3.4.

Table 3.4: Summary of the rotational propulsion characteristics of the SHMs with different magnetization phases.

Model	Magnetic part	Number of magnetization phases	Swimming characteristics
SHM1-mh8	head	1	cut-off gentle
SHM5-none	tail	several	cut-off brutal
SHM5-cylinder	tail	several	cut-off brutal
SHM5-sphere	tail	several	cut-off brutal
SHM5-square	tail	several	cut-off brutal
SHM1-cylinder	tail	infinite	saturation

According to the rotational propulsion characteristics, we predict that the helical microswimmers with uniformly coated magnetic tails will be the most promising artificial helical microswimmers, because they exhibit a saturation of frequency. Their propulsion performance will not substantially decrease with the external rotating magnetic field at high rotation frequency. Whereas the rotation frequency of the helical microswimmers with a plate magnetic head will decrease beyond the cut-off frequency. However, it is difficult to predict the values of the cut-off frequency and the values of the saturation for helical microswimmers from the results of the SHMs, because those values also depend on the strength of the external magnetic field and the total dipole moment of the helical microswimmers. The coating process during micro-fabrication should be carefully managed, because if the coated magnetic layer is not uniform, the propulsion performance will be largely limited. The prediction regarding the rotational propulsion characteristic of helical microswimmers at the microscale will be validated in future works.

3.2.4 Choice of the helical swimmer design

Since the head shape has no significant influence on the rotation performance of the helical swimmer, it can be designed according to the requirements. For example, a cylindrical head can be a good design to hold objects. The choice of the magnetic positioning design of the helical swimmer is discussed in two cases: at the millimeter scale and at the microscale.

3.2.4.1 At the millimeter scale

As discussed in Section 3.2.1.2, at the millimeter scale, the total dipole moment of the SHM with an uniformly coated magnetic tail is not strong enough due to the limited thickness of the coated magnetic layer. The value of the saturation frequency of the

SHM with a coated magnetic tail is low compared to the value of the cut-off frequency of the SHM with a magnetic head, which is made of a permanent magnet. Therefore, a SHM with a permanent magnet head is more promising of the swimming at the millimeter scale. Henceforth, only SHM1-mh8 is used in the visual servoing experiments, because it shows the best performance on the cut-off frequency and swimming velocity.

3.2.4.2 At the microscale

However, at the microscale, the helical swimmer with a uniformly coated magnetic tail will be more promising, because the total dipole moment of the magnetic head and the coating magnetic tail have the same order of magnitude. The magnetic torques applied on the helical microswimmers with the same total dipole moment are the same with the same rotating magnetic field. As a result, the value of the cut-off frequency of a helical microswimmer with a magnetic head and the value of the saturation frequency of a helical microswimmer with an uniformly coated magnetic tail should be similar. But beyond this value of the rotation frequency of the external magnetic field, the rotation performance of the helical microswimmer with a magnetic head decreases, and the rotation performance of the helical microswimmer with an uniformly coated magnetic tail stabilizes at this rotation frequency. Moreover, in high-frequency rotating magnetic field, the helical microswimmer with a magnetic head stops rotating, and the helical microswimmer with a coated magnetic tail rotates at the saturation frequency. In conclusion, we predict that the optimal magnetic positioning of the helical microswimmer is the helical microswimmer with an uniformly coated magnetic tail, and the coating process should be carefully managed to ensure the uniformity of the coated layer.

3.3 Propulsion velocity, advance velocity and torque analysis

In this section, the propulsion velocity generated by the helical propulsion, and the required magnetic torque are studied. The linear and angular velocities and the applied forces and torques of a SHM are related by the propulsion matrix. Therefore, the propulsion matrices of SHM1-mh8 are at first identified in different viscous liquids. Then, the linear velocity of SHM1-mh8 is studied based on the estimated propulsion matrix. The magnetic torque required to maintain the propulsion is also analysed based on the propulsion matrix.

3.3.1 Propulsion matrix identification

The current propulsion matrix identification method has shown in Section 2.5.3, that:

$$a = \frac{f_{app} - b\omega_2}{v_2} \tag{3.7}$$

$$b = \frac{f_{app}}{\omega_1} \tag{3.8}$$

$$c = \frac{-bv_2}{\omega_2} \tag{3.9}$$

where f_{app} is applied nonfluidic force on the SHM1-mh8. As the SHM swims vertically, the applied force is thus the apparent weight f_a (the resultant of the gravity and buoyancy forces) of the SHM. ω_1 is the rotation velocity at which the height of SHM1-mh8 stay motionless, ω_2 and v_2 is the rotation and translation velocity at which SHM1-mh8 drops down freely without applied forces and torques.

The propulsion matrix of SHM1-mh8 is at first estimated in pure glycerol liquid. The Reynolds number is 0.001. The applied magnetic field is 10 mT. In order to estimate the applied force f_{app}, the gravitation and buoyancy forces of SHM1-mh8 should be estimated. The mass of SHM1-mh8 is measured at 0.02 g ($\pm$0.001 g) with its magnetic head. The volume of SHM1-mh8 without its magnetic head V_{helix} is estimated through a Catia software model as 9×10^{-9} m^3. The head is a cylinder with 1.5 mm diameter (d) and 0.5 mm thickness (k). The volume of the head is calculated as follows

$$V_{head} = \pi \times \left(\frac{d}{2}\right)^2 \times k = 1 \times 10^{-9} \text{ m}^3 \tag{3.10}$$

The buoyancy force exerted by SHM1-mh8 in glycerol is then estimated as:

$$f_{buoyancy} = \rho g(V_{helix} + V_{head}) = 1 \times 10^{-4} \text{ N} \tag{3.11}$$

The applied nonfluidic force f_{app}, which is the apparent weight in this case, is then calculated as

$$f_{app} = f_a = G - f_{buoyancy} = -1 \times 10^{-4} \text{ N} \tag{3.12}$$

Note that the direction of the gravity is defined as the negative direction (cf Figure 2.22 in Section 2.5.3).

The rotation frequency corresponding to ω_1 is measured as 1.9 Hz. From (3.8), the parameter b is then estimated as:

$$b = \frac{f_{app}}{\omega} = \frac{-1 \times 10^{-4}}{1.9 \times 2\pi} = -8.38 \times 10^{-6} \text{ N} \cdot \text{s} \tag{3.13}$$

The free dropping velocity is measured as 0.59 mm/s. However, the rotation velocity of the free dropping could not be observed by eyes. Another method of parameters estimation should be used. As presented in Section 1.3.3.1, in the case of the magnetic field actuated helical swimmers, the translation velocity can be expressed as a function of the rotation velocity with the nonfluidic applied force as a second input. The relationship between the translation velocity and the rotation velocity is linear if the applied force is fixed, and can be expressed as:

$$v = \frac{f_{app}}{a} - \frac{b}{a}\omega \tag{3.14}$$

The measured translation velocities of SHM1-mh8 as a function of the rotation velocities is depicted in Figure 3.7 with the nonfluidic applied force is the apparent weight of SHM1-mh8. The linear relationship is validated experimentally. The red line is the linear regression calculated by the basic fitting tool of Matlab. The equation is given as:

$$v = 4.9 \times 10^{-5}\omega - 5.6 \times 10^4 \tag{3.15}$$

The parameter a can be estimated by the slope of the line as:

$$a = \frac{-b}{4.9 \times 10^{-5}} = 0.17 \text{ N} \cdot \text{s/m} \tag{3.16}$$

Note that the value of a can be also calculated by the v-intercept.

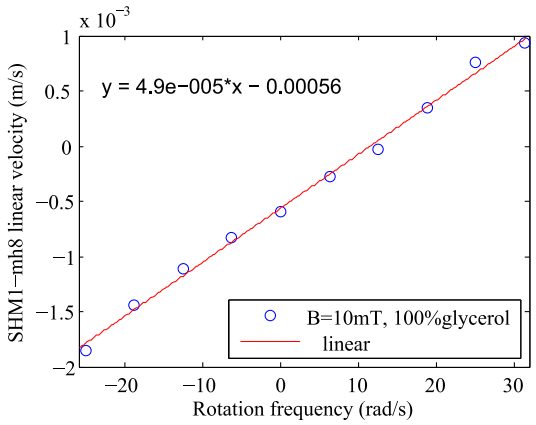

Figure 3.7: Translation velocity of SHM1-mh8 as a function of rotation frequency in glycerol with a 10 mT magnetic field. The red line is the linear regression by Matlab.

Then with the expression (3.7), the rotation velocity of the free dropping ω_2 is obtained as:

$$\omega_2 = \frac{f_{app} - av_2}{b} = -0.106 \text{ rad/s} \tag{3.17}$$

The corresponding rotation frequency is 0.017 Hz. It means that SHM1-mh8 takes 58 s to rotate one turn in free dropping. This explains why no rotation is observed during the free dropping experiments. At last, from (3.9) the parameter c can be estimated as:

$$c = 4.66 \times 10^{-8} \text{ N} \cdot \text{m} \cdot \text{s} \tag{3.18}$$

Then, the propulsion matrices of SHM1-mh8 in 95% and 90% glycerol solutions are estimated in the same way. The rotation frequency SHM1-mh8 used to balance its apparent weight are respectively 4 Hz and 11.3 Hz in 95% and 90% glycerol solutions. The corresponding angular velocities are calculated in Table 3.5. The linear relationships between the linear velocity and the rotation velocity of SHM1-mh8 in the two glycerol solutions are shown in Figure 3.8a and 3.8b. The free dropping velocities are measured and angular velocities during the free dropping are estimated. They are all summarized in Table 3.5.

The estimated parameters of the propulsion matrices of SHM1-mh8 in three glycerol solutions with different viscosities are summarized in Table 3.6.

The parameters a and c are positive, and they increase with the viscosity of the liquid. The parameter b is negative, and it decreases with the viscosity of the liquid. These parameters are used to estimate the propulsion velocity generated by the propulsion and the required magnetic torque.

Table 3.5: Angular and linear velocities used to estimate the propulsion matrices of SHM1-mh8 in different viscous liquids, where ω_1, v_1, v_2 are measured, and ω_2 is estimated.

% glycerol	ω_1 (rad/s)	v_1 (mm/s)	ω_2 (rad/s)	v_2 (mm/s)
100	11.93	0	-0.11	-0.59
95	25.12	0	-0.25	-0.91
90	70.96	0	-0.41	-2.13

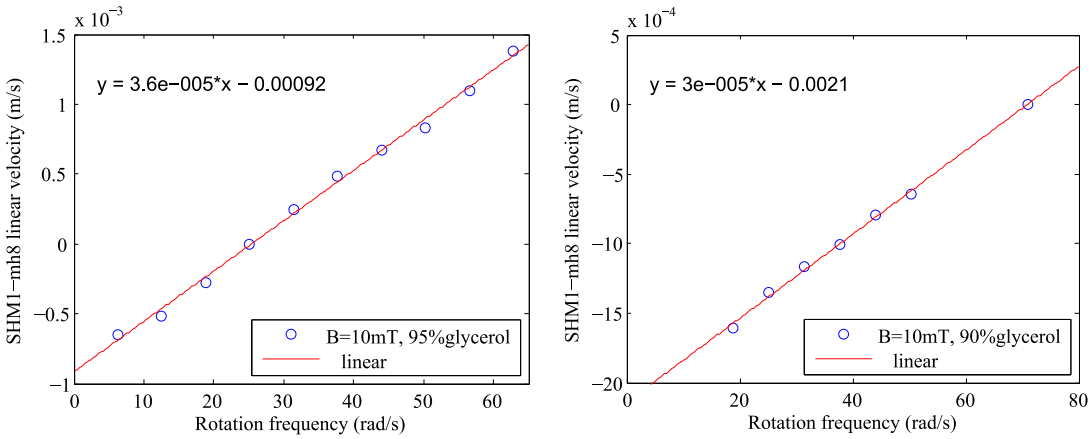

(a) (b)

Figure 3.8: Translation velocity of SHM1-mh8 as a function of rotation frequency in (a) 95% glycerol and (b) 90% glycerol solutions with a 10 mT magnetic field. The red line is the linear regression by Matlab.

Table 3.6: Summary of the estimated a, b, c parameters of the propulsion matrices of SHM1-mh8 in different viscous liquids.

% glycerol	a ($\mathrm{N \cdot s/m}$)	b ($\mathrm{N \cdot s}$)	c ($\mathrm{N \cdot m \cdot s}$)
100	0.171	-8.38×10^{-6}	4.66×10^{-8}
95	0.111	-3.98×10^{-6}	1.42×10^{-8}
90	0.047	-1.41×10^{-6}	0.73×10^{-8}

3.3.2 Propulsion velocity and advance velocity

As presented in Section 1.3.3.2, in the helical microswimmers applications, we point them in a direction at an angle with the horizontal plane to overcome its gravity. Here, we define the angle between the axis of the SHM and the horizontal plane yOz as the inclination angle, which is noted as θ_i, as shown in Figure 3.9. The inclination angle varies from 0° to 90°.

In the case of a helical swimmer actuated by a pure rotating magnetic field, the

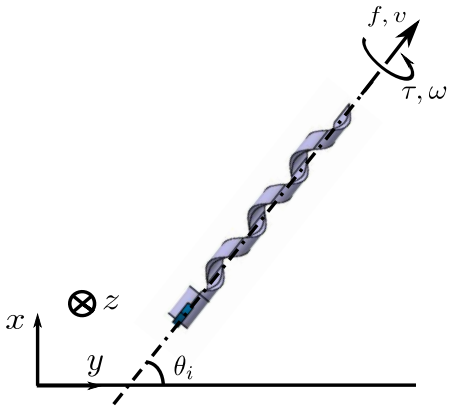

Figure 3.9: Inclination angle θ_i is defined as the angle between the axis of the SHM and the horizontal plane yOz.

applied nonfluidic force only depends on the apparent weight and the inclination angle, which can be expressed as:

$$f_{app} = f_a \sin\theta_i \tag{3.19}$$

where f_a is the apparent weight of the SHM.

In the case of a magnetic field actuated SHM, the fundamental input is the rotation frequency of the magnetic field, and the nonfluidic applied force can be considered as the second input. As the nonfluidic applied force depends on the inclination angle, thus the inclination angle can be the secondary input. The propulsion velocity of SHM1-mh8 based on its propulsion matrix as a function of the rotation frequency of the magnetic field and its inclination angle can be expressed as:

$$v = \frac{f_a \sin\theta_i}{a} - \frac{b}{a}\omega \tag{3.20}$$

with ω the angular velocity of SHM1-mh8. As proved earlier, the SHM rotates in sync with the rotating magnetic field until the cut-off frequency. Therefore, the propulsion velocity of SHM1-mh8 can be expressed as :

$$v = \frac{f_a \sin\theta_i}{a} - \frac{b}{a}2\pi f \tag{3.21}$$

before the cut-off frequency, with f the rotation frequency of the applied magnetic field. Recall that the cut-off frequency of SHM1-mh8 in pure glycerol with a 10 mT magnetic field is 5 Hz. The propulsion velocity of SHM1-mh8 with different inclination angles in pure glycerol with a 10 mT magnetic field between -5 Hz and 5 Hz is then simulated and shown in Figure 3.10.

The advance velocity is defined as the linear velocity projected on the horizontal plane, which depends on the propulsion velocity and the inclination angle. The advance velocity of the SHM, noted as v_h, can be easily calculated as:

$$v_h = v\cos\theta_i \tag{3.22}$$

The propulsion velocity is expressed in Equation (3.21), then we obtain:

$$v_h = \frac{f_a \sin 2\theta_i}{2a} - \frac{b}{a}2\pi f\cos\theta_i \tag{3.23}$$

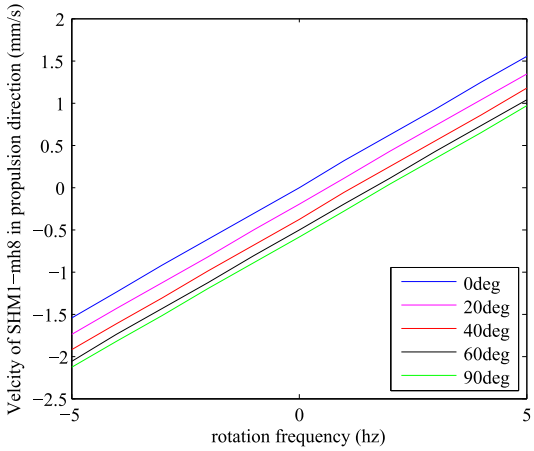

Figure 3.10: Estimated propulsion velocity of SHM1-mh8 in the propulsive direction based on the propulsion matrix in pure glycerol.

with f the rotation frequency of the magnetic field and θ_i the inclination angle of SHM1-mh8. The advance velocities of SHM1-mh8 in pure glycerol with different inclination angles are estimated and shown in Figure 3.11a. The advance velocity of SHM1-mh8 in pure glycerol with a 3 Hz rotating magnetic field and with an inclination angle of 0° is calculated as 0.93 mm/s based on the estimated propulsion matrix, which is measured as 1.09 mm/s in Section 3.1.3 (cf Table 3.3). The error is estimated as:

$$e = (1.09 - 0.93)/1.09 = 15\% \tag{3.24}$$

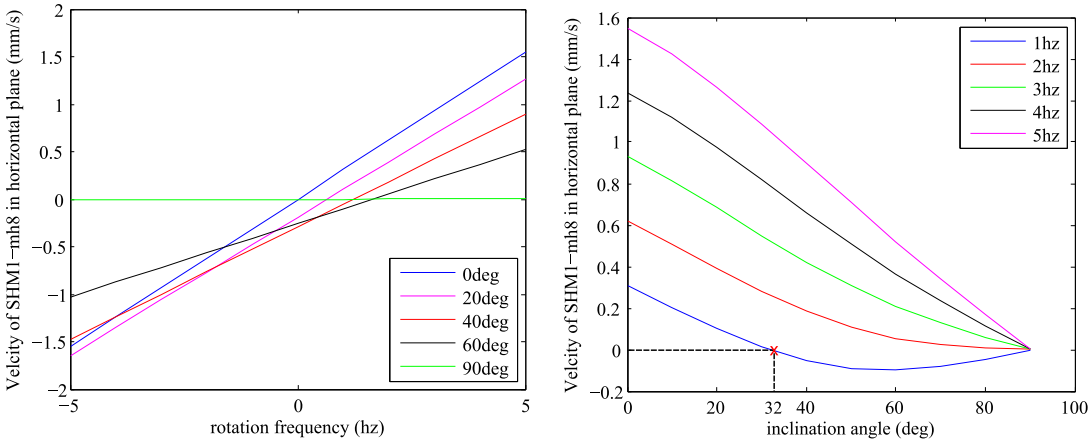

(a) (b)

Figure 3.11: Estimated linear advance velocity of floating SHM1-mh8 on the horizontal plane as a function of (a) the rotation frequency of the magnetic field and (b) the inclination angle based on the propulsion matrix in pure glycerol.

This linear advance velocity on the horizontal plane can also be expressed as a function of the inclination angle, as shown in Figure 3.11b. We notice that the advance velocity of SHM1-mh8 on the horizontal can be negative, for example SHM1-mh8 with

inclination angles from 32° with a 1 Hz rotating magnetic field, which should be avoided in the future for SHM swimming control. With a 2 Hz rotating magnetic field, the advance velocity of floating SHM1-mh8 should be positive with any inclination angle.

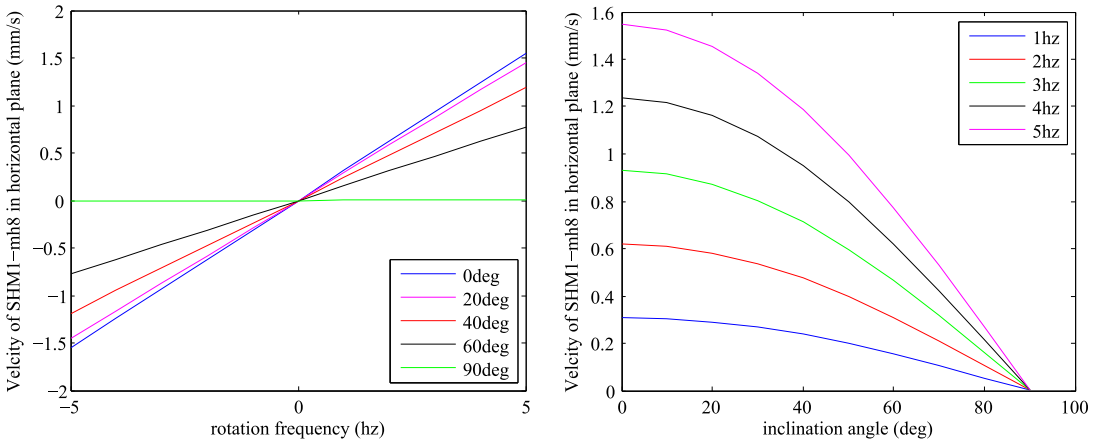

(a) (b)

Figure 3.12: Linear advance velocity of SHM1-mh8 sinking down to the bottom on the horizontal plane as a function of (a) the rotation frequency of the magnetic field and (b) the inclination angle based on the propulsion matrix in pure glycerol.

When the SHM sinks down to the bottom, the applied nonfluidic force is 0 N if the friction is neglected. The friction can be neglected if the inclination angle of the SHM is not 0°, because the contact between the SHM and bottom is just a point contact. In the case of the SHM sinking down to the bottom, the linear advance velocity on the horizontal plane is always positive, which is shown in Figure 3.12a and 3.12b. The linear velocity on the horizontal plane decreases with the inclination angle, and the decrease rate increases. The advance velocity of the SHM is largely limited if the inclination angle is higher than 60°.

3.3.3 Applied torque analysis

The magnetic torque required to maintain propulsion is estimated based on the propulsion matrix. From Equation (1.8) based on the propulsion model, the required applied torque should be:

$$\tau = bv + c\omega \tag{3.25}$$

Replacing the expression of the propulsion velocity by Equation (3.21), the required torque can be expressed as:

$$\tau = \frac{b}{a} f_a \sin\theta_i - \frac{b}{a} 2\pi f + c\omega \tag{3.26}$$

The required torques are estimated at the vertical position of SHM1-mh8, which means the inclination angle $\theta_i = 90°$. The required torque at the vertical position is higher than at any other position for the same propulsion.

The estimated required magnetic torques for the propulsion of SHM1-mh8 before the cut-off frequencies in different viscous liquids based on the estimated propulsion

matrices are depicted in Figure 3.13a. More torque is required for a SHM to rotate in more viscous liquids (at lower Reynolds number) at the same frequency. Theoretically, the required magnetic torques for the maximal rotation frequency of the SHM at different Reynolds numbers should be the same, as shown in Figure 3.13b. The difference of the required torques for the rotation of SHM1-mh8 at the maximal rotation frequency, which is the cut-off frequency presented in Section 3.2.1.1, in different viscous liquids is due to the bias of the propulsion matrix estimation.

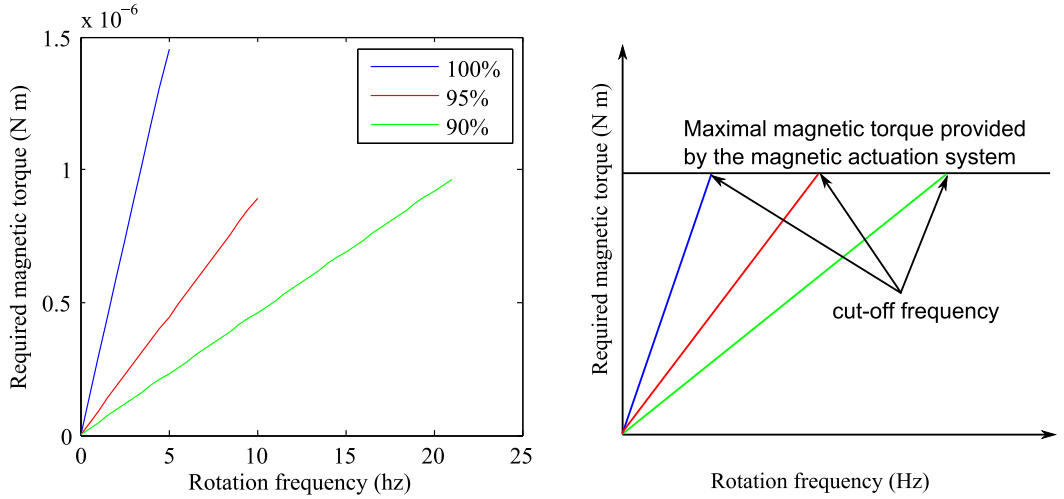

Figure 3.13: (a) Simulated magnetic torque required for the propulsion of SHM1-mh8 in different viscous liquids based on the estimated propulsion matrices. (b) Theoretical magnetic torque required for the propulsion of a helical swimmer in different viscous liquids.

The magnetic torque provided by a magnetic actuation system to one magnetic device is limited. If the required torque to maintain a helical swimmer rotating at a frequency surpasses the maximum magnetic torque that the actuation system can provide to it, the helical swimmer can not rotate at that frequency. That is why there is a maximal rotation frequency (cut-off frequencies and saturations of frequency) for a magnetically actuated helical swimmer. It also explains how the value of the cut-off frequency or the value of the saturation frequency increases with the Reynolds number, because less torque is required to maintain the rotation of the helical swimmer at a higher Reynolds number.

3.4 Open-loop 3D steering control

The steering of the SHM is very important to realize a 3D motion, but it has not been extensively studied in the state of the art. In this section, an open-loop 3D steering control of the SHM is investigated. The steering efficiency is characterized by the response time to a step function. A strategy to improve the steering efficiency in open-loop steering control is proposed at the end.

3.4.1 Open-loop steering principle

The open-loop steering of the SHM can be applied both on the inclination angle and the direction angle. The inclination angle θ_i has been defined in the last section as the angle between the axis of the SHM and the horizontal plane yOz. Here we define the direction angle θ_d as the angle between the z axis and the projection of the helical swimmer axis on the yOz plane, which is shown in Figure 3.14. By controlling the direction angle of the helical swimmer, its advance direction projected on the horizontal plane can be controlled.

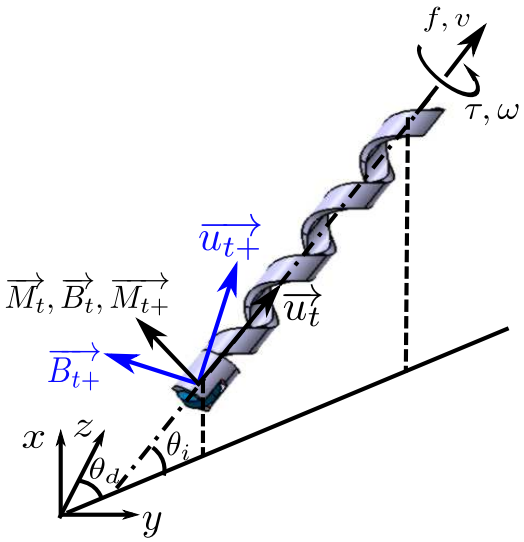

Figure 3.14: Magnetic helical swimmer steering model. The inclination angle and direction angle of steering are respectively θ_i and θ_d.

At the equilibrium regime, the helical swimmer rotates synchronously with the external rotating magnetic field around $\overrightarrow{u_t}$. The axis direction of the SHM should be in the direction of $\overrightarrow{u_t}$. The magnetization of the SHM is noted as $\overrightarrow{M_t}$, and the magnetic field is noted as $\overrightarrow{B_t}$. Both $\overrightarrow{M_t}$ and $\overrightarrow{B_t}$ are perpendicular to the axis $\overrightarrow{u_t}$. The magnetic torque exerted on the SHM τ_t can be expressed as:

$$\overrightarrow{\tau_t} = \overrightarrow{M_t} \times \overrightarrow{B_t} \tag{3.27}$$

should be also in the direction of $\overrightarrow{u_t}$, which keep the SHM rotating around $\overrightarrow{u_t}$.

At time t, the axis of the rotating magnetic field changes to $\overrightarrow{u_{t+}}$. The magnetic field $\overrightarrow{B_{t+}}$ becomes perpendicular to $\overrightarrow{u_{t+}}$. However, the magnetization of the SHM $\overrightarrow{M_{t+}}$ is still perpendicular to the initial axis $\overrightarrow{u_t}$. The magnetic torque $\overrightarrow{\tau_{t+}}$ exerted on the SHM after the axis change of the rotating magnetic field can be now expressed as:

$$\overrightarrow{\tau_{t+}} = \overrightarrow{M_{t+}} \times \overrightarrow{B_{t+}} \tag{3.28}$$

where the magnetic field can be decomposed in the directions perpendicular and parallel to the direction of $\overrightarrow{u_t}$. Then, the magnetic field $\overrightarrow{B_{t+}}$ can be expressed as:

$$\overrightarrow{B_{t+}} = \overrightarrow{B_{\perp u_t}} + \overrightarrow{B_{\parallel u_t}} \tag{3.29}$$

Therefore, the magnetic torque exerted on the SHM after the axis of the rotating magnetic field changes can then be written as:

$$\overrightarrow{\tau_{t+}} = \underbrace{\overrightarrow{M_{t+}} \times \overrightarrow{B_{\perp u_t}}}_{\overrightarrow{\tau_{\parallel u_t}}} + \underbrace{\overrightarrow{M_{t+}} \times \overrightarrow{B_{\parallel u_t}}}_{\overrightarrow{\tau_{\perp u_t}}} \tag{3.30}$$

As the magnetization $\overrightarrow{M_{t+}}$ is perpendicular to the $\overrightarrow{u_t}$ direction, this magnetic torque can be decomposed in the directions perpendicular and parallel to $\overrightarrow{u_t}$ as well. The torque $\overrightarrow{\tau_{\parallel u_t}}$ is the magnetic torque in the direction of $\overrightarrow{u_t}$, which makes the SHM rotate around its actual axis $\overrightarrow{u_t}$. The magnetic torque $\overrightarrow{\tau_{\perp u_t}}$ is the magnetic torque perpendicular to $\overrightarrow{u_t}$, which makes the SHM rotate around the direction of $\overrightarrow{u_t} \times \overrightarrow{M_t}$. That means the direction of the axis of the SHM changes. The axis direction change of the SHM is called the steering of the SHM.

3.4.2 Direction angle steering characterization

The change of the direction angle of the SHM is defined as the direction angle steering. The direction angle of SHM1-mh8 in this section is considered as the angle between the axis z and the axis of the SHM projected on the image taken from the top camera tracked by ViSP. It is not exactly the direction angle in the 3D space. The exact direction angle of the SHM will be calculated from the axis of the SHM in the 3D space for the visual servo control, which is introduced in the next chapter.

The direction angle steering is characterized by the response to a step command to the direction angle with a constant inclination angle. Therefore, this direction angle steering is open-loop. This step command is realized by a step function of the magnetic field, which can be expressed as:

$$\mathbf{B} = \begin{cases} \mathbf{B}(\mathbf{n}_i, f, t), & 0\ \mathrm{s} \leqslant t < 2\ \mathrm{s} \\ \mathbf{B}(\mathbf{n}, f, t), & t \geqslant 2\ \mathrm{s} \end{cases} \tag{3.31}$$

where $\mathbf{n}_i$ is the initial axis of SHM1-mh8, and $\mathbf{n}$ is the commanded axis of SHM1-mh8. $\mathbf{n} = (n_x, n_y, n_z)^T$ can be expressed by the direction angle θ_d and the inclination angle θ_i as:

$$\mathbf{n} = \begin{bmatrix} n_x \\ n_y \\ n_z \end{bmatrix} = \begin{bmatrix} \sin\theta_i \\ \cos\theta_i \sin\theta_d \\ \cos\theta_i \cos\theta_d \end{bmatrix} \tag{3.32}$$

Same calculation is applied for $\mathbf{n}_i$, and the initial direction angle is fixed at 0°. The function $\mathbf{B}(\mathbf{n}, f, t)$ is given by Equation (2.9). The rotation frequency f of SHM1-mh8 is kept at 3 Hz in the following experiments. SHM1-mh8 is floating in pure glycerol. The positive direction of the direction angle steering is defined as the clockwise direction. The direction angle steering of SHM1-mh8 is characterized with different inclination angles, such as 0°, 45°, and 65°.

3.4.2.1 Inclination angle of 0°

It is well-known that, with an inclination angle of 0°, if the direction angle changes by 180°, the helical swimmer will just reverse its rotation direction to reverse the advance

direction. However, the position of the head relative to its body does not change. In other words, the head can not be always kept in the front of or at the back of the helical swimmer. So, we can say that a helical swimmer can not turn by 180° with an inclination angle of 0°.

The step response to a small direction angle steering, such as a 30° angle, is shown in Figure 3.15. The response shows first order system characteristics. The response time is 4.6 s. An oscillation of the direction angle appears at 3 Hz. As the frequency of the oscillation corresponds exactly to the rotation frequency of the SHM, we deduce that this oscillation is caused by the dissymmetry of the helical morphology relative to its axis. The oscillation will allow the analysis of the SHM's self-rotation phase in future works.

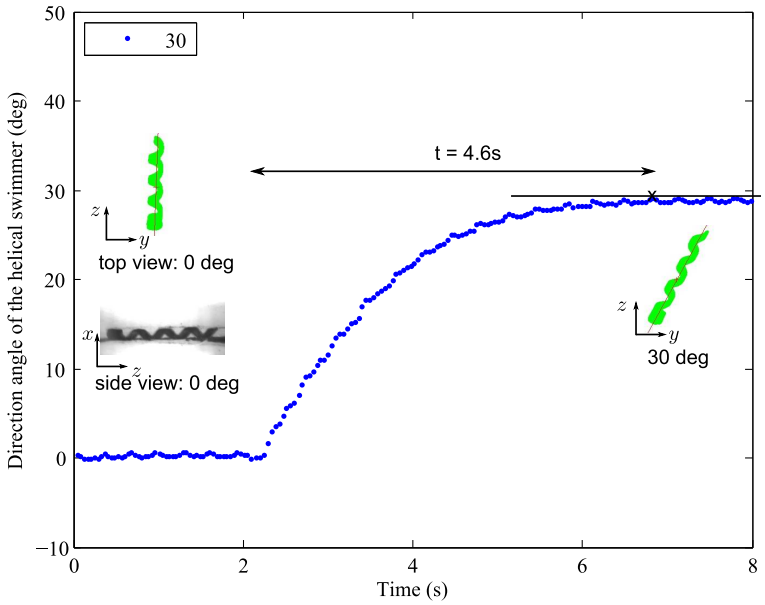

Figure 3.15: Step response to the 30° direction angle steering with a 0° inclination angle.

The direction of SHM1-mh8 can not be steered towards 90° with an inclination angle of 0°. We observe that SHM1-mh8 stopped its self-rotation after the application of the step command to the direction angle, because its axis is no longer along the axis of the rotating magnetic field. The magnetic field parallel to the axis of SHM1-mh8, which contributes to the steering, is not strong enough to steer SHM1-mh8 towards 90°. The direction angle of SHM1-mh8 stays at 0°.

3.4.2.2 Inclination angle of 45°

Then, SHM1-mh8 is inclined up with an inclination angle of 45°. The direction steerings at 30°, 90°, 180°, and −90° angles are respectively studied. The step responses to the different direction angle steering are shown in Figure 3.16. The direction steerings of SHM1-mh8 at 180° can be achieved with a 45° inclination angle. Not only the advance direction, but also the head position changes. The head stays at the back of the helical swimmer no matter what the advance direction is. The 90° angle direction steering can

be easily achieved with a 45° inclination angle. The response times to the direction angle steering are summarized in Table 3.7. It shows that the steering performance, which is characterized by the response time to a step command, is improved by inclining SHM1-mh8 up at 45°.

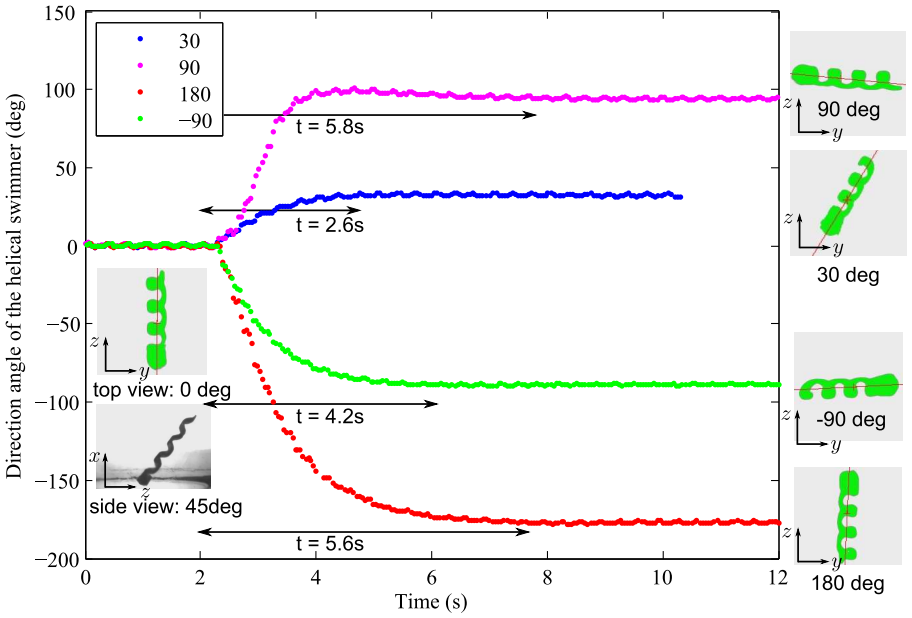

Figure 3.16: Step responses to the 30°, 90°, 180°, and −90° angle direction steering with a 45° inclination angle.

Table 3.7: Response times of direction angle steering of SHM1-mh8 with different inclination angles (unit: s).

	Command angle of direction steering			
Inclination angle	30°	90°	180°	−90°
0°	4.6	∞	∞	∞
45°	2.6	5.8	5.6	4.2
65°	2.3	4.4	4.8	3.5

The responses of the direction angle of SHM1-mh8 to the step command of 30°, −90°, and 180° show first order system characteristics. However, the response to a 90° angle direction steering shows second order system characteristics. Figure 3.17 and Figure 3.18 depict the image sequences of SHM1-mh8 during the direction angle steering at 90° and −90° respectively from the top and the side cameras. From the apparent length of the SHM1-mh8 viewed on the images from the top camera, we deduce that the inclination angle of SHM1-mh8 increases during the direction angle steering towards 90°. This increase of the inclination angle is not obvious for the direction angle steering towards −90° from the apparent length. In the next chapter, we introduce a method to estimate the axis of the SHM in the 3D space from the two images, in order to clearly observe the real-time inclination angle of the SHM. The increase of the inclination

angle is caused by the inertia of the self-rotation of SHM1-mh8. This also explains why SHM1-mh8 turned towards the counter clockwise direction for the direction angle steering of 180°. To validate this assumption in future works, we have to fabricate the SHM with the same geometry parameters but with the left-hand chirality, and see if it turns towards the clockwise direction for the direction angle steering of 180°.

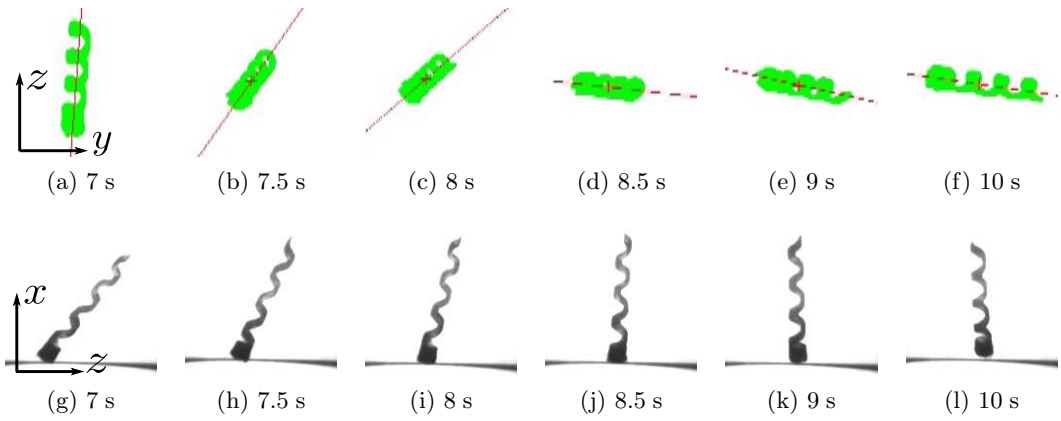

(a) 7 s (b) 7.5 s (c) 8 s (d) 8.5 s (e) 9 s (f) 10 s

(g) 7 s (h) 7.5 s (i) 8 s (j) 8.5 s (k) 9 s (l) 10 s

Figure 3.17: Image sequence of 90° angle direction steering with a 45° inclination angle. (a)-(f) show the top view of SHM1-mh8, and (g)-(l) show the side view.

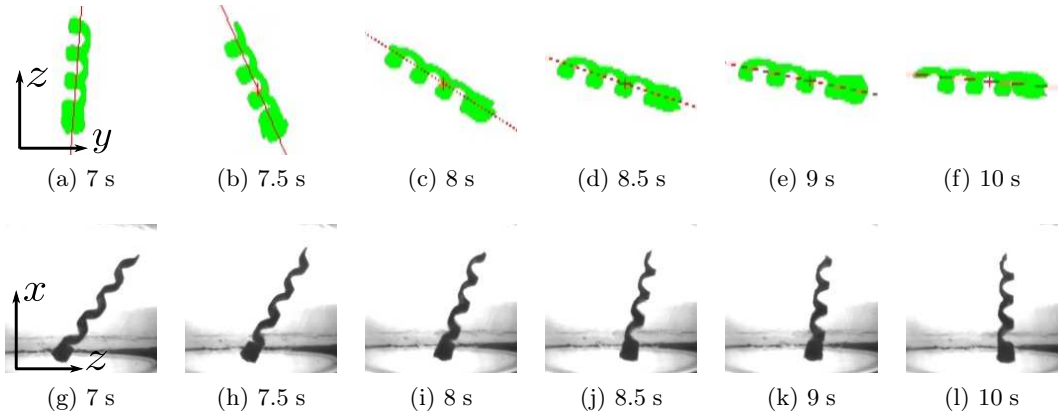

(a) 7 s (b) 7.5 s (c) 8 s (d) 8.5 s (e) 9 s (f) 10 s

(g) 7 s (h) 7.5 s (i) 8 s (j) 8.5 s (k) 9 s (l) 10 s

Figure 3.18: Image sequence of −90° angle direction steering with a 45° inclination angle. (a)-(f) show the top view of SHM1-mh8, and (g)-(l) show the side view.

3.4.2.3 Inclination angle of 65°

The direction angle steering of SHM1-mh8 is tested with an even higher inclination angle such as 65°. The step responses to the 30°, 90°, 180°, and −90° direction angle steerings with a 65° inclination angle are depicted in Figure 3.19. The characteristics of direction steering responses with a 65° inclination angle are similar to those with a 45° inclination angle. Their response times are summarized in Table 3.7. It shows that the direction angle steering with a 65° inclination angle is more efficient than that with a 45° inclination angle.

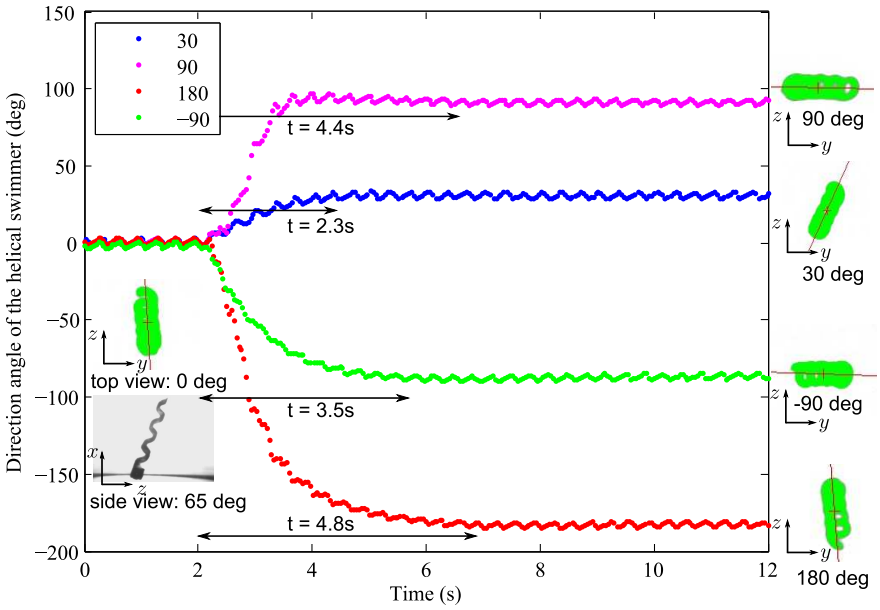

Figure 3.19: Step responses to the 30°, 90°, 180°, and −90° direction angle steering with a 65° inclination angle.

In conclusion, in open-loop direction angle steering, the steering performance can be improved by increasing the inclination angle of the SHM.

3.4.3 Inclination angle steering characterization

The change of the inclination angle of the SHM is defined as the inclination angle. In the following experiments of inclination angle steering of SHM1-mh8, the direction angle is kept at 0°. Therefore, the inclination angle of SHM1-mh8 can be considered as the angle between the axis z and the axis of SHM1-mh8 projected on the image taken from the side camera tracked by ViSP.

The inclination angle steering is characterized by the inclination angle response to a step command. This step command is realized by a step function of the magnetic field, which is expressed in Equation (3.31). The rotation frequency of SHM1-mh8 is 3 Hz. The initial inclination angle is 10°. The SHM is floating in pure glycerol.

The inclination angle steering of SHM1-mh8 requires to steer its inclination angle towards respectively 30°, 60°, and 90°. The inclination steering is achieved for all the control angles. Figure 3.20 shows the step responses to the different inclination angle steerings. All the responses exhibit first order system characteristics.

Thus, we develop a 3D steering strategy by combining inclination and direction steering for the open-loop steering of the SHM. In the case where the SHM can not respond to the direction angle steering, we can increase the inclination angle of the SHM to realize the direction angle steering. For example, the direction angle steering of SHM1-mh8 from 0° to 90° with a 0° inclination angle can not be achieved, as presented in Section 3.4.2.1. Here we use the 3D steering strategy to firstly incline SHM1-mh8 at 45°. The direction angle steering at 90° can be achieved, and then we lay SHM1-mh8 down to 0°. Therefore, the direction angle steering of SHM1-mh8 from

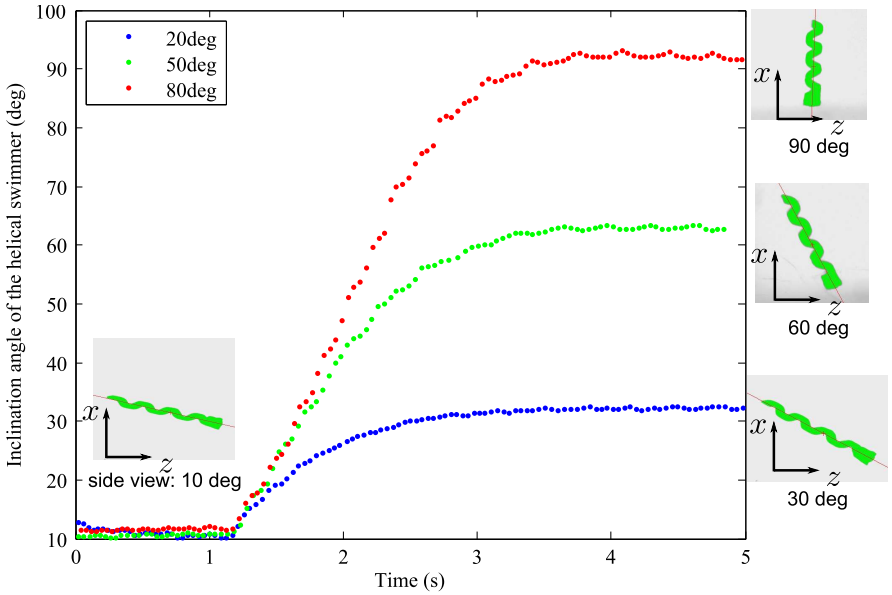

Figure 3.20: Step responses of the inclination angle steering at 30°, 60°, and 90° with the initial inclination angle at 10°.

0° to 90° with a 0° inclination angle can be achieved by using this 3D steering strategy.

3.4.4 Direction angle steering on a sticky substrate

A helical swimmer is not always floating in liquids: sometimes it sinks down to the bottom. A sticky substrate, such as Polydimethylsiloxane (PDMS), is used to simulate high surface friction at the microscale. The direction angle steering of SHM1-mh8 is studied with different inclination angles on a PDMS substrate.

Table 3.8 summarizes the response times to a direction angle direction steering of 30°, 90°, 180°, and −90° on a PDMS substrate. The response time to the direction angle steering of 30° with a 0° inclination angle on PDMS is much greater than that in floating conditions, which reveals that the steering performance is limited by high surface friction. The direction angle steering performance is greatly improved by increasing the inclination angle of SHM1-mh8.

Table 3.8: Response times of direction angle steering of SHM1-mh8 with different inclination angles on PDMS (unit: s).

	Command angle of direction steering			
Inclination angle	30°	90°	180°	−90°
0°	7.8	∞	∞	∞
45°	4.0	6.9	8.5	5.6
65°	2.7	5.6	4.6	3.9

The direction angle steering of 90° of SHM1-mh8 with a 0° inclination angle can not be achieved. By using the proposed 3D steering strategy, we first increase the

inclination angle of SHM1-mh8 to 45°. Then, the direction angle steering of 90° is achieved. We predict that this 3D steering strategy can improve steering performance at the microscale.

3.5 Summary

In this chapter, the swimming performance of the SHMs with different geometry parameters has been compared. We found that the pitch of the helical swimmer is the most influential factor on the swimming performance. The swimming performance of the SHM is improved by using longer pitch.

The rotational propulsion characteristics of the SHM with different magnetic positionings are also compared. The SHM with a magnetic head shows a cut-off frequency, and the SHM with a coated magnetic layer shows a saturation of frequency. The head shape does not influence the rotational propulsion characteristics. At the millimeter scale, the SHM with a magnetic head shows better rotation performance than the SHM with a coated magnetic tail, because the total dipole moment of the coated thin magnetic layer is not as strong as the permenant magnetic head. As a result, the cut-off frequency of the SHM with a magnetic head is much higher than the saturation frequency of the SHM with a coated magnetic tail. However, at the microscale, as the total dipole moment of the magnetic head and the coated magnetic layer are comparable, we predict that the SHM with a coated magnetic layer has better rotation performance, because the rotation frequency of the SHM with a magnetic head decreases beyond the cut-off frequency down to zero, and the rotation frequency of the SHM with a coated magnetic layer stabilizes at a non-zero value called the saturation frequency. Note that the magnetic layer should be uniform, otherwise the SHM with a non-uniformly coated magnetic layer risks to have a cut-off frequency as well. The prediction regarding the rotational propulsion of helical swimmers at the microscale will be validated in future works. The design of SHM1-mh8 is chosen for the visual servo control experiment, because of its performance at the millimeter scale.

The propulsion matrices of SHM1-mh8 is estimated in different viscous liquids. The linear velocity and advance velocity generated by the helical propulsion is simulated based on the estimated propulsion matrices, as well as the required magnetic torque for the propulsion.

An open-loop steering control both on the direction angle and the inclination angle of SHM1-mh8 is studied. The steering efficiency of the direction angle steering of SHM1-mh8 can be increased by increasing its inclination angle. Therefore, we proposed a 3D steering strategy that increases the SHM's inclination angle if its direction angle steering can not be achieved. The closed-loop steering of the SHM is studied in the next chapter.

Chapter 4

Visual servo control of helical swimmers

Contents

The open-loop control of the orientation of helical swimmers has been studied in the previous chapter. In this chapter, a closed-loop control of the orientation of helical swimmers in the 3D space by visual servoing is demonstrated. Then, a path following task on the 2D horizontal plane of helical swimmers is proposed based on the control law of the magnetic field. The visual servo control of the 2D path following is tested with a straight line. A 3D path following task in the space is also discussed for the perspectives. Real-time orientation and position of the helical swimmer are required for the visual servoing tasks. The methods for the reconstruction of the 3D position and orientation of helical swimmers from tracking in the top and side views are presented. In order to realize the 3D reconstruction of helical swimmers from multiple images, we start the chapter with the camera calibration.

4.1 Camera calibration

4.1.1 Introduction

A camera is a mapping between the 3D world and a 2D image [Hartley 2004]. The camera calibration is a necessary step in 3D computer vision in order to extract metric information from 2D images. Based on the dimension of calibration objects, most calibration techniques can be classified into four categories:
- 3D reference object-based calibration [Agrawal 2003]: These methods employ a calibration object that has precise 3D geometric features. Calibration can be done very efficiently. The calibration object usually consists of two or three planes that are orthogonal to each other. Sometimes, a plane undergoing a precisely known translation is also used, which equivalently provides 3D reference points. This approach requires an expensive calibration apparatus and an elaborate setup, because its accuracy directly depends on the quality of the calibration object.
- 2D plane-based calibration [Zhang 2000, Sturm 1999]: This kind of methods uses a specially-designed planar pattern with corners, dots or any features that can be easily extracted from the image at a few different orientations. Here again, the accuracy of the calibration depends on the quality of the calibration planar pattern. Yet, a 2D pattern is far simpler to make accurately than a 3D pattern: a laser printer does the job perfectly.
- 1D line-based calibration [Zhang 2004, Hammarstedt 2005]: This method uses a 1D stick with three or more collinear points. A camera can be calibrated by observing a moving line around a fixed point. The main advantage of this method is that no special pattern is needed. We can for example use a string of balls hanging from the ceiling. This technique is relatively new. Few softwares are available.
- self-calibration [Hartley 1997]: This kind of calibration techniques uses only point correspondences in multiple views, without needing to know either the 3D location of the points or the camera location. But this requires a stronger background in computer vision and more complex algorithms.

In the last couple of years, calibration with a 2D apparatus turned to be the best choice in most situations because of its ease of use and good accuracy [Medioni 2004]. Moreover, there exists several open softwares that are both easy to use and efficient (camera calibration toolbox for Matlab, OpenCV). As far as we are concerned, ViSP also implements a convenient camera calibration algorithm.

4.1.2 Notation and perspective projective model

The projection matrix relating a point of the 3D object to its 2D image should be defined. Figure 4.1 shows a camera with center of projection C and the optical axis z_c. The image plane is at focus that is at the focal length f away from C. We use $\mathcal{R}_w = (O, x, y, z)$ to denote the 3D world coordinate system, $\mathcal{R}_c = (C, x_c, y_c, z_c)$ to denote the camera coordinate system, $\mathcal{R}_{ip} = (o_{ip}, u, v)$ to denote the 2D image pixel coordinate system, and $\mathcal{R}_{im} = (o_{im}, x, y)$ to denote the 2D image metric coordinate system.

Let us consider a 3D point Q which coordinates in the world coordinate system are given by ${}^w\mathbf{Q} = ({}^wX, {}^wY, {}^wZ)^T$. This point written in the camera coordinate system

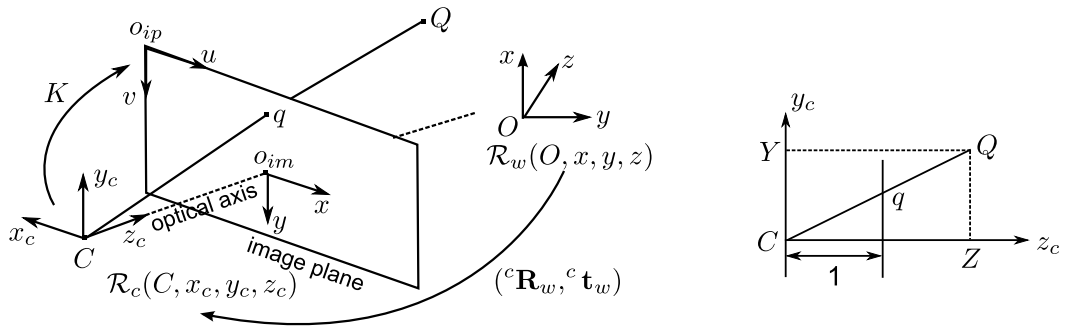

Figure 4.1: Perspective projective model.

is ${}^c\mathbf{Q} = ({}^cX, {}^cY, {}^cZ)^T$. The transformation from the point Q written in the world coordinate system to the camera coordinate system is composed of a rotation ${}^c\mathbf{R}_w$ and a translation ${}^c\mathbf{t}_w$. The relationship between the homogeneous coordinates ${}^c\tilde{\mathbf{Q}} = ({}^cX, {}^cY, {}^cZ, 1)^T$ and ${}^w\tilde{\mathbf{Q}} = ({}^wX, {}^wY, {}^wZ, 1)^T$ can be expressed as:

$$ {}^c\tilde{\mathbf{Q}} = \begin{bmatrix} & {}^c\mathbf{R}_w & & {}^c\mathbf{t}_w \\ & & & \\ 0 & 0 & 0 & 1 \end{bmatrix} {}^w\tilde{\mathbf{Q}} \tag{4.1} $$

where ${}^c\mathbf{R}_w$ and ${}^c\mathbf{t}_w$ are called the extrinsic parameters of the camera. Equivalently, the extrinsic parameters define the position of the camera center and the camera's heading in world coordinate system.

The point q is the image of the point Q on the camera's image plane with metric coordinates ${}^{im}\mathbf{q} = ({}^{im}x, {}^{im}y)^T$. The main property of the camera model is that the relationship between the 3D point Q and its image projection q is linear projective. The relationship between the point Q and its image q can be written as:

$$ s\ {}^{im}\tilde{\mathbf{q}} = \mathbf{P}\ {}^c\tilde{\mathbf{Q}} \tag{4.2} $$

where s is an arbitrary scale factor, $\mathbf{P}$ is a 3×4 matrix called the perspective projection matrix without loss of generality. The focal length of the camera can be arbitrarily taken to 1, then $\mathbf{P}$ can be simply written as:

$$ \mathbf{P} = \begin{bmatrix} \mathbf{I}_{33} & \mathbf{0}_{13} \end{bmatrix} \tag{4.3} $$

In general, the origin of the 2D image pixel coordinate system does not coincide with that of the 2D image metric coordinate system where the z_c axis intersects the image plane. Let (u_0, v_0) be the translation. Therefore, the relationship between the homogeneous coordinates of the image point q in 2D image pixel coordinate system ${}^{ip}\tilde{\mathbf{q}} = ({}^{ip}x, {}^{ip}y, 1)^T$ and 2D metric coordinate system ${}^{im}\tilde{\mathbf{q}} = ({}^{im}x, {}^{im}y, 1)^T$ without distortion can be written as:

$$ {}^{ip}\tilde{\mathbf{q}} = \begin{bmatrix} p_x x + u_0 \\ p_y y + v_0 \\ 1 \end{bmatrix} = \underbrace{\begin{bmatrix} p_x & 0 & u_0 \\ 0 & p_y & v_0 \\ 0 & 0 & 1 \end{bmatrix}}_{\mathbf{K}} {}^{im}\tilde{\mathbf{q}} \tag{4.4} $$

where p_x and p_y correspond respectively to the scale factor (in pixels) along the x and y axis. The matrix $\mathbf{K}$ is called the camera calibration matrix. Note that $\mathbf{K}$ only depends on the intrinsic parameters of the camera.

In conclusion, camera calibration is necessary to determine the extrinsic and intrinsic parameters of the camera. The transformations between the coordinate systems are presented in Figure 4.2. The relationship between the 3D point Q in world coordinate system ${}^{w}\tilde{\mathbf{Q}} = ({}^{w}X, {}^{w}Y, {}^{w}Z, 1)^T$ and its image projection q in 2D pixel coordinate system ${}^{ip}\tilde{\mathbf{q}} = ({}^{ip}x, {}^{ip}y, 1)^T$ can be written as:

$$ {}^{ip}\tilde{\mathbf{q}} \equiv \mathbf{K} \begin{bmatrix} \mathbf{I}_{33} & \mathbf{0}_{13} \end{bmatrix} \begin{bmatrix} {}^{c}\mathbf{R}_{w} & {}^{c}\mathbf{t}_{w} \\ \mathbf{0}_{31} & 1 \end{bmatrix} {}^{w}\tilde{\mathbf{Q}} \tag{4.5} $$

where $\equiv$ is the projective equality, which means the equality up to any non-zero scale factor.

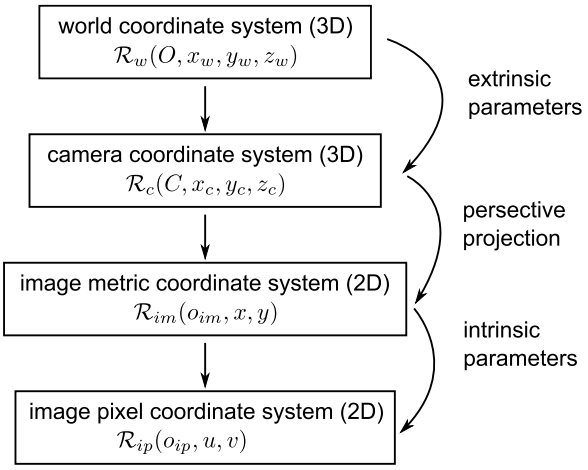

Figure 4.2: Parameters to be determined in camera calibration.

In addition, one must take into account the lens distortion. The transformation of the image point m from meters to pixels can be expressed as:

$$ u = u_0 + p_x x(1 + k_{ud} r^2) \tag{4.6} $$

$$ v = v_0 + p_y y(1 + k_{ud} r^2) \tag{4.7} $$

where r is the radial distance, with $r^2 = x^2 + y^2$. The transformation of the image point m from pixels to meters can be expressed as:

$$ x = (u - u_0)(1 + k_{du} r^2)/p_x \tag{4.8} $$

$$ y = (v - v_0)(1 + k_{du} r^2)/p_y \tag{4.9} $$

where $r^2 = ((u - u_0)/p_x)^2 + ((v - v_0)/p_y)^2$, and k_{du} is defined as the distorted to undistorted distortion parameter, and k_{ud} is defined as the undistorted to distorted distortion parameter.

4.1.3 Calibration of the vision system

As presented in Section 2.2.3, the vision system is composed of two cameras: one is besides the 3D Helmholtz coil pairs, and the other one is on the top, as shown in Figure

4.3a. An endoscope is connected to the side camera instead of a optical lens in order to solve the line of sight problem. The camera calibration matrices composed of the intrinsic parameters of the top and the side cameras ($\mathbf{K}_t$ and $\mathbf{K}_s$) need to be calibrated. The transformation matrices between the two camera coordinate systems and the world coordinate system, as shown in Figure 4.3b need to be determined. The calibration of the vision system is studied as follows with the determination of the calibration matrices, and the transformation matrices between the world coordinate system and the two camera coordinate systems.

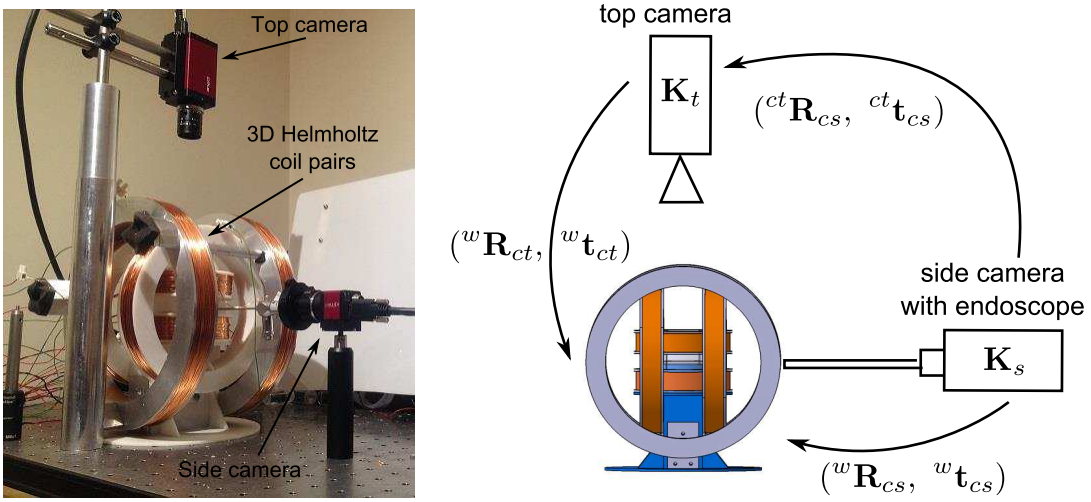

(a) (b)

Figure 4.3: (a) The vision system composed of the top and the side cameras with the 3D Helmholtz coil pairs. (b) Transformation between the world and the camera coordinate systems.

4.1.3.1 Identification of intrinsic parameters

A test pattern with 6×6 dots matrix, as shown in Figure 4.4a, is used to calibrate the intrinsic and extrinsic parameters of the camera. The metric distance between two dots is 4 mm. The origin of the test pattern coordinate system $\mathcal{R}_{tp} = (O_{tp}, x_{tp}, y_{tp}, z_{tp})$ is defined as the center of the dot in the first row and the first column. The x_{tp} axis is in the direction of the column, the y_{tp} axis is in the direction of the row, and the z_{tp} axis is defined as $z_{tp} = x_{tp} \times y_{tp}$, as shown in Figure 4.4a. The positions of the dots in the test pattern coordinate system are known. The positions of the dots in the 2D pixel image coordinate system can be estimated by the tracking function in ViSP. Twelve pictures with different positions of the test pattern are taken by convention to estimate the camera parameters. Figure 4.4 shows the different positions of the test pattern, and for each position, the test pattern coordinate system is calculated by the function of ViSP.

The intrinsic parameters for the top camera are $p_x = 3722.94$, $p_y = 3723.41$, $u_0 = 546.99$, and $v_0 = 452.54$. The distortion is estimated as $k_{ud} = -0.261$ and $k_{du} = 0.265$. Therefore, the calibration matrix without distortion of the top camera $\mathbf{K}_t$ can

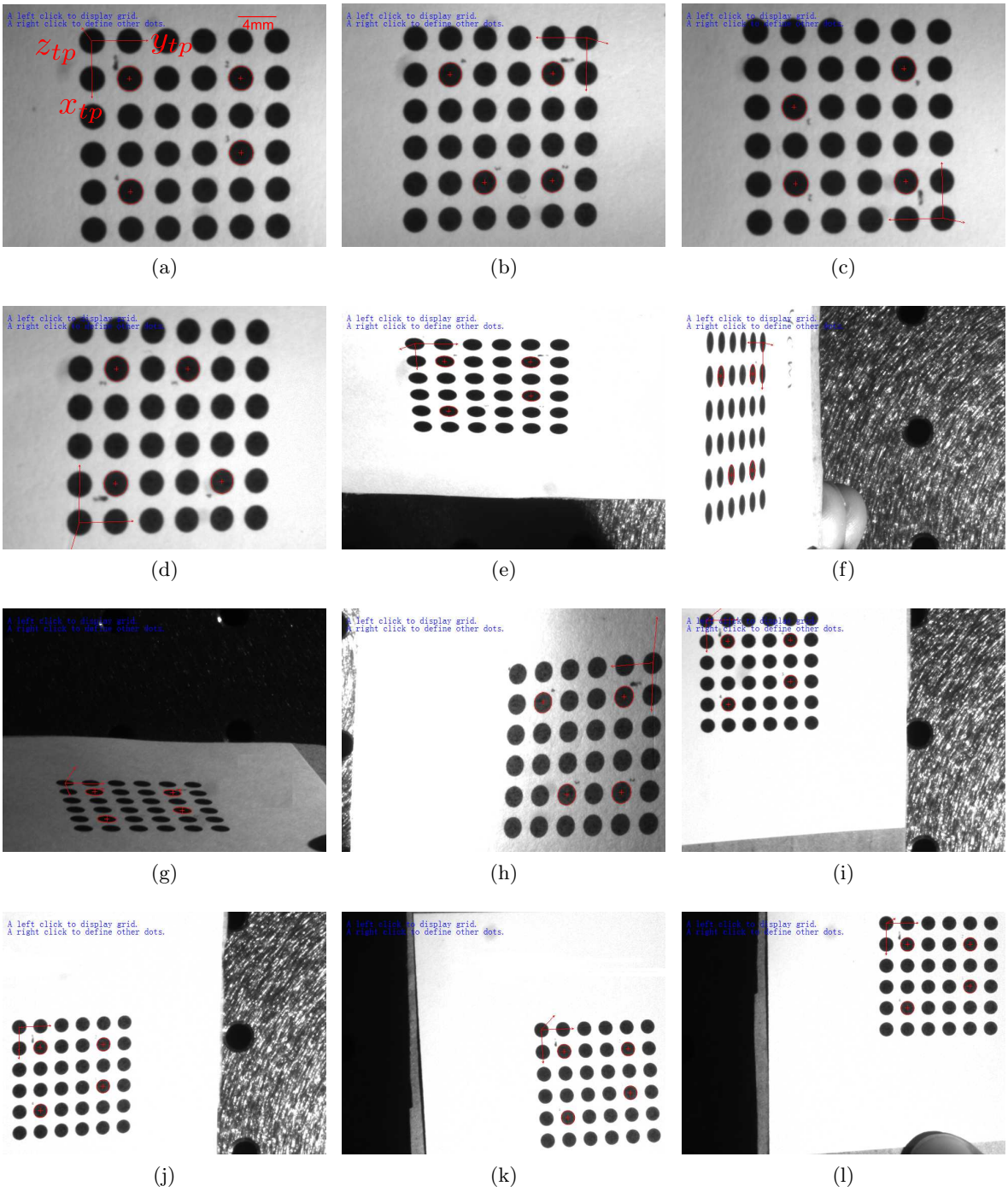

(a) (b) (c)

(d) (e) (f)

(g) (h) (i)

(j) (k) (l)

Figure 4.4: Twelve pictures with different positions of the test pattern are taken to estimate the camera parameters. The test pattern coordinate system for each picture is computed and marked by the function of ViSP.

be written as:

$$\mathbf{K}_t = \begin{bmatrix} 3722.94 & 0 & 546.99 \\ 0 & 3723.41 & 452.54 \\ 0 & 0 & 1 \end{bmatrix} \tag{4.10}$$

The intrinsic parameters for the side camera are $p_x = 751.71$, $p_y = 749.72$, $u_0 = 298.62$, and $v_0 = 208.29$. The distortion is estimated as $k_{ud} = -0.372$ and $k_{du} = 0.414$. Therefore, the calibration matrix without distortion of the side camera $\mathbf{K}_s$ can be written as:

$$\mathbf{K}_s = \begin{bmatrix} 751.71 & 0 & 298.62 \\ 0 & 749.72 & 208.29 \\ 0 & 0 & 1 \end{bmatrix} \tag{4.11}$$

The calibration matrices of the top and the side cameras are then identified. They are used to convert for example the image point of the barycenter of the helical swimmer from the metric image coordinate system to the pixel image coordinate system, and vice versa.

4.1.3.2 Transformation between the camera coordinate systems

Once the relative position of the top and the side camera is fixed, the transformation matrix between the two camera coordinate systems ${}^{ct}\mathbf{M}_{cs}$ should be found. Note that $\mathcal{R}_{ct} = (C_t, x_{ct}, y_{ct}, z_{ct})$ denotes the top camera coordinate system, and $\mathcal{R}_{cs} = (C_s, x_{cs}, y_{cs}, z_{cs})$ denotes the side camera coordinate system.

The test pattern is put at the position where it could be viewed by both cameras, as shown in Figure 4.5a. The images viewed by the top and the side camera are depicted respectively in Figure 4.5b and 4.5c.

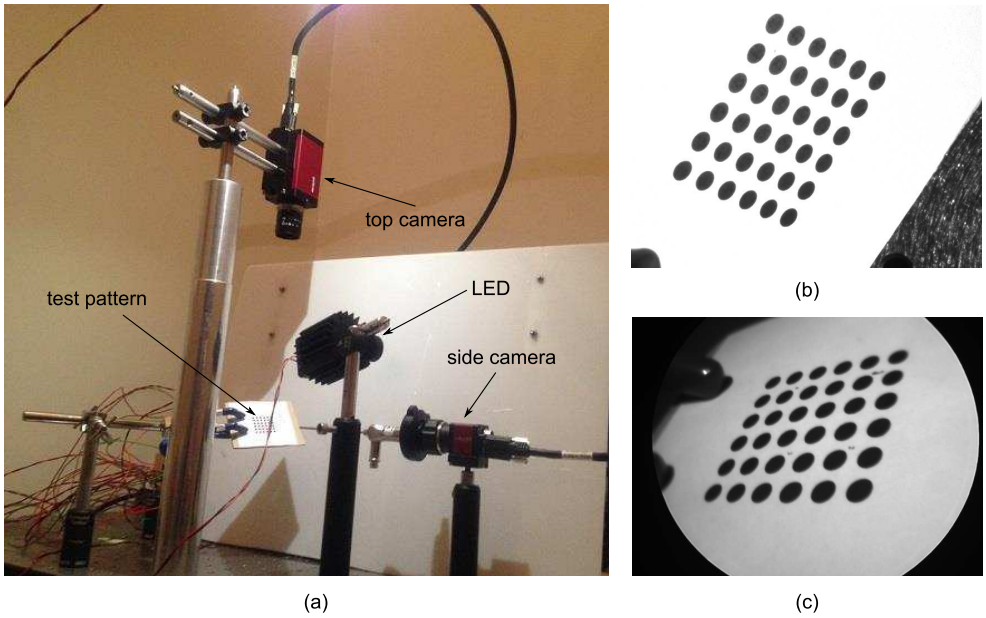

Figure 4.5: (a) Calibration for the determination of the transformation matrix between the two camera coordinate systems. (b) Image viewed by the top camera. (c) Image viewed by the side camera.

The transformation matrices ${}^{ct}\mathbf{M}_{tp}$ and ${}^{cs}\mathbf{M}_{tp}$ from test pattern coordinate system $\mathcal{R}_{tp}$ respectively to the top and the side camera coordinate systems $\mathcal{R}_{ct}$ and $\mathcal{R}_{cs}$ depend on the rotation and the translation matrices between them, with ${}^{ct}\mathbf{M}_{tp} = \begin{bmatrix} {}^{ct}\mathbf{R}_{tp} & {}^{ct}\mathbf{t}_{tp} \\ \mathbf{0}_{31} & 1 \end{bmatrix}$ and ${}^{cs}\mathbf{M}_{tp} = \begin{bmatrix} {}^{cs}\mathbf{R}_{tp} & {}^{cs}\mathbf{t}_{tp} \\ \mathbf{0}_{31} & 1 \end{bmatrix}$. The rotation and translation matrices are shown in Figure 4.6.

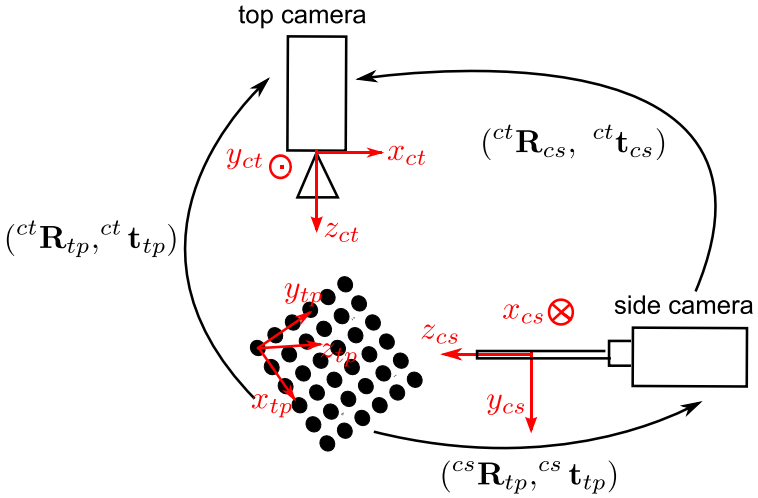

Figure 4.6: Transformation between the two camera coordinate systems.

The relationship between a point Q in camera coordinate systems (${}^{ct}\mathbf{Q}$ in $\mathcal{R}_{ct}$ and ${}^{cs}\mathbf{Q}$ in $\mathcal{R}_{cs}$) and in test pattern coordinate system (${}^{tp}\mathbf{Q}$) can be expressed as:

$$ {}^{ct}\tilde{\mathbf{Q}} = {}^{ct}\mathbf{M}_{tp}\ {}^{tp}\tilde{\mathbf{Q}} \tag{4.12} $$

$$ {}^{cs}\tilde{\mathbf{Q}} = {}^{cs}\mathbf{M}_{tp}\ {}^{tp}\tilde{\mathbf{Q}} \tag{4.13} $$

Therefore, the relationship between the point Q in two camera coordinate systems can be expressed as:

$$ {}^{ct}\tilde{\mathbf{Q}} = \underbrace{{}^{ct}\mathbf{M}_{tp}\ {}^{cs}\mathbf{M}_{tp}^{-1}}_{{}^{ct}\mathbf{M}_{cs}}\ {}^{cs}\tilde{\mathbf{Q}} \tag{4.14} $$

With the images taken by the top and the side camera of the test pattern, the two transformation matrices from the test pattern coordinate system to the two camera coordinate systems are obtained as:

$$ {}^{ct}\mathbf{M}_{tp} = \begin{bmatrix} -0.396 & 0.679 & 0.619 & -0.013 \\ 0.884 & 0.098 & 0.458 & -0.013 \\ 0.250 & 0.728 & -0.639 & 0.242 \\ 0 & 0 & 0 & 1 \end{bmatrix} \tag{4.15} $$

and

$$ {}^{cs}\mathbf{M}_{tp} = \begin{bmatrix} -0.880 & -0.129 & -0.457 & 0.006 \\ 0.224 & 0.736 & -0.639 & -0.011 \\ 0.419 & -0.665 & -0.618 & 0.058 \\ 0 & 0 & 0 & 1 \end{bmatrix} \tag{4.16} $$

Remark that the center of the top camera coordinate system with a lens is estimated on the sensor plane of the top camera. But the center of the side camera coordinate system is not on the sensor plane of the side camera. The center of the side camera coordinate system is shown in Figure 4.6. Then, the transformation matrix ${}^{ct}\mathbf{M}_{cs}$ from the side camera to the top camera coordinate system can be estimated as:

$$ {}^{ct}\mathbf{M}_{cs} = {}^{ct}\mathbf{M}_{tp}\ {}^{cs}\mathbf{M}_{tp}^{-1} = \begin{bmatrix} -0.0220 & 0.0152 & -0.9996 & 0.0448 \\ -0.9995 & -0.0222 & 0.0217 & -0.0084 \\ -0.0219 & 0.9996 & 0.0157 & 0.2518 \\ 0 & 0 & 0 & 1 \end{bmatrix} \tag{4.17} $$

This transformation matrix ${}^{ct}\mathbf{M}_{cs}$ from the side camera to the top camera coordinate system can be approximated as:

$$ {}^{ct}\mathbf{M}_{cs} = {}^{ct}\mathbf{M}_{tp}\ {}^{cs}\mathbf{M}_{tp}^{-1} = \begin{bmatrix} 0 & 0 & -1 & 0.04 \\ -1 & 0 & 0 & -0.01 \\ 0 & 1 & 0 & 0.25 \\ 0 & 0 & 0 & 1 \end{bmatrix} \tag{4.18} $$

The first three columns of this matrix represents the axes of the side camera coordinates expressed in the top camera coordinate system. The last column of this matrix represents the center of the side camera coordinate system expressed in the top camera coordinate system.

4.1.3.3 Transformation between the world and the camera coordinate systems

The world coordinate system $\mathcal{R}_w = (O, x, y, z)$ is defined by the three-orthogonal arranged Helmholtz coil pairs, as presented in Section 2.2.4.2. We remind here that the origin O of the world coordinate system is defined at the center of the Helmholtz coils setup. The x axis is defined as the magnetic field direction when is applied a positive current to the small coil pair. Thus, the x axis is in the direction of the axis of the small coil pair, which can be shown in Figure 4.7. Similarly, the y axis is defined as the magnetic field direction when is applied a positive current to the medium coil pair, and the z axis is defined as the magnetic field direction when is applied a positive current to the big coil pair.

The rotation matrix ${}^{w}\mathbf{R}_{ct}$ from the top camera coordinate system $\mathcal{R}_{ct}$ to the world coordinate system $\mathcal{R}_w$ can be written by expressing the three axes of the top camera system in the world coordinates, which is approximately:

$$ {}^{w}\mathbf{R}_{ct} = \begin{bmatrix} 0 & 0 & -1 \\ 1 & 0 & 0 \\ 0 & -1 & 0 \end{bmatrix} \tag{4.19} $$

The Helmholtz coil pairs system is placed where the optical center of the top camera projects on the origin of the world coordinate system. The translation matrix ${}^{w}\mathbf{t}_{ct}$ from $\mathcal{R}_{ct}$ to $\mathcal{R}_w$ can be expressed by the coordinates of the center C_t in world coordinate system, which is approximately: ${}^{w}\mathbf{t}_{ct} = (0.25, 0, 0)^T$.

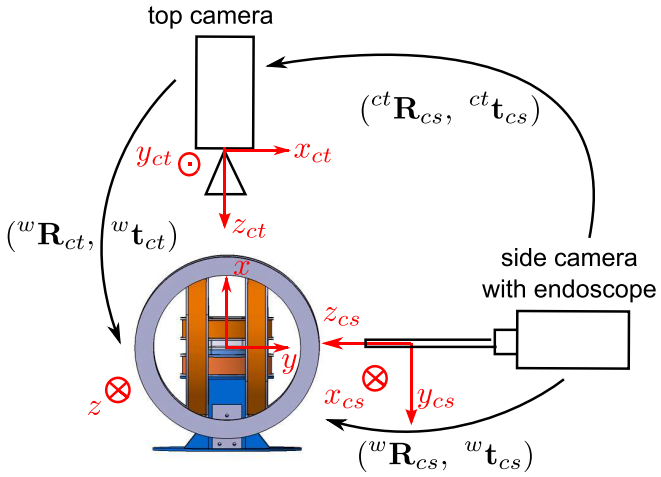

Figure 4.7: Transformation between the world and the camera coordinate systems.

The two matrices can be verified by the calibration of ViSP using a test pattern with the origin of the test pattern coincident with the center of the Helmholtz coil pairs setup.

In conclusion, the transformation matrix ${}^{w}\mathbf{M}_{ct}$ from the top camera coordinate system $\mathcal{R}_{ct}$ to the world coordinate system $\mathcal{R}_{w}$ can be expressed as:

$${}^{w}\mathbf{M}_{ct} = \begin{bmatrix} 0 & 0 & -1 & 0.25 \\ 1 & 0 & 0 & 0 \\ 0 & -1 & 0 & 0 \\ 0 & 0 & 0 & 1 \end{bmatrix} \tag{4.20}$$

The transformation matrix ${}^{w}\mathbf{M}_{cs}$ from the side camera coordinate system $\mathcal{R}_{cs}$ to the world coordinate system $\mathcal{R}_{w}$ can be expressed as:

$${}^{w}\mathbf{M}_{cs} = {}^{w}\mathbf{M}_{ct}\ {}^{ct}\mathbf{M}_{cs} = \begin{bmatrix} 0 & -1 & 0 & 0 \\ 0 & 0 & -1 & 0.04 \\ 1 & 0 & 0 & 0.01 \\ 0 & 0 & 0 & 1 \end{bmatrix} \tag{4.21}$$

All the transformation matrices are identified. The vision system with two cameras is therefore calibrated. The calibration matrices of the two cameras and the transformation matrices between the world and the camera coordinate systems are used for the pose estimation of the helical swimmer.

This basic algorithm allows to estimate the parameters of the cameras. This estimation method is not perfect. However, the highly precise camera calibration is very expensive in time, and it is not the objective of this thesis.

4.2 Visual servo control for the 3D orientation

An open-loop steering control of the SHM is presented in Section 3.4. In this section, a visual servo control of the magnetic field to achieve the steering of the SHM to any target orientation in the 3D space is studied. In order to realize the control, the real-time orientation of the SHM in the 3D space should be at first estimated.

4.2.1 Real-time orientation estimation in the 3D space

The orientation of the SHM is considered as the axis of the SHM in the 3D space. A method to estimate the normal vector of the SHM axis $\overrightarrow{n}$ in world coordinate system $\mathbf{n}$ is introduced here, using the axes that are tracked in the two images taken with the top and the side cameras with known calibration and poses. Recall that $\mathcal{R}_{ct} = (C_t, x_{ct}, y_{ct}, z_{ct})$ depicts the coordinate system of the top camera, $\mathcal{R}_{imt} = (O_{imt}, x_{imt}, y_{imt})$ depicts the undistorted metric image coordinate system of the top camera, and $\mathcal{R}_{ipt} = (O_{ipt}, u_{ipt}, v_{ipt})$ depicts the undistorted pixel image coordinate system of the top camera. Similarly, $\mathcal{R}_{cs} = (C_s, x_{cs}, y_{cs}, z_{cs})$, $\mathcal{R}_{ims} = (O_{ims}, x_{ims}, y_{ims})$ and $\mathcal{R}_{ips} = (O_{ips}, u_{ips}, v_{ips})$ depict respectively the coordinate system, the undistorted metric image coordinate system, and the undistorted pixel image coordinate system of the side camera. $\mathcal{R}_w = (O, x, y, z)$ depicts the world coordinate system, which is defined in section 4.1.3.3.

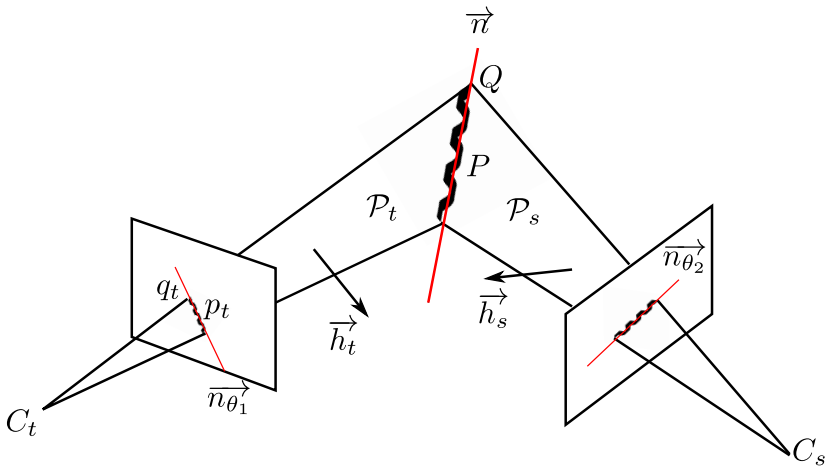

Figure 4.8: Determination of the axis of the SHM in the world coordinate system.

The projection center of the top camera C_t and the axis of the SHM defines a plane $(C_t, \overrightarrow{n})$ named as $\mathcal{P}_t$, as shown in Figure 4.8. The equation of the plane $\mathcal{P}_t$ in the top camera coordinate system $\mathcal{R}_{ct}$ can be written as:

$$h_{tx}x + h_{ty}y + h_{tz}z + d = 0 \tag{4.22}$$

where ${}^{ct}\mathbf{h}_t = (h_{tx}, h_{ty}, h_{tz})^T$ is the unit normal vector of the plane $\mathcal{P}_t$. As $\mathcal{P}_t$ passes through the origin C_t, then we have $d = 0$.

The point P, with ${}^{ct}\mathbf{P} = ({}^{ct}X, {}^{ct}Y, {}^{ct}Z)^T$ in the top camera coordinate system, is a point on the axis of the SHM, for example the barycenter of the SHM. Thus, P is in the plane $\mathcal{P}_t$. Therefore, we have:

$$h_{tx}\,{}^{ct}X + h_{ty}\,{}^{ct}Y + h_{tz}\,{}^{ct}Z = 0 \tag{4.23}$$

Then,

$$h_{tx}\frac{{}^{ct}X}{{}^{ct}Z} + h_{ty}\frac{{}^{ct}Y}{{}^{ct}Z} + h_{tz} = 0 \tag{4.24}$$

By definition, the point p_t with ${}^{im}\mathbf{p}_t = \left(\frac{{}^{ct}X}{{}^{ct}Z}, \frac{{}^{ct}Y}{{}^{ct}Z}\right)^T$ is the image of the point P in the metric image plane of the top camera. ${}^{im}\tilde{\mathbf{p}}_t = \left(\frac{{}^{ct}X}{{}^{ct}Z}, \frac{{}^{ct}Y}{{}^{ct}Z}, 1\right)^T$ is its homogeneous coordinates. We can write the relationship under the matrix form:

$$ {}^{ct}\mathbf{h}_t^T \ {}^{imt}\tilde{\mathbf{p}}_t = 0 \tag{4.25}$$

Then we multiply by $\mathbf{K}_t^{-1}\mathbf{K}_t$, which is the identity matrix $\mathbf{I}$, with $\mathbf{K}_t$ the intrinsic parameters matrix of the top camera.

$$ {}^{ct}\mathbf{h}_t^T\mathbf{K}_t^{-1}(\mathbf{K}_t \ {}^{imt}\tilde{\mathbf{p}}_t) = 0 \tag{4.26}$$

From the relationship between the metric coordinates and the pixel coordinates in the image plane, we have:

$$ {}^{ct}\mathbf{h}_t^T\mathbf{K}_t^{-1} \ {}^{ipt}\tilde{\mathbf{p}}_t = 0 \tag{4.27}$$

We define $\mathbf{K}_t^{-T} = (\mathbf{K}_t^{-1})^T = (\mathbf{K}_t^T)^{-1}$, then

$$ (\mathbf{K}_t^{-T} \ {}^{ct}\mathbf{h}_t)^T \ {}^{ipt}\tilde{\mathbf{p}}_t = 0 \tag{4.28}$$

Let us introduce

$$ {}^{ipt}\mathbf{h}_t = \frac{\mathbf{K}_t^{-T} \ {}^{ct}\mathbf{h}_t}{\| \ \mathbf{K}_t^{-T} \ {}^{ct}\mathbf{h}_t \ \|} \tag{4.29}$$

Then, we have

$$ {}^{ipt}\mathbf{h}_t^T \ {}^{ipt}\tilde{\mathbf{p}}_t = 0 \tag{4.30}$$

The point p_t, which is the image of the point P (barycenter of the SHM), can be tracked in the image plane by ViSP, as presented in Section 2.4.2. The coordinates of p_t in the image pixel plane can be expressed as ${}^{ipt}\tilde{\mathbf{p}}_t = (u_p, v_p, 1)^T$. Another point q_t, which is the image of a point Q on the axis of the SHM, can be obtained from the barycenter and the axis orientation of the SHM. This point in the top camera image plane can be expressed as ${}^{ipt}\tilde{\mathbf{q}}_t = (u_q, v_q, 1)^T$. Then ${}^{ipt}\mathbf{h}_t^T = (h_{ipx}, h_{ipy}, h_{ipz})^T$ can be calculated from these two points p_t and q_t, with:

$$ \begin{cases} h_{ipx}u_p + h_{ipy}v_p + h_{ipz} = 0 \\ h_{ipx}u_q + h_{ipy}v_q + h_{ipz} = 0 \\ h_{ipx}^2 + h_{ipy}^2 + h_{ipz}^2 = 1 \end{cases} \tag{4.31}$$

The unit normal vector of the plane $\mathcal{P}_t$ written in the top camera coordinate system $\mathcal{R}_{ct}$ can be obtained from the inverse of (4.29):

$$ {}^{ct}\mathbf{h}_t = \frac{\mathbf{K}_t^T \ {}^{ipt}\mathbf{h}_t}{\| \ \mathbf{K}_t^T \ {}^{ipt}\mathbf{h}_t \ \|} \tag{4.32}$$

By the same method, the unit normal vector $\overrightarrow{h_s}$ of the plane $\mathcal{P}_s$ defined by the projection center C_s of the side camera and the axis of the SHM $\overrightarrow{n}$ written in the side camera coordinate system $\mathcal{R}_{cs}$ can be obtained by:

$$ {}^{cs}\mathbf{h}_s = \frac{\mathbf{K}_s^T \ {}^{ips}\mathbf{h}_s}{\| \ \mathbf{K}_s^T \ {}^{ips}\mathbf{h}_s \ \|} \tag{4.33}$$

where $\mathbf{K}_t$ is the intrinsic parameters matrix of the top camera, and ${}^{ips}\mathbf{h}_s$ is calculated from two points on the axis of the SHM in the image of the side camera.

The axis of the SHM is the intersection of the two planes $\mathcal{P}_t$ and $\mathcal{P}_s$. It then can be calculated by the vector product of the two normal vectors $\overrightarrow{h_t}$ and $\overrightarrow{h_s}$ of the two planes. Therefore, the axis of the SHM $\overrightarrow{n}$ in the top camera coordinate system ${}^{ct}\mathbf{n}$ can be expressed as:

$$ {}^{ct}\mathbf{n} = {}^{ct}\mathbf{h}_t \times {}^{ct}\mathbf{h}_s = {}^{ct}\mathbf{h}_t \times ({}^{ct}\mathbf{R}_{cs}\ {}^{cs}\mathbf{h}_s) \tag{4.34} $$

where ${}^{ct}\mathbf{R}_{cs}$ is the rotation matrix from the side camera coordinate system $\mathcal{R}_{cs}$ to the top camera coordinate system $\mathcal{R}_{ct}$, which is given in section 4.1.3.2. Then, the normal vector of the SHM's axis in 3D world coordinate system can be written as:

$$ \mathbf{n} = {}^{w}\mathbf{R}_{ct}\ {}^{ct}\mathbf{n} \tag{4.35} $$

where ${}^{w}\mathbf{R}_{ct}$ is the rotation matrix from the top camera coordinate system $\mathcal{R}_{ct}$ to the world coordinate system $\mathcal{R}_w$, which is given in section 4.1.3.3. The orientation of the SHM is considered as $\mathbf{n}$ as well.

Once the orientation of the SHM in the 3D space $\mathbf{n} = (n_x, n_y, n_z)^T$ is known, the direction angle θ_d and the inclination angle θ_i of the SHM previously defined in Section 3.4.1 can be easily obtained by:

$$ \theta_d = \arctan\left(\frac{n_y}{n_z}\right) \tag{4.36} $$

$$ \theta_i = \arctan\left(\frac{n_x}{\sqrt{n_y^2 + n_z^2}}\right) \tag{4.37} $$

The direction and inclination angles are used to analyse the orientation steering of the helical swimmer, and the direction angle is used as an intermediate control variable for the 2D path following task.

4.2.2 Control law design

In general, the control variable of the helical swimmer system is the magnetic field $\mathbf{B}$. In our system, the control variables are the output voltages of the PCI card, which depends on the required magnetic field $\mathbf{B}$. A control law of the magnetic field $\mathbf{B}$ to achieve the 3D orientation steering of the SHM is designed as follows.

The normal vector of the SHM's real-time orientation is noted as $\overrightarrow{n}$. The magnetization of the SHM is $\overrightarrow{M}$. The magnetic field is $\overrightarrow{B}$. The magnetic torque $\overrightarrow{\tau}$ exerted on the SHM can be expressed as :

$$ \overrightarrow{\tau} = \overrightarrow{M} \times \overrightarrow{B} \tag{4.38} $$

The magnetic field $\overrightarrow{B}$ can be decomposed in the directions perpendicular to $\mathbf{n}$, $\overrightarrow{B_{\perp\mathbf{n}}}$, and colinear to $\mathbf{n}$, $\overrightarrow{B_{\parallel\mathbf{n}}}$:

$$ \overrightarrow{B} = \overrightarrow{B_{\perp\mathbf{n}}} + \overrightarrow{B_{\parallel\mathbf{n}}} \tag{4.39} $$

Therefore, the magnetic torque exerted on the SHM can then be written as:

$$\overrightarrow{\tau} = \underbrace{\overrightarrow{M} \times \overrightarrow{B_{\perp \mathbf{n}}}}_{\overrightarrow{\tau_{\parallel \mathbf{n}}}} + \underbrace{\overrightarrow{M} \times \overrightarrow{B_{\parallel \mathbf{n}}}}_{\overrightarrow{\tau_{\perp \mathbf{n}}}} \tag{4.40}$$

As the magnetization of the SHM is always perpendicular to its own axis $\overrightarrow{n}$, the magnetic torque can also be decomposed in the directions perpendicular and parallel to $\overrightarrow{n}$. The torque $\overrightarrow{\tau_{\parallel \mathbf{n}}}$ is the magnetic torque colinear to $\overrightarrow{n}$, which makes the SHM rotate around its current axis $\overrightarrow{n}$. The torque $\overrightarrow{\tau_{\perp \mathbf{n}}}$ is the magnetic torque perpendicular to $\overrightarrow{n}$, which makes the SHM rotate around $\overrightarrow{M} \times \overrightarrow{n}$. That means the steering of the SHM can be managed by controlling these two torques.

4.2.2.1 Self-rotation control

The magnetic field $\overrightarrow{B_{\perp \mathbf{n}}}$ which makes the SHM rotate around its real-time axis $\mathbf{n}$, with $\mathbf{n} = (n_x, n_y, n_z)^T$ in the world coordinate system, depends on $\mathbf{n}$, the frequency, and the time.

$$\mathbf{B}_{\perp \mathbf{n}} = f(\mathbf{n}, f, t) \tag{4.41}$$

where $\mathbf{B}_{\perp \mathbf{n}}$ is $\overrightarrow{B_{\perp \mathbf{n}}}$ expressed in the world coordinate system. It can be expressed in matrix form as (cf Section 2.2.4.4):

$$\mathbf{B}_{\perp \mathbf{n}} = \frac{B_0 \cos(2\pi f t)}{\|\mathbf{u}\|} \begin{bmatrix} n_y \\ -n_x \\ 0 \end{bmatrix} + \frac{B_0 \sin(2\pi f t)}{\|\mathbf{v}\|} \begin{bmatrix} n_x n_z \\ n_y n_z \\ -n_x^2 - n_y^2 \end{bmatrix} \tag{4.42}$$

with $\|\mathbf{u}\| = \sqrt{n_y^2 + n_x^2}$ and $\|\mathbf{v}\| = \sqrt{(n_x n_z)^2 + (n_y n_z)^2 + (-n_x^2 - n_y^2)^2}$. B_0 is the magnetic flux density at the center of the Helmholtz coil pairs, which depends on the output voltage of the PCI card (cf Section 2.2.4.1).

4.2.2.2 Steering control

The magnetic field parallel to the axis of the SHM $\overrightarrow{B_{\parallel \mathbf{n}}}$ creates a torque which is not in its axis direction $\overrightarrow{n}$. Therefore, it changes the direction of the axis of the SHM. That means that the magnetic field $\overrightarrow{B_{\parallel \mathbf{n}}}$ contributes to the steering. The normal vector of the target direction of the SHM is noted as $\overrightarrow{n}^*$, which is expressed as $\mathbf{n}^*$ in the world coordinate system. In the case of open-loop control, we choose $\overrightarrow{B} = \overrightarrow{B_{\perp \mathbf{n}^*}}$ and wait, because the magnetization $\overrightarrow{M}$ tends naturally to align with $\overrightarrow{B}$. However, this is not compatible with the self-rotation. Indeed, for keeping the SHM rotating at a known frequency, the magnetic field must satisfy (4.42). As shown in Section 3.4, the SHM can not steer to all the target directions $\overrightarrow{n}^*$ in the 3D space. We need to properly define a $\overrightarrow{B_{\parallel \mathbf{n}}}$.

Here, the error between the normal vector of the SHM's real-time direction and the normal vector of the target direction is defined as the sine of the angle between them: $\sin(\mathbf{n}, \mathbf{n}^*)$. It is equivalent to $\| \mathbf{n} \times \mathbf{n}^* \|$, because $\mathbf{n}$ and $\mathbf{n}^*$ are unit vectors. $\mathbf{n} \times \mathbf{n}^*$ is known as the geodesic error. It defines the shortest path on the unit sphere from $\mathbf{n}$ to $\mathbf{n}^*$. Let us define a control proportional to this error. As shown in Figure 4.9, the direction of $\overrightarrow{B_{\parallel \mathbf{n}}}$ depends on the projection of the magnetic field $\overrightarrow{B_{\perp \mathbf{n}}}$, which contributes to propelling the SHM around its axis, on the target direction. If this projection is

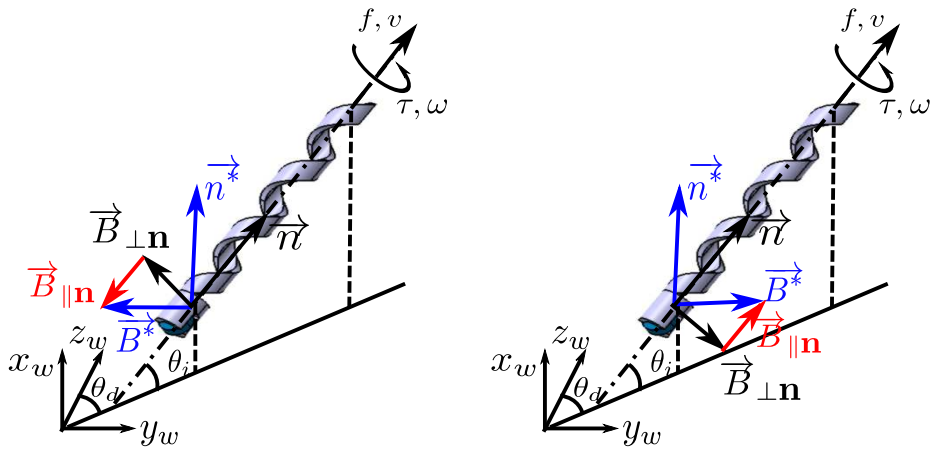

(a) $\mathbf{B}_{\perp\mathbf{n}} \cdot \mathbf{n}^* > 0$ (b) $\mathbf{B}_{\perp\mathbf{n}} \cdot \mathbf{n}^* < 0$

Figure 4.9: Modelling of the magnetic field for SHM steering with the projection of $\mathbf{B}_{\perp\mathbf{n}}$ on the target direction of the SHM $\mathbf{n}^*$ (a) along $\mathbf{n}^*$, and (b) along $-\mathbf{n}^*$.

positive $\overrightarrow{B_{\perp\mathbf{n}}} \cdot \overrightarrow{n}^* > 0$, the magnetic field $\overrightarrow{B_{\parallel\mathbf{n}}}$ which contributes to the steering should be in the direction of $-\overrightarrow{n}$. If this projection is negative, $\overrightarrow{B_{\parallel\mathbf{n}}}$ should be in the same direction as $+\overrightarrow{n}$. Therefore, $\overrightarrow{B_{\parallel\mathbf{n}}}$ in the world coordinate system $\mathbf{B}_{\parallel\mathbf{n}}$ can be expressed as:

$$\mathbf{B}_{\parallel\mathbf{n}} = -\text{sign}(\mathbf{B}_{\perp\mathbf{n}} \cdot \mathbf{n}^*) \cdot \lambda \parallel \mathbf{n} \times \mathbf{n}^* \parallel \mathbf{n} \tag{4.43}$$

with λ the control parameter.

In conclusion, the block-diagram of the visual servo control of the SHM orientation in the 3D space is depicted in Figure 4.10. The input of the system is the target orientation $\mathbf{n}^*$ of the SHM. The 3D axis of the SHM $\mathbf{n} = (n_x, n_y, n_z)^T$ in the world coordinate system can be constructed from the real-time tracking on the images obtained with the top and the side cameras. The control law of the magnetic field to steer a SHM at the target orientation $\mathbf{n}^*$ in the 3D space can be written as:

$$\mathbf{B} = \underbrace{\frac{B_0 \cos(2\pi f t)}{\|\mathbf{u}\|} \begin{bmatrix} n_y \\ -n_x \\ 0 \end{bmatrix} + \frac{B_0 \sin(2\pi f t)}{\|\mathbf{v}\|} \begin{bmatrix} n_x n_z \\ n_y n_z \\ -n_x^2 - n_y^2 \end{bmatrix}}_{\mathbf{B}_{\perp\mathbf{n}}}$$
$$\underbrace{-\text{sign}(\mathbf{B}_{\perp\mathbf{n}} \cdot \mathbf{n}^*) \cdot \lambda \parallel \mathbf{n} \times \mathbf{n}^* \parallel \begin{bmatrix} n_x \\ n_y \\ n_z \end{bmatrix}}_{\mathbf{B}_{\parallel\mathbf{n}}} \tag{4.44}$$

where B_0 is the magnetic flux density generated in the center of the workspace, f is the frequency of the rotation, $\|\mathbf{u}\| = \sqrt{n_y^2 + n_x^2}$, $\|\mathbf{v}\| = \sqrt{(n_x n_z)^2 + (n_y n_z)^2 + (-n_x^2 - n_y^2)^2}$, and λ is the control parameter.

In our system, the magnetic field is controlled by the output voltages of PCI card to the three Helmholtz coil pairs. According to (2.10), the output voltages (U_s, U_m, U_b)

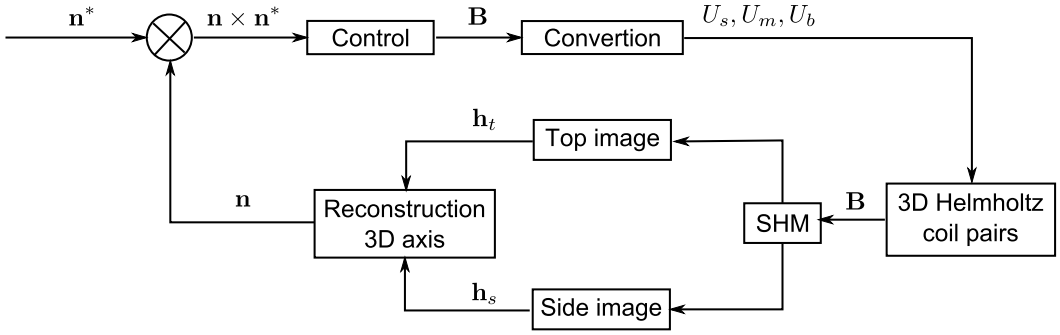

Figure 4.10: Block-diagram of the visual servo control of the SHM orientation in the 3D space.

can be expressed as:

$$\begin{bmatrix} U_s \\ U_m \\ U_b \end{bmatrix} = \frac{\cos(2\pi ft)}{\|\mathbf{u}\|} \begin{bmatrix} U_x n_y \\ -U_y n_x \\ 0 \end{bmatrix} + \frac{\sin(2\pi ft)}{\|\mathbf{v}\|} \begin{bmatrix} U_x n_x n_z \\ U_y n_y n_z \\ -U_z(n_x^2 + n_y^2) \end{bmatrix} - \text{sign}(\mathbf{B}_{\perp \mathbf{n}} \cdot \mathbf{n}^*) \cdot \lambda_U \parallel \mathbf{n} \times \mathbf{n}^* \parallel \begin{bmatrix} n_x \\ U_y/U_x n_y \\ U_z/U_x n_z \end{bmatrix} \tag{4.45}$$

where λ_U is the control parameter for the output voltage. U_x, U_y, and U_z are respectively the output voltage from the PCI card to the small, medium, and big coils to generate a magnetic field of amplitude B_0. The values are given in Table 2.6.

According to our knowledge, the control law of the magnetic field for the closed-loop control of the orientation steering of helical swimmers is established for the first time.

4.2.3 Results

The results of the visual servo control of the SHM orientation in the 3D space are presented in this section. First, the estimation method of the orientation of the SHM is validated in the 3D space. Then, the control parameter λ_U is determined. At last, the visual servo control of SHM orientation steering is studied with different control angles.

4.2.3.1 Real-time axis estimation

In order to verify the method of the reconstruction of the axis of the SHM in the 3D space, the SHM is tracked in an open-loop orientation control. Here, one example of input angles for the open-loop control is a direction angle of $\theta_d = 60°$ and an inclination angle of $\theta_i = 60°$. Then, the 3D orientation should be calculated according to the barycenter tracked on the two images, to deduce the real-time direction and inclination angles, and compare with the input direction and inclination angles.

Figure 4.11 presents SHM1-mh8 tracked by the top and the side cameras during the open-loop orientation control. The SHM is tracked in both images. The axes of the SHM are estimated and marked with red lines. With the intrinsic parameters of the

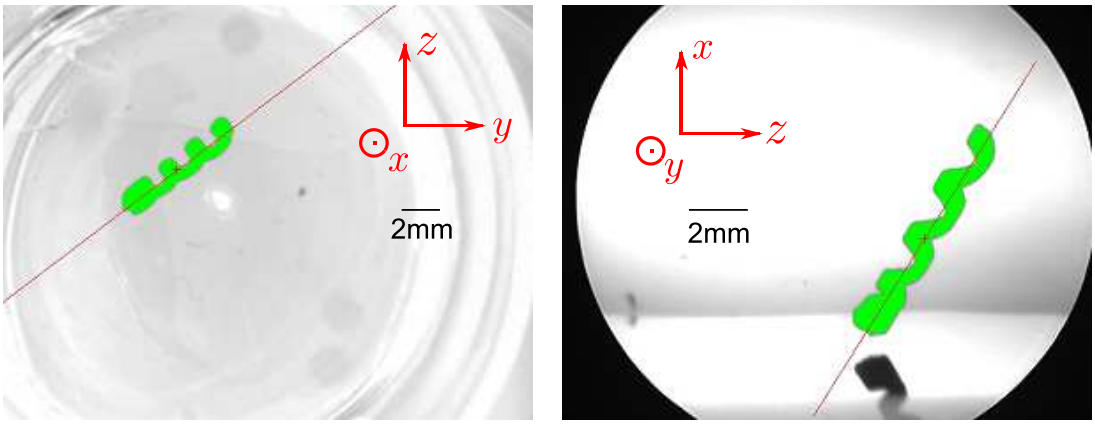

(a) top view (b) side view

Figure 4.11: SHM1-mh8 tracked from (a) the top and (b) the side cameras for a open-loop orientation control at the direction angle $\theta_d = 60°$ and the inclination angle $\theta_i = 60°$.

two cameras and the transformation matrices between the two cameras and the world coordinate system, the orientation of the SHM at instant t in 3D world coordinate system is estimated as:

$$\mathbf{n} = (0.8758, 0.4150, 0.2466)^T \tag{4.46}$$

According to (4.36) and (4.37), the direction angle θ_d and the inclination angle θ_i of the SHM are deduced as $\theta_d = 59.3°$ and $\theta_i = 61.1°$. The errors for the direction angle and inclination angle are estimated respectively as 1.2% and 1.8%. These errors are acceptable for the orientation steering study. The method of the estimation of the orientation of the SHM in the 3D space from the axes tracked in the two images taken with the top and the side cameras with known calibrations is then validated.

4.2.3.2 Determination of the control parameter

The control parameter λ_U should be determined. The output voltage for the big coils is limited to 3 V (cf Section 2.2.4.1). The maximal error between the real-time axis of the SHM and the target axis is $\| \mathbf{n} \times \mathbf{n}^* \| = 1$, because both $\mathbf{n}$ and $\mathbf{n}^*$ are unit vectors. Therefore, according to (4.45), the control parameter should not be higher than 3. Consequently, we compare only the visual servo control of the orientation of the SHM with the control parameter under three.

The control parameter is chosen by the performance of the visual servo control of the direction angle of SHM1-mh8. The direction angle is controlled from 0° to 60° by a step function, with the inclination angle kept at 40°. The rotation frequency is 2 Hz. Figure 4.12a depicts the responses of the direction angle calculated by the real-time estimation to the same step function with different control parameters $\lambda_U = 1, 2, 3$. The control parameter is chosen as 2, because of the response time and reasonable overshooting.

The inclination angle of SHM1-mh8 is also monitored. Figure 4.12b depicts the real-time inclination angle of SHM1-mh8. We observe that there is an impulse of the

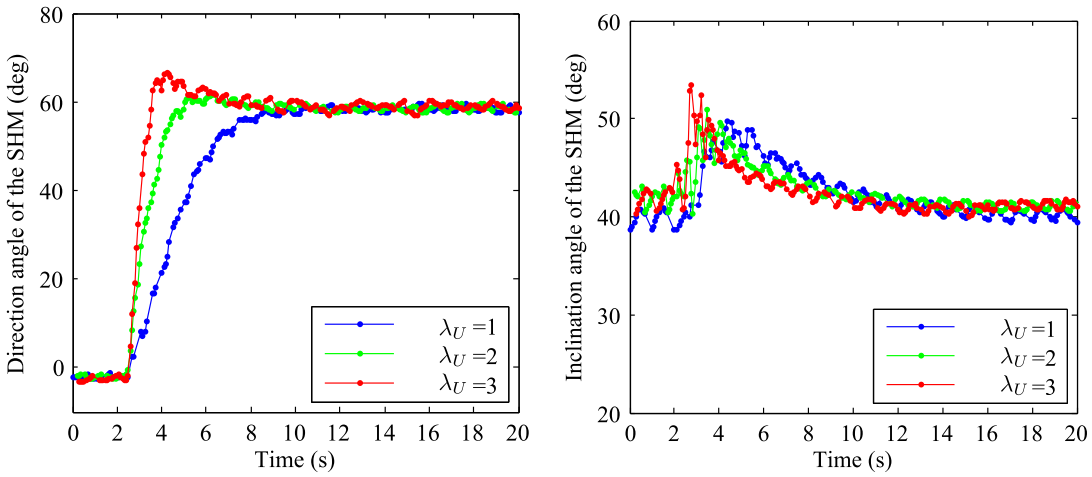

Figure 4.12: Responses of the real-time (a) direction angle and (b) inclination angle of SHM1-mh8 to the same step function of direction angle control with different control parameters $\lambda_U = 1, 2, 3$.

inclination angle, although the control is only on direction angle. The inclination angle increases and then decreases to the initial value. The inclination angle increases more with higher control parameter, because the magnetic torque exerted on SHM1-mh8 is higher. Remark that the oscillation of the response angle of the axis of the SHM is due to the unsymmetry of the helix geometry.

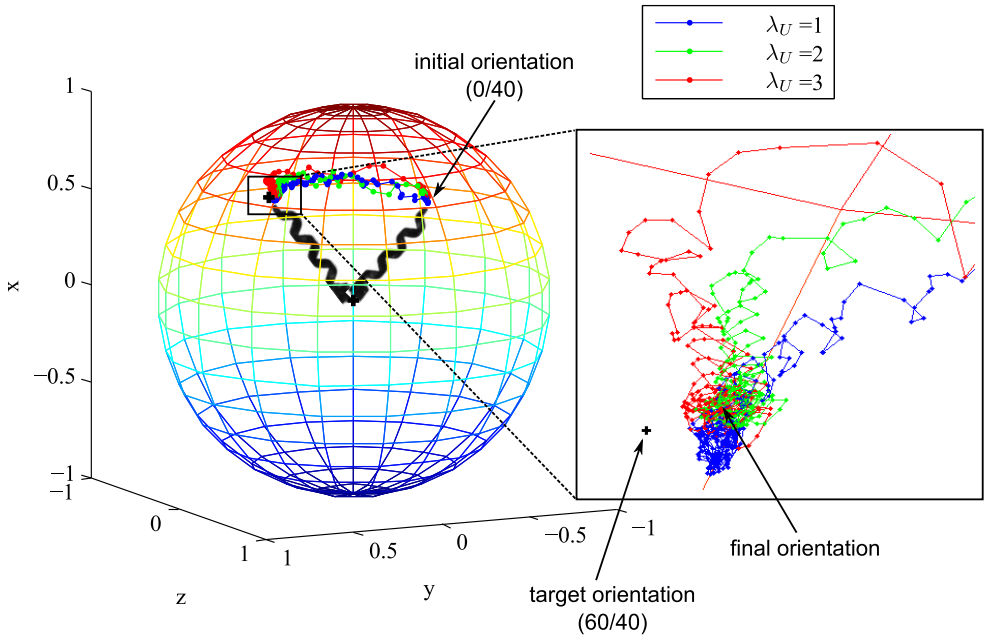

Figure 4.13: Trajectories of SHM1-mh8 for the visual servo control of the direction angle with different control parameters on an unit sphere.

The trajectory of the visual servo control of the direction angle of the SHM with

different control parameters is traced in Figure 4.13. The movements are described in the reference frame relative to the center of the head of SHM1-mh8. The trajectory of the end point of SHM1-mh8's tail is thus traced on an unit sphere, with the center defined as the center of SHM1-mh8's head. There are static errors between the target orientation and the final orientation of the SHM1-mh8. These errors are the same for the different parameters, and are about $-2°$. That is about 3%. These errors are due to the calibration of the cameras.

Once the control parameter is chosen, the direction angle control with more command angles can be tested in the following experiments.

4.2.3.3 Visual servo control of different direction angles

The visual servo control of the direction angle with chosen control parameter $\lambda_U = 2$ is firstly validated with a zero angle command. It means that a visual servo control of the direction angle without initial error is tested. The direction angle of SHM1-mh8 does not change. SHM1-mh8 keeps going in the same direction. The visual servo control of direction angle with small angle command is tested with $5°$. The angular error between the target direction angle and the final direction angle of SHM1-mh8 after the visual servo control of the direction angle with $5°$ is shown in Figure 4.14. We can see that the visual servo control is sensitive to small angle control such as $5°$.

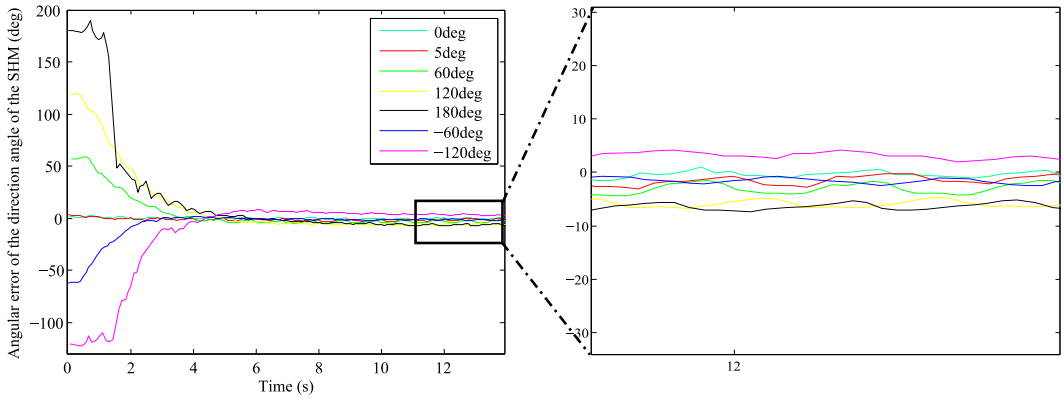

Figure 4.14: Angular error of the visual servo control of the direction angle of SHM1-mh8.

Later, the visual servo control is tested with target angles that are every $60°$ in a turn. They are $60°$, $120°$, $180°$, $-120°$, and $-60°$. All these visual servo control of the direction angle are with the same inclination angle of $40°$. It means that SHM1-mh8 can steer at any direction in the horizontal plane with $40°$ of inclination angle. The angular errors between the target direction angle and the final direction angle of SHM1-mh8 are shown in Figure 4.14. These errors vary from $-6°$ to $3°$. The desired $\mathbf{n}^*$ is given in absolute value. This error can be removed by computing $\mathbf{n}^*$ from a pair of desired orientation of the SHM taken by the cameras.

The trajectories of the end of SHM1-mh8 for the visual servo control of different direction angles with initial direction angle of $0°$ and inclination angle of $40°$ on an unit sphere are shown in Figure 4.15. Remark that for the visual servo control of

direction angles with negative command angles, such as $-60°$ and $-120°$, the inclination decreases and then increases during the control. Reversely, for the visual servo control of direction angles with positive command angles, the inclination increases and then decreases during the control, which is shown in Figure 4.12b. Up to disturbance, the

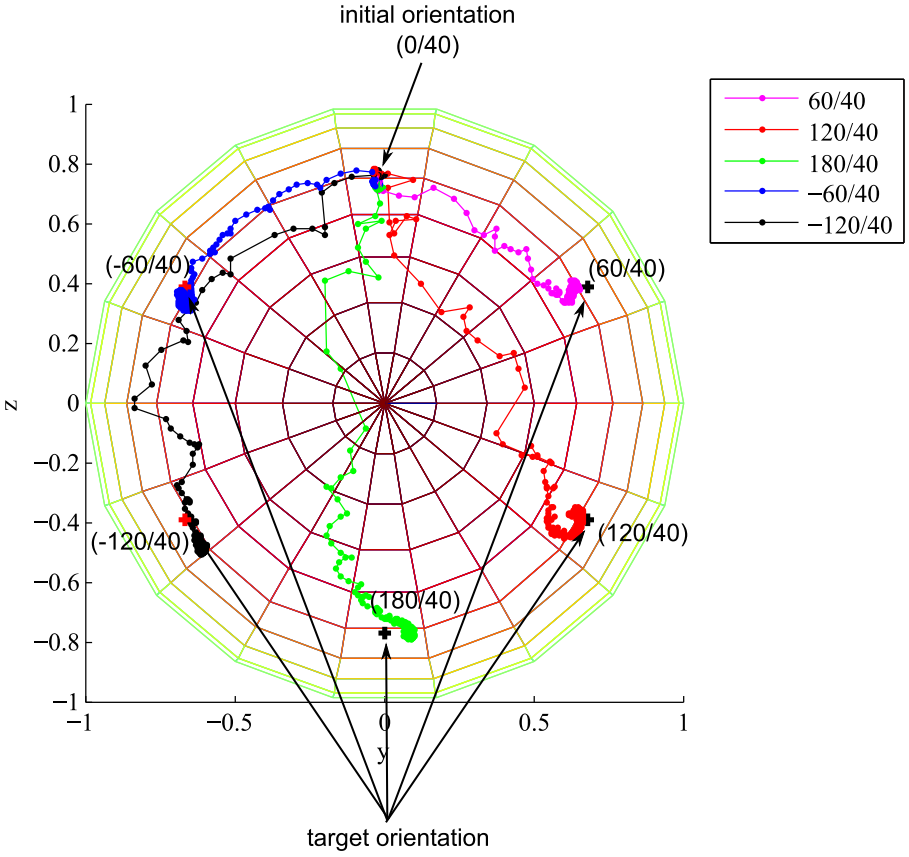

Figure 4.15: Trajectories of SHM1-mh8 for the visual servo control of different direction angles with inclination angle of 40° on an unit sphere.

control takes the shortest path on the unit sphere as expected by using the geodesic error $\mathbf{n} \times \mathbf{n}^*$. If one would like to follow a parallel path (inclination angle constant) on the unit sphere, then one should take a desired orientation as a function of time: $\mathbf{n}^*(t)$.

4.2.3.4 Visual servo control for both direction and inclination angles

Since SHM1-mh8 can steer at any direction in the horizontal plane with 40° of inclination angle, we combine the visual servo control of the direction angle with the inclination angle. The initial direction angle and inclination angle of SHM1-mh8 are respectively 0° and 40°. Here, the direction angle command is fixed at 60°. The inclination command angle of the inclination angles are tested with 30° and 60°. The trajectories of the end of SHM1-mh8 for the visual servo control are traced on an unit sphere, as shown in Figure 4.16.

The visual servo control of the orientation of the SHM in the 3D space is validated. According to our knowledge, the closed-loop control of the orientation of the SHM

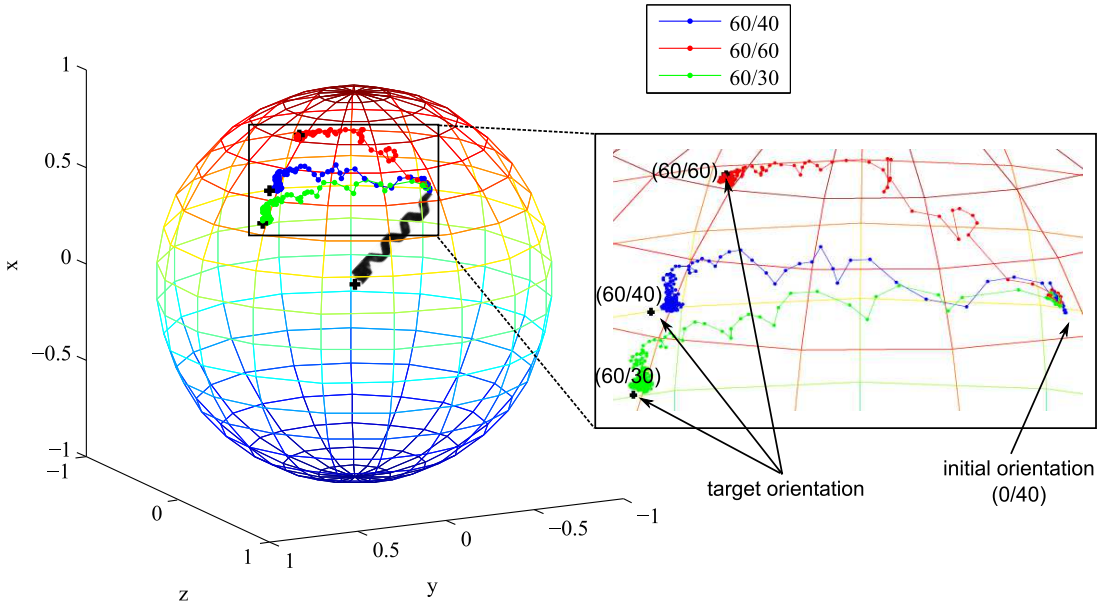

Figure 4.16: Trajectories of the SHM for the visual servoing control for both direction and inclination angles on an unit sphere.

is realized for the first time. The closed-loop steering control of helical swimmers is crucial to realize a controlled 3D motion.

4.3 Visual servo control for the path following

As the visual servo control of the orientation of the SHM has been succeeded, we are ambitious to realize more complicated tasks, for example a path following task for the SHM. Notice that the SHM is a nonholonomic system. Nonholonomic systems are, roughly speaking, mechanical systems with constraints on their velocity that are not derivable from position constraints [Bloch 2005]. The configuration of the SHM is represented by the position and orientation of its main body. The SHM must reach and follow a geometric path in the Cartesian space starting from a given initial configuration (on or off the path).

4.3.1 Real-time position estimation in the 3D space

The orientation of the SHM in the 3D space is presented in Section 4.2.1. In order to know the distance between the SHM and the path, the position of the SHM should also be known. The real-time position of the SHM is described by its barycenter in the 3D space. A method to estimate the real-time position of the SHM in the 3D space from its positions in the two images taken with the top and the side cameras with known calibrations and poses is introduced as follows.

This process requires the intersection of two known rays in space, and is commonly known as triangulation. When noise is present, the two rays will not generally meet, in which case it is necessary to estimate the best solution of the point in 3D space. The barycenter of the SHM in 3D space is measured as g_t and g_s in the two images

taken with the top and side cameras. The two camera perspective projection matrices $\mathbf{P}_t$ and $\mathbf{P}_s$ corresponding to the two images are known. Since there are errors in the measured points g_t and g_s, the rays back-projected from the points are skewed. It means that there will not be a point $\mathbf{G}$ in 3D space which exactly satisfies $\mathbf{g}_t = \mathbf{P}_t\mathbf{G}$ and $\mathbf{g}_s = \mathbf{P}_s\mathbf{G}$, and the images points do not satisfy the epipolar constraint $\mathbf{g}_s^T\mathbf{F}\mathbf{g}_t = 0$. A desirable feature of the method of triangulation used is that it should be invariant under transformation of the appropriate class. Denote by τ a triangulation method to compute the 3D space point $\mathbf{G}$ from the measured points and a pair of camera matrices.

$$\mathbf{G} = \tau(\mathbf{g}_t, \mathbf{g}_s, \mathbf{P}_t, \mathbf{P}_s) \tag{4.47}$$

The triangulation is said to be invariant under a transformation $\mathbf{H}$ if:

$$\tau(\mathbf{g}_t, \mathbf{g}_s, \mathbf{P}_t, \mathbf{P}_s) = \mathbf{H}^{-1}\tau(\mathbf{g}_t, \mathbf{g}_s, \mathbf{P}_t\mathbf{H}^{-1}, \mathbf{P}_s\mathbf{H}^{-1}) \tag{4.48}$$

This means that triangulation using the transformed cameras results in the transformed point. If the camera matrices are known only up to an affine (or projective) transformation, then it is clearly desirable to used an affine (or projective) invariant triangulation method to compute the 3D space point. Therefore, it is inappropriate to minimize errors in the 3D space. Only image distances are minimized with simple linear triangulation methods.

The linear triangulation method is the direct analogue of the Direct Linear Transformation (DLT) method [Hartley 2004]. In each image, based on the projective model of the camera, we have the relationship between the point on the metric image and the point in the 3D camera coordinate system:

$$\begin{cases} {}^{imt}\tilde{\mathbf{g}}_t \equiv (\mathbf{I} \;\; \mathbf{0}) \; {}^{ct}\tilde{\mathbf{G}} \\ {}^{ims}\tilde{\mathbf{g}}_s \equiv (\mathbf{I} \;\; \mathbf{0}) \; {}^{cs}\tilde{\mathbf{G}} \end{cases} \tag{4.49}$$

The points in the metric image coordinate system can be obtained from the points measured in the pixel image coordinate system as:

$$\begin{cases} {}^{imt}\tilde{\mathbf{g}}_t = \mathbf{K}_{ct}^{-1} \; {}^{ipt}\tilde{\mathbf{g}}_t \\ {}^{ims}\tilde{\mathbf{g}}_s = \mathbf{K}_{cs}^{-1} \; {}^{ips}\tilde{\mathbf{g}}_s \end{cases} \tag{4.50}$$

The points in the metric images coordinate system and the 3D points in camera coordinate systems are linearly dependent. Therefore, the cross products are then zero.

$$\begin{cases} {}^{imt}\tilde{\mathbf{g}}_t \times \; {}^{ct}\mathbf{G} = \mathbf{0} \\ {}^{ims}\tilde{\mathbf{g}}_s \times \; {}^{cs}\mathbf{G} = \mathbf{0} \end{cases} \tag{4.51}$$

With the transformation between the two camera coordinate systems, we can write:

$${}^{ct}\mathbf{G} = \; {}^{ct}\mathbf{R}_{cs} \; {}^{cs}\mathbf{G} + \; {}^{ct}\mathbf{t}_{cs} \tag{4.52}$$

with ${}^{ct}\mathbf{R}_{cs}$ the rotation matrix and ${}^{ct}\mathbf{t}_{cs}$ the translation matrix from the side camera to the top camera, which are known from the calibration. The cross products are then:

$$\begin{cases} {}^{imt}\tilde{\mathbf{g}}_t \times (\; {}^{ct}\mathbf{R}_{cs} \; {}^{cs}\mathbf{G}) + \; {}^{imt}\tilde{\mathbf{g}}_t \times \; {}^{ct}\mathbf{t}_{cs} = \mathbf{0} \\ {}^{ims}\tilde{\mathbf{g}}_s \times \; {}^{cs}\mathbf{G} = \mathbf{0} \end{cases} \tag{4.53}$$

We can combine the two equations in a matrix form such that as:

$$\begin{bmatrix} \left[{}^{imt}\mathbf{g}_t\right]_\times \, {}^{ct}\mathbf{R}_{cs} \\ \left[{}^{ims}\mathbf{g}_s\right]_\times \end{bmatrix} {}^{cs}\mathbf{G} = \begin{bmatrix} -\left[{}^{imt}\mathbf{g}_t\right]_\times \, {}^{ct}\mathbf{t}_{cs} \\ 0 \end{bmatrix} \tag{4.54}$$

We note $[\mathbf{m}]_\times$ the skew-symetric matrix of the vector $\mathbf{m} = (m_x, m_y, m_z)^T$ such that:

$$[\mathbf{m}]_\times = \begin{bmatrix} 0 & -m_z & m_y \\ m_z & 0 & -m_x \\ -m_y & m_x & 0 \end{bmatrix} \tag{4.55}$$

The cross product of the vectors $\mathbf{m}$ and $\mathbf{x}$ can be expressed in matrix form: $[\mathbf{m}]_\times \mathbf{x} = \mathbf{m} \times \mathbf{x}$. Then we solve the system (4.54) with Singular Value Decomposition (SVD) method to get the point G in the side camera coordinate system ${}^{cs}\mathbf{G}$. The position of the barycenter G in the 3D world coordinate system can be expressed with the transformation from $\mathcal{R}_{cs}$ to $\mathcal{R}_w$ as:

$${}^{w}\tilde{\mathbf{G}} = {}^{w}\mathbf{M}_{cs} \, {}^{cs}\tilde{\mathbf{G}} \tag{4.56}$$

The 3D position of the barycenter of the helical swimmer in the world coordinate system can be then determined from the barycenter on the two images. The position of the barycenter is used to determine the distance between the SHM and the reference path. Note that this is also the basic algorithm to estimate a point in the 3D space. A better performance can be achieved by using advanced methods for computer vision, which is costly in time and is not the objective of this thesis.

4.3.2 2D Path following on the horizontal plane

For lots of in-vitro applications of helical swimmers, such as the applications for lab-on-a-chip, the altitude of the helical swimmer is constant and usually at the center of the channels. The planned path to be followed is thus only on the horizontal plane. The helical swimmer is a car-like robot. It means that a helical swimmer can only advance in the direction of its axis, but can not instantaneously move sideways. The control of the path following of the SHM on the horizontal plane can be inspired by an unicycle model. Let us start with the notations.

4.3.2.1 Notations

The notations of the 2D path following of the SHM on the horizontal plane is depicted in Figure 4.17:

- $\mathcal{C}(s)$ is the predefined reference path with respect to the curvilinear coordinate s of the curve. The curve should be twice differentiable in $\mathbb{R}^2$ for pose-based schema, and once differentiable for image-based schema [Cherubini 2008b, Cherubini 2008a]. The control is pose-based in our case, so the curve should be twice differentiable.

- θ_d is the direction angle of the SHM.

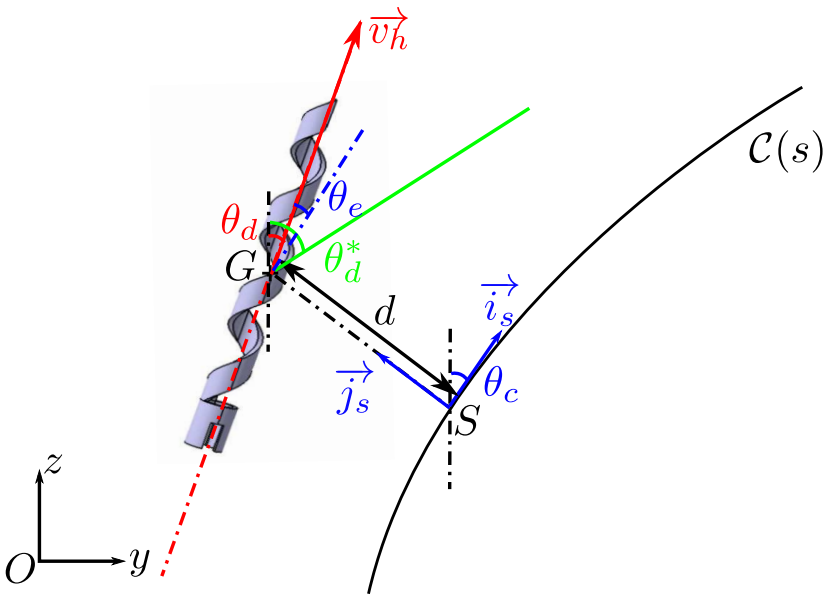

Figure 4.17: Helical swimmer modelling of the 2D path following on the horizontal plane.

- $\overrightarrow{v_h}$ is the advance velocity of the SHM on the horizontal plane.
- G is the barycentre of the SHM.
- S is the curvilinear coordinate of the nearest point on the path to the SHM.
- $d = \|SG\|$ is the distance between the SHM and the path.
- $\overrightarrow{i_s}$ is the tangent of path $\mathcal{C}$ at S. $\overrightarrow{j_s}$ is perpendicular to $\overrightarrow{i_s}$.
- c denotes the curvature of the path $\mathcal{C}$, and R denotes the radius of curvature at S, with $R = 1/c$.
- θ_c is the angle between the current tangent of the path and the z axis, which can be considered as the direction angle of the path.
- $\theta_e = \theta_d - \theta_c$ defines the direction angle error of the SHM to the path.
- θ_d^* is the calculated target direction angle of the SHM for the command to achieve the path.

4.3.2.2 Kinematic equations

The aim of the path following control is to minimize the lateral and angular errors. We propose here to express the state coordinates with respect to the path $\mathcal{C}$. More precisely, the position G and the direction angle θ_d of the SHM are described by the curvilinear coordinate s, the distance error of the SHM to the path defined as $d = \|SG\|$,

and the direction angle error of the SHM to the path defined as $\theta_e = \theta_d - \theta_c$. The state vector is then written as:

$$\mathbf{q} = \begin{bmatrix} s \\ d \\ \theta_e \end{bmatrix} \tag{4.57}$$

The intermediate control variables of the system are the linear advance velocity and the angular velocity of the steering of the SHM on the horizontal plane:

$$\mathbf{u} = \begin{bmatrix} v_h \\ \Omega_x \end{bmatrix} \tag{4.58}$$

The real control variables are the output voltage of the PCI card (U_s, U_m, U_b), which control the magnetic field $\mathbf{B}$ generated by the 3D Helmholtz coil pairs, can be deduced from the intermediate control variables.

The derivation of s is relied on Figure 4.18, in which O denotes the curvature center of the path $\mathcal{C}$ at the curvilinear coordinate S. The intercept theorem allows us to write:

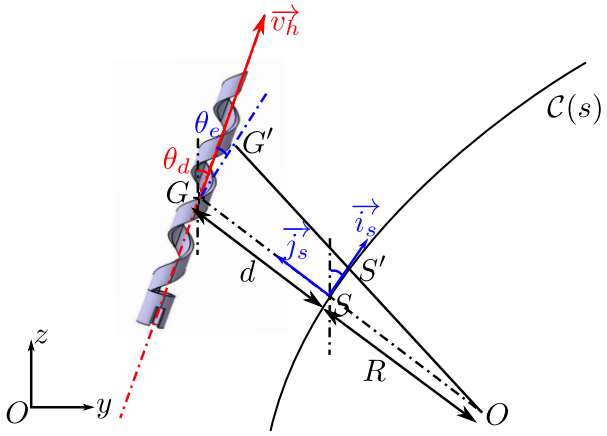

Figure 4.18: Derivation of s equation.

$$\frac{GG'}{SS'} = \frac{GS}{GO} \tag{4.59}$$

Thus:

$$\frac{v_h \cos\theta_e}{\dot{s}} = \frac{d+R}{R} \tag{4.60}$$

From where:

$$\dot{s} = \frac{v_h \cos\theta_e}{1 + d/R} \tag{4.61}$$

The derivation of the lateral error d is expressed as follows:

$$\dot{d} = v_h \sin\theta_e \tag{4.62}$$

The derivation of the direction angle error θ_e can be expressed by:

$$\dot{\theta}_e = \dot{\theta}_d - \dot{\theta}_c \tag{4.63}$$

where $\dot{\theta}_d = \Omega_x$ is the angular velocity of the steering of the SHM on the horizontal plane, and $\dot{\theta}_c = \frac{\mathrm{d}\theta_c}{\mathrm{d}s}\frac{\mathrm{d}s}{\mathrm{d}t} = c\dot{s}$. Therefore, the derivation of the direction angle error is then:

$$\dot{\theta}_e = \Omega_x - \frac{v_h \cos\theta_e}{R+d} \tag{4.64}$$

In conclusion, the state space model of the SHM moving on the 2D horizontal plane is expressed as:

$$\begin{cases} \dot{s} = \dfrac{v_h \cos\theta_e}{1+d/R} \\ \dot{d} = v_h \sin\theta_e \\ \dot{\theta}_e = \Omega_x - \dfrac{v_h \cos\theta_e}{R+d} \end{cases} \tag{4.65}$$

4.3.2.3 Control law designed with chained form

The control objective is to ensure the convergence of the SHM to the reference path $\mathcal{C}$. Therefore, the state variables d and θ_e are expected to be brought and kept at zero. $d = 0$ means that the barycenter of the SHM G belongs to path $\mathcal{C}$. $\theta_e = 0$ ensures the direction angle of the SHM is in the same direction as the tangent of the path $\mathcal{C}$.

The state space model of the SHM (4.65) is clearly nonlinear. Bell proposed to linearize the model around the equilibrium $d = \theta_e = 0$ using linear systems theory. In that case, control design does not rely on the actual model of the SHM, but on an approximated one. Samson have established in control theory that models of mobile robots can be converted into almost linear models, namely chained forms, in an exact way [Samson 1995]. Such an approach is attractive and used by lots of researchers for car-like mobile robots [Laumond 2001, Thuilot 2002], since it allows us to use linear systems theory while still relying upon the actual nonlinear model of the SHM. This approach is followed hereafter.

The model of the SHM (4.65) can be converted into chained form dedicated to systems with two inputs and limited to dimension three. The general chained system of dimension three is written as:

$$\begin{cases} \dot{x_1} = m_1 \\ \dot{x_2} = x_3 m_1 \\ \dot{x_3} = m_2 \end{cases} \tag{4.66}$$

where $\mathbf{X} = (x_1, x_2, x_3)^T$ and $\mathbf{M} = (m_1, m_2)^T$ are respectively the state and control vectors. In order to verify that a chained form system is almost linear, just replace the time derivative by a derivation with respect to the state variable x_1. Using the notations:

$$\frac{\mathrm{d}}{\mathrm{d}x_1} x_i = x_i' \quad \text{and} \quad m_3 = \frac{m_2}{m_1} \tag{4.67}$$

the chained form (4.66) can be rewritten as:

$$\begin{cases} x_1' = 1 \\ x_2' = x_3 \\ x_3' = m_3 \end{cases} \tag{4.68}$$

The last two equations of system (4.68) constitute a linear system.

Let us convert the model of the SHM into chained form by using the change of the coordinates.

$$x_1 = s \tag{4.69}$$

considering (4.61), which imposes:

$$m_1 = \dot{x_1} = \frac{v_h \cos\theta_e}{1 + dc} \tag{4.70}$$

The virtual command variable m_1 is associated with the evolution of the curvilinear coordinate. Moreover, for the simplicity of the transformation into chained form, we choose:

$$x_2 = d \tag{4.71}$$

It follows then:

$$\dot{x_2} = v_h \sin\theta_e = x_3 m_1 \tag{4.72}$$

Therefore, from (4.70) and (4.72), the last state variable x_3 is given by:

$$x_3 = (1 + dc)\tan\theta_e \tag{4.73}$$

Finally, from (4.66) the last control variable m_2 is given by:

$$\begin{aligned} m_2 &= \dot{x_3} = \frac{\mathrm{d}}{\mathrm{d}t}((1 + dc)\tan\theta_e) && (4.74)\\ &= \tan\theta_e \frac{\mathrm{d}}{\mathrm{d}t}(1 + dc) + (1 + dc)\frac{\mathrm{d}}{\mathrm{d}t}\tan\theta_e && (4.75)\\ &= c\dot{d}\tan\theta_e + \frac{\mathrm{d}c}{\mathrm{d}t} d\tan\theta_e + (1 + dc)\frac{1}{\cos^2\theta_e}\frac{\mathrm{d}}{\mathrm{d}t}\theta_e && (4.76) \end{aligned}$$

considering (4.65), m_2 can be written as follows:

$$m_2 = cv_h \sin\theta_e \tan\theta_e + \frac{\mathrm{d}c}{\mathrm{d}s}\frac{v_h \cos\theta_e}{1 + dc} d\tan\theta_e + \frac{1 + dc}{\cos^2\theta_e}\left(\Omega_x - \frac{v_h \cos\theta_e c}{1 + dc}\right) \tag{4.77}$$

These transformations are invertible as long as $d \neq -\frac{1}{c}$, $v \neq 0$ and $\tan\theta_e \neq \frac{\pi}{2}[\pi]$. From a practical point of view, the SHM respects these conditions once properly initialized.

Now that the model of the SHM is converted to linear model, the control techniques for linear system can be applied. We use a simple expression for the virtual control law:

$$m_3 = -k_t x_3 - k_d x_2 \qquad (k_t, k_d) \in \mathbb{R}^{+2} \tag{4.78}$$

where k_t and k_d are the control parameters and are strictly positive. Replacing (4.78) into (4.68) gives:

$$x_2'' + k_t x_2' + k_d x_2 = 0 \tag{4.79}$$

which implies that both x_2 and x_3 converge to 0. In view of (4.71) and (4.73), d and θ_e converge to 0 as well. The reference path following is therefore achieved. Moreover, since the evolution of the error dynamics (4.79) is driven by $x_1 = s$, the gains (k_t, k_d) impose a settling distance instead of a settling time. Consequently, the helical swimmer trajectory will be identical if the initial error is the same. The guidance performances will be velocity independent.

The actual control law expression on the angular velocity of the steering of the SHM is as follows, by reporting (4.70) and (4.77) into (4.78):

$$\Omega_x = -\frac{\cos^3\theta_e}{1+dc}\left(k_d d + k_t(1+dc)\tan\theta_e + \frac{\mathrm{d}c}{\mathrm{d}s}d\tan\theta_e + c\tan^2\theta_e(1+dc)\right) + \frac{v_h\cos\theta_e}{R+d} \tag{4.80}$$

where v_h is the advance velocity on the horizontal plane, which is usually constant, and calculated from (3.23). For the case that the reference path is a straight line, the control of the angular speed of the steering on the horizontal plane can be simplified as:

$$\Omega_x = -\cos^3\theta_e(k_d d + k_t\tan\theta_e) \tag{4.81}$$

The target direction angle can be obtained by the real-time direction angle and the angular velocity of the steering of the SHM, which can be expressed as:

$$\theta_d^*(t) = \theta_d(t) + \Omega_x \mathrm{d}t \tag{4.82}$$

with $\mathrm{d}t$ the sample time. The target orientation of the SHM ($\mathbf{n}^*$) can be calculated with the target direction angle (θ_d^*) and target inclination angle (θ_i^*) from (3.32). The inclination angle can be at 0° for some tasks, such as the transport of micro objects in micro channels. The inclination angle can also be used to compensate the gravity in the case of the SHMs. The control of the magnetic field (4.44) depends on the real-time orientation ($\mathbf{n}$) and the target 3D orientation ($\mathbf{n}^*$) of the SHM, and can be expressed by (4.44). Then, the control of the output voltage of the PCI card can be expressed as (4.45) with the real-time orientation ($\mathbf{n}$), the target orientation $\mathbf{n}^*$.

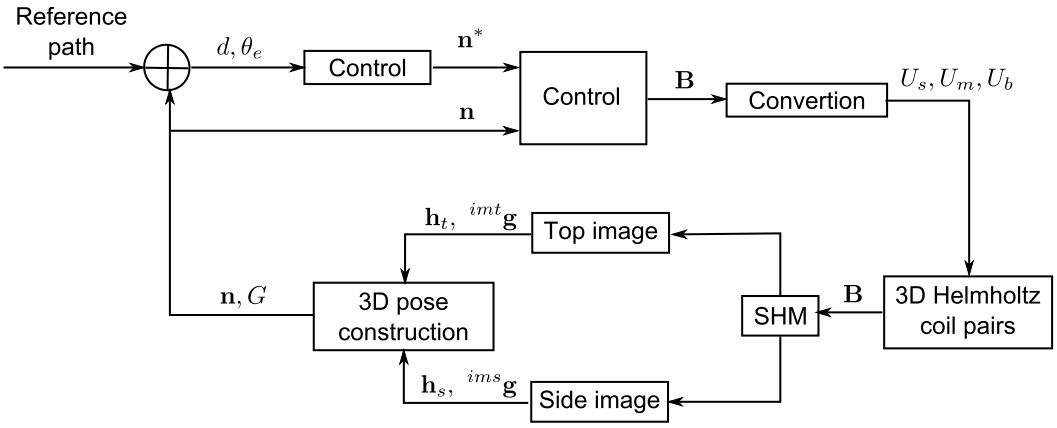

Figure 4.19: Block-diagram of the visual servo control of path following of the SHM on the 2D horizontal plane.

In conclusion, the block-diagram of the visual servo control of path following of the SHM on the 2D horizontal plane is shown in Figure 4.19. The 3D orientation and position of the SHM can be obtained from the tracked SHM in the images taken by the two cameras using the proposed estimation methods. The distance and direction angle error between the SHM to the reference path can be then calculated. Using the

proposed control law, the real-time target orientation of the SHM can be obtained. The control of the magnetic field can be established by the real-time and target orientation of the SHM. The output voltages of the PCI card can be converted from the magnetic field. According to our knowledge, the control law of the path following of helical swimmers is proposed for the first time. A visual servo control of the path following of the SHM with a reference path of a straight line on the horizontal plane is tested and presented as follows.

4.3.3 Results

First, the estimation method of the barycenter of the SHM is validated in the 3D space. The visual servo control of the path following is tested with a straight line in the 2D horizontal plane. The trajectories of the SHM differ depending on the control parameters, which is shown as follows.

4.3.3.1 Real-time position estimation

In order to verify the method of the reconstruction of the barycenter of the SHM in the 3D space, SHM1-mh8 is tracked in an open-loop control from the top and side images. The direction angle and the inclination angle of SHM1-mh8 in the open-loop control are respectively $\theta_d = 0°$ and $\theta_i = 40°$. The rotation frequency of the magnetic field is 2 Hz. With this inclination angle and rotation frequency, SHM1-mh8 moves on the substrate. The advance velocity is estimated as $v_h = 0.47$ mm/s from (3.23) and Figure 3.12b. The real-time 3D position of the barycenter of SHM1-mh8 ($G = (x, y, z)^T$) is estimated with the method presented in Section 4.3.1. Figure 4.20a depicts the evolution of the coordinates x, y, and z. The trajectory of the barycenter of SHM1-mh8 traced on the horizontal planed is presented in Figure 4.20b.

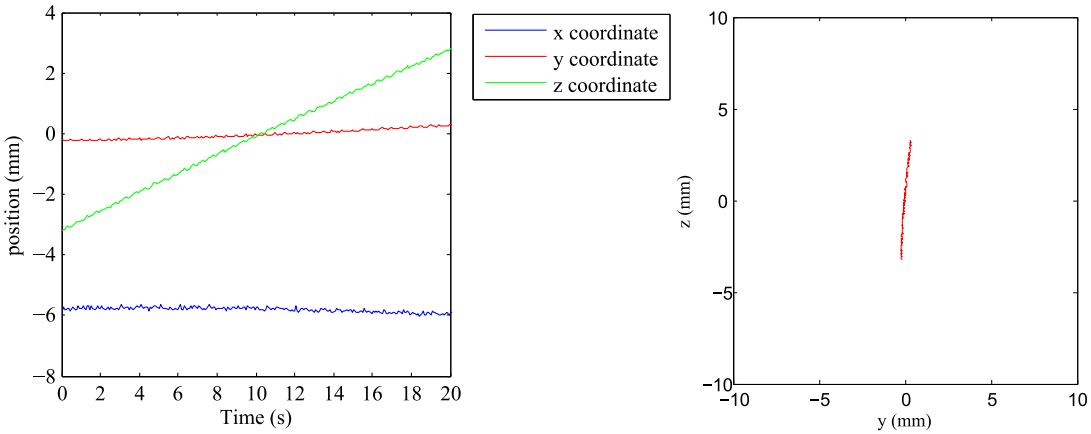

(a) (b)

Figure 4.20: (a) Real-time position of the barycenter of the SHM in the 3D space. (b) Trajectories of the barycenter of the SHM are traced on the horizontal plane yOz.

With this open-loop control, SHM1-mh8 should move forward in the z direction. Therefore, the coordinate z increases. The current advance velocity of the SHM is

calculated as $v_h = 0.3\,\text{mm/s}$, which is smaller than the estimated advance velocity. We assume that it is due to the friction between the SHM and the substrate. The altitude of the SHM x is kept at constant. However, the coordinate y of the SHM is not constant, which should be. The 3D Helmholtz coil pairs are not perfect. Therefore, the magnetic field generated at the center is not perfectly uniform. Magnetic gradient may be created. The fact that SHM1-mh8 does not advance exactly in the z direction is due to the presence of the magnetic gradient. We expect that this error can be eliminated with a closed-loop control, which is now discussed as follows.

4.3.3.2 Trajectories for the visual servo control of the path following

Then, the visual servo control of the path following of SHM1-mh8 is tested with reference path of a straight line on the 2D horizontal plane. The function of the straight line is $z = 0$. The SHM is initially off the path, with an initial distance error of about $-5\,\text{mm}$, and without initial direction angle error. Trajectories of the barycenter of the SHM for the visual servo control of the 2D path following with different control parameters are traced in Figure 4.21. The choice of the control parameters depends on the requirement of the system: reaching the reference quickly or travelling less. For the three cases, with $k_t = 0.1$ and $k_d = 0.1$, the travelled path of the SHM is the shortest; with $k_t = 0.1$ and $k_d = 0.8$, the SHM reaches the reference path the fastest.

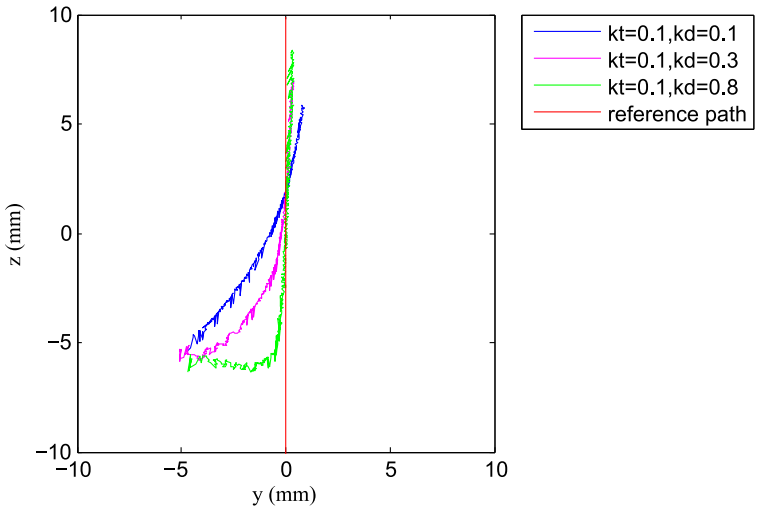

Figure 4.21: Visual servo control of a 2D path following on the horizontal plane with different parameters.

An image sequence of the SHM taken by the top camera during the visual servo control of the 2D path following of a straight line is shown in Figure 4.22. The reference path is drawn with a blue line on the image. The SHM reaches the reference path, then advances along this reference path. We observe that the direction angle of the SHM is negative for the barycenter of the SHM advancing along the z axis. The generated propulsive force has a composition is the $-y$ direction, in order to counterbalance the magnetic force created by the magnetic gradient.

Afterwards, the trajectories of the open-loop control and visual servo control of the SHM to advance in the z direction are compared. The visual servo control of

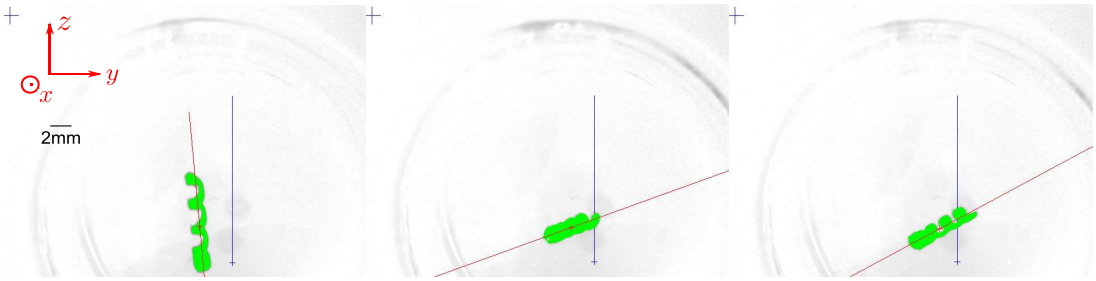

(a) 0 s (b) 1 s (c) 2 s

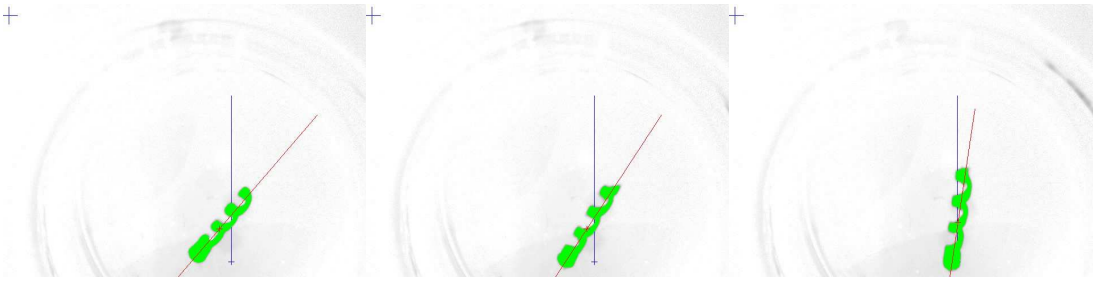

(d) 3 s (e) 5 s (f) 6 s

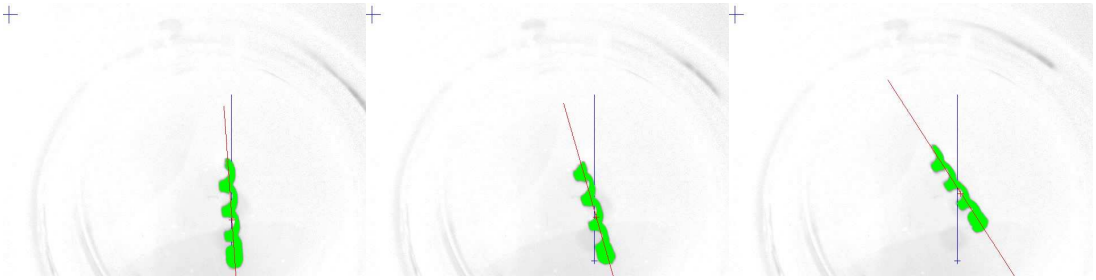

(g) 7 s (h) 8 s (i) 11 s

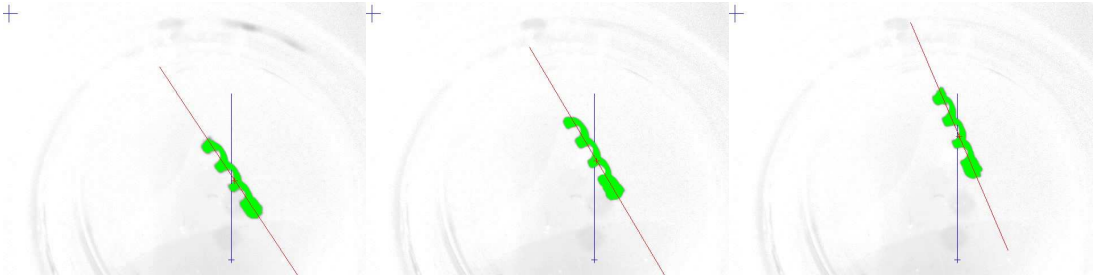

(j) 13 s (k) 16 s (l) 19 s

Figure 4.22: Image sequence of the visual servo control of the 2D path following for a straight line of the SHM with the control parameters $k_t = 0.1$ and $k_d = 0.8$ taken by the top camera.

the SHM for a straight line path following with initial position on the path is tested. The trajectory of the barycenter of the SHM for the visual servo control to follow the straight line $z = 0$ on the horizontal plane yOz is traced in Figure 4.23. This trajectory is compared with the trajectory of the open loop control with the same initial position.

Observed on Figure 4.23, the movement of the SHM is perturbed by the unexpected magnetic gradient. For the closed-loop control by visual servoing, the SHM returns onto the reference line after the perturbation. Therefore, the visual servo control of the path following of the SHM is advantageous, because the SHM can follow the reference path with the presence of the unexpected magnetic gradient.

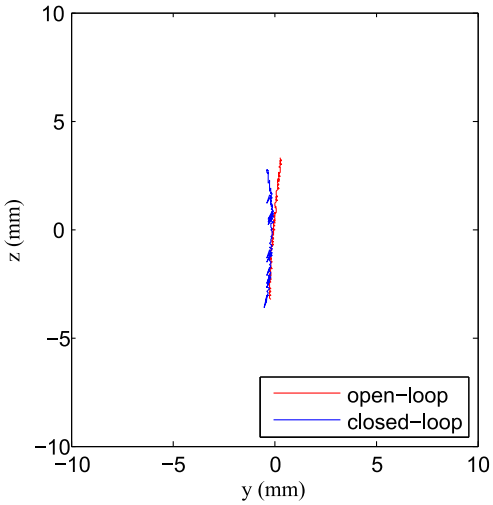

Figure 4.23: Comparison of the trajectories of the open-loop control and visual servo control of SHM to advance in the z direction.

According to our knowledge, the closed-loop control of the path following of helical swimmers is realized for the first time. More complicated reference paths, such as a circle or a square will be tested in future works.

4.3.4 Perspectives for 3D path following

For the applications in an open space, for example for the in-vivo applications in eyeballs, or in the urinary system, the planned path to be followed is in general in the 3D space. Different from the path in the horizontal plane for the applications for lab-on-a-chip, the altitude of the path varies as well. For the 3D path following in the space, the kinematic equations is written directly in the 3D space. The control law design will be studied in future works. We now present the notations.

4.3.4.1 Notations

The notations of the 3D path following of the SHM in the space is depicted in Figure 4.24:

- $\mathcal{C}(s)$ is the predefined reference path with respect to the curvilinear coordinate s of the curve. The curve should be twice differentiable in $\mathbb{R}^3$.
- $\overrightarrow{n}$ is the real-time axis of the SHM.
- $\overrightarrow{v_p}$ is the propulsive velocity of the SHM, which is in the same direction as $\overrightarrow{n}$.

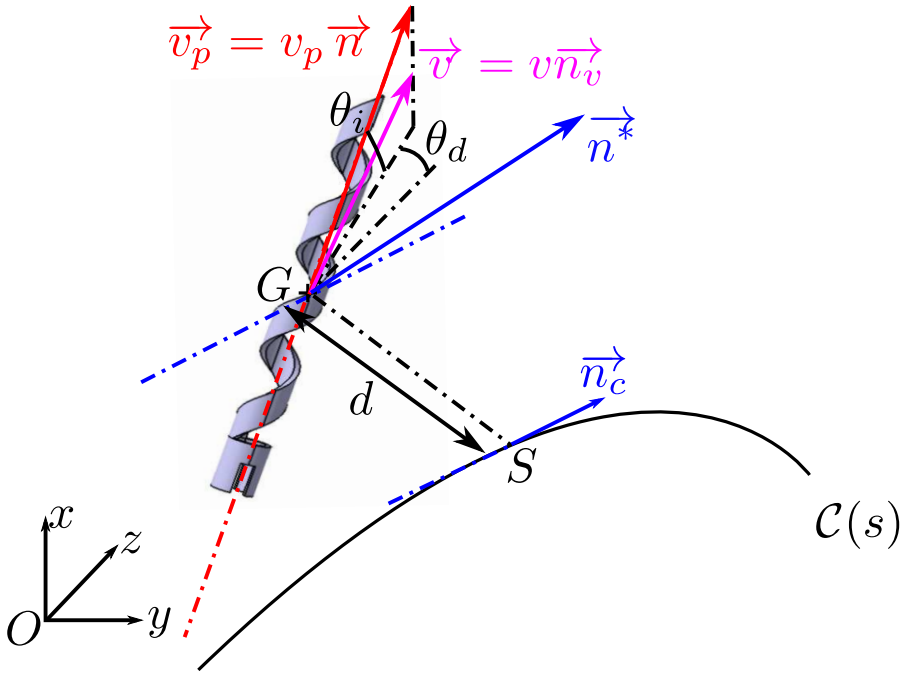

Figure 4.24: Helical swimmer model of the 3D path following.

- $\overrightarrow{v}$ is the total velocity of the SHM, considering the gravity of the SHM, which is in the direction of $\overrightarrow{n_v}$.
- θ_d is the direction angle of the SHM.
- θ_i is the inclination angle of the SHM.
- G is the barycentre of the SHM.
- S is the curvilinear coordinate of the nearest point on the path to the SHM.
- $d = \|SG\|$ is the distance between the SHM and the path.
- $\overrightarrow{n_c}$ is the tangent of path $\mathcal{C}$ at S.
- θ_c is the angle between the current tangent of the path and the z axis, which is the direction angle of the path.
- $c(S)$ denotes the curvature of the path $\mathcal{C}$.
- $\overrightarrow{n^*}$ is the calculated target orientation of the SHM to achieve the path.

4.3.4.2 Kinematic equations

Similar to the 2D path following, the aim of the control is to minimize the distance and orientation errors to the reference path. The position P and the orientation $\overrightarrow{n}$ of the SHM are described respectively by the curvilinear coordinate s, the distance error of the SHM to the path defined as $d = |SG|$, and the orientation error of the SHM to

the path. The orientation error of 3D path following is a vector, which is defined as $\mathbf{e}_\theta = \mathbf{n} \times \mathbf{n}_c$. The state vector can be then written as:

$$\mathbf{q} = \begin{bmatrix} s \\ e_d \\ \mathbf{e}_\theta \end{bmatrix} \tag{4.83}$$

The intermediate control variables of the system are the total velocity and the total angular velocity of the SHM in the 3D space:

$$\mathbf{u} = \begin{bmatrix} \mathbf{v} \\ \boldsymbol{\Omega} \end{bmatrix} \tag{4.84}$$

The real control variables are the output voltage of the PCI card (U_s, U_m, U_b), which control the magnetic field $\mathbf{B}$ generated by the 3D Helmholtz coil pairs, can be deduced from the intermediate control variables.

Similar to (4.61), $\dot{s}$ in the 3D space can be expressed as:

$$\dot{s} = \frac{\mathbf{n}_c}{1 + d/R}\mathbf{v} \tag{4.85}$$

Then, the derivation of the distance error d can be expressed as follows:

$$\dot{d} = \frac{\mathrm{d}\overrightarrow{SG}}{\mathrm{d}t} = \frac{\overrightarrow{SG}^T}{\parallel \overrightarrow{SG} \parallel}(\mathbf{v} - \dot{s}\mathbf{n}_c) \tag{4.86}$$

As $\mathbf{n}_c$ is always perpendicular to $\overrightarrow{SG}$, we have $\overrightarrow{SG}^T \dot{s}\mathbf{n}_c = 0$ Then $\dot{e_d}$ can be expressed as:

$$\dot{d} = \frac{\overrightarrow{SG}^T}{\parallel \overrightarrow{SG} \parallel}\mathbf{v} \tag{4.87}$$

The orientation error vector is defined as

$$\mathbf{e}_\theta = \mathbf{n} \times \mathbf{n}_c \tag{4.88}$$

Then, the derivation of the orientation error e_θ can be expressed in $\mathcal{R}_w$ as:

$$\dot{\mathbf{e}_\theta} = \dot{\mathbf{n}} \times \mathbf{n}_c + \mathbf{n} \times \dot{\mathbf{n}_c} \tag{4.89}$$

$$= (\boldsymbol{\Omega} \times \mathbf{n}) \times \mathbf{n}_c - \mathbf{n} \times \left(\frac{\partial \mathbf{n}_c}{\partial s}\dot{s}\right) \tag{4.90}$$

$$= \mathbf{n}_c \times (\mathbf{n} \times \boldsymbol{\Omega}) - \mathbf{n} \times \left(\frac{\partial \mathbf{n}_c}{\partial s}\dot{s}\right) \tag{4.91}$$

with $\boldsymbol{\Omega}$ the steering angular velocity of the SHM. Recall that $[\mathbf{m}]_\times$ is the skew-symetric matrix of the vector $\mathbf{m} = (m_x, m_y, m_z)^T$, whose expression is given in (4.55). Then the derivation of the orientation error can be expressed as:

$$\dot{\mathbf{e}_\theta} = [\mathbf{n}^*]_\times [\mathbf{n}]_\times \boldsymbol{\Omega} - \mathbf{n} \times \left(\frac{\partial \mathbf{n}^*}{\partial s}\dot{s}\right) \tag{4.92}$$

with

$$[\mathbf{n}_c]_\times[\mathbf{n}]_\times = \begin{bmatrix} -n_{yc}n_y - n_{zc}n_z & n_{yc}n_x & n_{zc}n_x \\ n_{xc}n_y & -n_{zc}n_z - n_{xc}n_x & n_{zc}n_y \\ n_{xc}n_z & n_{yc}n_z & -n_{xc}n_x - n_{yc}n_y \end{bmatrix} \tag{4.93}$$

Therefore, with the expression of the $\dot{s}$, $\dot{\mathbf{e}_\theta}$ can be expressed as:

$$\dot{\mathbf{e}_\theta} = [\mathbf{n}_c]_\times[\mathbf{n}]_\times \boldsymbol{\Omega} - \left(\mathbf{n} \times \frac{\partial \mathbf{n}_c}{\partial s}\right) \frac{\mathbf{n}_c^T}{1 + d/R}\mathbf{v} \tag{4.94}$$

In conclusion, the state space model of the SHM in the world coordinate system can be expressed as:

$$\begin{bmatrix} \dot{d} \\ \dot{\mathbf{e}_\theta} \end{bmatrix}_{4\times1} = \begin{bmatrix} \dfrac{\overrightarrow{SG}^T}{\| \overrightarrow{SG} \|} & \mathbf{0}_{1\times3} \\ -\left(\mathbf{n} \times \dfrac{\partial \mathbf{n}_c}{\partial s}\right) \dfrac{\mathbf{n}_c^T}{1 + d/R} & [\mathbf{n}_c]_\times[\mathbf{n}]_\times \end{bmatrix}_{4\times6} \begin{bmatrix} \mathbf{v} \\ \boldsymbol{\Omega} \end{bmatrix}_{6\times1} \tag{4.95}$$

The linear velocity can be expressed as $\mathbf{v} = v\mathbf{n}_v$, where $\mathbf{n}_v$ is total velocity direction of the SHM. Remark that, in the microscale, because the gravity of the SHM is neglected, this direction is in general coincides with the orientation of the SHM $\mathbf{n}_v = \mathbf{n}$.

The state space model of the SHM can be expressed as:

$$\begin{bmatrix} \dot{d} \\ \dot{\mathbf{e}_\theta} \end{bmatrix}_{4\times1} = \underbrace{\begin{bmatrix} \dfrac{\overrightarrow{SG}^T}{\| \overrightarrow{SG} \|}\mathbf{n}_v & \mathbf{0}_{1\times3} \\ -\left(\mathbf{n} \times \dfrac{\partial \mathbf{n}_c}{\partial s}\right) \dfrac{\mathbf{n}_c^T\mathbf{n}}{1 + d/R} & [\mathbf{n}_c]_\times[\mathbf{n}]_\times \end{bmatrix}_{4\times4}}_{\mathbf{L}_{d,\theta}^T} \begin{bmatrix} v \\ \boldsymbol{\Omega} \end{bmatrix}_{4\times1} \tag{4.96}$$

where $\mathbf{L}_{d,\theta}^T$ is named the 3D interaction matrix of the SHM, by reference to the task function approach [Samson 1991]. Remark that with the projection on the horizontal plane yOz, we find the same kinematic equations with (4.65).

The control law design for the nonlinear system (4.96) should be studied in future works. We hope that helical swimmers can follow more complicated 3D reference paths in the future.

4.4 Summary

In Chapter 3, an open-loop control of the orientation of the SHM has been studied. In this chapter, a closed-loop control of the orientation of the SHM in the 3D space by visual servoing is presented. The visual servo control of the orientation of the SHM is Pose-Based Visual Servoing (PBVS). Therefore, a method to estimate the orientation of the SHM in the 3D space from its axes tracked in the two images taken with the top and the side cameras is proposed in the first place.

The intrinsic parameters of the two cameras and the transformation matrices between the camera coordinate systems and the world coordinate system need to be preliminarily determined. The control of the magnetic field is based on the orientation error between the real-time 3D orientation of the SHM and the target orientation. The magnetic field can be decomposed in the directions perpendicular to the axis of the SHM, which contributes to the rotation of the SHM, and in the direction parallel to the axis of the SHM, which contributes to steer the SHM. The visual servo control of the orientation of the SHM in the 3D space is tested with different command angles both for the direction and inclination angles. According to our knowledge, the closed-loop control of the orientation of helical swimmers is realized for the first time.

Then, a path following task is proposed for the SHM. The SHM is described by the its position and orientation. The aim of the path following task is to minimize the distance and orientation errors to the reference path. A method to estimate the real-time 3D position of the SHM from its barycenter tracked in the two images taken with the top and the side cameras is proposed. A control law design with chained form is proposed for the 2D path following task. The visual servo control for the path following of the SHM is tested with reference path of a straight line on the plane, and with the SHM initially both on and off the path. According to our knowledge, the closed-loop control for the path following task of helical swimmers is realized for the first time.

A 3D state model of the SHM is proposed. The control design for the 3D path following of the SHM in the space will be studied in future works, as well as more reference paths, such as a circle or a helix.

Conclusion and perspectives

Helical microswimmers capable of propulsion at low Reynolds numbers have the potential applications on microfluid, lab-on-a-chip, and minimally invasive medicine, due to their micro sizes and controllability. Several magnetically actuated artificial helical swimmers have appeared. They have different geometry parameters, head shapes, and magnetic positionings, but their influences on swimming performance have not been demonstrated. As far as we know, none of them have been controlled by a close-loop controller. Therefore, this thesis aims to improve the design of helical swimmers and to realize their closed-loop control.

In order to improve the design of helical microswimmers, we have compared the swimming performance of scaled-up helical microswimmers (SHMs) at the millimeter scale with different geometry parameters in viscous liquids. We have found that the most influential factor is the pitch. The SHMs with longer pitches show better swimming performance.

The rotational propulsion performance of the SHMs with different head shapes and magnetic positioning are compared. The SHM with a magnetic head shows a cut-off frequency, but the SHM with an uniformly coated magnetic tail shows a saturation of frequency. The head shapes did not influence the rotational propulsion characteristics (cut-off frequency or saturation of frequency), but they influence on the values of the cut-off frequency. We predict that at the microscale, as the total dipole moment of the magnetic head and the coated magnetic layer are similar, the SHM with an uniformly coated magnetic tail is better, because its rotation frequency stabilizes at the saturation frequency, and will not decrease down to zero with the external applied field beyond the cut-off frequency. The magnetic layer should be coated uniformly, otherwise the SHM with a non-uniformly coated magnetic layer risks having a cut-off frequency as well. The prediction of the rotational propulsion characteristics of the helical swimmers at the microscale will be validated in future works. However, at the millimeter scale, the SHM with a magnetic head shows better rotational propulsion performance, because the total dipole moment of the coated thin magnetic layer is not as strong as the magnetic head's. As a result, the value of the cut-off frequency is much higher than the value of the saturation of frequency for a SHM at the millimeter scale.

The linear propulsion velocity of the SHM has been studied based on the estimated propulsion matrix. An open-loop control of the orientation of the SHM including the direction angle and the inclination angle of the SHM has been studied. The direction angle steering efficiency of the SHM can be improved by increasing its inclination angle. Therefore, a 3D steering strategy of the SHM has been proposed.

A closed-loop control of the orientation of the SHM is proposed using pose-based visual servoing. A method of real-time orientation estimation of the SHM in the 3D space is introduced. The intrinsic parameters of the two cameras and the transformation matrices between them and the world coordinate system need to be preliminarily determined. The control law of the magnetic field is designed proportional to the geodesic error of the 3D orientation of the SHM to the target orientation. The magnetic field can be decomposed in the directions perpendicular to the axis of the SHM,

which contributes to its self-rotation, and in the direction parallel to the axis of the SHM, which contributes to its steering. According to our knowledge, the visual servo control of the orientation of the SHM in the 3D space is realized for the first time.

Then, a path following task has been proposed for the SHM, as a SHM is a non-holonomic system. The aim of the path following task is to minimize the distance and orientation errors to the reference path. A method to estimate the real-time 3D position of the SHM has been also proposed in order to estimate the distance to the path. The control law for the path following on the 2D horizontal plane has been designed with a linearisation of the system thanks to the chained forms. The visual servo control of the path following of the SHM has been tested with a reference path of a straight line, and with the SHM initially both on and off the path. According to our knowledge, the closed-loop control of the path following of the helical swimmers is realized for the first time. The path following tasks in the 3D space will be studied in future works.

The results of the entire work in this thesis will be applied on helical microswimmers at the microscale, as the micro-fabrication of the helical micro swimmers has been mastered. We will at first validate the saturation frequency of the helical microswimmer with a uniformly coated magnetic tail, and show that its swimming performance will not decrease with the high rotation frequency of the external magnetic field. Secondly, the closed-loop control of the orientation of the SHM will be applied on helical microswimmers by using suitable optical devices with a high resolution. The visual servo control of the 2D path following task on the horizontal plane will be also applied on helical microswimmers. Furthermore, the control law of the 3D path following task should be studied. More complicated 3D reference paths, such as a 3D line, a circle or a helix, will be tested at first on the SHMs, then on helical microswimmers. We hope that the 3D motion of helical microswimmers can be controlled by a closed-loop controller in order to achieve more tasks for in vitro and in vivo applications in the near future.

Bibliography

[Abbott 2007] J.J. Abbott, Z. Nagy, F. Beyeler et B.J. Nelson. *Robotics in the Small, Part I: Microbotics*. Robotics Automation Magazine, IEEE, vol. 14, no. 2, pages 92–103, 2007. (Cited on page 4.)

[Abbott 2009] J.J. Abbott, M. Cosentino Lagomarsino, L. Zhang, L. Dong et B.J. Nelson. *How Should Microrobots Swim?* The International Journal of Robotics Research, vol. 28, no. 11-12, pages 1434–1447, 2009. (Cited on pages 9, 10, 21, 22 and 23.)

[Agrawal 2003] M. Agrawal et L.S. Davis. *Camera calibration using spheres: a semi-definite programming approach*. In Computer Vision, 2003. Proceedings. Ninth IEEE International Conference on, pages 782 –789 vol.2, oct. 2003. (Cited on page 98.)

[Antonuk 2000] L. E. Antonuk, K.-W. Jee, Y. El-Mohri, M. Maolinbay, S. Nassif, X. Rong, Q. Zhao, J. H. Siewerdsen, R. A. Street et K. S. Shah. *Strategies to improve the signal and noise performance of active matrix, flat-panel imagers for diagnostic x-ray applications*. Medical Physics, vol. 27, no. 2, pages 289–306, 2000. (Cited on page 30.)

[Araki 1992] M. Araki. Control systems, robotics, and automation. EOLSS, 1992. (Cited on page 57.)

[Azmi 2003] Hooman Azmi et Michael Schulder. *Stereotactic accuracy of a 3-tesla magnetic resonance unit*. Stereotact. Funct. Neurosurg., vol. 80, no. 1-4, pages pp. 140–145, 2003. (Cited on page 29.)

[Behkam 2005] Bahareh Behkam et Metin Sitti. *Modeling and testing of a biomimetic flagellar propulsion method for microscale biomedical swimming robots*. In Proceedings of, pages 37–42, 2005. (Cited on page 10.)

[Behkam 2006] Bahareh Behkam et Metin Sitti. *Design methodology for biomimetic propulsion of miniature swimming robots*. Transactions-American Society of Mechanical Engineers Journal of Dynamic Systems Measurement and Control, vol. 128, no. 1, page 36, 2006. (Cited on page 10.)

[Bell 2006] Dominik J. Bell, Lixin X. Dong, Bradley J. Nelson, M. Golling, Li Zhang et D. Grutzmacher. *Fabrication and Characterization of Three-dimensional InGaAs/GaAs Nanosprings*. Nano Letters, vol. 6, no. 4, pages pp. 725–729, 2006. (Cited on page 11.)

[Bell 2007] D.J. Bell, S. Leutenegger, K.M. Hammar, L.X. Dong et B.J. Nelson. *Flagella-like Propulsion for Microrobots Using a Nanocoil and a Rotating Electromagnetic Field*. In Robotics and Automation, 2007 IEEE International Conference on, pages 1128 –1133, april 2007. (Cited on page 15.)

[Berg 1973] H.C. Berg et R.A. Anderson. *Bacteria swim by rotating their flagellar filaments.* Nature, vol. 245, no. 5425, pages 380–382, 1973. (Cited on page 10.)

[Berg 2004] H.C. Berg. E. coli in motion. Springer-Verlag, 2004. (Cited on pages 10 and 16.)

[Bloch 2005] Anthony M. Bloch, Jerrold E. Marsden et Dmitry V. Zenkov. *Nonholonomic Dynamics.* In CONTROL OF NONHOLONOMIC SYSTEMS ON RIEMANNIAN MANIFOLDS. PROCEEDINGS OF NOLCOS 92, 2005. (Cited on page 117.)

[Bolopion 2009] A. Bolopion, B. Cagneau, S. Haliyo et S. Régnier. *Analysis of stability and transparency for nanoscale force feedback in bilateral coupling.* Journal of Micro - Nano Mechatronics, vol. 4, pages 145–158, 2009. (Cited on page 4.)

[Bolopion 2012] A. Bolopion, H. Xie, S. Haliyo et S. Régnier. *Haptic Teleoperation for 3D Microassembly of Spherical Objects.* IEEE/ASME Transaction on Mechatronics, vol. 17, no. 1, pages 116–127, 2012. (Cited on page 4.)

[Bouchebout 2012] S. Bouchebout, A. Bolopion, M. Kharboutly, I.A. Ivan, J. Agnus et S. Régnier. *Design and first experiments on MagPieR, the magnetic microrobot.* In ISOT'12 International Symposium on Optomechatronic Technologies, pages 1–2, 2012. (Cited on page 26.)

[Carrozza 2003] Maria C. Carrozza, Paolo Dario et Louis P. Jay. *Micromechatronics in surgery.* Transactions of the Institute of Measurement and Control, vol. 25, no. 4, pages 309–327, Octobre 2003. (Cited on page 5.)

[Cervera 1999] E. Cervera et P. Martinet. *Visual servoing with indirect image control and a predictable camera trajectory.* In Intelligent Robots and Systems, 1999. IROS '99. Proceedings. 1999 IEEE/RSJ International Conference on, volume 1, pages 381 –386 vol.1, 1999. (Cited on page 34.)

[Chaillet 2013] N. Chaillet et S. Régnier. Microrobotics for micromanipulation. ISTE. Wiley, 2013. (Cited on page 4.)

[Chaumette 1998] François Chaumette. *Potential problems of stability and convergence in image-based and position-based visual servoing.* In D. Kriegman, G . Hager et A.S. Morse, editeurs, The Confluence of Vision and Control, pages 66–78. LNCIS Series, No 237, Springer-Verlag, 1998. (Cited on page 34.)

[Chaumette 2006] F. Chaumette et S. Hutchinson. *Visual servo control. I. Basic approaches.* Robotics Automation Magazine, IEEE, vol. 13, no. 4, pages 82 –90, dec. 2006. (Cited on pages 32 and 34.)

[Chaumette 2007] F. Chaumette et S. Hutchinson. *Visual servo control. II. Advanced approaches.* Robotics Automation Magazine, IEEE, vol. 14, no. 1, pages 109 –118, march 2007. (Cited on page 32.)

[Cherubini 2008a] A. Cherubini, F. Chaumette et G. Oriolo. *An image-based visual servoing scheme for following paths with nonholonomic mobile robots.* In Control, Automation, Robotics and Vision, 2008. ICARCV 2008. 10th International Conference on, pages 108 –113, dec. 2008. (Cited on page 119.)

[Cherubini 2008b] A. Cherubini, F. Chaumette et G. Oriolo. *A position-based visual servoing scheme for following paths with nonholonomic mobile robots.* In Intelligent Robots and Systems, 2008. IROS 2008. IEEE/RSJ International Conference on, pages 1648 –1654, sept. 2008. (Cited on page 119.)

[Chinzei 1999] Kiyoyuki Chinzei, Ron Kikinis et Ferenc A. Jolesz. *MR Compatibility of Mechatronic Devices: Design Criteria.* volume 1679, pages 1020–1030. Springer, 1999. (Cited on page 29.)

[DiSalvo 1999] F. DiSalvo. *Thermoelectric cooling and power generation.* Science, vol. 285, no. 5428, pages 703–6, 1999. (Cited on page 24.)

[Dreyfus 2005] R Dreyfus, J Baudry, M.L Roper, M Fermigier, HA Stone et J Bibette. *Microscopic artificial swimmers.* Nature, vol. 437, no. 5, pages 862–5, 2005. (Cited on page 10.)

[Duryea 2008] J. Duryea, M. Magalnick, S. Alli, L. Yao, M. Wilson et R. Goldbach-Mansky. *Semiautomated three-dimensional segmentation software to quantify carpal bone volume changes on wrist CT scans for arthritis assessment.* Medical Physics, vol. 35, page 2321, 2008. (Cited on page 29.)

[Felfoul 2004] O. Felfoul, S. Martel, G. Beaudoin et J. Mathieu. *Microdevice's susceptibility difference based MRI positioning system, a preliminary investigation.* Conf Proc IEEE Eng Med Biol Soc, vol. 2, 2004. (Cited on page 29.)

[Feng 2011] L. Feng, M. Hagiwara, H. Uvet, Y. Yamanish, T. Kawahara, K. Kosuge et F. Arai. *High-speed delivery of microbeads in microchannel using magnetically driven microtool.* In Solid-State Sensors, Actuators and Microsystems Conference (TRANSDUCERS), 2011 16th International, pages 1312–1315, 2011. (Cited on page 5.)

[Fisher 1935] R. A. Fisher. The design of experiments. Olyver and Boyd Edinburgh, 1935. (Cited on pages 70 and 71.)

[Fitton 2007] I. Fitton, R.J.H.M. Steenbakkers, L. Zijp, J.C. Duppen, E.F.I. Comans, S.H. Muller, P.J.C.M. Nowak, C.R.N. Rasch et M. van Herk. *Retrospective attenuation correction of PET data for radiotherapy planning using a free breathing CT.* Radiotherapy & Oncology, vol. 83, no. 1, pages 42–48, April 2007. (Cited on page 29.)

[Fluckiger 2007] M. Fluckiger et B.J. Nelson. *Ultrasound Emitter Localization in Heterogeneous Media.* In Engineering in Medicine and Biology Society, 2007. EMBS 2007. 29th Annual International Conference of the IEEE, pages 2867–2870, 2007. (Cited on page 30.)

[Fountain 2010] T.W.R. Fountain, P.V. Kailat et J.J. Abbott. *Wireless control of magnetic helical microrobots using a rotating-permanent-magnet manipulator*. In Robotics and Automation (ICRA), 2010 IEEE International Conference, pages 576 –581, may 2010. (Cited on pages 28 and 55.)

[Furlani 2001] E.P. Furlani. Permanent magnet and electromechanical devices: Materials, analysis, and applications. Electromagnetism. Elsevier Science, 2001. (Cited on page 55.)

[Gauthier 2010] M. Gauthier et S. Régnier. Robotic micro-assembly. IEEE press, 2010. (Cited on page 4.)

[Ghosh 2009] Ambarish Ghosh et Peer Fischer. *Controlled Propulsion of Artificial Magnetic Nanostructured Propellers*. Nano Letters, vol. 9, no. 6, pages 2243–2245, 2009. (Cited on pages 11, 12 and 17.)

[Goupy 2006] J. Goupy et L. Creighton. Introduction aux plans d'expériences - 3ème édition. Technique et ingénierie: Série conception. Dunod, 2006. (Cited on page 70.)

[Gray 1955] J. Gray et G. J. Hancock. *The Propulsion of Sea-Urchin Spermatozoa*. J Exp Biol, vol. 32, no. 4, pages 802–814, Décembre 1955. (Cited on page 21.)

[Guo 2008] Shuxiang Guo, Qinxue Pan et Mir Behrad Khamesee. *Development of a novel type of microrobot for biomedical application*. Microsyst. Technol., vol. 14, no. 3, pages 307–314, Janvier 2008. (Cited on page 10.)

[Hagiwara 2012] M. Hagiwara, T. Kawahara, T. Iijima, Y. Yamanishi et F. Arai. *High speed microrobot actuation in a microfluidic chip by levitated structure with riblet surface*. In Robotics and Automation (ICRA), 2012 IEEE International Conference on, pages 2517–2522, 2012. (Cited on page 5.)

[Hagiwara 2013] M. Hagiwara, T. Kawahara, T. Iijima et F. Arai. *High-Speed Magnetic Microrobot Actuation in a Microfluidic Chip by a Fine V-Groove Surface*. Robotics, IEEE Transactions on, vol. 29, no. 2, pages 363–372, 2013. (Cited on page 5.)

[Hammarstedt 2005] P. Hammarstedt, P. Sturm et A. Heyden. *Degenerate cases and closed-form solutions for camera calibration with one-dimensional objects*. In Computer Vision, 2005. ICCV 2005. Tenth IEEE International Conference on, volume 1, pages 317 – 324 Vol. 1, oct. 2005. (Cited on page 98.)

[Hartley 1997] Richard I. Hartley. *Self-calibration of stationary cameras*. International Journal of Computer Vision, vol. 22, pages 5–23, 1997. (Cited on page 98.)

[Hartley 2004] R. I. Hartley et A. Zisserman. Multiple view geometry in computer vision. Cambridge University Press, ISBN: 0521540518, second édition, 2004. (Cited on pages 98 and 118.)

[Hildebrand 1959] Milton Hildebrand. *Motions of the running cheetah and horse*. Journal of Mammalogy, vol. 40, no. 1, pages 481–495, 1959. (Cited on page 16.)

[Hill 1979] J. Hill et W.T. Park. *Real time control of a robot with a mobile camera.* In Proc. 9th ISIR, Washington, D.C., pages 233–246, Mar. 1979. (Cited on page 32.)

[Honda 1996] T. Honda, K.I. Arai et K. Ishiyama. *Micro swimming mechanisms propelled by external magnetic fields.* Magnetics, IEEE Transactions on, vol. 32, no. 5, pages 5085 –5087, sep 1996. (Cited on pages 14 and 22.)

[Horn 1986] B.K. Horn. Robot vision. The MIT Press McGraw-Hill Higher Education, 1st édition, 1986. (Cited on page 60.)

[Hu 2006] Chao Hu, M. Q-H Meng et M. Mandal. *The Calibration of 3-Axis Magnetic Sensor Array System for Tracking Wireless Capsule Endoscope.* In Intelligent Robots and Systems, 2006 IEEE/RSJ International Conference on, pages 162–167, 2006. (Cited on page 29.)

[Hutchinson 1996] S. Hutchinson, G.D. Hager et P.I. Corke. *A tutorial on visual servo control.* Robotics and Automation, IEEE Transactions on, vol. 12, no. 5, pages 651 –670, oct 1996. (Cited on pages 32, 33 and 34.)

[Hwang 2009] Gilgueng Hwang, Hideki Hashimoto, Dominik J. Bell, Lixin X. Dong, Bradley J. Nelson et S. Schon. *Piezoresistive InGaAs/GaAs Nanosprings with Metal Connectors.* Nano Letters, vol. 9, no. 2, pages pp. 554–561, February 2009. (Cited on pages 11 and 12.)

[Hwang 2010] G. Hwang, S. Haliyo et S. Régnier. *Remotely Powered Propulsion of Helical Nanobelts.* In Robotics Science and Systems, 2010. (Cited on pages 11, 16, 29, 42 and 43.)

[Hwang 2011] G. Hwang, R. Braive, L. Couraud, A. Cavanna, O. Abdelkarim, I. Robert-Philip, A. Beveratos, I. Sagnes, S. Haliyo et S. Régnier. *Electro-osmotic propulsion of helical nanobelt swimmers.* The International Journal of Robotics Research, vol. 30, no. 7, pages 806–819, 2011. (Cited on pages 11, 16, 25, 44 and 74.)

[Hwang 2013] Gilgueng Hwang, Ioan Alexandru Ivan, Joel Agnus, Hugo Salmon, Sébastien Alvo, Nicolas Chaillet, Stéphane Régnier et Anne-Marie Haghiri-Gosnet. *Mobile microrobotic manipulator in microfluidics.* Sensors and Actuators A: Physical, 2013. (Cited on page 5.)

[Hwang 2014] G. Hwang, A. Ivan, J. Agnus, H. Salmon, S. Alvo, N. Chaillet, S. Régnier et AM Gosnet-Haghiri. *Mobile microrobotic manipulator in microfluidics.* Sensors and Actuators: A. Physical, 2014. to appear. (Cited on page 26.)

[Ishiyama 2000] K. Ishiyama, K.I. Arai, M. Sendoh et A. Yamazaki. *Spiral-type micro-machine for medical applications.* In Micromechatronics and Human Science, 2000. MHS 2000. Proceedings of 2000 International Symposium on, pages 65 –69, 2000. (Cited on pages 14, 16 and 22.)

[Ishiyama 2001a] K. Ishiyama, M. Sendoh, A. Yamazaki et K.I. Arai. *Swimming micromachine driven by magnetic torque*. Sensors and Actuators A: Physical, vol. 91, no. 1-2, pages 141 – 144, 2001. Third European Conference on Magnetic Sensors & Actuators. (Cited on pages 14 and 75.)

[Ishiyama 2001b] K. Ishiyama, M. Sendoh, A. Yamazaki, M. Inoue et K.I. Arai. *Swimming of magnetic micro-machines under a very wide-range of Reynolds number conditions*. Magnetics, IEEE Transactions on, vol. 37, no. 4, pages 2868 –2870, jul 2001. (Cited on page 14.)

[Ivan 2013] A. Ivan, G. Hwang, J. Agnus, N. Chaillet et S. Régnier. *MagPieR: The fastest mobile microrobots in the world.* In NIST Micrororobotics Challenge, pages 63–70, 2013. (Cited on page 26.)

[Jacobson 2003] S. A. Jacobson et A. H. Epstein. *An informal survey of power MEMS*. In The International Symposium on Micro-Mechanical Engineering, volume 12, pages 513–519, Janvier 2003. (Cited on page 24.)

[Jiles 1998] D. Jiles. Introduction to magnetism and magnetic materials; 2nd ed. Chapman and Hall, Boca Raton, FL, 1998. (Cited on page 25.)

[Kalambur 2005] Venkatasubramaniam S. Kalambur, Bumsoo Han, Bruce E. Hammer, Thomas W. Shield et John C. Bischof. *In vitro characterization of movement, heating and visualization of magnetic nanoparticles for biomedical applications*. Nanotechnology, vol. 16, no. 8, pages 1221–1233, Août 2005. (Cited on page 29.)

[Kim 1991] Sangtae Kim et Seppo J. Karrila. Microhydrodynamics: Principles and selected applications. Butterworth-Henemann, Boston, Juin 1991. (Cited on page 7.)

[Kratochvil 2009] B.E. Kratochvil, L.X. Dong et B.J. Nelson. *Real-time Rigid-Body Visual Tracking in a Scanning Electron Microscope*. International Journal of Robotics Research, vol. 28, no. 4, pages 498–511, March 2009. (Cited on pages 34 and 35.)

[Kummer 2010] M.P. Kummer, J.J. Abbott, B.E. Kratochvil, R. Borer, A. Sengul et B.J. Nelson. *OctoMag: An Electromagnetic System for 5-DOF Wireless Micromanipulation*. Robotics, IEEE Transactions on, vol. 26, no. 6, pages 1006 –1017, dec. 2010. (Cited on pages 26 and 27.)

[Lauga 2009] E. Lauga et T.R. Powers. *The hydrodynamics of swimming microorganisms*. Reports on Progress in Physics, vol. 72, no. 9, page 096601, 2009. (Cited on pages 7 and 44.)

[Laumond 2001] Jean-Paul Laumond, editeur. La robotique mobile. Traité IC2. Hermés science, Paris, 2001. (Cited on page 122.)

[Lee 2009] Ju-Sung Lee, Byungkyu Kim et Yeh-Sun Hong. *A flexible chain-based screw propeller for capsule endoscopes*. International Journal of Precision Engineering and Manufacturing, vol. 10, no. 4, pages 27–34, 2009. (Cited on page 55.)

[Lighthill 1976] James Lighthill. *Flagellar Hydrodynamics.* SIAM Review, vol. 18, no. 2, pages 161–230, 1976. (Cited on page 21.)

[Mack 2001] MJ Mack. *MInimally invasive and robotic surgery.* JAMA, vol. 285, no. 5, pages 568–572, 2001. (Cited on page 5.)

[Mahoney 2011] Arthur W. Mahoney, John C. Sarrazin, Eberhar Bamberg et Jake J. Abbott. *Velocity Control with Gravity Compensation for Magnetic Helical Microswimmers.* Advanced Robotics, vol. 25, no. 8, pages 1007–1028, 2011. (Cited on pages 11, 17, 18, 23, 24 and 28.)

[Mahoney 2012a] A.W. Mahoney et J.J. Abbott. *Control of untethered magnetically actuated tools with localization uncertainty using a rotating permanent magnet.* In Biomedical Robotics and Biomechatronics (BioRob), 2012 4th IEEE RAS EMBS International Conference on, pages 1632 –1637, june 2012. (Cited on page 55.)

[Mahoney 2012b] A.W. Mahoney, D.L. Cowan, K.M. Miller et J.J. Abbott. *Control of untethered magnetically actuated tools using a rotating permanent magnet in any position.* pages 3375–3380. IEEE, 2012. (Cited on pages 28, 55 and 56.)

[Malis 1999] Ezio Malis, François Chaumette et Sylvie Boudet. *2 1/2 D Visual Servoing.* Robotics and automation, IEEE Transactions on, vol. 15, pages 238–250, 1999. (Cited on page 34.)

[Marchand 2005] E. Marchand, F. Spindler et F. Chaumette. *ViSP for visual servoing: a generic software platform with a wide class of robot control skills.* Robotics Automation Magazine, IEEE, vol. 12, no. 4, pages 40 –52, dec. 2005. (Cited on page 60.)

[Marey 2010] Mohammed Marey. *Contributions to control modeling in visual servoing, task redundancy, and joint limits avoidance.* These, Université Rennes 1, Décembre 2010. (Cited on page 34.)

[Martel 2009] Sylvain Martel, Mahmood Mohammadi, Ouajdi Felfoul, Zhao Lu et Pierre Pouponneau. *Flagellated Magnetotactic Bacteria as Controlled MRI-trackable Propulsion and Steering Systems for Medical Nanorobots Operating in the Human Microvasculature.* The International Journal of Robotics Research, vol. 28, no. 4, pages 571–582, 2009. (Cited on pages 24 and 29.)

[Mason 2003] Robert L. Mason, Richard F. Gunst et James L. Hess. Statistical design and analysis of experiments. WILEY SERIES IN PROBABILITY AND STATISTICS. WILEY & SONS, 2nd édition, 2003. (Cited on page 70.)

[McNeil 1995] R.G. McNeil, Rogers C. Ritter, B. Wang, M.A. Lawson, G.T. Gillies, K.G. Wika, E.G. Quate, III Howard M.A. et M.S. Grady. *Characteristics of an improved magnetic-implant guidance system.* Biomedical Engineering, IEEE Transactions on, vol. 42, no. 8, pages 802–808, 1995. (Cited on page 26.)

[Medioni 2004] Gerard Medioni et Sing Bing Kang. Emerging topics in computer vision. Prentice Hall PTR, Upper Saddle River, NJ, USA, 2004. (Cited on page 98.)

[Melle 2003] S. Melle, O.G. Calder¨®n, M.A. Rubio et G.G. Fuller. *Microstructure evolution in magnetorheological suspensions governed by Mason number.* Phys Rev E Stat Nonlin Soft Matter Phys, vol. 68, no. 4 Pt 1, page 041503, 2003. (Cited on page 10.)

[Mikawa 1996] M. Mikawa, K. Yoshida, M. Kubota et T. Morimitsu. *Visual servoing for micro mass axis alignment device.* In Intelligent Robots and Systems '96, IROS 96, Proceedings of the 1996 IEEE/RSJ International Conference on, volume 3, pages 1091–1096 vol.3, 1996. (Cited on page 35.)

[Miller 2012] K.M. Miller, A.W. Mahoney, T. Schmid et J.J. Abbott. *Proprioceptive magnetic-field sensing for closed-loop control of magnetic capsule endoscopes.* In Intelligent Robots and Systems (IROS), 2012 IEEE/RSJ International Conference on, pages 1994–1999, 2012. (Cited on page 28.)

[Nelson 2010] B.J. Nelson, I.K. Kaliakatsos et J.J. Abbott. *Microrobots for Minimally Invasive Medicine.* Annual Review of Biomedical Engineering, vol. 12, no. 1, pages 55–85, 2010. (Cited on pages 5, 6 and 29.)

[Peyer 2013] K.E. Peyer, L. Zhang et B.J. Nelson. *Bio-inspired magnetic swimming microrobots for biomedical applications.* Nanoscale, vol. 5, no. 4, pages pp. 1259–1272, 2013. (Cited on page 13.)

[Purcell 1977] E.M. Purcell. *Life at low Reynolds number.* American Journal of Physics, vol. 45, no. 1, pages 3–11, 1977. (Cited on pages 6, 7, 8, 9 and 21.)

[Purcell 1997] E.M. Purcell. *The efficiency of propulsion by a rotating flagellum.* Proc Natl Acad Sci U S A, vol. 94, no. 21, pages 11307–11, 1997. (Cited on page 22.)

[Rankin 2005] S. Rankin. *CT and MRI.* Surgery, vol. 23, no. 5, pages pp. 162–165, 2005. (Cited on page 29.)

[Roper 2006] Marcus Roper, Rémi Dreyfus, Jean Baudry, Marc Fermigier, Jérôme Bibette, Howard A Stone*et al.* *On the dynamics of magnetically driven elastic filaments.* Journal of Fluid Mechanics, vol. 554, pages 167–190, 2006. (Cited on page 10.)

[Samson 1991] C. Samson, M.L. Borgne et B. Espiau. Robot control: the task function approach. Oxford engineering science series. Clarendon Press, 1991. (Cited on page 131.)

[Samson 1995] Claude Samson. *Control of chained systems application to path following and time-varying point-stabilization of mobile robots.* Automatic Control, IEEE Transactions on, vol. 40, no. 1, pages 64–77, 1995. (Cited on page 122.)

[Sanchez 2011] S Sanchez, AA Solovev, SM Harazim et OG Schmidt. *Microbots Swimming in the Flowing Streams of Microfluidic Channels*. Journal of the American Chemical Society, vol. 133, no. 4, pages 701–703, 2011. (Cited on page 5.)

[Sanderson 1980] A. C. Sanderson et L. Weiss. *Image-based visual servo control using relational graph error signals*. In 1980 Interaltional conference on cybernetics and society, 1980. (Cited on page 32.)

[Schick 2005] Fritz Schick. *Whole-body MRI at high field: technical limits and clinical potential*. Eur. Radiol., vol. 15, no. 5, pages pp. 946–959, 2005. (Cited on page 29.)

[Sievers 2005] T. Sievers et S. Fatikow. *Visual servoing of a mobile microrobot inside a scanning electron microscope*. In Intelligent Robots and Systems, 2005. (IROS 2005). 2005 IEEE/RSJ International Conference on, pages 1350–1354, 2005. (Cited on page 30.)

[Sleigh 1988] M. A. Sleigh, J. R. Blake et N. Liron. *The propulsion of mucus by cilia.* The American review of respiratory disease, vol. 137, no. 3, pages 726–741, Mars 1988. (Cited on page 7.)

[Sturm 1999] P.F. Sturm et S.J. Maybank. *On plane-based camera calibration: A general algorithm, singularities, applications*. In Computer Vision and Pattern Recognition, 1999. IEEE Computer Society Conference on., volume 1, pages 2 vol. (xxiii+637+663), 1999. (Cited on page 98.)

[Tamadazte 2009] B. Tamadazte, T. Arnould, S. Dembele, N. Le Fort-Piat et E. Marchand. *Real-time vision-based microassembly of 3D MEMS*. In Advanced Intelligent Mechatronics, 2009. AIM 2009. IEEE/ASME International Conference on, pages 88–93, 2009. (Cited on page 35.)

[Tendick 1998] F. Tendick, S.S. Sastry, R.S. Fearing et M. Cohn. *Applications of micromechatronics in minimally invasive surgery*. Mechatronics, IEEE/ASME Transactions on, vol. 3, no. 1, pages 34–42, 1998. (Cited on page 5.)

[Thuilot 2002] B. Thuilot, C. Cariou, P. Martinet et M. Berducat. *Automatic Guidance of a Farm Tractor Relying on a Single CP-DGPS*. Auton. Robots, vol. 13, no. 1, pages 53–71, Juillet 2002. (Cited on page 122.)

[Tottori 2012] S. Tottori, L. Zhang, F. Qiu, K. Krawczyk, A. Franco-Obreg¨®n et B.J. Nelson. *Magnetic Helical Micromachines: Fabrication, Controlled Swimming, and Cargo Transport*. Advanced Materials, vol. 24, no. 6, pages pp. 811–816, February 2012. highlighted as the front cover. (Cited on pages 13, 18 and 19.)

[Truper 2004] T. Truper, A. Kortschack, M. Jahnisch, H. Hulsen et S. Fatikow. *Transporting cells with mobile microrobots*. Nanobiotechnology, IEE Proceedings -, vol. 151, no. 4, pages 145–150, 2004. (Cited on page 5.)

[Vilkomerson 1997] D. Vilkomerson et David Lyons. *A system for ultrasonic beacon-guidance of catheters and other minimally-invasive medical devices*. Ultrasonics,

Ferroelectrics and Frequency Control, IEEE Transactions on, vol. 44, no. 2, pages 496–504, 1997. (Cited on page 30.)

[Williams 2014] Brian J Williams, Sandeep V Anand, Jagannathan Rajagopalan et M Taher A Saif. *A self-propelled biohybrid swimmer at low Reynolds number.* Nat Commun, vol. 5, page 3081, 2014. (Cited on page 10.)

[Xie 2012] H. Xie et S. Régnier. *High-Efficiency Automated Nanomanipulation with Parallel Imaging/Manipulation Force Microscopy.* IEEE Transaction on Nanotechnology, vol. 11, no. 1, pages 21 – 33, 2012. (Cited on page 4.)

[Xu 2005] Xiao-Chen Xu, Chang-Hong Hu, Lei Sun, J. Yen et K.K. Shung. *High-frequency high frame rate ultrasound imaging system for small animal imaging with linear arrays.* In Ultrasonics Symposium, 2005 IEEE, volume 3, pages 1431–1434, 2005. (Cited on page 30.)

[Xu 2012] T. Xu, G. Hwang, N. Andreff et S. Régnier. *Scaled-Up Helical Nanobelt Modeling and Simulation at Low Reynolds Numbers.* In ICRA'12 IEEE International Conference on Robotics and Automation, pages 4045 – 4051, 2012. (Cited on pages 22, 28 and 42.)

[Yesin 2006] Kemal Berk Yesin, Karl Vollmers et Bradley J. Nelson. *Modeling and control of Untethered Biomicrorobots in a Fluidic environment using Electromagnetic Fields.* International Journal of Robotics Research, vol. 25, no. 5-6, pages 527–536, 2006. (Cited on page 26.)

[Zhang 2000] Z. Zhang. *A flexible new technique for camera calibration.* Pattern Analysis and Machine Intelligence, IEEE Transactions on, vol. 22, no. 11, pages 1330 – 1334, nov 2000. (Cited on page 98.)

[Zhang 2004] Zhengyou Zhang. *Camera calibration with one-dimensional objects.* Pattern Analysis and Machine Intelligence, IEEE Transactions on, vol. 26, no. 7, pages 892 –899, july 2004. (Cited on page 98.)

[Zhang 2009a] L. Zhang, J.J. Abbott, L. Dong, B.E. Kratochvil, D. Bell et B.J. Nelson. *Artificial bacterial flagella: Fabrication and magnetic control.* Appl. Phys. Lett., vol. 94, no. 6, 2009. (Cited on pages 4, 15, 22, 26 and 35.)

[Zhang 2009b] L. Zhang, J.J. Abbott, L. Dong, K.E. Peyer, B.E. Kratochvil, H. Zhang, C. Bergeles et B. J. Nelson. *Characterizing the Swimming Properties of Artificial Bacterial Flagella.* Nano Letters, vol. 9, pages 3663–3667, Octobre 2009. (Cited on pages 11, 15, 22 and 75.)

[Zhang 2010a] L. Zhang, K.E. Peyer et B.J. Nelson. *Artificial bacterial flagella for micromanipulation.* Lab Chip, vol. 10, pages 2203–2215, 2010. (Cited on pages 11, 13, 15 and 28.)

[Zhang 2010b] L. Zhang, K.E. Peyer, T. Petit, B.E. Kratochvil et B.J. Nelson. *Motion control of artificial bacterial flagella.* In Nanotechnology (IEEE-NANO), 2010 10th IEEE Conference on, pages 893 –896, aug. 2010. (Cited on page 15.)

[Ziegler 1942] J. G. Ziegler et N. B. Nichols. *Optimum Settings for Automatic Controllers*. Transactions of ASME, vol. 64, pages 759–768, 1942. (Cited on page 58.)

Publications

1. **T. Xu**, G. Hwang, N. Andreff, and S. Régnier
   Modeling and Swimming Property Characterizations of Scaled-Up Helical Microswimmers.
   Mechatronics, IEEE/ASME Transactions on. vol.PP, no.99, pp.1,11, 0.

2. **T. Xu**, G. Hwang, N. Andreff, and S. Régnier
   The rotational propulsion characteristics of scaled-up helical microswimmers with different heads and magnetic positioning.
   Advanced Intelligent Mechatronics (AIM), 2013 IEEE/ASME International Conference on, pp.1114-1120, 9-12 July 2013, **Best Paper Finalist**

3. **T. Xu**, G. Hwang, N. Andreff, and S. Régnier
   Scaled-up helical nanobelt modeling and simulation at low reynolds numbers.
   Robotics and Automation (ICRA), 2012 IEEE International Conference on, pp.4045-4051, 14-18 May 2012

4. **T. Xu**, G. Hwang, N. Andreff, and S. Régnier
   Characterization of Three-dimensional Steering for Helical Swimmers.
   Robotics and Automation (ICRA), 2014 IEEE International Conference on, May 31 - June 7, 2014